CO_2 GEOLOGICAL STORAGE: HYDRO-CHEMO-MECHANICALLY COUPLED PHENOMENA AND ENGINEERED INJECTION

A Ph.D. Dissertation
Presented to
The Academic Faculty

by

Seunghee Kim

In Partial Fulfillment
of the Requirements for the Degree
Ph.D. in the
School of Civil and Environmental Engineering

Georgia Institute of Technology
December 2012

CO_2 GEOLOGICAL STORAGE: HYDRO-CHEMO-MECHANICALLY COUPLED PHENOMENA AND ENGINEERED INJECTION

Approved by:

Dr. J. Carlos Santamarina, Advisor
School of Civil and Environmental Engineering
Georgia Institute of Technology

Dr. Susan E. Burns
School of Civil and Environmental Engineering
Georgia Institute of Technology

Dr. Christian Huber
School of Earth and Atmospheric Sciences
Georgia Institute of Technology

Dr. Costas Tsouris
School of Civil and Environmental Engineering
Georgia Institute of Technology

Dr. Guillermo Goldsztein
School of Mathematics
Georgia Institute of Technology

Date Approved: July 27, 2012

To my wife Jung Hyun Hong and daughter Sua Kim

ACKNOWLEDGEMENTS

I would like to express my sincere gratitude to my advisor, Dr. J. Carlos Santamarina, for giving me such a wonderful time in my life. He is a great academician, an outstanding teacher, and exceptional human being. Thank you for teaching me patience and endurance and pushing me beyond the boundaries of knowledge. I also thank the thesis dissertation committee members for their contribution and feedback.

Frequent discussion and interactions with Particulate Media Research Laboratory members enriched my research as well as my personal life: Hosung Shin, Douglas Cortes, Jongwon Jung, Nicolas Espinoza, Jaewon Jang, Changho Lee, Cesar Pasten, Sheng Dai, Minsu Cha, Lucio Cruz, Sylvain Cardon, Eunseok Bang, Alessio Savioli, Junbong Jang, Songhun Chong, Shahrzad Roshankhah, Marco Terzariol, Aswathy Sivaram, Efthymios Papadopoules, Xingwei Ren, Norimasa Yoshimoto, and Andrea Mezencevova. I am also sincerely grateful to all faculty members and colleagues in the Geo-Society.

I would like to acknowledge my Korean fellows in the School of Civil and Environmental Engineering for always supporting me. CRC members - Sihyun Kim and Sehoon Lee have been a great foundation to keep myself in shape to pursue a doctoral degree.

Without the support from my parents and parents-in-law, I could not finish this long journey. My daughter Sua has always been a great energy source. I thank for the endless support, love, and sacrifice of you, my love, Jung Hyun Hong. Finally, I am grateful for the love and guidance from my Lord.

TABLE OF CONTENTS

LIST OF TABLES

LIST OF FIGURES

SUMMARY

Global energy consumption will increase in the next decades and it is expected to largely rely on fossil fuels. The use of fossil fuels is intimately related to CO_2 emissions and the potential for global warming. Geological CO_2 storage aims to mitigate the global warming problem by sequestering CO_2 underground. Coupled hydro-chemo-mechanical phenomena determine the successful operation and long term stability of CO_2 geological storage.

This research explores various coupled phenomena, identifies different zones in the storage reservoir, and investigates their implications in CO_2 geological storage. Spatial patterns in mineral dissolution and precipitation are examined based on a comprehensive mass balance formulation. CO_2-dissolved fluid flow is modeled using a novel technique that couples laminar flow, advective and diffusive mass transport of species, mineral dissolution, and consequent pore changes to study the reactive fluid transport at the scale of a single rock fracture. The methodology is extended to the scale of a porous medium using pore network simulations to study both CO_2 reservoirs and caprocks. The two-phase flow problem between immiscible CO_2 and the formation fluid (water or brine) is investigated experimentally. Plug tests on shale and cement specimens are used to investigate CO_2 breakthrough pressure. Sealing strategies are explored to plug existing cracks and increase the CO_2 breakthrough pressure. Finally, CO_2-water-surfactant mixtures are evaluated to reduce the CO_2-water interfacial tension in view of enhanced sweep efficiency. Results can be used to identify optimal CO_2 injection and remediation strategies to maximize the efficiency of CO_2 injection and to attain long-term storage.

CHAPTER 1

INTRODUCTION

Fossil fuels have been a major energy source since the Industrial Revolution. The dependency on fossil fuels is expected to continue for the next several decades, until alternative energy sources satisfy anticipated energy demands. Carbon capture and sequestration CCS has emerged as a potential option for the more sustainable use of fossil fuels in the near future. In CCS, carbon dioxide CO_2 is captured at carbon emission sources and injected into geological formations. Two key criteria for the successful operation of geological CO_2 storage are injectivity and long-term system integrity. Both require careful understanding of complex hydro-chemo-mechanically coupled phenomena.

This thesis addresses emergent hydro-chemo-mechanically coupled phenomena, their implications on CO_2 geological storage, and the development of engineered CO_2 injection methods to improve sweep efficiency and storativity. The research approach is based on analytical solutions, numerical simulations, and complementary experimental studies. The research is organized into seven stand-alone chapters, followed by a chapter where global conclusions are identified.

Chapter 2 explores geotechnical concepts and implications of CO_2 geological storage. A comprehensive review of the water-CO_2-mineral system, reservoir conditions, and the fundamentals of CO_2 geological storage is followed by the identification of various hydro-chemo-mechanically coupled processes that may lead to emergent phenomena and increase the probability of geotechnical hazards. This chapter was developed in collaboration with D.N. Espinoza.

Chapter 3 identifies distinct regions in a CO_2 storage reservoir and their characteristic geochemical conditions. Each region is analyzed at equilibrium. Mass balance formulations that account for temperature, pressure, brine salinity, mineralogy, and porosity provide insight into the system response in different scenarios. The discussion addresses the impact of dissolution and precipitation on injectivity and system integrity.

Chapter 4 uses kinetic rate laws to investigate the evolution of a saline aquifers following CO_2 injection. The finite element method is used to simulate reactive fluid transport where CO_2-dissolved water flows through a rock fracture plane. The simulation couples laminar flow, selective mass transport of species, mineral dissolution, and consequent channel enlargement. Results help us understand the interactions between processes and parameters such as advection, diffusion, species concentration, and geometry at the pore scale during reactive fluid transport. The model can be readily extended to larger porous systems.

Chapter 5 develops a network simulation code for a reservoir system based on mineral dissolution and kinetic rate laws to upscale pore/joint scale results obtained in Chapter 4. Simulations examine CO_2-dissolved fluid transport through a porous reservoir for different Damköhler numbers, Peclet numbers, and heterogeneity of the porous network. Network simulations provide information such as the distribution of species concentration, the evolution of channel diameter, flow rate, pressure field, and permeability. Simulation results suggest that the reservoir may experience either compact dissolution or localized channel formation, depending on injection conditions.

Chapter 6 extends the previous study to the low-permeability cap rock layer. Preliminary analyses show that transversely homogeneous diffusive transport prevails over advective transport, hence, simulations are restricted to 1-D conditions. Simulations are conducted for two different mineralogies with end-member reactivities for typical field situations: calcium carbonate and kaolinite. Simulation results and analyses highlight the interplay between mineral reactivity/dissolution and diffusive transport.

Chapter 7 reports an experimental study designed to examine the transport of CO_2 through formations selected as barriers. Plugs cut from shale or prepared with well cement are tested to gain information on CO_2-breakthrough pressures and the main transport mechanisms. We devise a remediation method to seal discontinuities in the shale that can otherwise act as preferential paths for CO_2 leakage. Pressure tests after remediation treatments demonstrate that micron-size particles can fill cracks and increase the CO_2-breakthrough pressure.

Chapter 8 explores engineering CO_2 injection strategies to prevent viscous fingering and to improve sweep efficiency. This chapter begins with the evaluation of modified interfacial tension between CO_2 and water when adding surfactants. Pore-scale CO_2 injection experiments use a micro-model to provide insights on parameters that affect the sweep efficiency and the interface between the two fluid phases. Complementary network simulations support experimental observations and show different CO_2 displacement topologies.

Finally, salient observations from this thesis are summarized in Chapter 9.

CHAPTER 2

CO_2 GEOLOGICAL STORAGE – GEOTECHNICAL IMPLICATIONS

2.1 Introduction

Quality of life, in terms of education, infant mortality, and life expectancy, correlates with energy consumption. Global energy consumption will increase dramatically in the next decades, and it is expected to largely rely on fossil fuels because of the available reserves, their low cost, the investment in current infrastructure, and the still limited development of renewable energy. Currently, 90% of the total primary energy sources in the world are fossil fuels, and more than 85% in the USA (DOE, 2010).

The use of fossil fuels is intimately linked to the emission of CO_2 into the atmosphere. The current concentration of CO_2 in the atmosphere is ~385ppm (parts per million), which is almost twice the concentration before the Industrial Revolution (200 ppm - IPCC, 2001). Anthropogenic CO_2 global emissions add to ~7 GtC/year (see Figure 2.1). The USA releases 1.59 GtC/yr and China 1.78 GtC/yr – 2007 data (CDIAC, 2009). Power plants account for ~40% of total CO_2 emissions. Once released into the atmosphere, CO_2 enters into the global carbon cycle and interacts with the ocean and terrestrial sinks as shown in Figure 2.2.

The estimated net annual increase of CO_2 concentration in the atmosphere is problematic since CO_2 is a greenhouse gas. The mean surface temperature has increased ~0.6±0.2°C since the industrial revolution, and atmospheric models forecast as much as a ~3°C increase by 2100 if anthropogenic CO_2 emissions continue current trends (Figure 2.3).

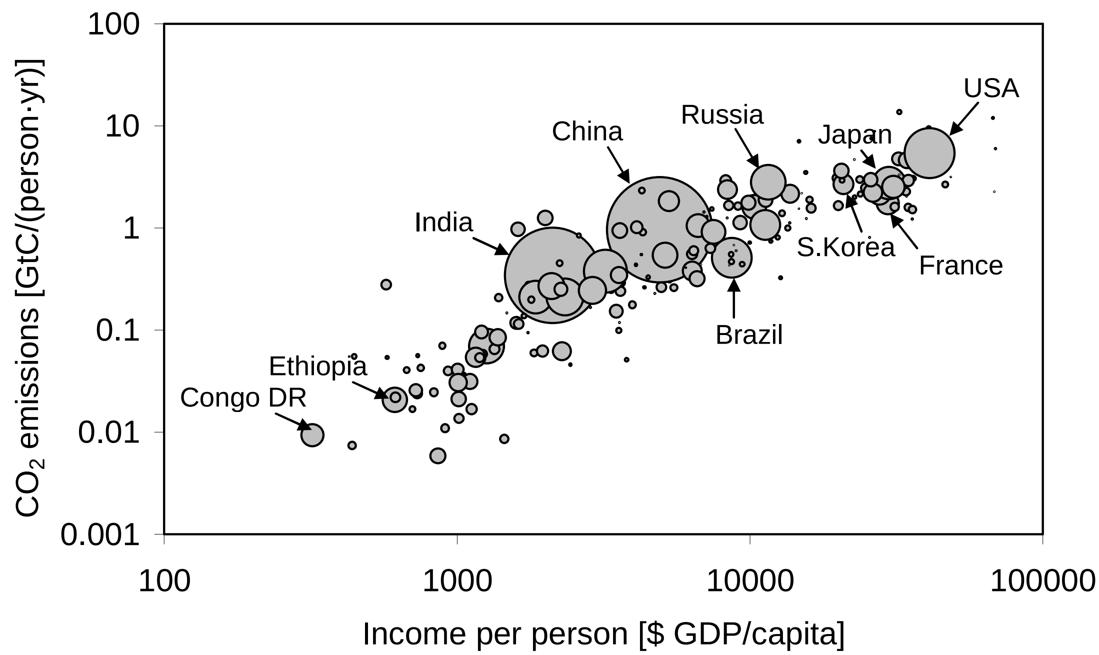

Figure 2.1 Annual CO_2 emissions per person as a function of Gross Domestic Product (adjusted for inflation) for different countries. Data from the Carbon Dioxide Information Analysis Center (www.cdiac.ornl.gov) and (www.gapminder.org).

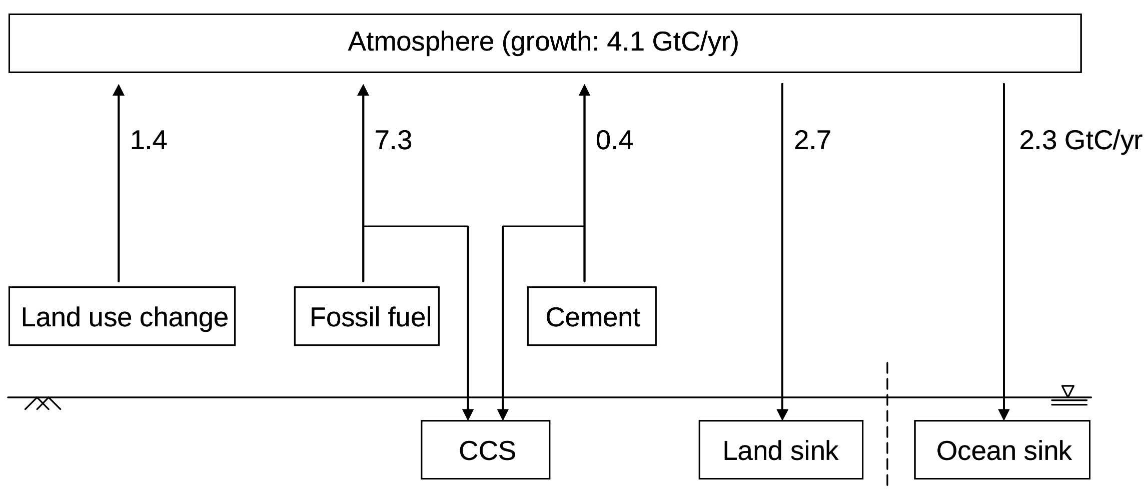

Figure 2.2 Anthropogenic perturbation of the carbon dioxide cycle – Values show the annual contribution of various components (data from: Global-Carbon-Project, 2010).

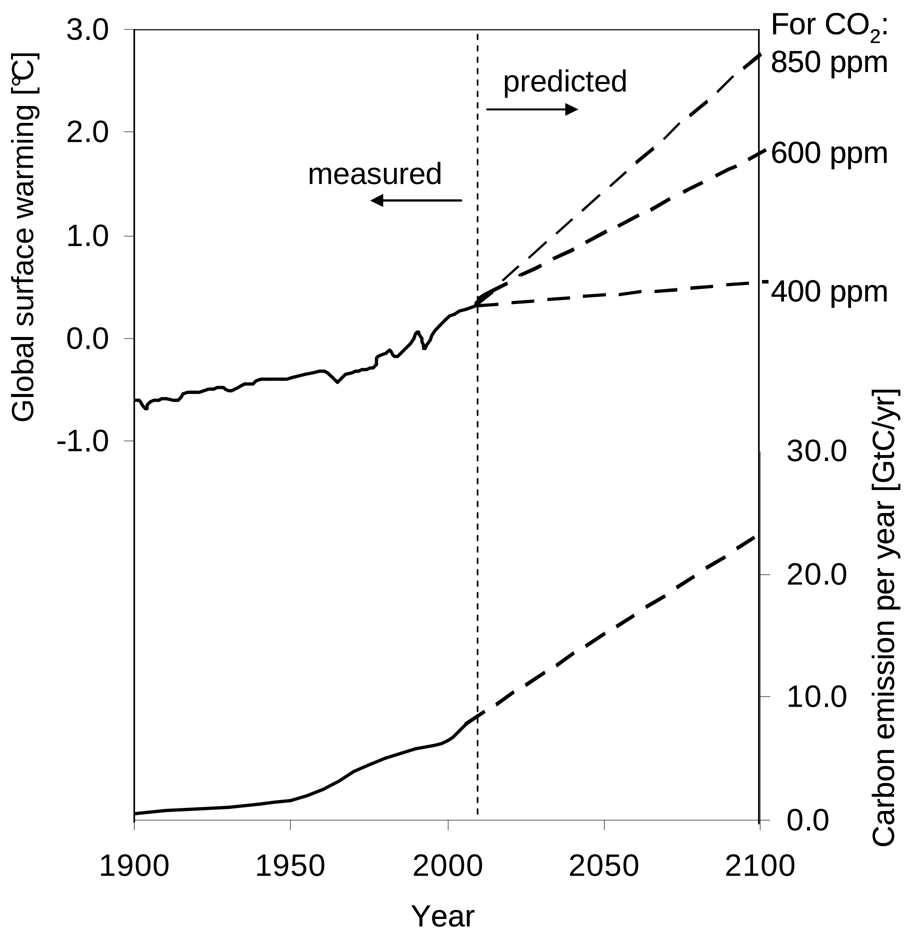

Figure 2.3 Past and extrapolated future CO_2 emissions (data from: Pacala and Socolow, 2004; World-Resources-Institute, 2010) and global warming predictions for different CO_2 levels (data from: Solomon, 2007).

The UN Framework Convention on climate change has suggested that the atmospheric concentration of CO_2 should not exceed 450ppm to prevent a major impact on climate conditions. Several technologies have been proposed for mitigating the emission of CO_2 into the atmosphere (Table 2.1). Two clear options call for reducing the combustion of fossil fuels, and capturing the generated CO_2 followed by permanent sequestration.

Table 2.1 CO_2 Emission Mitigation Technologies

CO_2 emission mitigation technology	Advantages	Difficulties	Capacity and certainty of execution
DIRECT - capture, transport, and final sequestration of CO_2 generated from fossil fuel power plants,			
CO_2 geological storage coupled or not with fuel switching	- Available injection technology - Large capacity - May give additional revenue by enhanced hydrocarbon production	- Cost: it needs additional energy consumption ~20% for carbon capture and storage (1) - Monitoring, contamination, and liability	- Large capacity: 10^3~10^4 $GtCO_2$, mostly in saline aquifers (2)
Ocean storage	- Easy and relatively inexpensive. - No porous media involved	- Water acidification and effects on aquatic life (3) - Transportation to the site	- Very large capacity >> 10^3 $GtCO_2$ (volume of the ocean deeper than ~3,000m)
Chemical carbonation	- Thermodynamically stable	- Expensive and labor intensive	- Very limited; for example: annual production of concrete is ~15Gt concrete
INDIRECT - produce CO_2-free energy, improve energy conservation and efficiency, or increase CO_2 natural uptake			
Alternative energy sources			
Renewables, Solar, Wind, Geothermal	- Almost C-free	- Small contribution to the energy portfolio	- Currently provide 4% of the energy demand (4)
Nuclear fission	- Almost C-free - Available technology	- Nuclear waste - Non-commercial use of nuclear power technology	- Currently provide 6% of the energy demand (4)
Biofuels	- Consume bio-products in excess, e.g. sugar cane and corn	- Competes with food supply	- In Brazil ethanol accounts for less than 5% of the energy production (5)
Conservation and efficiency			
Change in people's habits - e.g. promote mass transit	- Almost no cost	- Requires time and policy	- Some countries are already highly efficient.
More efficient end-use energy technologies and appliances - HVAC	- In progress	- It needs market-transforming policies (6)	- Efficient implementation could reduce carbon emissions from the building sector to levels equivalent to those 20 years ago.
CO_2 surface uptake			
Terrestrial uptake	- Relatively inexpensive	- Difficult to increase natural sinks (trees, algae) - Uncertainties about land use in the future (7)	- Currently at maximum - Uptake about ~20% of total emissions.

(1) (Heddle et al., 2003; Dooley et al., 2006); (2) (IPCC, 2005); (3) (Golomb, 1993; House et al., 2006); (4) (IEA, 2009); (5) (World-Resources-Institute, 2010); (6) (Brown and Southworth, 2006); (7) (Jaccard, 2005)

Suggested minimum storage time for CO_2 geological storage ranges between 1,000 and 10,000 years. This requirement is less demanding than for nuclear waste in part due to the expectation that future technological developments might find other methods to mitigate global warming, and because of natural climate fluctuations such as the average glacial cycle period of 28,000 years (Augustin et al., 2004). Figure 2.4 shows a comparison of time scales for different processes related to human activities and geologic processes relevant to energy. The dramatic contrast between political, engineering, and geological time scales add difficulty to short-time decision making.

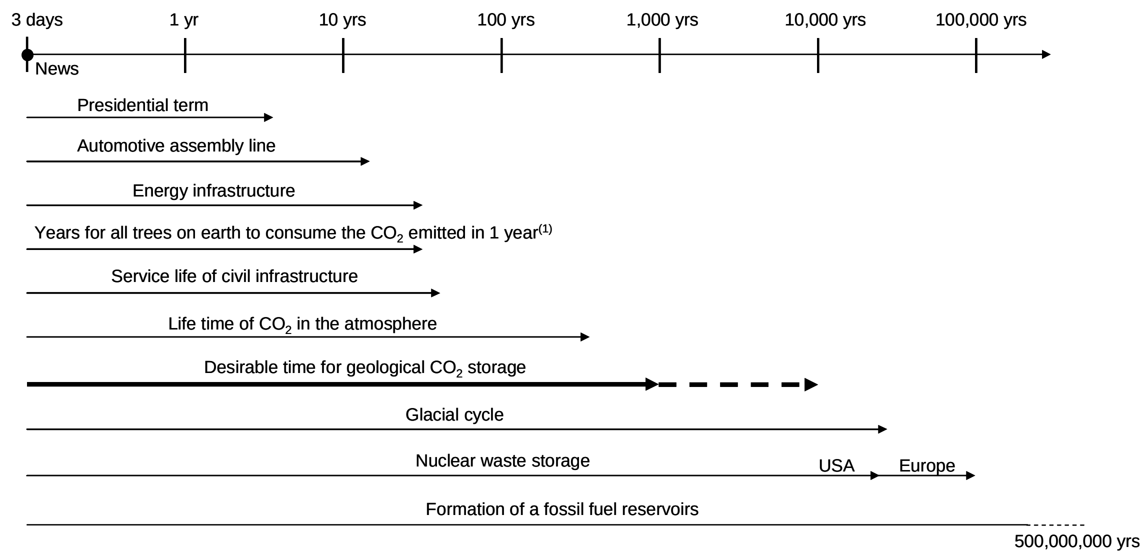

Figure 2.4 Time scales of relevant energy-related activities and processes (Note: (1) Estimation based on the capacity of forest to absorb carbon in the atmosphere, 0.17GtC/yr; from IPCC, 2001).

The purpose of this manuscript is to explore geotechnical concepts relevant to carbon dioxide geological storage. First, we review the chemo-physical properties of water-CO_2-mineral systems, reservoir conditions, and the fundamentals of CO_2 geological storage. Next, we explore various hydro-chemo-mechanical coupled processes that may lead to emergent phenomena and increase the probability of geotechnical hazards. Finally, we investigate potential geophysical strategies to monitor the evolution of CO_2 storage projects.

2.2 CO_2 Geological Storage and Reservoir Conditions

2.2.1 Volume Estimation

The injected CO_2 displaces the original fluids that fill the voids in geological formations. The volume of the geological formation V_{bulk} affected by the injection of a volume of CO_2 V_{CO2} is a function of the average porosity of the reservoir n:

$$V_{bulk} = \frac{1}{\psi} \frac{V_{CO2}}{n} \tag{1}$$

where the displacement efficiency coefficient is ψ~0.6 in media with spatially correlated random porosity and can be very low ψ<0.1 if fingered invasion takes place. Let's assume a target sequestration of 4GtC/year (for a flat trend based on present data – Figure 2.3). The total amount of CO_2 to be sequestered in the next 50 years is 200 GtC or 730 GtCO_2. In a compressed state (ρ_{CO2}~0.7 tonnes/m^3), this mass would occupy a volume V_{CO2} = 1,050 km^3. The geological volume for storage would be V_{bulk}~27,500km^3 for a porosity n~0.2, and displacement efficiency ψ=0.5. A 100m thick reservoir would extend ~325km in each direction.

2.2.2 CO_2 Trapping

The trapping mechanisms to keep CO_2 within deep geological formations rely on physical as well as chemical processes (IPCC, 2005; Jaccard, 2005; Dooley et al., 2006). Physical trapping mechanisms include structural and stratigraphic trapping by cap rocks, hydrodynamic trapping by slow aquifer currents, and capillary trapping by interfacial forces. Chemical trapping mechanisms include dissolution of CO_2 in water, mineralization, CO_2 adsorption on coal and rich-organic shales, and CO_2 hydrate formation. Most trapping mechanisms and safe disposal conditions are found and favored at depth. We note that there are natural accumulations of CO_2 in the Earth's upper crust where CO_2 has been contained for geological times such as the Ladbroke Grove and Katnook Gas Fields in southeastern Australia (Watson et al., 2004).

2.2.3 Geological Formations

Stable sedimentary basins facilitate CO_2 storage, particularly when they are near emission points. These basins are found in most continents (IPCC, 2005). The USA, Canada and Australia have extensive storage capacity (Dooley et al., 2006).

Favorable storage sites must have a thick accumulation of permeable sediments to maximize storage capacity and injectivity, overlain by a highly impermeable seal or cap rock (generally shale and evaporites).

The increase in effective stress with depth z leads to low porosity fine grained sediment barriers. Pore size depends on porosity and specific surface. In high specific surface montmorillonitic shales, the mean pore size can be in the order of 10^{-8}m (Hildenbrand et al., 2002; Armitage et al., 2010). High pore fluid pressure at depth also lowers the mass density difference between water and CO_2, increases the solubility of CO_2 in water, and increases the adsorption of CO_2 in coal.

The geological system should be structurally simple. Candidate storage sites are assessed for reservoir size, depth and hydrogeology, geology and petrophysical characteristics of the reservoir and the seal cap rock, surface temperature and geothermal gradient, tectonic stability and faulting intensity, accessibility, infrastructure, and proximity to major CO_2 sources.

Figure 2.5 shows schematic diagrams of various formations for CO_2 geological storage. The principal targets for CO_2 injection are deep saline aquifers and depleted/semi-depleted hydrocarbon reservoirs (which inherently include physical barriers and cap rocks). Injection into coal seams benefits from the co-production of CH_4. Similarly, hydrate-bearing sediments can also be used to sequester CO_2 while at the same time releasing CH_4 (a pilot test in the Alaska North Slope is planned for 2011, US DOE-

NETL, project DE-NT0006553). Deep saline aquifers are most abundant and could store 110 to 2700 GtC (Gale, 2004).

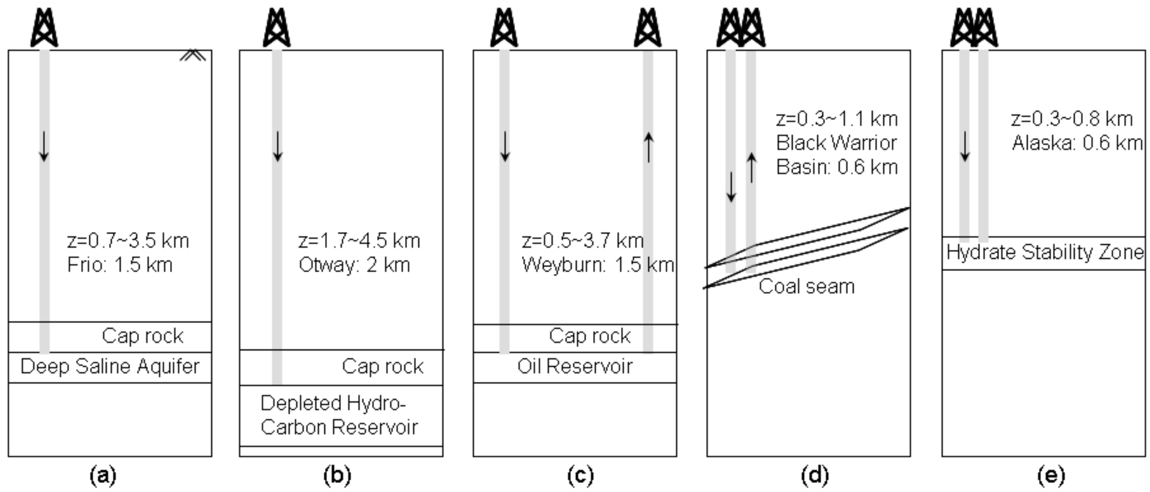

Figure 2.5 CO_2 storage alternatives. (a) Deep saline aquifers. (b) Depleted hydrocarbon reservoirs. (c) CO_2-enhanced oil recovery. (d) CO_2-enhanced gas recovery from coal bed methane. (e) CO_2-CH_4 replacement in hydrate bearing sediments. Depths shown for selected pilot projects.

2.2.4 Pilot Projects

There are more than 50 CO_2 injection projects reported worldwide (NETL, 2010). Figure 2.6 shows the mean pressure-temperature conditions at these storage sites. Most projects involve supercritical CO_2 and relatively small volumes.

2.2.5 Implementation

The injection of CO_2 underground can be implemented with technology developed for petroleum and gas production. In fact, acid gas injection is routinely done in Alberta, and CO_2-enhanced oil recovery is a common practice in oil reservoirs around the world, and there are more than ~5,000km of CO_2 pipelines in North America (Dooley et al., 2006). Still, the systematic geological storage of CO_2 will require improvements in risk assessment, adequate evaluation of regional capacity and reservoir integrity, matching emission sources with sinks, and enhanced monitoring technology (Gale, 2004). In addition to these technical difficulties, economical, political, and legal obstacles have hindered the adoption of carbon capture and sequestration (CCS) technologies.

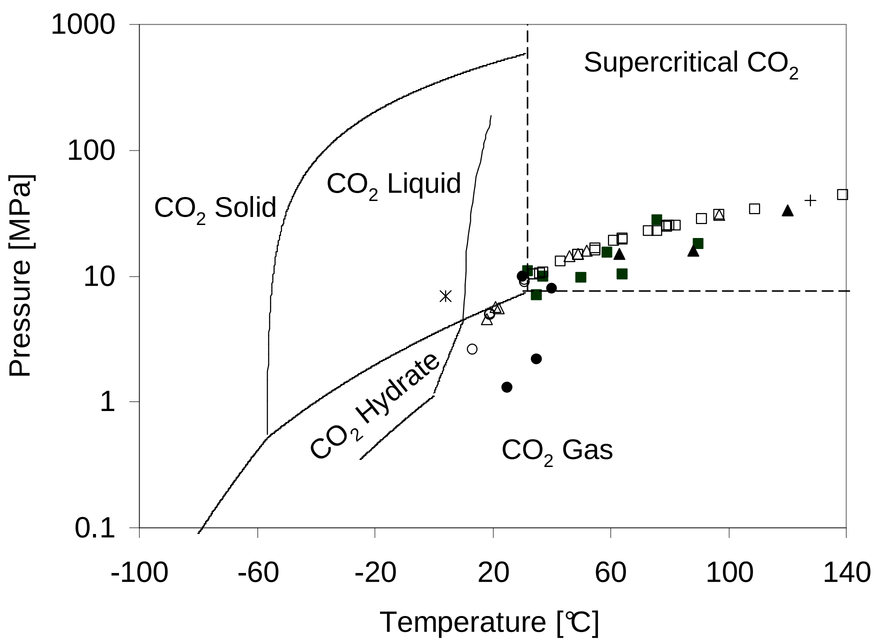

Saline aquifer: ■ P-T record □ Estimated value	CO_2-EOR: ▲ P-T record △ Estimated value	CO_2-ECBM: ● P-T record ○ Estimated value
EGR: +	CO_2-CH_4 replacement: ⚹	

Figure 2.6 Pressure-temperature dependent CO_2 phases. Pilot CO_2 injection projects are superimposed on this plot. Unless reported in the original sources, the PT conditions are estimated as: $P = g\,\rho_w\,z$, $T = T_0\,(4°C) + 30°C/km \cdot z$. ($CO_2$ hydrate phase boundary from: Takenouchi and Kennedy, 1965; Sloan and Koh, 2008).

2.3 Underlying Concepts and Implications

2.3.1 Geochemical Concepts

Properties of CO_2. The combustion of fossil fuels yields CO_2 among other byproducts. For example, burning methane produces

$$CH_4 + 2\ O_2 \rightarrow CO_2 + 2\ H_2O \qquad (2)$$

The physical properties of CO_2 depend on pressure-temperature P-T conditions. The CO_2 phase diagram is shown in Figure 2.6. CO_2 is a gas at normal temperature and pressure, it turns into liquid at moderate pressures ~6.4MPa at 298K, and becomes supercritical when the temperature is higher than 304.1K and the pressure is greater than 7.38 MPa. The mass density ρ of CO_2 varies widely, in fact, CO_2 is heavier than seawater at pressures above ~28MPa at 277.15K (ρ_{CO2}=1,035kg/m^3). Mass density can be approximated with a cubic equation of state (Peng and Robinson, 1976) or using more accurate but complex equations (Span and Wagner, 1996). The mass densities of water and CO_2 are plotted in Figure 2.7 for typical P-T conditions present in onshore and offshore applications.

Other important P-T dependent properties of CO_2 include high bulk compressibility, typically an order of magnitude higher than that of water (Span and Wagner, 1996), and very low viscosity, typically 10 times lower than that of water as shown in Figure 2.7 ($\mu_{CO2}=10^{-4}$ Pa·s at 10MPa and 280K - Fenghour et al., 1998).

Water-CO_2 interaction and properties. CO_2 dissolves in water to form aqueous carbon dioxide CO_2(aq). The solubility of CO_2 in water x_{CO2} [mol/L] can be estimated using Henry's law

$$x_{CO2} = k_H\ \varphi\ P_{CO2} \qquad (3)$$

where the Henry's coefficient is approximately $k_H \approx 10^{-1.46}=0.0347$ and the fugacity coefficient $\varphi \leq 1$ can be estimated with an equation of state. Water at room temperature and at 0.1MPa contains $x_{CO2} \approx 0.03$-to-0.04 mol/L. That solubility increases by two orders of magnitude x_{CO2}≈1-to-2 mol/L as pressure and temperature increase to reservoir conditions, i.e., one to two moles of CO_2 per liter of brine (Figure 2.8).

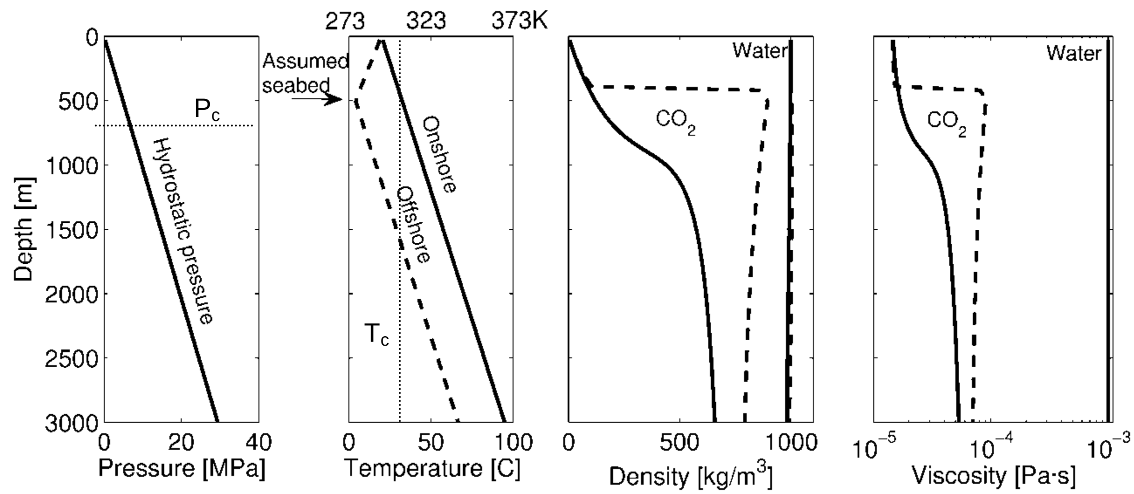

Figure 2.7 Density and viscosity of CO_2 and water as a function of depth, both on-shore and off-shore (for an assumed seabed at 500 m). P_c and T_c are the critical pressure and temperature for CO_2. Note: the density of liquid CO_2 exceeds the density of deep seawater when the seabed is deeper than 3000m.

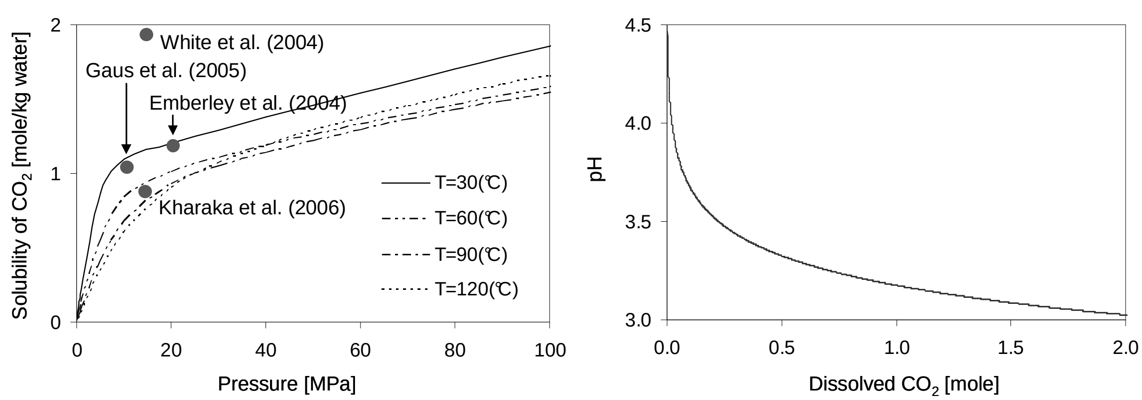

Figure 2.8 CO_2 solubility in water and pH. (a) CO_2 solubility in 1m NaCl aqueous solution (Note: an increase in salinity reduces CO_2 solubility). (b) pH as a function of dissolved CO_2 (Note: Solubility data from Duan and Sun, 2003).

Part of the aqueous carbon dioxide mixes with water to produce carbonic acid and ionizes stepwise:

$CO_2(g) \rightleftharpoons CO_2(aq)$ Henry's law (4)

$CO_2(aq) + H_2O(l) \rightleftharpoons H_2CO_3(aq) \rightleftharpoons H^+ + HCO_3^-(aq)$ $\log K_{eq} = -6.35$

$HCO_3^-(aq) \rightleftharpoons H^+ + CO_3^{2-}(aq)$ $\log K_{eq} = -10.33$

The final result of adding CO_2 to water is the production of ion bicarbonates, an increase in H^+, and a decrease in pH. At reservoir conditions, CO_2 dissolution in water yields a pH ≈ 3 (Figure 2.8).

Other relevant properties of the water-CO_2 system include (a) solubility of water in liquid and supercritical CO_2 (~0.05 mol of water per kg of liquid CO_2 at 10MPa and 285K - Spycher et al., 2003), (b) high diffusivity of water into liquid CO_2 ($D \approx$ 2-to-20x $10^{-8}m^2/s$ at 7-25MPa and 305±10K - Espinoza and Santamarina, 2010), and (c) CO_2 hydrate formation at high pressure and low temperature (Figure 2.6; Sloan and Koh, 2008).

Water-CO_2-Mineral interaction. Table 2.2 summarizes representative chemical reactions, typical reaction rates and related comments. The equilibrium constant for dissolution reaction denotes the concentration of produced species relative to the concentration of reactant species at steady state conditions, i.e., a function of mineral solubility. The solubility of minerals in water depends on pH (Stumm et al., 1996). Furthermore, the reaction rate of minerals in CO_2-water depends on temperature, pressure (i.e., CO_2 solubility and pH), and the concentration of other species (Fredd and Fogler, 1998; Pokrovsky et al., 2005; Renard et al., 2005; Algive et al., 2009). Dissolution rates for calcite $CaCO_3$, anorthite $CaAl_2Si_2O_8$, and kaolinite $Al_2Si_2O_5(OH)_4$ are plotted as a function of pH in Figure 2.9. Silicates yield more dissolved cations (pH up to 8) than carbonates (pH up to 5) but the reaction rate is much slower (Gunter et al., 2000). Consider 1 mm spheres of calcite, anorthite, and kaolinite submerged into water acidified by 1 mole of dissolved CO_2 per liter (pH~3). Using dissolution rates in Figure 2.9 and assuming that the system is far from equilibrium, the time required to dissolve each sphere is 4 hours for calcite, 16 years for anorthite, and 226 years kaolinite.

Table 2.2 Mineral reactions with CO_2-acidified water

Mineral	Typical reaction	Reaction rate	Notes
1) Silicates[a)]	$SiO_{2(s)} + 2H_2O \rightleftharpoons H_4SiO_4 \rightleftharpoons H^+ + H_3SiO_4^- \rightleftharpoons H^+ + H_2SiO_4^{2-}$	1.26×10^{-14} mol·m^{-2}s^{-1} (White et al., 2005)	·Solubility of quartz does not change with concentration of dissolved CO_2
2) Aluminosilicates[b)]	Anorthite: $CaAl_2Si_2O_{8(s)} + 8H^+ \rightleftharpoons Ca^{2+} + 2Al^{3+} + 2H_4SiO_4$, $K_{eq} = 10^{21.7}$ Kaolinite: $Al_2Si_2O_5(OH)_4(s) + 6H^+ \rightleftharpoons 2Al^{3+} + 2H_4SiO_4 + H_2O$, $K_{eq} = 10^{3.8}$	Anorthite: 1.2×10^{-5} mol·m^{-2}s^{-1} Oligiocalse: 1.2×10^{-8} mol·m^{-2}s^{-1} Albite: 3.6×10^{-9} mol·m^{-2}s^{-1} Kaolinite: 10^{-14}-to-10^{-15} mol·m^{-2}s^{-1} (Gaus et al., 2005)	·Include feldspars, micas, and clays. ·Reaction rate is slow. ·Yields more dissolved cations than carbonate. ·Results in pH up to 8.
3) Carbonates[c)]	$CaCO_{3(s)} + H^+ \rightleftharpoons Ca^{2+} + HCO_3^-$, $K_{eq} = 10^{1.85}$ $CaCO_{3(s)} + CO_2 + H_2O \rightleftharpoons Ca^{2+} + 2HCO_3^-$, $K_{eq} = 10^{-4.5}$ $CaCO_{3(s)} + H_2O \rightleftharpoons Ca^{2+} + HCO_3^- + OH^-$, $K_{eq} = 10^{-8.48}$	Calcite: 1.6-to-3.2×10^{-5} mol·m^{-2}s^{-1} (Brosse et al., 2005)	·Faster than aluminosilicates. ·Solubility depends on T, P, Salinity, ionic concentration, and pH. ·Dissolution rate is fast, but overall amount of reaction is small. ·Results in pH from 3 to 5

Sources: (a) Drever, 1997; (b) Li et al., 2006; (c) Stumm et al., 1996; Fredd and Fogler, 1998; Renard et al., 2005; Algive et al., 2009

CO_2 adsorption on organic surfaces. Coal and organic shales adsorb CO_2 (Larsen, 2004; NETL, 2010). Langmuir-type sorption isotherms are commonly used to characterize the kinetics of the reaction at pressures <10MPa (Ceglarska-Stefanska and Zarebska, 2002; Mazumder et al., 2006). For reference, about ~1.6 moles of CO_2 can be adsorbed per kg of coal at 3MPa and 298K (37 cm^3 of gas CO_2 at normal pressure and temperature per gram of coal). A higher fluid pressure promotes higher and faster uptake.

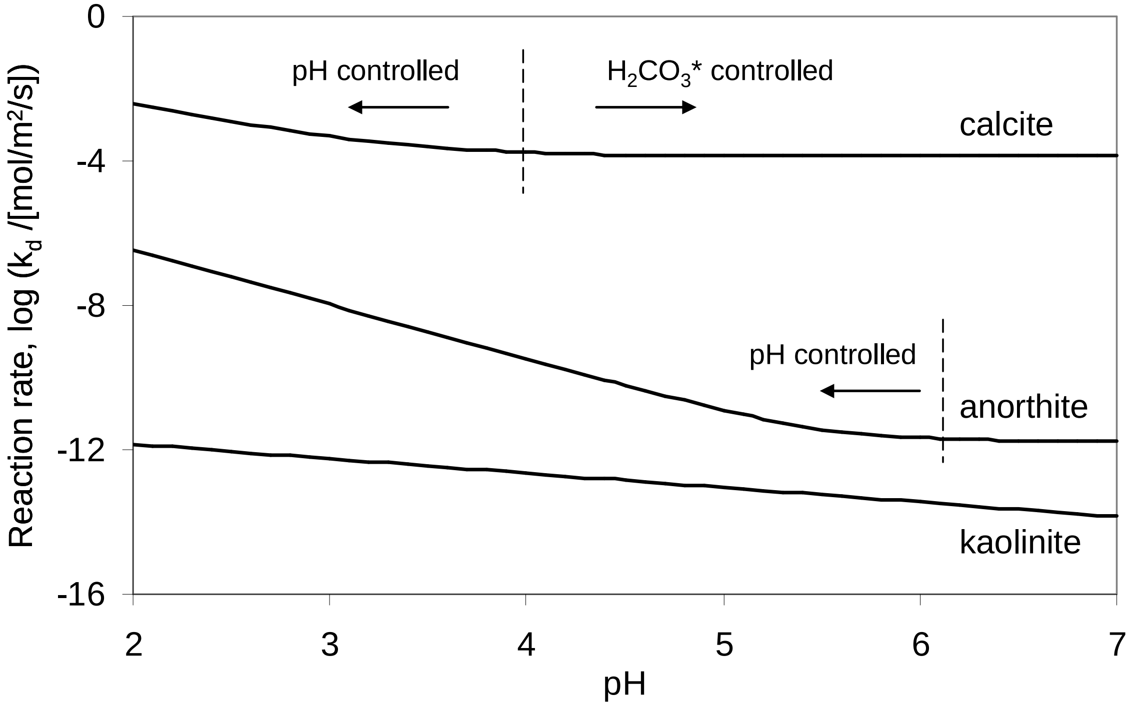

Figure 2.9 Reaction rate log (k_d/[mol/m^2/s]) for dissolution of calcite $CaCO_3$, anorthite $CaAl_2Si_2O_8$, and kaolinite $Al_2Si_2O_5(OH)_4$ at temperature T=40°C and fixed concentration of aqueous carbon dioxide [$CO_{2(aq)}$] = 1mol/L. For calcite, $k_d=k_1[H^+]+k_2[H_2CO_3*]$ where k_1=0.745mol/m^2/s, k_2=8.6x10^{-4}mol/m^2/s at T=40°C (Fredd and Fogler, 1998; Pokrovsky et al., 2005; Renard et al., 2005; Algive et al., 2009). For anorthite, $k_d=k_H[H^+]^{1.5}+k_{H2O}+k_{OH}[OH^-]^{0.33}$ where k_H=6.883x10^{-4}mol/m^2/s, k_{H2O}=3.58x10^{-12}mol/m^2/s, and k_{OH}=4.51x10^{-14}mol/m^2/s at T=40°C (Li et al., 2006). For kaolinite, $k_d=k_H[H^+]^{0.4}+k_{OH}[OH^-]^{0.3}$ where k_H=2.79x10^{-11}mol/m^2/s and k_{OH}=3.51x10^{-16}mol/m^2/s at T=40°C (Li et al., 2006).

Summary. High fluid pressure and temperature bring CO_2 into liquid or supercritical phases and promote CO_2 solubility in water and adsorption onto organic surfaces. In the presence of CO_2, water acidifies and more intense and faster mineral dissolution takes place. Liquid and supercritical CO_2 exhibit much lower viscosity than water.

2.3.2 Mixed Fluid Conditions

Pressure dependent T_s and θ. The water-CO_2 interfacial tension decreases from T_s~72 to 25mN/m as the pressure increases from 0.1MPa to 6.4MPa at ~298K, eventually T_s reaches a plateau at $T_s \approx 25 \pm 5$mN/m in the supercritical state (Kvamme et al., 2007; Espinoza and Santamarina, 2010). Furthermore, the contact angle formed by the CO_2-water interface on mineral surfaces varies with fluid pressure in response to changes in CO_2-water interfacial tension: as the fluid pressure increases, the contact angle increases on non-wetting surfaces such as oil-wet quartz and coal and slightly decreases in water-wet quartz and calcite surfaces (Chi et al., 1988; Dickson et al., 2006; Chiquet et al., 2007; Chalbaud et al., 2009; Espinoza and Santamarina, 2010).

Changes in interfacial tension T_s and contact angle θ will affect the capillary pressure, the evolution of flooding, the residual saturation, relative permeabilities, and capillary effects. In its simplest form, capillary pressure ΔP_c [Pa] is estimated from Laplace's equation:

$$\Delta P_c = P_{CO2} - P_w = \frac{2T_s}{r}\cos\theta \tag{5}$$

Breakthrough pressure. The breakthrough pressure P^*_{thru} when CO_2 percolates through a porous medium depends on the mean pore size expressed in terms of specific surface S_s and void ratio $e = e_{1kPa} - C_c \log(p'/1kPa)$, the wettability of the minerals in the presence of water and CO_2, and the standard deviation in pore size distribution. We can extend Laplace's capillary pressure equation to obtain the following expression for the breakthrough pressure (Espinoza and Santamarina, 2010):

$$P^*_{thru} = \psi \frac{S_s \rho T_s \cos\theta}{e_{1\mathrm{kPa}} - C_c \log \frac{p`}{1\mathrm{kPa}}} \tag{6}$$

where p' is the in situ effective stress, and the factor ψ depends on clay fabric and grain size distribution; a value of $0.04 \le \psi \le 0.08$ applies to smectite clay barriers. The sealing capacity of cap rocks will depend on this breakthrough pressure; thereafter, the leak rate will be determined by the cap rock permeability to CO_2 (Fleury et al., 2010; Pusch et al., 2010).

Differences in mass density – Convection and self mixing. CO_2 is lighter than water or brine at reservoir P-T conditions (Figure 2.7). The Bond number B quantifies gravity-driven CO_2 migration as a function of the mass density difference ($\rho_w - \rho_{CO2}$) relative to capillary forces $T_s \cdot \cos\theta$ (Pennell et al., 1996):

$$B = \frac{(\rho_w - \rho_{CO_2}) g k k_{rCO2}}{T_s \cos\theta} \tag{7}$$

The mass density of the water with CO_2 in solution ρ_{sol} [kg/m^3] is slightly heavier than the formation water and can be estimated from the mass density of pure water ρ_w [kg/m^3] and the concentration of CO_2 in water x_{CO2} [mol/m^3] as:

$$\rho_{sol} = \rho_w + m_{CO2} x_{CO2} - x_{CO2} \rho_w V_\varphi \tag{8}$$

where m_{CO2}[kg/mol] is the molecular weight of CO_2, and V_φ [m^3/mol] is the apparent molar volume of dissolved CO_2 as a function of temperature, $V_\varphi = 37.51 - 9.585 \cdot 10^{-2} T + 8.740 \cdot 10^{-4} T^2 - 5.044 \cdot 10^{-7} T^3$ (Garcia, 2001). For example, there is an increase in density $\Delta\rho \sim 10$kg/m^3, for water saturated with CO_2 at 10MPa and 313K ($x_{CO2} \sim 1{,}230$ moles/m^3). Dissolution-densification and gravity-driven flow will cause convective transport which will accelerate CO_2 mixing in the reservoir water (Riaz et al., 2006; Kneafsey and Pruess, 2010).

Differences in viscosity: Fingering. Two dimensionless numbers control the pattern of fluid displacement: (1) the ratio of viscosities M between the invading fluid μ_{CO2} and the displaced fluid μ_w, and (2) the capillary number C which is the ratio between viscous and capillary forces:

$$M = \frac{\mu_{CO2}}{\mu_w} \tag{9}$$

$$C = \frac{q \mu_{CO2}}{T_s \cos\theta} \tag{10}$$

where q[m^3/s/m^2] is the injection rate, T_s[N/m] is the interfacial tension between water and CO_2, and θ is the contact angle formed by the water-CO_2 interface and the mineral surface. Stable displacement takes place when M>1 and C>1, viscous fingering when M<<1, and capillary fingering when C<<1 (Lenormand et al., 1988). Since the viscosity of CO_2 is at least one order of magnitude lower than that of water at reservoir P-T conditions (Figure 2.7), CO_2 may displace water from the pore space in the form of viscous fingers; in this case, the bulk volume of sediment V_{bulk} involved in storage will increase dramatically (Equation 1).

CO_2 lowers the viscosity of oil. CO_2 dissolves in crude oil (typically alkanes with less than 13 carbon atoms at reservoir conditions with P>10MPa and T>320K), lowers the viscosity of the crude oil, and favors oil recovery (Blunt et al., 1993).

Summary. Interfacial tension and the capillary entry pressure for CO_2 into a water saturated seal cap rock decrease with pressure. The dissolution of CO_2 in water increases the density of water, promote gravity-driven flow and accelerate mixing. Pronounced differences in viscosity between liquid or supercritical CO_2 and water tend to promote viscous fingering during CO_2 injection.

2.3.3 Chemo-Hydro-Mechanical Coupling

Increased fluid pressure and fault reactivation. The increase in pore fluid pressure during CO_2 injection can reactivate nearby faults if the state of effective stress approaches failure conditions (Rutqvist and Tsang, 2002; Streit and Hillis, 2004).

Capillary-driven deformation. The invasion of immiscible CO_2 in a water saturated reservoir gives rise to capillary forces and can cause significant volumetric deformation in fine-grained sediments (Delage et al., 2008).

Fluid-driven fracture formation. Hydraulic fracture can take place in both cohesive-cemented and cohesionless-frictional sediments (Bjerrum et al., 1972; Jaworski et al., 1981; Zhai and Sharma, 2005). Particle-scale mechanisms compatible with the effective-stress dependent strength of sediments take into consideration capillary forces induced by the tensile membrane between CO_2 and water, seepage drag forces, and skeletal forces to explain particle displacement and localization (Shin and Santamarina, 2010).

Effects of pH and permittivity on interparticle electrical forces – Changes in clay fabric. Two fluid-mineral interactions anticipate changes in interparticle forces after CO_2 injection: (1) water acidification changes the mineral surface charge, and (2) the low permittivity of CO_2 (κ'~ 2 to 3) compared to water (κ'= 80) implies changes in van der Waal's attraction (Obriot et al., 1993; Palomino and Santamarina, 2005; Israelachvili, 2011). These fluid-mineral phenomena will alter the equilibrium between van der Waal's attraction and double layer repulsion forces at the clay platelet scale, cause changes in clay fabric, and affect the seal capacity of cap rocks.

Reactive fluid transport – Wormholes. Acidified water dissolves minerals and enlarges pores along transport channels (Emberley et al., 2004; Watson et al., 2004; Kaszuba et al., 2005). The hydraulic conductivity may increase by a factor of 10-to-100 (Verdon and Woods, 2007), with even small changes in global porosity, as can be predicted using the Kozeny-Carman model. Two dimensionless numbers control the evolution of dissolution patterns: Damköhler number represents the ratio between advection and reaction times $Da= \kappa l/v$ (reaction rate κ[1/s], characteristic length l[m], velocity v[m/s]), while the Peclet number is the ratio between advection and diffusion time $Pe=vl/D$ (diffusion coefficient D[m^2/s]). The process is mass-transfer limited if a chemical reaction is very fast compared to mass-transfer kinetics $Da>>1$ (e.g., more likely in the dissolution of carbonates). Otherwise, the process is reaction-rate limited $Da<<1$ (e.g., more likely if the dissolution of aluminosilicates is involved). The dissolution pattern during reactive transport can be categorized as face/global dissolution ($Da>10^{-3}$, $Pe<10^{-3}$), dominant wormholes ($Da>10^{-3}$, $Pe>10^{-2}$), or uniform dissolution ($Da<10^{-3}$) (Golfier et al., 2002). A rapid mineral dissolution rate combines with the inherent sediment heterogeneity to facilitate a dominant wormholes tendency (Fredd and Fogler, 1998). Wormhole formation would lead to marked CO_2 leakage.

Dissolution – Horizontal effective stress k_0 – Shear and tensile fractures. Complementary analytical, numerical (DEM and FEM), and experimental techniques show the effects of mineral dissolution and ensuing particle-level volume contraction on the evolution of the state of stress under constant overburden at zero-lateral strain boundary conditions during mineral dissolution. In particular, the stress ratio at zero lateral strain $k_0=\sigma'_h/\sigma'_v$ (Jaky, 1944; Mayne and Kulhawy, 1982) experiences a pronounced decrease during mineral dissolution, and it may reach the Rankine active failure condition k_a on the Coulomb failure plane (Shin and Santamarina, 2009). Strain localization along shear planes may follow (Shin et al., 2008). Furthermore, mineral dissolution causes sediment compaction, and the cap rock may experience bending and tensile failure.

Coal swelling pressure. Coal swells, its fluid conductivity decreases, and the effective stress increases with the adsorption of CO_2 (Somerton et al., 1975; Pekot and Reeves, 2002; Mazumder et al., 2006). Eventually, CO_2-CH_4 replacement in coal may become self-limiting because of coal swelling and reduced fracture porosity (Ceglarska-Stefańska and Zaręba, 2002).

Summary. The trapping mechanisms of CO_2 in geological formations rely on physical, chemical, and mechanical processes identified above. Each has different time and spatial scales. We summarize potential implications on CO_2 storage in Table 2.3.

Table 2.3 Coupling and emergent phenomena

Coupling	Emergent phenomenon
Multiphase fluid phenomena	- Relative hydraulic conductivities - Differences in mass density and buoyancy - Differences in viscosity and viscous fingering - Fluid segregation - Pressure dependent surface tension and contact angle - Percolation and break through pressure
Chemo-Hydro	- Reduction of oil viscosity by CO_2 - Dissolution followed by increased porosity and pore size - Reactive transport and wormhole formation - Spatial changes in hydraulic conductivity - Gravity-driven self mixing, CO_2 diffusion, pendular water, mineral precipitation - Coal CO_2 adsorption: reduced fluid conductivity and swelling pressure - Hydrate formation and depressurization: fluid volume expansion, possible gas-driven fractures
Hydro-Mechanical	- Increased fluid pressure and lower effective stress - Fault reactivation; hydraulic fracture of the cap rock - Capillarity-driven contraction - Fluid-driven fracture formation
Chemo-Mechanical	- pH and permittivity effects on DLVO, changes in clay fabric - Pressure solution/precipitation - Mineral dissolution and sediment compaction - Cap rock bending failure - Decrease in horizontal effective stress k_0. Shear fractures in contraction
Chemo-Hydro-Mechanical	- Combination of previous phenomena

2.4 Monitoring Strategies and Risk Assessment

CO_2 leakage from storage sites back into the atmosphere decreases the efficiency of CO_2 storage. Faults and abandoned wells are preferential flow paths that add to the slow transport and diffusion through otherwise continuous strata (Calabrese et al., 2006; Dooley et al., 2006; Leuning et al., 2008). Monitoring is required to assess the movement of CO_2 and to detect leaks. The design of a monitoring strategy must consider the large areal extent of CO_2 storage reservoirs (on the order of ~km^2) and account for spatial and temporal variability.

Potential monitoring methods, most of them already available for other applications, are summarized in Table 2.4. These monitoring methods take advantage of differences between physical properties (mass density, bulk stiffness, electrical resistivity and dielectric permittivity, and thermal characteristics), the detection of byproducts from chemical reactions, or coupled process effects such as subsidence or micro-seismicity. Tracers such as $\delta^{13}C$ and SF_6 may be included in the injected CO_2 to facilitate detection (Leuning et al., 2008). The most common subsurface geophysical methods for deep reservoir applications are based on elastic wave propagation and electrical resistivity (Kiessling et al., 2010; Nakatsuka et al., 2010). The following analysis expresses their applicability to CO_2 geological storage. The bulk modulus B_{mix} of the sediment can be estimated from the Biot-Gassman equation:

$$B_{mix} = B_{sk} + \left(1 - \frac{B_{sk}}{B_g}\right)^2 \left[n \left(\frac{S_w}{B_w} + \frac{S_{CO2}}{B_{CO2}} \right) + \frac{1-n}{B_g} - \frac{B_{sk}}{B_g^2} \right]^{-1} \tag{11}$$

where subindices represent the skeleton *sk*, the mineral that makes the grains *g*, the water *w*, and the CO_2. The density of the mixture is:

$$\rho_{mix} = (1-n)\rho_s + n(S_{CO2}\rho_{CO2} + S_w\rho_w) \tag{12}$$

Then, the compressional V_P and shear V_S wave velocities are:

$$V_P = \sqrt{\left(\frac{B_{mix} + 4/3 \cdot G_{sk}}{\rho_{mix}} \right)} \tag{13}$$

$$V_S = \sqrt{\frac{G_{sk}}{\rho_{mix}}} \tag{14}$$

where G_{sk} is the shear modulus of the mineral skeleton.

The electrical conductivity of a geological formation depends on the concentration and mobility of hydrated ions in the pore fluid and the volume fraction of fluid in the formation (Santamarina, 2001). The injection of CO_2 displaces the electrolyte (conductivity σ_{fl}) and the formation conductivity can be estimated using the Archie's equation (Mavko et al., 2009):

$$\sigma_{form} = \sigma_{fl} \left[n(S_{perc} - S_{CO2}) \right]^{\beta} \tag{15}$$

where $S_{CO2} \leq S_{perc}$, the maximum saturation of CO_2 at percolation. Figure 2.10 shows the variation of P-wave velocity V_P[m/s] and electrical conductivity σ_{form} as a function of the CO_2 saturation S_{CO2}. Because CO_2 is non conductive and has a much lower bulk modulus than water, both σ_{form} and V_P decrease as the relative saturation S_{CO2} increases. While forward predictions show a clear effect of CO_2 on V_p and σ_{form}, the inverse analysis is hindered by measurement errors and error propagation. Hence, the estimation of S_{CO2} from field measurements remains challenging.

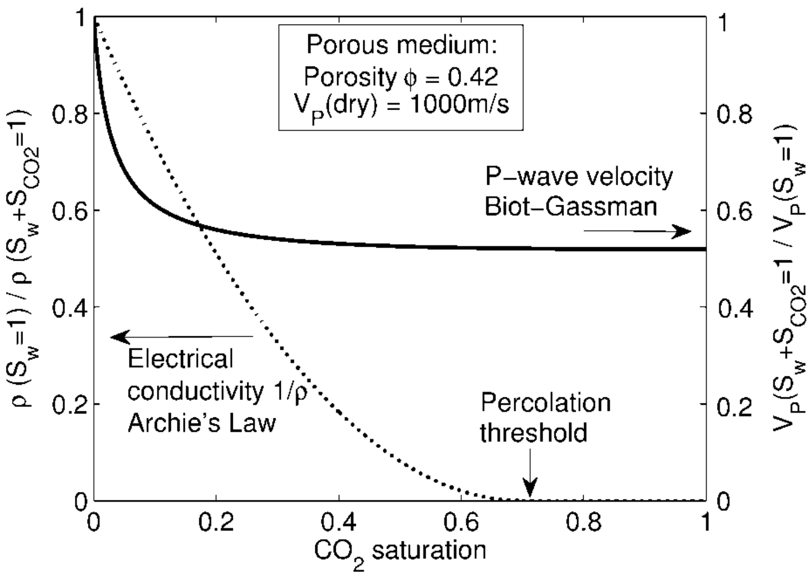

Figure 2.10 Reduction of P-wave velocity and electrical conductivity $\sigma_{form}=1/\rho_{form}$ with CO_2 saturation for a sediment with porosity n=0.42. Ratio of P-wave velocity computed with V_P(Brine) = 1540m/s, $V_P(CO_2)$= 268m/s (at T=40°C and P=10MPa), V_P(dry sediment)=1000m/s, and ν_{sk}=0.1. Electrical conductivity computed with an exponent β=2 for relative saturation and porosity, and a percolation threshold S_{perc}=0.7.

Table 2.4 CO_2 monitoring techniques

Method	Property measured	Principle, comments and issues
1. SUBSURFACE MONITORING		
Porewater geochemistry (1)	CO_2, HCO_3^-, CO_3^{2-}, DIC, major ions, pH, alkalinity, salinity, and isotopes	CO_2 dissolves in water and changes water geochemistry
Seismic techniques (2)	P-wave velocity and amplitude	The bulk modulus of CO_2 is one order of magnitude lower than that of water
Electromagnetic techniques (3)	Resistivity and electromagnetic waves	High impedance mismatch of electrical conductivity and dielectric permittivity between CO_2 and formation water.
Temperature signal (4)	Temperature	CO_2 causes non-isothermal events such as expansion induced cooling of CO_2 and thermal heat dissipation from CO_2 dissolution
Infrared monitoring (5)	Infrared absorption	CO_2 gas shows characteristic absorption spectrum for infrared waves.
2. NEAR SURFACE MONITORING		
Analysis of near-surface water (6)	Isotopic composition, tracers, bulk gas composition, and DIC	CO_2 dissolves in water. A meaningful analysis requires a thorough understanding of the geochemical cycle at the site.
Surface analysis of soil gas (7)	Composition of gas fluxes through the soil	CO_2 leaks would eventually percolate through the soil. Point measurements $<1m^2$ are accurate but they lack spatial resolution
Near surface analysis of air composition (8)	CO_2 concentration in the near surface by infrared gas analyzer, eddy correlation tower, and light detection and ranging measure	CO_2 from leaks readily mix with other atmospheric gases. Local changes in turbulence and biological sources and sinks of CO_2 make the identification difficult.
3. ON-SURFACE MONITORING		
Time-lapse 3D reflection seismic imaging (9)	P-wave velocity and amplitude	Takes advantage of low bulk modulus of CO_2. It is routinely used in the petroleum industry and can track the plume subsurface movement.
Gravity (10)	Mass density	CO_2 is generally lighter than water
Ground displacements (11)	Subsidence and heave, vertical displacement	CO_2 injection alters pore pressure and effect on effective stress, and therefore strata compressibility
Surface analysis of carbon content in soil (12)	Carbon content by Inelastic Neutron Scattering INS	Increased CO_2 levels asphyxiate aerobic organisms.
Remote sensing of air composition (7)	CO_2 atmospheric concentration by hyperspectral remote sensing of vegetative stress and long open path infrared absorption	Applicable at large scales

(1) Gunter et al., 2000; Emberley et al., 2004; Newell et al., 2008; (2) laboratory studies (Xue et al., 2005; Shi et al., 2007; Lei and Xue, 2009) and pilot tests (Daley et al., 2007; Daley et al., 2008; Onishi et al., 2009; Bohnhoff et al., 2010); (3) Gasperikova and Hoversten, 2006; Nakatsuka et al., 2010; (4) Bielinski et al., 2008; (5) Charpentier et al., 2009; (6) Oldenburg et al., 2003; (7) Oldenburg et al., 2003; Leuning et al., 2008; (8) Strazisar et al., 2009; (9) Arts et al., 2004; (10) Alnes et al., 2008; (11) Alnes et al., 2008; Kempka et al., 2008; (12) Wielopolski and Mitra, 2010

2.5 Conclusions

The volume of the geological formation that is affected by the injection of CO_2 depends on geometric boundaries, spatial variability, flow conditions, and the emergence of viscous fingering. The physical properties of CO_2 such as density, viscosity, interfacial tension, and bulk compressibility vary with pressure and temperature conditions, and must be properly modeled in numerical simulations of CO_2 geological storage. In particular, the CO_2-water interfacial tension decreases with fluid pressure. Lower interfacial tension reduces the capillary entry pressure for CO_2 into a water saturated seal cap rock.

High CO_2 injection pressures can induce fluid driven fractures and trigger displacements along preexisting faults. The solubility of CO_2 in water is high under reservoir pressure conditions. The density of water increases with dissolved CO_2, and convective self-mixing takes place. Water acidification in the presence of CO_2 enhances mineral dissolution and alters the sediment fabric when clay minerals prevail. Silicates have solubility higher than calcite but the reaction rate is much slower. The evolution of dissolution and ensuing dissolution patterns depend on the interplay between the rates of advection, diffusion, and dissolution. Dissolution may cause settlement, change in effective stress, and the formation of preferential channels for fluid flow, particularly in carbonates.

The presence of CO_2 decreases the fluid bulk modulus, mass density, and electrical conductivity. These changes support the application of geophysical methods based on elastic and electromagnetic waves to monitor deep storage reservoirs. While forward predictions are manageable, inverse analysis is hindered by measurement difficulties and error propagation. Hence, the monitoring of CO_2 geological storage remains challenging.

CHAPTER 3

CO_2 GEOLOGICAL STORAGE: A MASS BALANCE ANALYSIS AND IMPLICATIONS

3.1 Introduction

The injectivity of CO_2 and the integrity of the reservoir-caprock system are affected by mineral precipitation and dissolution (Gaus et al., 2008). Mineral precipitation reduces porosity, lowers permeability, and hinders the injectivity of CO_2. The CO_2 injection pressure can be increased to overcome the compromised injectivity, but this approach may cause hydraulic fractures in the reservoir (Rutqvist and Tsang, 2002; Streit and Hillis, 2004; Shin and Santamarina, 2010). On the other hand, mineral dissolution triggered by CO_2 driven brine acidification will increase permeability, change the state of stresses in the reservoir (Shin and Santamarina, 2009), and cause caprock bending.

In this manuscript, different zones in the reservoir around injection wells are identified in terms of the prevailing conditions and phenomena. Then, we analyze key phenomena in each zone taking into account parameters such as temperature, pressure, brine salinity, mineralogy, and porosity. These zone-specific storage reservoir analyses provide robust guidelines to understand short and long-term reservoir performance.

3.1.1 Zones

The CO_2 reservoir can be analyzed into four different zones around a CO_2 injection well (Figure 3.1 - modified from an early zonation by Azaroual et al. 2007). The far-field Zone I is not affected by the CO_2 injection, and brine saturation is S_B=1. Acidified brine dominates Zone II and mineral dissolution prevails over precipitation;

loaded with dissolved CO_2 and minerals, denser brine experiences convection and sustains further dissolution in this zone (Weir et al., 1996; Riaz et al., 2006; Hassanzadeh et al., 2007; Kneafsey and Pruess, 2010). The ionic strength in brine increases as water is removed by the injected CO_2, and salt precipitation may occur in Zone III; in fact, brine acidification and brine dissolution into CO_2 coexist in the transition Zone III and there is partial compensation between mineral dissolution and precipitation. The CO_2 saturation approaches $S_{CO2}\approx1$ near the injection well (Zone IV) where the continuous influx of "dry" CO_2 first displaces and dries all the residual brine and causes salt precipitation.

3.1.2 Geological Formations

Sandstones and carbonates are common candidate formations for CO_2 geological storage (Gale, 2004; Dooley et al., 2006). Table 3.1 summarizes the mineralogical composition of sandstone and carbonate formations being considered for CO_2 storage. Sandstone reservoirs are made of oxides (e.g., quartz and hematite), and some aluminosilicates (e.g., various feldspars, micas, and clays) and carbonates (e.g., calcite, dolomite, and siderite). The dominant mineral in the carbonate reservoirs is calcite, followed by a small fraction of aluminosilicates and clays.

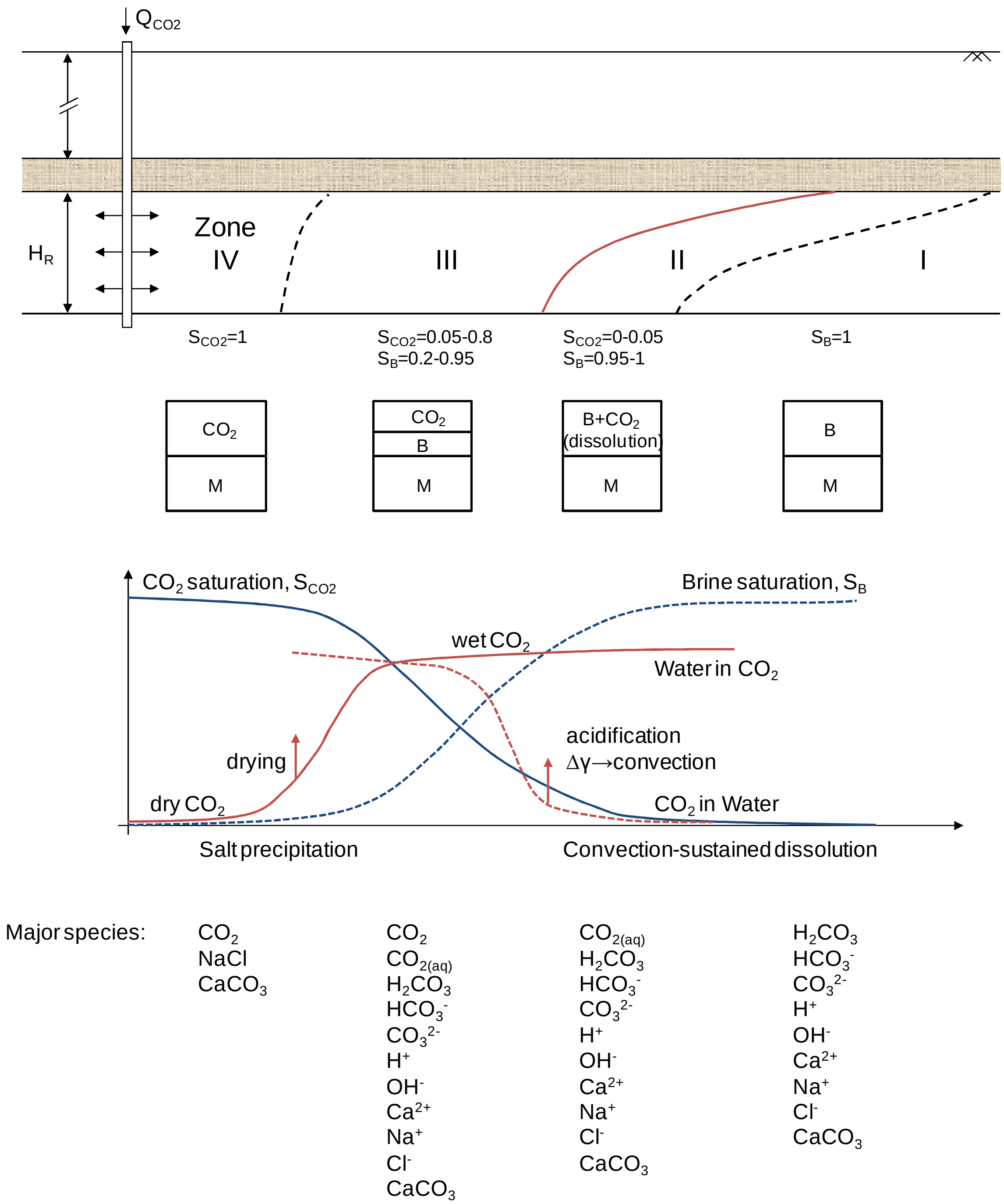

Figure 3.1 Zones around a CO_2 injection well (modified from Azaroual et al., 2007). *M*: Mineral, *B*: Brine, S_{CO2}: saturation of CO_2, S_B: saturation of brine.

Table 3.1 Mineralogical compositions (volume percentage) of reservoir sites for the CO_2 geological storage

	Sandstone						Carbonate	
Mineral	(1)	(2)	(3)	(4)	(5)	(6)	(7)	(8)
Quartz	58	70	77	60	75	80	30	0
Calcite	1.93	8	1.3	0	3	0	45	70
Dolomite	0	13.8	0	0	0	0	0	10
Siderite	0	0.2	0	0	0	2	0	5
Kaolinite	2.02	1	2.25	0	0	3	0	0
Illite	1	0	0	11	0	10	5	5
Oligoclase	19.8	0	0	15	0	0	7	0
K-feldspar	8.2	5	0.6	3	13	1	8	5
Albite	0	1	0.6	0	3	2	0	5
Anorthite	0	0	0.66	0	0	0	0	0
Na-smectite	4	0	2.25	0	0	0	0	0
Chlorite	4.55	0	0	11	0	0	4	0
Hermatite	0.5	0	0	0	0	0	1	0

(Data source: (1) Gulf Coast, Frio (Xu et al., 2005), (2) Rose Run, Ohio (Zerai et al., 2006), (3) Colorado Plateau, Utah (White et al., 2005), (4) & (7) Arno River Plain, Italy (Biagi et al., 2006), (5) Utsira, Sleipner (Hellevang, 2006), (6) Hettangium and Contorta, Germany (Meyer et al., 2008), (8) Dogger, France (André et al., 2007))

3.2 Geochemical Analyses

Let's analyze the four different zones that develop around injection wells at CO_2 storage sites (Figure 3.1), starting with the composition of the formation water.

3.2.1 Far-Field Zone I

The formation water in a geologic basin originates from the subaerial evaporation of sea water, the subsurface dissolution of minerals including evaporates, membrane filtration, and dilution by meteoric water (Land and Prezbindowski, 1981; Connolly et al., 1990; Pauwels et al., 1993; Hanor, 1994; Kharaka et al., 2006). The resulting formation water is either a *Na-Cl* or a *Na-Ca-Cl* type at most candidate sites for CO_2 storage (Figure

3.2). The pore fluid evolves towards equilibrium with the formation minerals, but the time interval may be insufficient for complete equilibrium in relatively active systems (Pauwels et al., 1993; Baines and Worden, 2004; Lagneau et al., 2005). In general, the formation water is: (1) under-saturated in terms of evaporate minerals such as halite and anhydrite, and (2) either under-saturated or in equilibrium with other minerals in the formation (Connolly et al., 1990 – see estimation in Xu et al., 2005).

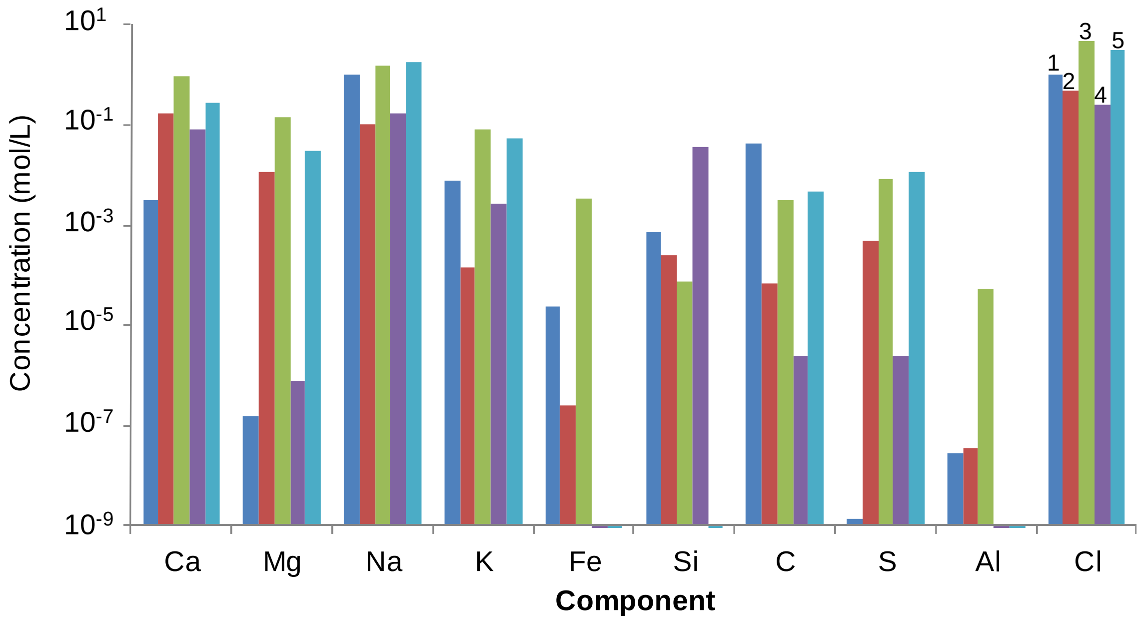

Number	Site	Pressure [MPa]	Temperature [°C]	Reference
1	Frio	20	75	Xu et al., 2005
2	Sleipner	10	37	Gaus et al., 2005
3	Rose Run	22	75	Zerai et al., 2006
4	Colorado Plateau	10	40	White et al., 2005
5	Paradox Valley	30	120	Rosenbauer et al., 2005

Figure 3.2 Chemical composition of formation water for candidate CO_2 sequestration sites.

In this analysis, we consider a single mineral formation, calcite $CaCO_3$, and assume that equilibrium has been reached (Lasaga, 1984; Baines and Worden, 2004). The formation water retains its original halite *NaCl* concentration ranging from *Sal*=0 to 6 [mol/kg-water] and is in equilibrium with the formation $CaCO_3$. The resulting geochemical composition of the pore fluid is under-saturated with halite *NaCl* and saturated with calcite $CaCO_3$ (Computation details in Chart 3.1). Two assumptions are made to formulate the mass balance calculations: 1) the initial system consists of mineral and brine only and there is no entrapped gas, and 2) water salinity is controlled by the initial concentration of halite *NaCl*. All symbols and conditions relevant to the mass balance analysis are listed in Table 3.2.

3.2.2 Zone II – Mixing and Mineral Dissolution

The CO_2 phase that reaches Zone II is water saturated. In the proximity of fresh brine, CO_2 dissolves into the brine and acidifies it; mineral dissolution follows. The concentrations of species in brine at equilibrium when CO_2 and mineral dissolves to its maximum solubility are evaluated based on the initial composition, pressure, and temperature (Computation details in Charts 3.2 to 3.4). The new equilibrium condition is used to compute the change in pH, density, and volume (Figure 3.3; Charts 3.5 to 3.7).

pH. Without any buffering by mineral dissolution, the dissolution of CO_2 acidifies brine to pH~3 (computed using CO_2 solubility and acidity constant K_{a1} for the dissociation of total $H_2CO_3^* \leftrightarrow H^+ + HCO_3^-$ where the total dissolved $H_2CO_3^*$ is the summation of aqueous carbon dioxide $CO_{2(aq)}$ and true carbonic acid H_2CO_3; for a depth~1km, pressure $P \approx 10$MPa, temperature $T \approx 40$°C - Figure 3.4; computation details in Chart 3.3). The drop in pH is more pronounced when the brine salinity is low. If mineral dissolution is accounted for, the pH of brine converges to around 5 for the same *P*-*T* condition (computed in PHREEQC with the input of concentration of dissolved CO_2 and ambient calcite environment; for a depth~1km, pressure $P \approx 10$MPa, temperature $T \approx 40$°C - Figure 3.4; computation details in Chart 3.4). Throughout all these calculations, brine remains under-saturated in terms of halite *NaCl*.

Table 3.2 Symbols used in the geochemical analysis

Notations		**Subscripts**	
Equilibrium constant	K [-]	Aqueous state	Aq
Fugacity	Φ [-]	Brine	B
Ionic concentration	C [mol/kg]	Calcium	Ca
Mass	M [kg]	Carbon	C
Mass density	ρ [kg/m^3]	Chloride	Cl
Mass fraction in aqueous phase	X [-]	Hydrogen	H
Mass fraction in gaseous phase	Y [-]	Oxygen	O
Mole fraction in aqueous phase	x [-]	Salt (halite NaCl)	S
Mole fraction in gaseous phase	y [-]	Sodium	Na
Amount of substance	n [mol]	Solid mineral (Calcite $CaCO_3$)	M
Molality	b [mol/kg]	Supercritical CO_2	CO_2
Molar volume	Vm [m^3/mol]	Total (=CO_2+mineral+water)	T
Molar mass	m [kg/mol]	Water	W
Pressure	P [Pa]	**Values**	
Porosity	φ [-]	Critical temperature, T_c	31.1°C
Salinity	Sal [mol/kg]	Critical pressure, P_c	7.39MPa
Saturation	S [-]	Molar volume of calcite, Vm_M	3.7*10^{-5} m^3/mol
Solubility	Sol [mol/kg]	Molar volume of halite, Vm_S	2.7*10^{-5} m^3/mol
Temperature	T [°K]	Molar mass of CO_2, m_{CO2}	44g/mol
Universal gas constant	R [J/K/mol]	Molar mass of NaCl, m_S	58g/mol
Volume	V [m^3]	Molar mass of calcite, m_M	100g/mol
		Molar mass of water, m_W	18g/mol
		Density of mineral, ρ_M	2700kg/m^3
Superscript			
Reference state	<0>	In CO_2 phase	CO_2
Right after CO_2 injection	<1>	In brine phase	B
At equilibrium	<2>	In water phase	W
Ensuing event	<3>	Total	T
		Salt (halite)	S
Equations			
Mass density of water[(1)]	f(P,T)	Mole fraction of water in CO_2[(3)]	f(P,T)
Mass density of brine[(1)]	f(P,T,Sal)	Solubility of CO_2[(2)]	f(P,T,Sal)
Mass density of CO_2[(2)]	f(P,T)	Solubility of halite NaCl[(4)]	f(P,T)
Geochemistry			
- Mineral dissolution (calcite): $CaCO_{3(s)} \rightarrow Ca^{2+} + CO_3^{2-}$; $K_M = 10^{-8.48}$			

[(1)] Bachu and Adams, 2003, [(2)] Duan and Sun, 2003, [(3)] Spycher et al., 2003, [(4)] Sawamura et al., 2007

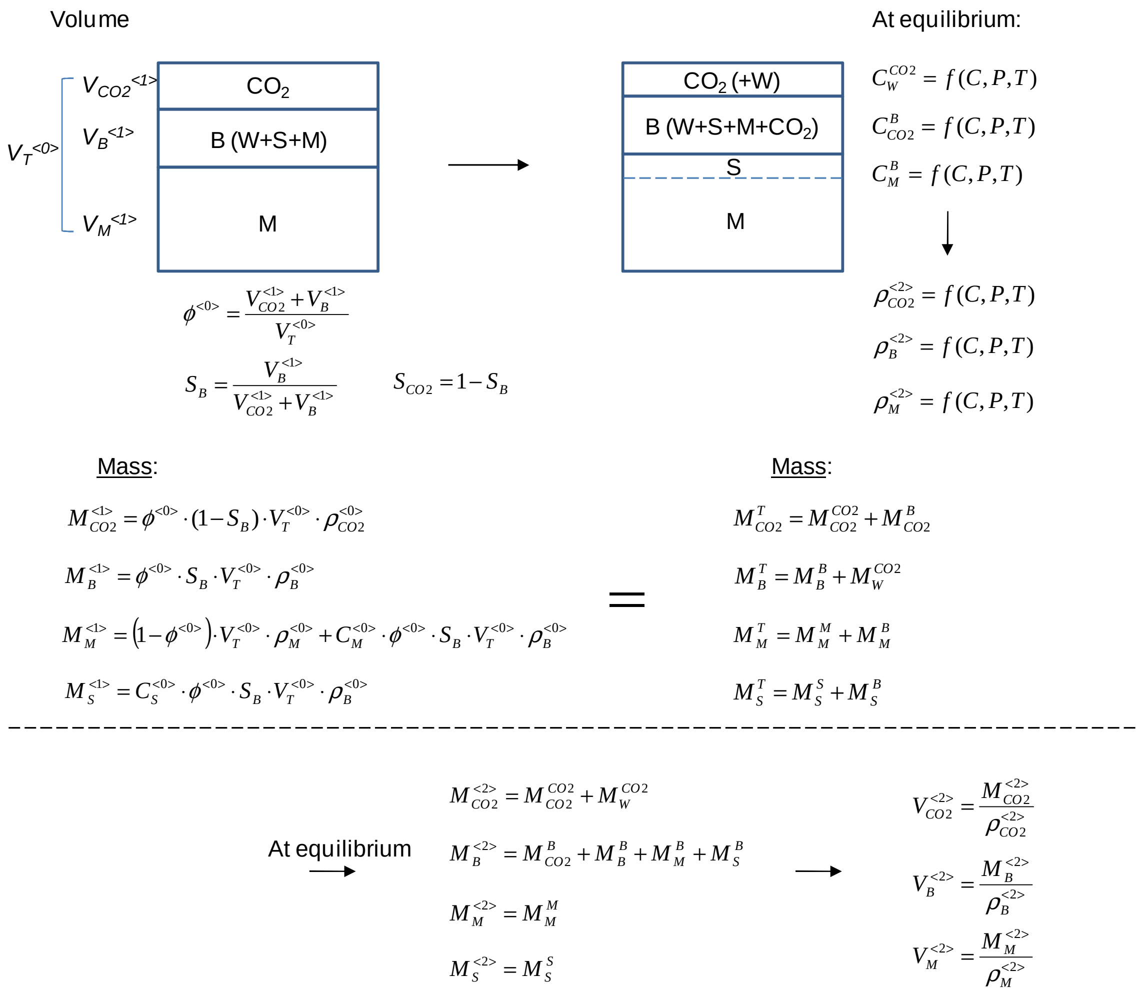

Figure 3.3 Mass balance formulation for Zone II. Symbols are *M*: Mass, *V*: Volume, *C*: Ionic concentration, *S*: Saturation, φ: Porosity, ρ: Density, *P*: Pressure, *T*: Temperature; Subscript – *M*: Mineral, *B*: Brine, *W*: Water (H_2O), *T*: Total, *S*: Salt (Halite, *NaCl*); Superscript – <0>: Reference state, <1>: Right after CO_2 injection, <2> At equilibrium, CO_2: In CO_2 phase, *B*: In brine phase, *T*: Total, *S*: Salt (Halite, *NaCl*).

Brine and CO_2 density. The detailed computation of the brine and CO_2 densities is summarized in Chart 3.5. The density of brine increases as CO_2 and mineral dissolution takes place (Figure 3.5-a). The ratio between the increase in density and the initial density is higher when the brine salinity is lower because the solubility of CO_2 decreases with increasing brine salinity (Figure 3.5-b). For conditions occurring at a 1km storage depth

($P \approx 10$MPa and $T \approx 40$°C), the maximum increase in brine density is ~1.2% (computation details in Chart 3.5; Figure 3.5-b – see also Pruess and Zhang, 2008). The denser brine can trigger convection and the dissolution-transport sequence persists.

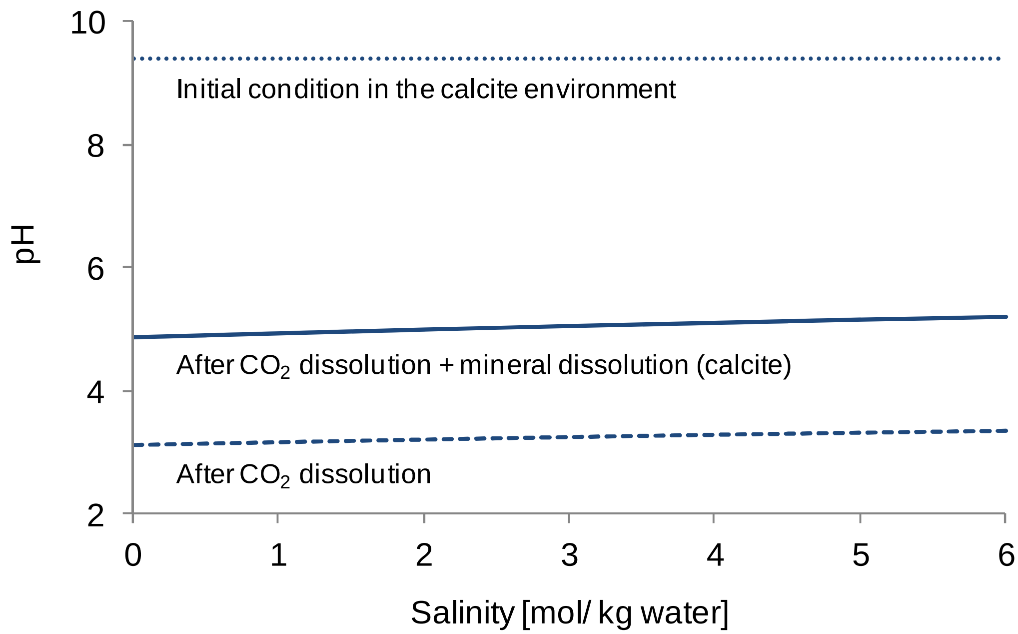

Figure 3.4 Acidity in Zone II of a CO_2 geological storage reservoir. Initial pH value in the calcite environment, pH after CO_2 dissolves in the brine, and pH after both CO_2 dissolution and consequent mineral dissolution occur (P=10MPa, T=40°C).

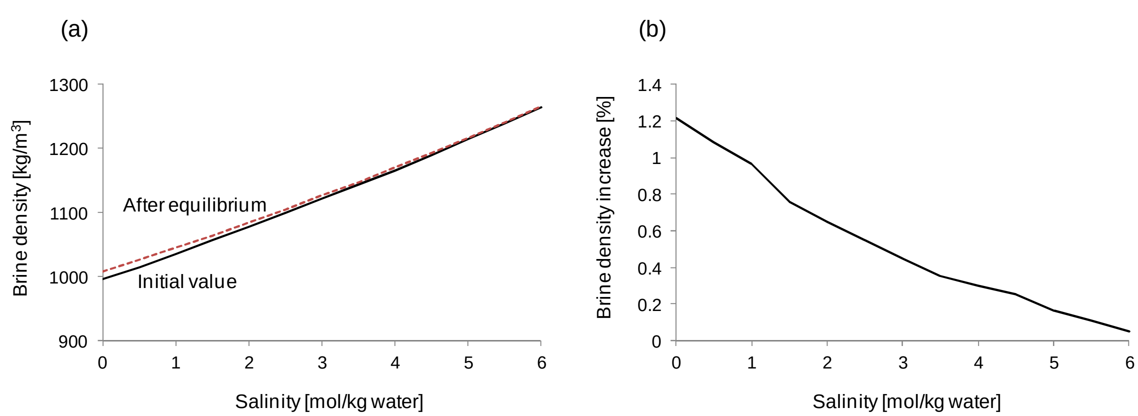

Figure 3.5 Brine density in Zone II of a CO_2 geological storage reservoir: (a) Change in the brine density and (b) the percentage of change in brine density with respect to the brine salinity (a storage depth~1km; P=10MPa, T=40°C).

Water also dissolves in the CO_2 phase, but its solubility is very low. Figure 3.6 shows the mutual solubility of CO_2 and water, as a function of brine salinity, for typical reservoir conditions (pressure P≈10MPa, temperature T≈40°). The increase in the density of supercritical CO_2 due to water dissolution is only ~0.08% for the same P-T conditions (computation details in Chart 3.5).

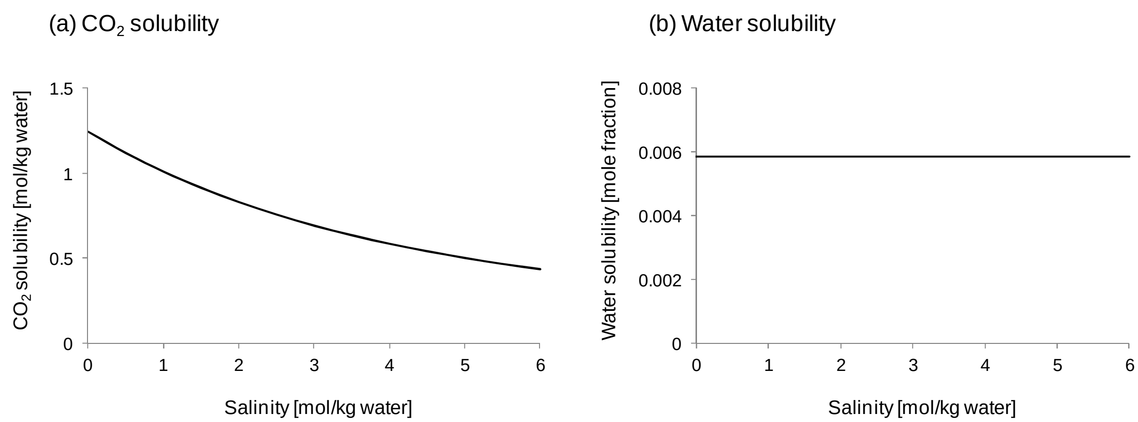

Figure 3.6 Mutual solubility in Zone II: (a) CO_2 solubility in brine and (b) water solubility in CO_2 with respect to the brine salinity (at Pressure P=10MPa and Temperature T=40°C). Results are obtained using formulae from Duan and Sun (2003), Spycher et al. (2003), and Hassanzadeh et al. (2008).

Porosity. Minerals are the dominant phase in CO_2 geological storage. The computation of the mineral volumetric change in outlined in Charts 3.6 to 3.7. The maximum decrease in the normalized mineral volume is $\Delta V_M/V_M$~0.2%, corresponds to zero brine salinity (for a depth~1km - Figure 3.7). This volumetric contraction in the combined solid-fluid mixture may cause geomechanical implications such as change in effective stress and shear failure.

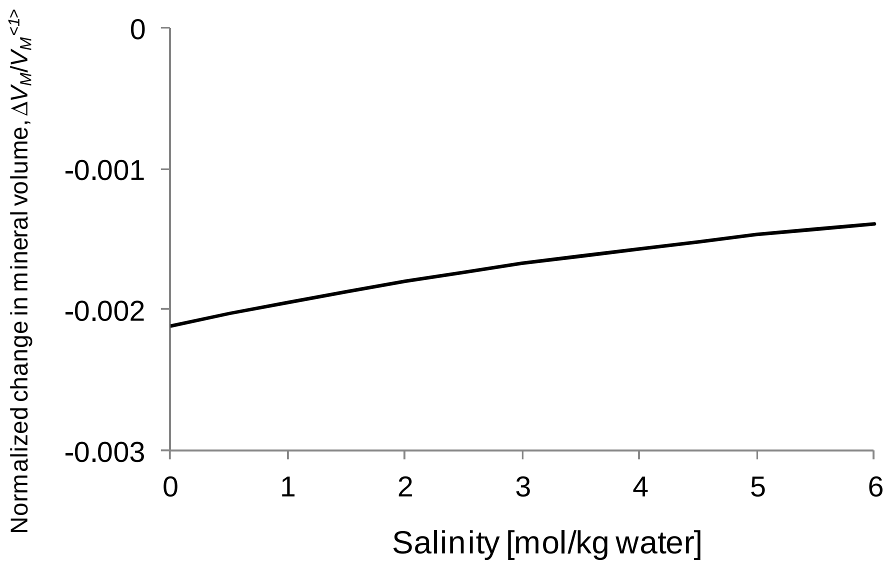

Figure 3.7 Normalized change in mineral volume $\Delta V_M/V_M^{<1>}$ for Zone II. Note: Maximum CO_2 solubility is considered (applied to P=10MPa, T=40°C).

3.2.3 Zone III – Transition Zone: Brine Displacement

Water saturated CO_2 displaces brine in Zone III. The residual brine fraction $V_B^{<1>}/V_T^{<0>}=\varphi^{<0>}\cdot S_B$ immediately after CO_2 injection is a function of the initial porosity $\varphi^{<0>}$ and the residual fluid saturation S_B (Figure 3.3). The evolution of species thereafter can be evaluated based on the initial composition, pressure, and temperature including: total dissolved carbonic acid H_2CO_3* and other dissolved ions, the mole fraction of water in CO_2 (y_w), and of CO_2 in brine (x_{CO2}).

3.2.4 Zone IV – Water Drying Near the Injection Well

The residual brine phase gradually dries when exposed to the continuous influx of dry CO_2 near the injection well. Mineral precipitation (e.g., halite and other minerals dissolved in the brine phase) increases the mineral volume fraction. The maximum amount of calcite and halite precipitation are computed from initial equilibrium condition (refer to Zone II – Computation details in Chart 3.8). Clearly, the increase in the mineral volume fraction after the water dries is more pronounced at higher initial brine saturation S_B and brine salinity *Sal* [mol/kg-water] (Figure 3.8). The contribution of initial salinity to the precipitated mass prevails over the contribution of dissolved carbonates in most cases because the amount of ions produced from brine acidification and carbonate dissolution is much lower than salts contained in the brine. The maximum increase in mineral volume is 5% for an initial salinity of *Sal*=4mol/kg-water and porosity $\varphi^{<0>}$=0.286 under a depth~1km (P≈10MPa, T≈40°C). This increase in mineral volume will hinder the injectivity of CO_2.

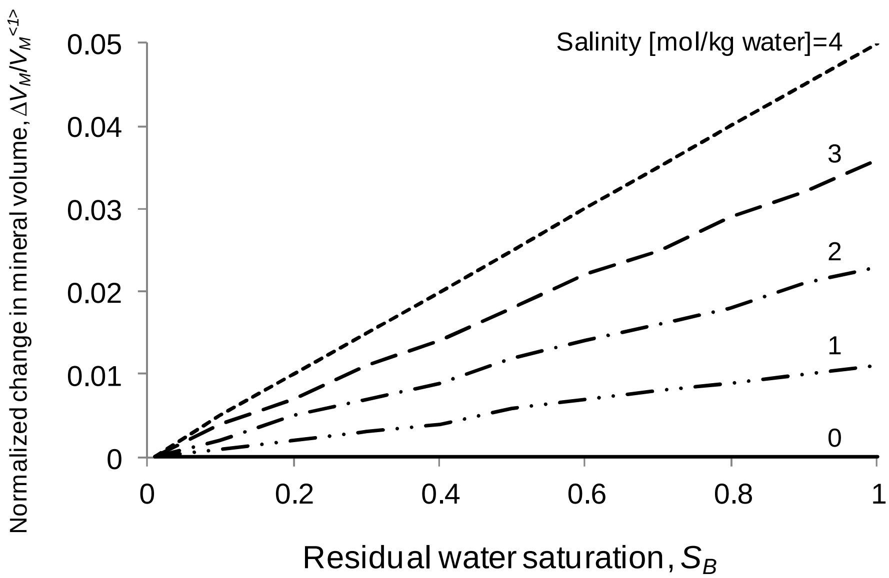

Figure 3.8 Normalized change in mineral volume $\Delta V_M/V_M^{<1>}$ for Zone IV as water is removed by dry CO_2 flushing (P=10MPa, T=40°C, and initial porosity $\varphi^{<0>}$=0.286).

3.3 Hydro-Geomechanical Analyses

Hydro-geomechanical implications associated to geochemical process identified above are addressed next.

3.3.1 Reservoir and CO_2 Plume Thickness

The quasi-static lateral spread of the CO_2 plume in the absence of geometric or stratigraphic features is determined by the balance between the excess buoyant pressure in the CO_2 and the capillary pressure required to invade the storage reservoir. Therefore, the CO_2 plume thickness H_{CO2} [m] is a function of the interfacial tension between CO_2 and brine T_s [mN/m], the characteristic pore radius in the storage reservoir R_{pore} [m], and the unit weights of CO_2 γ_{CO2} [N/m^3] and brine γ_w [N/m^3]:

$$H_{CO2} \leq \frac{2T_s}{R_{pore} \cdot (\gamma_w - \gamma_{CO2})} \tag{1}$$

For example, the plume thickness cannot exceed H_{CO2}=2.5m in a reservoir with characteristic pore size R_{pore}=10μm (assumed: T_s=50mN/m and γ_w-γ_{CO2}=4kPa/m). In general, we can anticipate that the thickness of CO_2 plumes in flat layered sediments will be smaller than H_{CO2}<10m in most cases. Thicker accumulations will require geometric traps.

3.3.2 State of Stress

Zone I. Consider a brine-saturated geological basin with an initial effective stress ratio $K_0=\sigma_{h0}'/\sigma_{v0}'$. Vertical total and effective stresses can be determined from formation depth z [m], unit weight of saturated media γ_{sat} [N/m^3], and unit weight of brine γ_w [N/m^3]. Thus, initial value of vertical total stress is σ_{v0} [Pa]=$\gamma_{sat}\cdot z$, pore-brine pressure is u_w [Pa]=$\gamma_w \cdot z$, and vertical effective stress is σ_{v0}' [Pa]=$(\gamma_{sat}-\gamma_w)\cdot z$. The horizontal effective stress is obtained from initial stress ratio σ_{h0}' [Pa]=$K_0\cdot(\gamma_{sat}-\gamma_w)\cdot z$. Finally, the horizontal total stress is σ_{h0} [Pa]= $K_0\cdot(\gamma_{sat}-\gamma_w)\cdot z+\gamma_w\cdot z$.

Zone II. Convection-sustained mineral dissolution causes a decrease in the horizontal effective stress $\sigma_{h0}' \rightarrow \sigma_h'$ while the vertical effective stress and pore-brine pressure may remain almost constant $\sigma_v' \approx \sigma_{v0}'$ and $u \approx u_w$. Therefore, Mohr circle enlarges leftwards, approaching the Coulomb failure criterion (Figure 3.9-a). The ratio of effective stress σ_h'/σ_v' also approaches the active pressure coefficient K_a (Shin et al., 2008).

Zone III. CO_2 partially displaces brine; the residual brine saturation is S_B in Zone III. Associated stress changes have been previously explored (Rutqvist and Tsang, 2002; Streit and Hillis, 2004; Rutqvist et al., 2007; Rutqvist et al., 2008; Shi and Durucan, 2009; Soltanzadeh and Hawkes, 2009; Ferronato et al., 2010; Vidal-Gilbert et al., 2010). The vertical effective stress σ_v' and horizontal effective stress σ_h' after CO_2 injection are a function of the unit weight of the saturated medium γ_{sat}, the unit weight of brine γ_w, depth z, brine saturation S_B, capillary pressure $u_c=u_{CO2}+u_w$, and the initial stress ratio K_0; following Bishop's effective stress approach:

$$\sigma_v' = \sigma_v - \left[S_B u_w + (1-S_B)u_{CO2}\right] = (\gamma_{sat} - \gamma_w)z - (1-S_B)u_c \quad (2)$$

$$\sigma_h' = (\sigma_h - u_w) - (1-S_B)u_c = K_0(\gamma_{sat} - \gamma_w)z - (1-S_B)u_c \quad (3)$$

To estimate changes in effective stresses as a result of CO_2 storage, we couple the saturation of brine S_B with the capillary pressure u_c (van Genuchten, 1980):

$$S_B = \left[1 + \left(\frac{u_c}{u_a}\right)^{\frac{1}{1-\lambda}}\right]^{-\lambda} \quad (4)$$

The model parameter u_a [Pa] is taken as the CO_2 entry pressure, and the parameter λ [-] relates to the sediment pore structure. Finer and denser sediments imply higher u_a and lower λ values. These simple analytical calculations can provide first-order estimation for changes in the state of stresses as a result of CO_2 injection. Note that this approach might not be applicable for the event of localized displacement such as viscous fingering.

Zone IV. During CO_2 injection, excess pressure is applied to cause the required pressure gradient. The excess injection pressure gradually vanished once injection stops. The asymptotic CO_2 pressure remaining above the brine pressure due to buoyancy and it is maintained by capillarity at the boundaries: $\Delta u=(\gamma_w-\gamma_{CO2})\cdot H_R \leq 2\cdot T_s/R_{pore}$, where H_R [m] is the thickness of storage reservoir. Thus, the vertical effective stress in Zone IV $\sigma_v'=\sigma_{v0}-u_w-\Delta u$ is lower than in Zone I. Capillarity pushed the lateral boundary away and the effective horizontal stress in Zone IV decreases by as much as $\Delta\sigma \leq 2\cdot T_s/R_{pore}$, but limited by the stress ratio $\sigma_h'/\sigma_v' \geq K_a$ (note: the formation strains away from the injection well, i.e., $\varepsilon_h>0$). Therefore, Figure 3.9-b shows anticipated stress path in Zone IV.

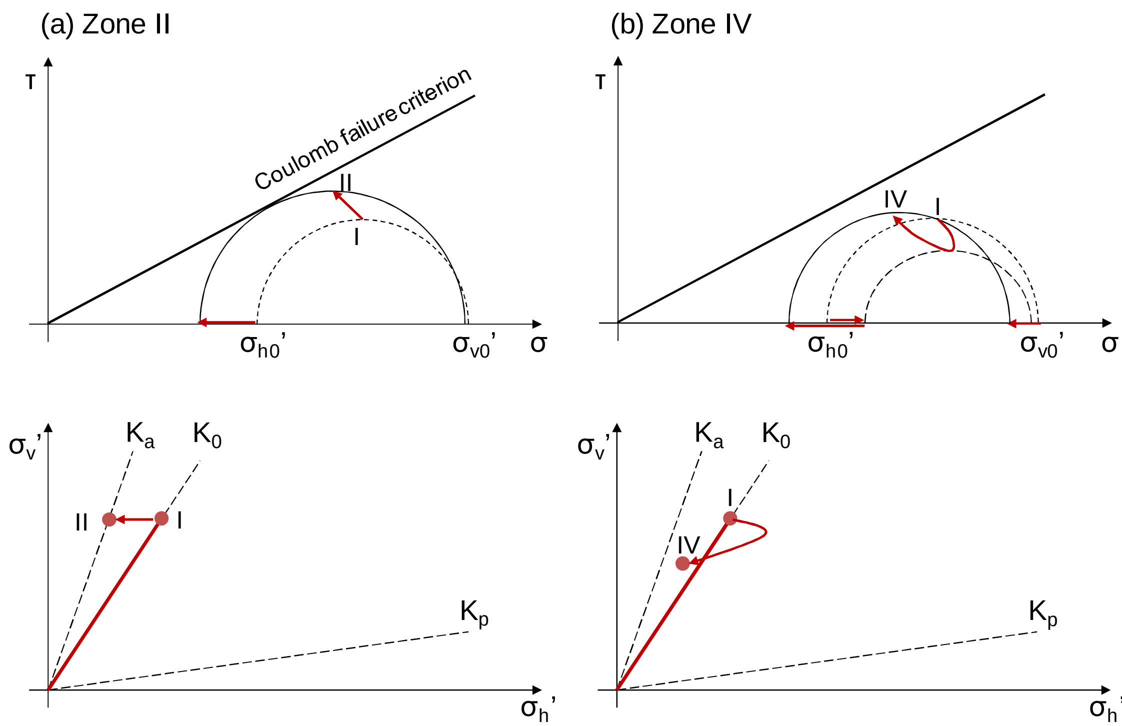

Figure 3.9 Geomechanical analysis - Change in the state of stresses: (a) in Zone II (Convection of CO_2-dissolved brine sustains mineral dissolution, which results in decrease in the horizontal effective stress σ_h' while vertical effective stress remains same; ratio of effective stress σ_h'/σ_v' approaches the active pressure coefficient K_a), and (b) in Zone IV (At equilibrium, CO_2 pressure is higher than initial pore brine pressure u_w because of buoyancy and capillary effect $\Delta u=(\gamma_w-\gamma_{CO2})\cdot H_R \leq 2\cdot T_s/R_{pore}$. The effective horizontal stress decreases by as much as $\Delta\sigma \leq 2\cdot T_s/R_{pore}$, but limited by the stress ratio $\sigma_h'/\sigma_v' \geq K_a$ (note: the formation strains away from the injection well, i.e., $\varepsilon_h>0$).

3.3.3 Implications of Dissolution (Zone II)

Convection. Rayleigh number Ra compares convective and diffusive transport. For a storage reservoir thickness H_R [m] with permeability k [md], diffusivity D [m^2/s], and fluid with viscosity μ [Pa·s] and density difference $\Delta\rho$ [kg/m^3] the Rayleigh number is (Hassanzadeh et al., 2007):

$$Ra = \frac{k \cdot \Delta\rho \cdot g \cdot H_R}{\mu \cdot D} \tag{5}$$

Denser CO_2-dissolved brine triggers instability when $Ra>4\pi^2$ (Kneafsey and Pruess, 2010). Persistent convective flow may sustain CO_2 dissolution in brine, its acidification, and ensuing mineral dissolution. The time for convection is $t_{conv}=H_R/v_{conv}$ where the Darcy velocity v_{conv} [m/s]$=k\cdot\Delta\rho\cdot g/\mu$ can be computed from the driving gradient and the hydraulic conductivity:

$$t_{conv} = \frac{\mu \cdot H_R}{k \cdot \Delta\rho \cdot g} \tag{6}$$

For a typical storage reservoir with permeability k=200md, thickness H_R=10m, and density difference $\Delta\rho$=20kg/m^3, the Rayleigh number is $Ra=4.4*10^3>4\pi^2$, convective fingering will take place, and convective fingers will touch the bottom of the reservoir after $t_{convection}\approx 9$ years. The mineral flux rate due to convection is in the order of $\Delta V_M \cdot \rho_M / t_{conv}$. Therefore, while the mineral dissolution may be low, short convection time may cause substantial mineral flux rate in Zone II.

Compaction-Driven Shear Failure. Convection-sustained mineral dissolution causes settlement and change in the state of stress under constant overburden stress conditions. In particular, the ratio between horizontal effective stress to vertical effective stress at zero-lateral strain $K_0=\sigma_h'/\sigma_v'$ (Jaky, 1944; Mayne and Kulhawy, 1982) may decrease as a result of mineral dissolution, and cause the system to meet the Rankine active failure condition K_a (Shin and Santamarina, 2009; Shin et al., 2010; Cha, 2012). In fact, mineral dissolution may cause shear failure within the reservoir in Zone II (Figure 3.1).

Caprock Bending Failure. In addition, convective flow and sustained dissolution may result in an poorly supported span beneath the caprock (Figure 3.10-a). Let's consider a uniformly-distributed load on a 2D beam overlying an elastic foundation (Hetényi and Michigan, 1946). The maximum tensile stress σ_{tmax} [kPa] that develops at the bottom of the caprock in the middle of the softer span is a function of the average density of the overlying layer ρ_c [kg/m^3], the depth of caprock z_c [m], the thickness H_c [m] and yield strength of the caprock σ_y [kPa], the length of the free span L_{free} [m]. The characteristic length scale of the system is λ [m^{-1}]=$\sqrt[4]{(k_r/4E_cI_c)}$, where k_r [kPa] is the stiffness of the reservoir, E_c [kPa] the Young's modulus of caprock, and I_c [m^4] the moment of inertia of caprock. Then, assuming lateral boundaries at infinite, the maximum tensile stress in the caprock is (Hetényi and Michigan, 1946):

$$\frac{\sigma_{t\max}}{\sigma_y} = 3\pi_1\pi_2\left(\frac{1}{4}\pi_2 + \frac{6-(\pi_2\pi_3)^2}{6\pi_3(2+\pi_2\pi_3)}\right),$$

$$\text{where } \pi_1 = \frac{\rho_c g z_c}{\sigma_y}, \ \pi_2 = \frac{L_{free}}{H_c}, \text{ and } \pi_3 = \lambda H_c \tag{7}$$

Figures 3.10-b and c suggest the maximum free span length to avoid bending failure of the caprock for conditions that resemble the Frio project (USA; Doughty et al., 2008) and the Weyburn project (Canada; White et al., 2004). Results suggest that the free span cannot exceed 20% of the caprock thickness, $L_{free}/H_c \leq 0.2$.

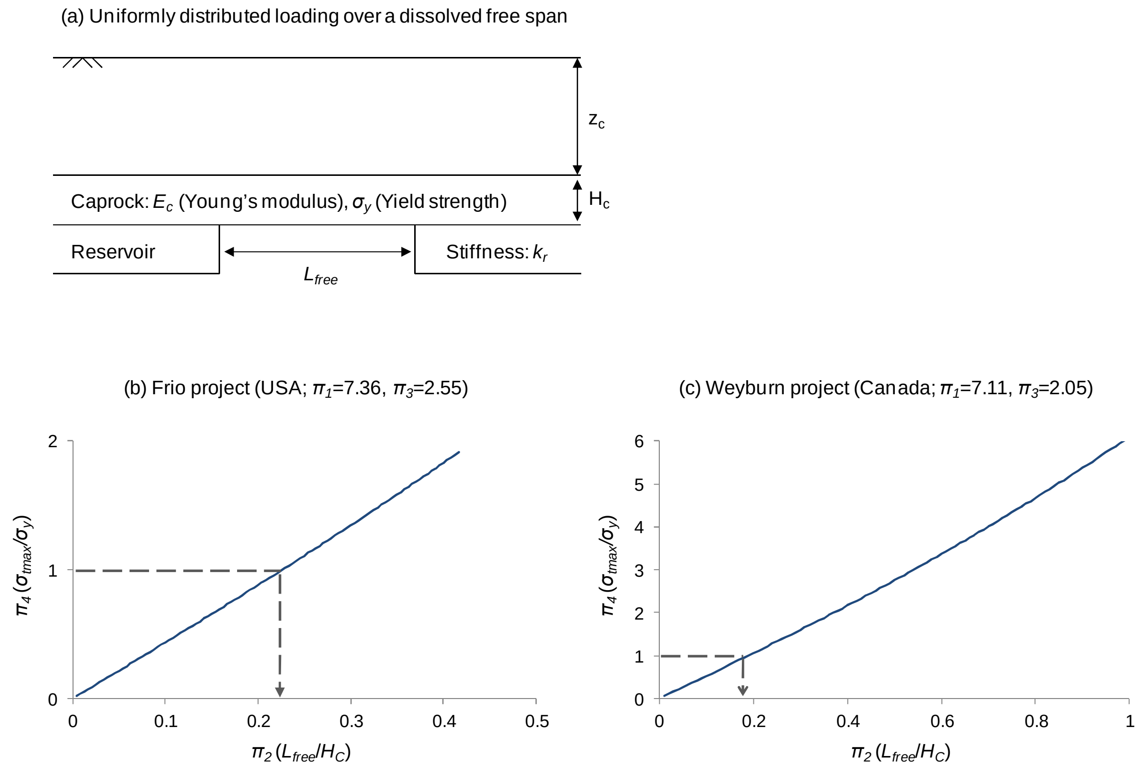

Figure 3.10 Mineral dissolution-induced bending failure of the caprock. (a) Uniformly distributed loading over a dissolved free span (dimensionless ratios: $\pi_1=\rho_c g z_c/\sigma_y$, $\pi_2=L_{free}/H_c$, $\pi_3=\lambda H_c$, and $\pi_4=\sigma_{tmax}/\sigma_y$). Application to CO_2 sequestration projects (L_{free} varies from 0 to 10m): (b) Frio project (USA; depth of caprock z_c=1500m, thickness of caprock H_c=24m) and (c) Weyburn project (Canada; z_c=1450m, H_c=10m). Note: average density of overlying layer ρ_c=2500kg/m^3, Young's modulus of caprock and reservoir $E_c=E_r$=10GPa, Poisson's ratio ν=0.2, stiffness of reservoir $k_r=1.6\cdot E_r\cdot(1-\nu)/(2\cdot(1+\nu)\cdot(1-2\nu))$, yield strength of caprock σ_y=5MPa.

3.3.4 Porosity and Permeability Change due to Dissolution (Zone II) and Precipitation (Zone IV)

Mineral precipitation decreases porosity and lowers the fluid permeability. The Kozeny-Carman formula defines a power-law relationship between normalized porosity φ/φ_0 and normalized permeability k/k_0 (Carman, 1956): $k/k_0=(\varphi/\varphi_0)^\alpha$ where φ_0 and k_0 are initial values for porosity and permeability. The analysis of Zone IV (the complete evaporation of water) shows that the mineral volume can increase by ≤5%. The exponent α has been reported to be at least larger than $\alpha \geq 3$ (e.g., α~3.4 from Wellman et al., 2003; α=5~6 from Mohamed and Nasr-El-Din, 2012). A value of α=3 yields a 16% decrease in permeability. Note that the power law represents the average value of porosity and permeability. Since a geological formation consists of heterogeneous porous media, the reduction in permeability could be locally different.

For a more rigorous analysis, consider a porous medium where CO_2 breaks through from one end to the other while residual brine remains (Figure 3.11-a). We simplify this structure into a parallel arrangement in which one phase is CO_2 and the other is brine (Figure 3.11-b). For this arrangement, the maximum attainable CO_2 permeability k_{CO2} [m^2] is:

$$k_{CO2} = S_{CO2} \cdot k_c + (1 - S_{CO2}) \cdot k_f \tag{8}$$

where k_c is the permeability of CO_2 layer and k_f the permeability of brine layer in Figure 3.11-b. Salt precipitation is likely to occur mostly in the brine layer, so the permeability of the brine layer will become k_f^m (computed using Kozeny-Carman formula). Then, the maximum attainable CO_2 permeability is (Figure 3.11-c):

$$k_{CO2}^m = S_{CO2} \cdot k_c + (1 - S_{CO2}) \cdot k_f^m \tag{9}$$

Figure 3.11-d suggests that the decrease in the maximum attainable CO_2 permeability is minor. Indeed, CO_2 will invade and displace brine from the larger interconnected pores and then dry the water from residual brine patches; salt precipitation in the pore space of these patches will not significantly decrease the maximum attainable CO_2 permeability. In summary, Salt precipitation will not cause clogging if continuous pumping occurs (i.e., channels remain open), and only a minor decrease in CO_2 permeability is anticipated.

Mineral dissolution increases porosity and enhances the fluid permeability in Zone II. A similar analysis predicts a very small increase in permeability <1% when the normalized decrease in the mineral volume is ~0.2%. However, convection-sustained mineral dissolution could cause more pronounced changes in permeability within the storage time.

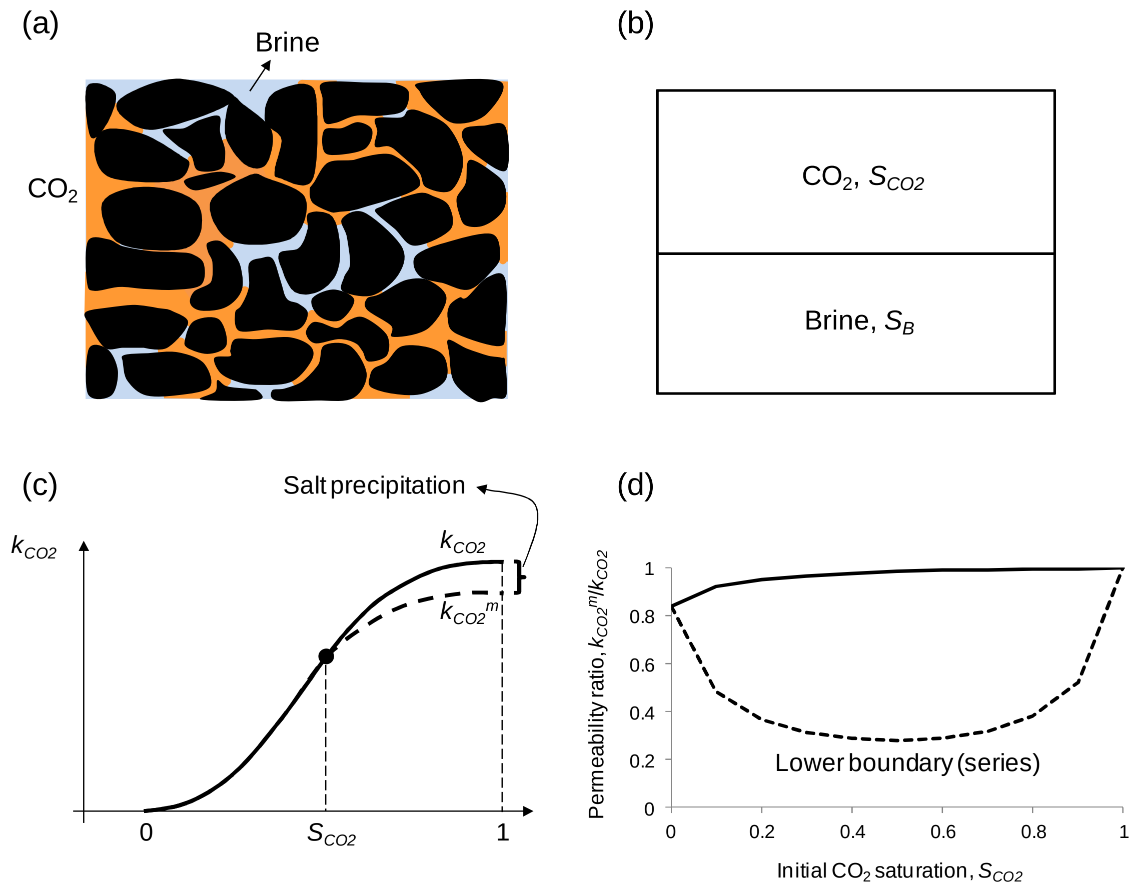

Figure 3.11 Change in the permeability of CO_2 after salt precipitation. (a) CO_2 invases and residual brine in the pore space. (b) Simplification into a parallel arrangement. (c) Original evolution of CO_2 permeability k_{CO2} with respect to CO_2 saturation S_{CO2} and modified CO_2 permeability after salt precipitation. and (d) Ratio of modified maximum attainable CO_2 permeability $k_{CO2}^m=S_{CO2}\cdot k_c+(1-S_{CO2})\cdot k_f^m$ to original maximum attainable CO_2 permeability $k_{CO2}=S_{CO2}\cdot k_c+(1-S_{CO2})\cdot k_f$ with respect to the initial CO_2 saturation S_{CO2} right before salt precipitation takes place, assuming parallel arrangement (solid line), and lower boundary when assuming series arrangement (dotted line) ($k_c=10\cdot k_f$; k_f^m is obtained from Kozeny-Carman formula with exponent α=3 and normalized porosity change φ/φ_0=0.95).

3.4 Conclusions

Four different zones are identified in the storage reservoir around injection wells. Mass balance calculations show the extent of mineral dissolution and precipitation. Density changes, fluid convection, and hydro-geomechanical analyses lead to the flowing conclusions.

• The formation water is under-saturated in terms of evaporate minerals such as halite and anhydrite and either under-saturated or in equilibrium with other minerals in the formation.

• In leveled sediments (i.e., no geometric trap), the CO_2 pool thickness may be limited by lateral capillary trapping rather than by the sediment layer thickness. Typical pools will be only a few meters thick in the absence of geometric traps.

• Brine densifies as CO_2 and mineral dissolve. Density changes are more pronounced when the brine salinity is low; the maximum increase in brine density is ~1.2%. The maximum decrease in mineral volume at equilibrium is $\Delta V_M/V_M \leq 0.2\%$ for the worst zero brine salinity case. The associated increase in permeability is <1%.

• The continuous influx of dry CO_2 dries the residual brine near the wellbore. The precipitation of secondary minerals increases the mineral volume by a maximum of 5%. A minor decrease in CO_2 permeability is anticipated.

• The time for convection may be as low as few years in pervious reservoirs. Short convection times will aggravate dissolution consequence in relatively short storage time. Convection-sustained mineral dissolution in the proximity of fresh brine causes a decrease in the horizontal effective stress $\sigma_{h0}' \rightarrow \sigma_{ha}'$. Either compaction-driven shear failure (system satisfies the Rankine active failure condition) or caprock bending failure (gradual development of a poorly supported span beneath the caprock) may occur as a result of mineral dissolution. In particular, the unsupported free span of the caprock cannot exceed 20% of the caprock thickness.

Computation Charts

Chart 3.1 Initial pore fluid composition (Zone I)

Only mineral and brine exists in the far-field Zone I, Volume terms are:

• Volume of mineral: $V_M^{<0>}=(1-\varphi^{<0>})\cdot V_T^{<0>}$ (C.1)

• Volume of brine: $V_B^{<0>}=\varphi^{<0>}\cdot V_T^{<0>}$ (C.2)

where $\varphi^{<0>}$ is the initial porosity, and $V_T^{<0>}$ is total volume.

• Concentration of salt $NaCl$ in brine: $b_{NaCl}^{<0>}$ [mol/kg-water]=Sal (C.3)

where salinity is preset between 0≤ Sal≤6 [mol/kg-water]

• Concentration of calcite in brine: $b_{Ca}^{<0>}$ [mol/kg-water]=$\sqrt{K_M}=10^{-4.24}$ (C.4)

• Mass of brine: $M_B^{<0>} = \rho_B^{<0>} \cdot \phi^{<0>} \cdot V_T^{<0>}$ (C.5)

Brine density $\rho_B^{<0>}$ is computed as a function of pressure, temperature, and dissolved species (expressions in Bachu and Adams, 2003):

• Water density:

$$\rho_W^{<0>}\,[\mathrm{g/cm^3}] = 1 + 10^{-6} \cdot (-80T - 3.3T^2 + 0.00175T^3 + 489P - 2TP + 0.016T^2P - 1.3\cdot 10^{-5}T^3P - 0.333P^2 - 0.002TP^2) \quad \text{(C.6)}$$

• Brine density:

$$\rho_B^{<0>}\,[\mathrm{g/cm^3}] = \rho_W^{<0>} + C_{SM} \cdot (0.668 + 0.44C_{SM} + 10^{-6} \cdot (300P - 2400PC_{SM} + T \cdot (80 - 3T - 3300C_{SM} - 13P + 47PC_{SM}))) \quad \text{(C.7)}$$

where temperature T in [°C], pressure P in [MPa], and Concentration of dissolved species (salt+calcite) C_{SM} in ppt (parts per thousand).

• Mass of mineral = Solid phase mineral + Mineral dissolved in brine

$$M_M^{<0>} = M_M^{<0,M>} + M_M^{<0,B>} = \rho_M^{<0>} \cdot \left(1-\phi^{<0>}\right)\cdot V_T^{<0>} \cdot + m_M \cdot b_{Ca}^{<0>} \cdot \rho_B^{<0>} \cdot \phi^{<0>} \cdot V_T^{<0>} \quad \text{(C.8)}$$

where the mineral mass density is $\rho_M^{<0>}$=2700kg/m^3, and the mineral molar mass is m_M=100g/mol.

• Mass of salt dissolved in brine: $M_S^{<0,B>} = Sal \cdot \rho_B^{<0>} \cdot \phi^{<0>} \cdot V_T^{<0>}$ (C.9)

Chart 3.2 Zone II: Before equilibrium

There are three phases. The corresponding volumes are:

• Volume of mineral: $V_M^{<1>}=(1-\varphi^{<0>})\cdot V_T^{<0>}$ (C.10)

• Volume of CO_2: $V_{CO2}^{<1>}=\varphi^{<0>}\cdot(1-S_B)\cdot V_T^{<0>}$ (C.11)

• Volume of residual brine: $V_B^{<1>}=\varphi^{<0>}\cdot S_B\cdot V_T^{<0>}$ (C.12)

where S_B denotes residual saturation of brine.

The mass of CO_2, brine, mineral, and salt *NaCl* follow:

• Mass of CO_2: $M_{CO2}^{<1>} = \rho_{CO2}^{<0>} \cdot \phi^{<0>} \cdot (1-S_B)\cdot V_T^{<0>}$ (C.13)

where CO_2 density $\rho_{CO2}^{<0>}$ is computed from formulae by Duan and Sun (2003).

• Mass of brine: $M_B^{<1>} = \rho_B^{<0>} \cdot \phi^{<0>} \cdot S_B \cdot V_T^{<0>}$ (C.14)

• Mass of mineral

$$M_M^{<1>} = M_M^{<1,M>} + M_M^{<1,B>} = \rho_M^{<0>} \cdot \left(1-\phi^{<0>}\right)\cdot V_T^{<0>} \cdot + m_M \cdot b_{Ca}^{<0>} \cdot \rho_B^{<0>} \cdot \phi^{<0>} \cdot S_B \cdot V_T^{<0>} \quad \text{(C.15)}$$

• Mass of salt: $M_S^{<1,B>} = Sal \cdot \rho_B^{<0>} \cdot \phi^{<0>} \cdot S_B \cdot V_T^{<0>}$ (C.16)

• Concentration of salt *NaCl* in brine: $b_{NaCl}^{<1>}$ [mol/kg-water]=*Sal* (C.17)

• Concentration of mineral in brine: $b_{Ca}^{<1>}$ [mol/kg-water]=$\sqrt{K_M}=10^{-4.24}$ (C.18)

Chart 3.3 Dissolution of supercritical CO_2

• The solubility of supercritical CO_2 in brine Sol_{CO2} is obtained from the semi-empirical formulae proposed by Duan and Sun (2003):

$$Sol_{CO2} = \exp\left[\ln\left(y_{CO2}\cdot P\right) - \frac{\mu_{CO2}^{l(0)}}{RT} + \ln\Phi_{CO2} - \sum_c 2\lambda_{CO2-c} n_c - \sum_a 2\lambda_{CO2-a} n_a - \sum_c\sum_a \zeta_{CO2-c-a} n_c n_a\right]$$

(C.19)

where symbol μ represents chemical potential, symbols λ and ζ denote dimensionless standard chemical potentials, and subscript c and a mean cations and anions, respectively. All expressions are described in Duan and Sun (2003).

• Concentration of total dissolved CO_2:

$$b_{CO2}^{<1>}\,[\text{mol/kg - water}] = \min\left(Sol_{CO2}, \frac{M_{CO2}^{<1>}/m_{CO2}}{M_B^{<1>}} \right) \tag{C.20}$$

where the molar mass of CO_2 is m_{CO2}=44g/mol. We compare Sol_{CO2} with the present concentration of CO_2 to account for the maximum amount of dissolvable CO_2.

• Concentration of hydrogen ion H^+:

$b_H^{<1>}$ [mol/kg-water]=$\sqrt{(K_{a1} \cdot b_{CO2}^{<1>})}$; acidity constant K_{a1}=$10^{-6.35}$ (C.21)

• pH=-log $b_H^{<1>}$ (C.22)

Chart 3.4 Mineral dissolution and concentrations of species at equilibrium

• The concentration of dissolved CO_2 $b_{CO2}^{<1>}$ and the presence of calcite $CaCO_3$ are input to PHREEQC software (Parkhurst et al., 1999) to compute chemical reactions. The output values are the concentrations of species such as H_2CO_3*, H^+, Ca^{2+}, HCO_3^-, and CO_3^{2-} at equilibrium - $b_{CO2}^{<2>}$, $b_H^{<2>}$, $b_{Ca}^{<2>}$, $b_{HCO3}^{<2>}$, and $b_{CO3}^{<2>}$ in [mol/kg-water].

• pH=-log $b_H^{<2>}$ (C.23)

• The mass faction of CO_2 X_{CO2} in the aqueous brine phase:

$$X_{CO2} = \frac{b_{CO2}^{<2>} \cdot m_{CO2}}{b_{CO2}^{<2>} \cdot m_{CO2} + 1 + Sal \cdot m_S + b_{Ca}^{<2>} \cdot m_M} \tag{C.24}$$

where the molar mass of salt $NaCl$ is m_S=58g/mol.

• The mass fraction of brine X_B in the aqueous brine phase:

$$X_B = \frac{1 + Sal \cdot m_S}{b_{CO2}^{<2>} \cdot m_{CO2} + 1 + Sal \cdot m_S + b_{Ca}^{<2>} \cdot m_M} \tag{C.25}$$

• The mass fraction of mineral X_M in the aqueous brine phase:

$$X_M = \frac{b_{Ca}^{<2>} \cdot m_M}{b_{CO2}^{<2>} \cdot m_{CO2} + 1 + Sal \cdot m_S + b_{Ca}^{<2>} \cdot m_M} \tag{C.26}$$

• The mole fraction of water y_w in the CO_2 phase:

$$y_W = \frac{K_W^0 (1 - x_{CO2})}{\Phi_W P} \exp\left(\frac{(P - P^0)\overline{V}_W}{RT} \right) \quad (C.27)$$

Equation C.25 is proposed by Spycher et al. (2003). Detailed calculations of molar fraction y_w can be found in Spycher et al. (2003) and Hassanzadeh et al., 2008).

• The molar fraction of CO_2 y_{CO2} in the supercritical CO_2 phase: $y_{CO2}=1-y_W$ (C.28)

• The mass fraction of CO_2 Y_{CO2} in the supercritical CO_2 phase:

$$Y_{CO2} = \frac{y_{CO2} \cdot m_{CO2}}{y_{CO2} \cdot m_{CO2} + y_W \cdot m_W} \quad (C.29)$$

where the molar mass of water is m_W=18g/mol.

• The mass fraction of water Y_W in the supercritical CO_2 phase:

$$Y_W = \frac{y_W \cdot m_W}{y_{CO2} \cdot m_{CO2} + y_W \cdot m_W} \quad (C.30)$$

Chart 3.5 Density estimation

• Density of brine: $\rho_B^{<2>} = \left(\frac{X_W}{\rho_B^W} + \frac{X_{CO2}}{\rho_{CO2}^W} + \frac{X_M}{\rho_M^W} \right)^{-1}$ (ref: Spycher et al., 2003) (C.31)

$\rho_{CO2}{}^W$ denotes density of CO_2 dissolved in water: $\rho_{CO2}^W = \frac{m_{CO2}}{V_\phi}$ (C.32)

V_φ: apparent molar volume of CO_2 dissolved in water (see - Garcia, 2001).

For simplicity, density of minerals dissolved in water is $\rho_M{}^W=\rho_M{}^{<0>}$.

• Density of CO_2: $\rho_{CO2}^{<2>} = \left(\frac{Y_{CO2}}{\rho_{CO2}^{<0>}} + \frac{Y_W}{\rho_W^{CO2}} \right)^{-1}$ (C.33)

$\rho_W{}^{CO2}$ denotes density of water dissolved in CO_2: $\rho_{CO2}^W = \frac{m_W}{V_{w\phi}}$ (C.34)

$V_{w\varphi}$=18.1cm^3/mol: average value for the partial molar volume of water (Hassanzadeh et al., 2008).

Chart 3.6 Mass balance of CO_2 and brine

• Mass of CO_2 dissolved in brine $M_{CO2}{}^{<2,B>}$: $M_{CO2}^{<2,B>} = X_{CO2} \cdot M_B^{<2>}$ (C.35)

• Mass of CO_2 in CO_2 $M_{CO2}{}^{<2,CO2>}$: $M_{CO2}^{<2,CO2>} = Y_{CO2} \cdot M_{CO2}^{<2>}$ (C.36)

• Mass of water dissolved in CO_2 $M_W{}^{<2,CO2>}$: $M_W^{<2,CO2>} = Y_W \cdot M_{CO2}^{<2>}$ (C.37)

• Mass of water in brine $M_B{}^{<2,B>}$: $M_B^{<2,B>} = X_B \cdot M_B^{<2>}$ (C.38)

where $M_{CO2}{}^{<2>}$ denotes the total mass of CO_2 at equilibrium, and $M_B{}^{<2>}$ the total mass of brine at equilibrium.

• Mass conservation of CO_2: $M_{CO2}^{<1>} = M_{CO2}^{<2,B>} + M_{CO2}^{<2,CO2>}$ (C.39)

• Mass conservation of brine: $M_B^{<1>} = M_B^{<2,B>} + M_W^{<2,CO2>}$ (C.40)

• Total mass of brine $M_B{}^{<2>}$:

$$M_B^{<2>} = \frac{\rho_{CO2}^{<0>} \cdot \phi^{<0>} \cdot (1 - S_B) \cdot V_T^{<0>} \cdot Y_W - \rho_B^{<0>} \cdot \phi^{<0>} \cdot S_B \cdot V_T^{<0>} \cdot Y_{CO2}}{Y_W \cdot X_{CO2} - Y_{CO2} \cdot X_B} \quad \text{(C.41)}$$

• Total mass of CO_2 $M_{CO2}{}^{<2>}$:

$$M_{CO2}^{<2>} = \frac{\rho_{CO2}^{<0>} \cdot \phi^{<0>} \cdot (1 - S_B) \cdot V_T^{<0>} \cdot X_B - \rho_B^{<0>} \cdot \phi^{<0>} \cdot S_B \cdot V_T^{<0>} \cdot X_{CO2}}{X_B \cdot Y_{CO2} - X_{CO2} \cdot Y_W} \quad \text{(C.42)}$$

Equations C.40 and C.41 are derived by rearranging Equations C.11~12 and C.35~40.

• Total mass of mineral $M_M{}^{<2>}$: $M_M^{<2>} = M_M^{<1>} - m_M \cdot \left(b_{Ca}^{<2>} - b_{Ca}^{<1>}\right) \cdot M_B^{<2>}$ (C.43)

• Total mass of salt $M_S{}^{<2,B>}$: $M_S^{<2,B>} = Sal \cdot \rho_B^{<0>} \cdot \phi^{<0>} \cdot S_B \cdot V_T^{<0>}$ (C.44)

Chart 3.7 Volume changes

• Volume of brine $V_B{}^{<2>}$: $V_B^{<2>} = \dfrac{M_B^{<2>}}{\rho_B^{<2>}}$ (C.45)

• Volume of CO_2 $V_{CO2}{}^{<2>}$: $V_{CO2}^{<2>} = \dfrac{M_{CO2}^{<2>}}{\rho_{CO2}^{<2>}}$ (C.46)

• Volume of mineral $V_M{}^{<2>}$: $V_M^{<2>} = \dfrac{M_M^{<2>}}{\rho_M^{<2>}}$ (C.47)

Chart 3.8 Mineral precipitation (Zone IV)

• Amount of calcium ion Ca^{2+} in brine $n_{Ca}{}^{<3>}$: $n_{Ca}^{<3>}\,[\mathrm{mol}] = b_{Ca}^{<2>} \cdot M_B^{<2>}$ (C.48)

• Amount of salt $NaCl$ in brine $n_S{}^{<3>}$: $n_S^{<3>}\,[\mathrm{mol}] = M_S^{<2,B>}$ (C.49)

If we assume all Ca^{2+} and $NaCl$ species precipitate as a result of complete evaporation, a corresponding volume increase ΔV is:

• Precipitation of calcite ΔV_M: $\Delta V_M = n_{Ca}^{<3>} \cdot Vm_M$ (C.50)

• Precipitation of halite ΔV_S: $\Delta V_S = n_S^{<3>} \cdot Vm_S$ (C.51)

where the molar volume of calcite is Vm_M =3.7*10^{-5}m^3/mol, and the molar volume of halite is Vm_S =2.7*10^{-5}m^3/mol.

• Increase in the mineral volume $\Delta V_M{}^{<3>}$: $\Delta V_M^{<3>} = \Delta V_M + \Delta V_S$ (C.52)

CHAPTER 4

CO_2 GEOLOGICAL STORAGE: PORE-SCALE REACTIVE FLUID TRANSPORT (ROCK JOINT AND PORES)

4.1 Introduction

Quality of life is correlated with energy consumption. The anticipated increase in both quality of life and energy demand in the coming decades will largely rely on fossil fuels because of readily available reserves, low cost, prevailing infrastructure, and insufficient energy production from renewable sources (EIA, 2010; Espinoza et al., 2011; Pasten and Santamarina, 2012). Currently, 90% of the world's consumption and more than 85% of the energy consumed in the USA comes from fossil fuels (DOE, 2010). Fossil fuel combustion produces CO_2. When released into the atmosphere, CO_2 acts as a green house gas and it is believed to be a main cause for global warming (IPCC, 2005). In this context, carbon capture and geologic sequestration emerges as an important alternative to mitigate global warming.

Supercritical CO_2 conditions are preferred to minimize CO_2 storage volume (temperature T>304.1K and pressure P>7.38MPa; Span and Wagner, 1996; Kaldi and Gibson-Poole, 2008). The injection of supercritical CO_2 triggers: advection of CO_2 (Saripalli and McGrail, 2002; Nordbotten et al., 2005; Ennis-King and Paterson, 2007), buoyancy in response to CO_2-brine density difference (Bachu and Adams, 2003; Bielinski et al., 2008; Okwen et al., 2010), convection of CO_2-dissolved water (Weir et al., 1996; Riaz et al., 2006; Hassanzadeh et al., 2007; Kneafsey and Pruess, 2010), diffusion and dissolution of CO_2 into the water phase (Gaus et al., 2005; Berne et al., 2010; Li et al., 2011), viscous fingering of CO_2 (Homsy, 1987; Fenghour et al., 1998; Cinar et al., 2007), capillary trapping of the immiscible CO_2 by the water-saturated porous formation (Juanes et al., 2006; Kopp et al., 2009; Saadatpoor et al., 2009), and reactive fluid transport due to the acidification of water following CO_2 dissolution (Li et al., 2008; Solomon et al., 2008; Szymczak and Ladd, 2009; Figure 4.1). We note that reactive fluid transport through a porous medium generates positive feedback and may lead to the formation of wormholes (Golfier et al., 2002).

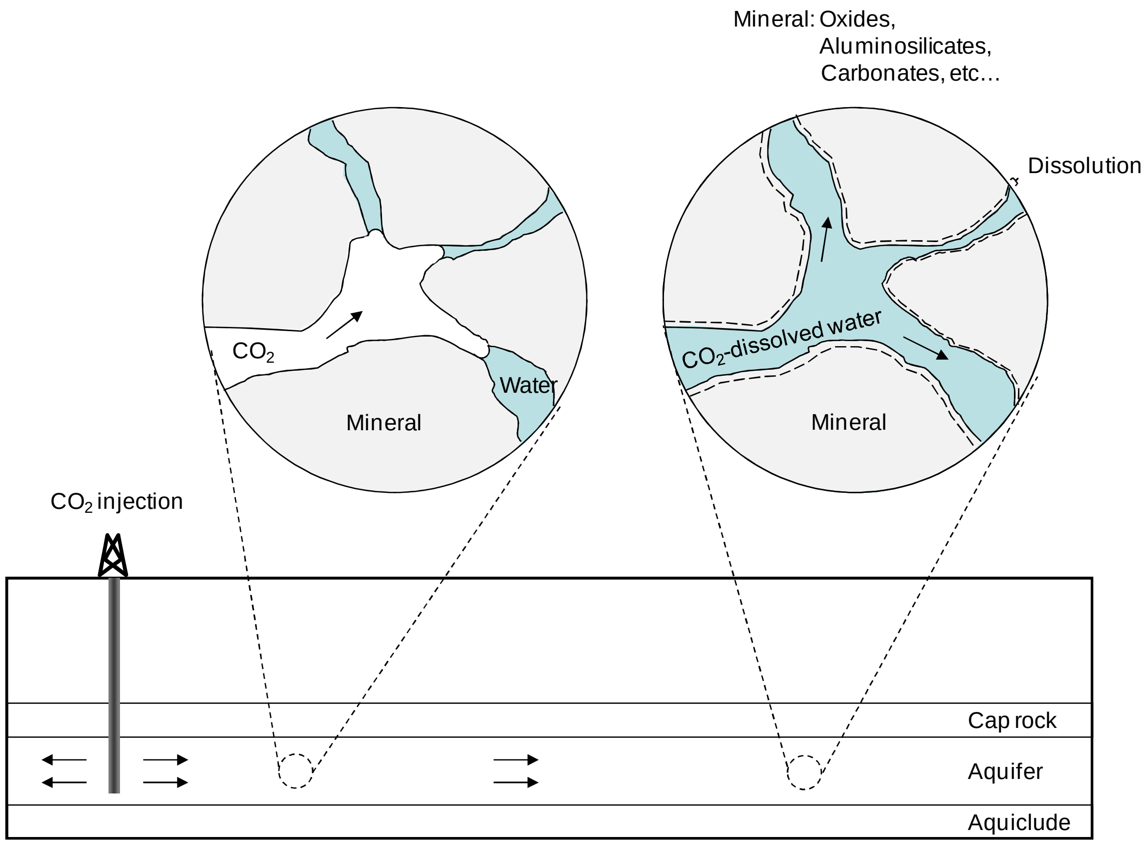

Figure 4.1 Schematic illustration of the CO_2 geological storage and consequent CO_2 invasion and flow of CO_2-dissolved fluid through rock joints/pores. Reactant species such as hydrogen ions H^+ and aqueous carbon dioxide $CO_{2(aq)}$ cause chemical reactions to occur at mineral surfaces as reactive fluid flows through rock joints/pores.

Preferred formations for CO_2 geological storage are either sandstones or carbonates (Gale, 2004; Dooley et al., 2006). Previous studies show that the overall amount of surface reaction between carbonates and acidified water is smaller than that between sandstones and the solute, but the reaction rate between carbonates and acidified fluid is much faster than that for sandstones (Stumm et al., 1996; Gunter et al., 2000; Gaus et al., 2005).

Injection could be engineered to prevent or minimize some of the negative consequences of CO_2 geological storage. However, a proper pore-scale understanding of reactive fluid transport is required when fluids are rich in total carbonic acid H_2CO_3* and hydrogen ions H^+. The kinetics of injected CO_2 is analyzed first followed by 2-D simulations of CO_2-dissolved fluid injection in a pore.

4.2 CO_2 Injection: Kinetic Rates

Injected carbon dioxide CO_2 dissolves in the formation water or brine to sequentially form aqueous carbon dioxide $CO_{2(aq)}$ and carbonic acid H_2CO_3, which consequently dissociates into bicarbonate ions HCO_3^- and hydrogen ions H^+ (Stumm et al., 1996; IPCC, 2005):

$$CO_{2(g)} \underset{k_{aq}}{\overset{k_g}{\leftrightarrow}} CO_{2(aq)}\,; \qquad K_H = \frac{k_g}{k_{aq}} = 10^{-1.47} \text{ (Henry's constant)} \tag{1}$$

$$CO_{2(aq)} + H_2O \underset{k_{H2CO3}}{\overset{k_{CO2}}{\leftrightarrow}} H_2CO_3\,; \quad K = \frac{k_{H2CO3}}{k_{CO2}} \tag{2}$$

$$H_2CO_3 \underset{k_{21}}{\overset{k_{12}(very\ fast)}{\leftrightarrow}} HCO_3^- + H^+\,;\ K_{H2CO3} = \frac{k_{12}}{k_{21}} \tag{3}$$

where capital K represents an equilibrium constant for each chemical reaction. The hydration reaction $CO_{2(aq)}+H_2O \rightarrow H_2CO_3$ (Equation 2) is first order with respect to aqueous $CO_{2(aq)}$ (Stumm et al., 1996). Likewise, dehydration $H_2CO_3 \rightarrow CO_{2(aq)}+H_2O$

(Equation 2) is first order with respect to carbonic acid H_2CO_3. Assuming that the reaction between carbonic acid and bicarbonate ion is linear, the following kinetic laws are obtained for the chemical reactions above:

$$\frac{d[CO_{2(g)}]}{dt} = -k_g[CO_{2(g)}] + k_{aq}[CO_{2(aq)}] \tag{4}$$

$$\frac{d[CO_{2(aq)}]}{dt} = k_g[CO_{2(g)}] - k_{aq}[CO_{2(aq)}] - k_{CO2}[CO_{2(aq)}] + k_{H2CO3}[H_2CO_3] \tag{5}$$

$$\frac{d[H_2CO_3]}{dt} = k_{CO2}[CO_{2(aq)}] - k_{H2CO3}[H_2CO_3] - k_{12}[H_2CO_3] + k_{21}[HCO_3^-][H^+] \tag{6}$$

$$\frac{d[H^+]}{dt} = \frac{d[HCO_3^-]}{dt} = k_{12}[H_2CO_3] - k_{21}[HCO_3^-][H^+] \tag{7}$$

where square brackets around species name indicates concentrations of the species. The reaction rate constants for hydration and dehydration reactions are: k_{CO2}=0.04s^{-1} at 25°C with the activation energy E_a=15kcal/mol, and k_{H2CO3}=20s^{-1} at 25°C with E_a=16kcal/mol (Stumm et al., 1996). The rate constants k_{CO2} and k_{H2CO3} permit the calculation of the equilibrium constant K (Equation 2). Then, we can obtain equilibrium constant K_{H2CO3} from K (Stumm et al., 1996):

$$K_{H2CO3} = K_1(1+K) \tag{8}$$

K_1 denotes the first acidity constant for the reaction in which $H_2CO_3^*$ dissociates to bicarbonate and hydrogen ion (the asterisk denotes combining both aqueous carbon dioxide and carbonic acid; Stumm et al., 1996). The value of the acidity constant is $K_1 \approx 10^{-6.35}$ under standard conditions (T=25°C and P=0.1MPa). The rate constants are: $k_{12} \approx 10^7$s^{-1} at ~40°C for the dissociation of carbonic acid (Zhang, 2008), $k_{21}=k_{12}/K_{H2CO3}$ for the reversed reaction (Equation 3), $k_g \approx 5\text{x}10^{-3}$s^{-1} at 40°C for the dissolution of gaseous carbon dioxide (4.6x10^{-3}s^{-1} at 25°C; Sposito, 1994), and $k_{aq}=k_g/K_H$ for the reversed reaction (Equation 1). These rate constants are summarized in Table 4.1.

Table 4.1 Parameters used in simulations

Parameter Name	Value	Description	
	CO_2 kinetics		
k_g	$5x10^{-3}s^{-1}$ (1)	Rate constant of $CO_{2(g)} \rightarrow CO_{2(aq)}$	
k_{aq}	k_g / K_H (1)	Rate constant of $CO_{2(g)} \leftarrow CO_{2(aq)}$	
k_{CO2}	$0.135s^{-1}$ (2)	Rate constant of $CO_{2(aq)} \rightarrow H_2CO_3$	
k_{H2CO3}	$72.982s^{-1}$ (2)	Rate constant of $CO_{2(aq)} \leftarrow H_2CO_3$	
k_{12}	10^7s^{-1} (3)	Rate constant of $H_2CO_3 \rightarrow H^+ + HCO_3^-$	
k_{21}	$4.1x10^{10}s^{-1}$ (3)	Rate constant of $H_2CO_3 \leftarrow H^+ + HCO_3^-$	
K_H	$10^{-1.47}$	Henry's constant	
Calcite fracture plane		Anorthite fracture plane	
$[H^+]_{inlet}$	10^{-6}mol/L to 10^{-3}mol/L	$[H^+]_{inlet}$	10^{-6}mol/L to 10^{-3}mol/L
$[H_2CO_3*]_{inlet}$	10^{-3}mol/L to 1mol/L	$[H_2CO_3*]_{inlet}$	10^{-3}mol/L to 1mol/L
$[Ca^{2+}]_{inlet}$	$1.36x10^{-3}$mol/L (4)	$[HCO_3^-]_{inlet}$	$6.68x10^{-4}$mol/L (4)
$[HCO_3^-]_{inlet}$	$6.68x10^{-4}$mol/L (4)	$[OH^-]_{inlet}$	$1.50x10^{-11}$mol/L (4)
$[OH^-]_{inlet}$	$1.50x10^{-11}$mol/L (4)	$[Ca^{2+}]_{inlet}$	$2.11x10^{-4}$mol/L (4)
$[Cl^-]_{inlet}$	$2.72x10^{-3}$mol/L (4)	$[Al^{3+}]_{inlet}$	$3.51x10^{-8}$mol/L (4)
		$[H_4SiO_4]_{inlet}$	$9.67x10^{-13}$mol/L (4)
		$[Cl^-]_{inlet}$	$4.22x10^{-4}$mol/L (4)
$[H^+]_{initial}$	$1.0x10^{-8}$mol/L (5)	$[H^+]_{initial}$	$1.0x10^{-8}$mol/L (6)
$[H_2CO_3*]_{initial}$	$1.0x10^{-5}$mol/L (5)	$[H_2CO_3*]_{initial}$	$1.0*10^{-5}$mol/L (6)
$[Ca^{2+}]_{initial}$	$1.59x10^{-3}$mol/L (5)	$[HCO_3^-]_{initial}$	$4.47x10^{-4}$mol/L (6)
$[HCO_3^-]_{initial}$	$4.47x10^{-4}$mol/L (5)	$[OH^-]_{initial}$	$1.0x10^{-6}$mol/L (6)
$[OH^-]_{initial}$	$1.0x10^{-6}$mol/L (5)	$[Ca^{2+}]_{initial}$	$4.35x10^{-4}$mol/L (6)
$[Cl^-]_{initial}$	$2.72x10^{-3}$mol/L (5)	$[Al^{3+}]_{initial}$	$3.51x10^{-8}$mol/L (6)
		$[H_4SiO_4]_{initial}$	$9.67x10^{-13}$mol/L (6)
		$[Cl^-]_{initial}$	$4.22x10^{-4}$mol/L (6)
k_1	0.745mol/m^2/s (7)	k_H	$3.4x10^{-4}$mol/m^2/s (8)
k_2	$8.6x10^{-4}$mol/m^2/s (7)	k_{H2O}	$1.8x10^{-12}$mol/m^2/s (8)
K_{tot}	$10^{-2.65}$ (7)	K_{tot}	$10^{21.7}$ (8)
v_0	10^{-3}cm/s to 1cm/s	Inlet velocity	
η	10^{-3}Pa·s	Viscosity of fluid	
ρ_f	1,100kg/m^3	Density of fluid	
S_s	0.06m^2/g (9)	Specific surface of calcite and anorthite	
M_m	100g/mol 277g/mol	Molar mass of calcite Molar mass of anorthite	
V_m	$3.7x10^{-5}$m^3/mol $10.1x10^{-5}$m^3/mol	Molar volume of calcite Molar volume of anorthite	
D	$2.0x10^{-9}$m^2/s	Average diffusion coefficient for all species	

(Rate constants are computed for temperature T=40°C from: (1) Sposito, 1994, (2) Stumm et al., 1996, (3) Zhang, 2008; species concentrations are computed for (4) pH=3.18, (5) pH=8 and $K_{tot}=10^{-2.65}$, (6) pH=8 and $K_{tot}=10^{21.7}$; (7) Renard et al., 2005; Wigand et al., 2008; Algive et al., 2009, (8) Li et al., 2006, (9) Gaus et al., 2005)

We can numerically examine the evolution of species concentrations with these kinetic rate laws. For instance, the solution of differential Equations 4 to 7 (using 4th order Runge-Kutta method in the Matlab) shows that the concentration of hydrogen ions $[H^+]$ converges to $10^{-3.28}$mol/L and the acidity level drops to pH≈3.28 under a partial pressure of CO_2 P_{CO2}=10MPa and temperature T=40°C.

4.3 Mineral Dissolutions: Kinetic Rates

Let's consider two representative minerals: calcite $CaCO_3$ (its dissolution may provide preferential leakage paths), and anorthite $CaAl_2Si_2O_8$ (it exhibits the fastest reaction rate among aluminosilicates). While the dissolution of aluminosilicates is much slower than that of calcite, aluminosilicates yield more dissolved cations in the long term: higher solubility (Gunter et al., 2000); therefore, aluminosilicates are good candidates for mineral trapping.

4.3.1 Calcite Dissolution

Calcite can act as a buffering agent when CO_2 is injected into a carbonate reservoir. Three chemical reactions involve calcite and occur in parallel albeit with different rate constants (Plummer et al., 1978):

$$CaCO_{3(s)} + H^+ \underset{k_{1b}}{\overset{k_{1f}}{\leftrightarrow}} Ca^{2+} + HCO_3^-; \qquad \log K_{eq}=1.85 \tag{9}$$

$$CaCO_{3(s)} + CO_{2(aq)} + H_2O \underset{k_{2b}}{\overset{k_{2f}}{\leftrightarrow}} Ca^{2+} + 2HCO_3^-; \qquad \log K_{eq}=-4.50 \tag{10}$$

$$CaCO_{3(s)} \underset{k_{3b}}{\overset{k_{3f}}{\leftrightarrow}} Ca^{2+} + CO_3^{2-}; \qquad \log K_{eq}=-8.48 \tag{11}$$

The rate constants are: $k_{1f}=5.1\times10^{-1}$mol/m^2/s, $k_{2f}=3.4\times10^{-4}$mol/m^2/s, and $k_{3f}=1.1\times10^{-6}$ mol/m^2/s at 20°C with the activation energy of E_1=14.5kJ/mol, E_2=35.4kJ/mol, and E_3=23.5 kJ/mol (Chou et al., 1989; Renard et al., 2005; Wigand et al., 2008; Algive et al., 2009). The third reaction (Equation 11) has a much smaller rate and equilibrium constants, hence, it is ignored and only the first two reactions are captured in the numerical simulation (Equations 9 and 10). One reaction consumes H^+ and produces Ca^{2+} and HCO_3^- (Equation 9). The other reaction consumes one mole of $CO_{2(aq)}$ in exchange for one mole of Ca^{2+} and two moles of HCO_3^- (Equation 10). The Transition State Theory enables us to express the overall dissolution rate R_d as follows (Lasaga, 1984; Li et al., 2008):

$$R_d = \left(k_{1f}[H^+] + k_{2f}[CO_{2(aq)}]\right)\left(1 - \frac{\Omega}{K_{eq}}\right) \text{ where } \Omega = \frac{[Ca^{2+}]^2[HCO_3^-]^3}{[H^+][CO_{2(aq)}]} \tag{12}$$

and the overall equilibrium constant becomes $\log K_{eq}$=1.85-4.50=-2.65 (refer to Equations 9 and 10).

4.3.2 Anorthite Dissolution

We adopt the model by Li et al. (2006) to represent the dissolution of anorthite. The reaction consumes eight moles of H^+ to produce one mole of Ca^{2+}, two moles of Al^{3+}, and two moles of H_4SiO_4:

$$CaAl_2Si_2O_{8(s)} + 8H^+ \leftrightarrow Ca^{2+} + 2Al^{3+} + 2H_4SiO_4 \tag{13}$$

Again, the overall dissolution rate is described as a function of rate constants, concentrations of reactant species and saturation:

$$R_d = \left(k_H[H^+]^{1.5} + k_{H_2O} + k_{OH}[OH^-]^{0.33}\right)\left(1 - \frac{\Omega}{K_{eq}}\right) \text{where } \Omega = \frac{[Ca^{2+}][Al^{3+}]^2[H_4SiO_4]^2}{[H^+]^8} \tag{14}$$

and $\log K_{eq}$=21.7, k_H=$10^{-3.32}$mol/m^2/s, k_{H2O}=$10^{-11.6}$mol/m^2/s, k_{OH}=$10^{-13.5}$mol/m^2/s at 25°C (Li et al., 2006). We omit the term $k_{OH}[OH^-]^{0.33}$ during the numerical simulation because both the rate constant and the concentration of hydroxide $[OH^-]$ are negligible. Figure 4.2 compares the overall mineral dissolution rates R_d when we fix the concentration of the total carbonic acid H_2CO_3* at [H_2CO_3*]=1mol/L as a consequence of CO_2 geological storage. Results show that the concentration of hydrogen ions [H^+] controls the reaction rate of calcite up to pH~4 beyond which high concentration of total carbonic acid [H_2CO_3*] takes control of it. Reaction rate of anorthite decreases gradually as [H^+] decreases until the acidity level drops to pH~6. Reaction rate of calcite is several orders of magnitude higher than that of anorthite in the range of 2<pH<7 (Figure 4.2).

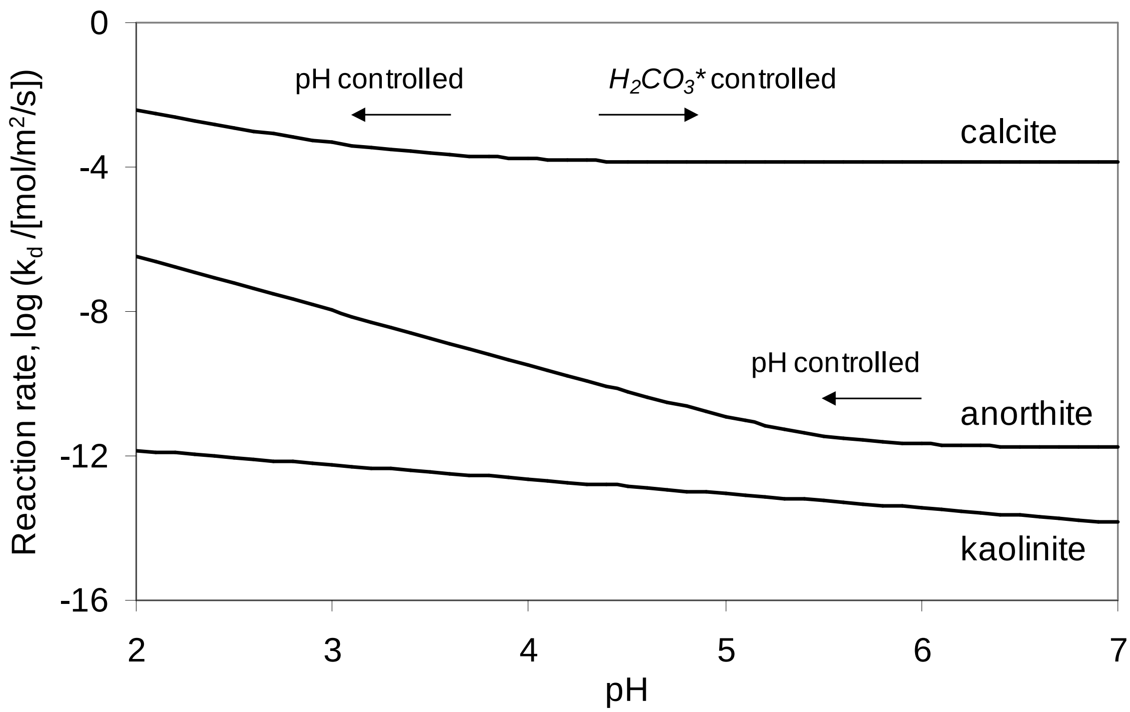

Figure 4.2 Reaction rate log(k_d/[mol/m^2/s]) for dissolution of calcite $CaCO_3$, anorthite $CaAl_2Si_2O_8$, and kaolinite $Al_2Si_2O_5(OH)_4$ at temperature T=40°C and fixed concentration of total dissolved carbon dioxide [H_2CO_3*]=1mol/L. For calcite, $k_d=k_1[H^+]+k_2[H_2CO_3^*]$ where k_1=0.745mol/m^2/s and k_2=8.6x10^{-4}mol/m^2/s at T=40°C (Fredd and Fogler, 1998; Pokrovsky et al., 2005; Renard et al., 2005; Algive et al., 2009). For anorthite, $k_d=k_H[H^+]^{1.5}+k_{H2O}+k_{OH}[OH^-]^{0.33}$ where k_H=6.883x10^{-4}mol/m^2/s, k_{H2O}=3.58x10^{-12}mol/m^2/s, and k_{OH}=4.51x10^{-14}mol/m^2/s at T=40°C (Li et al., 2006). For kaolinite, $k_d=k_H[H^+]^{0.4}+k_{OH}[OH^-]^{0.3}$ where k_H=2.79x10^{-11}mol/m^2/s and k_{OH}=3.51x10^{-16}mol/m^2/s at T=40 °C (Li et al., 2006).

4.4 Numerical Simulation of Reactive Fluid Flow

A numerical simulation study is implemented to explore the coupling between hydro-chemical phenomena during the transport of reactive CO_2-acidified water through a pore in a mineral system. Governing dimensionless ratios are introduced first.

4.4.1 Dimensionless Ratios

Consider a reactive fluid advecting with velocity v [m/s] through a rock joint (i.e., 2-D pore) driven by a pressure difference between inlet and outlet boundaries a distance l [m] from each other. Reactant species are transported towards the mineral surface by molecular diffusion so that the joint aperture d [m] and the diffusion coefficient D [m^2/s] determines the characteristic time for the transverse diffusion. Mineral dissolution at the fracture surface produces species that are carried away by both advection (downstream) and diffusion (towards the center).

Two dimensionless ratios capture the interplay between governing processes. The Damköhler number Da is the ratio between the advection time and the chemical reaction time (Fredd and Fogler, 1998). The Peclet number Pe compares the time for transverse diffusion to the time for longitudinal advection (Golfier et al., 2002):

$$Da = \frac{t_{advection}}{t_{reaction}} = \frac{\kappa d}{v} \tag{15}$$

$$Pe = \frac{t_{diffusion}}{t_{advection}} = \frac{d^2 v}{4lD} \tag{16}$$

where the kinetic rate κ [1/s]=$k_r \cdot S_s \cdot M_m$ is a function of the rate constant for mineral dissolution k_r [mol/m^2/s], the mineral specific surface S_s [m^2/g], and the mineral molar mass M_m [g/mol].

4.4.2 Simulation Method

Consider a slice of a rock joint or a long pore with length l much longer than the aperture d, i.e., $l >> d$, subjected to reactive fluid transport by the forced advection of CO_2-acidified water. The problem is simulated using the moving mesh function in COMSOL to reproduce the joint enlargement (COMSOL, 2008). Figure 4.3 summarizes the simulation scheme. Flow satisfies the Navier-Stokes' law; species experience both advective and diffusive transport. Mineral dissolution occurs at the interface between the fluid and the joint walls with dissolution rate R_d [mol/m^2/s]. The moving mesh function adjusts the mesh outwards or inwards according to the volume of dissolved mineral $R_d \cdot (v_s/v) \cdot V_m$ [m/s], where (v_s/v) denotes the stoichiometric ratio of dissolved mineral to reactant species and V_m [m^3/mol] is the molar volume of the mineral.

While results will be summarized in dimensionless form, the numerical simulation is implemented in a dimensional physical space to facilitate model validation and to add clarity to the discussion of results. Let's set the pore length l=100μm (Note: the channel length in Fontainebleau and Berea sandstones ranges from 20μm to 600μm - Lindquist et al., 2000; Dong and Blunt, 2009). The pore aperture varies from d=2μm to 28μm (Bachu and Bennion, 2008). The inlet velocity is varied from v_0=1cm/s to 10^{-3}cm/s. The inlet concentration of H^+ ranges from $[H^+]_{inlet}=10^{-3}$mol/L to 10^{-6}mol/L, and for H_2CO_3* between $[H_2CO_3*]$=1mol/L and 10^{-3}mol/L. Initial concentrations of all species are assigned so that the system is in thermodynamic-equilibrium and satisfies electro-neutrality at pH=8. Zero pressure is imposed at the outlet, and free flux of species is allowed to simulate an infinite boundary (Figure 4.3). Computations are conducted for every 0.001s until the total simulation time equals 10 times of advection time $10 \cdot l/v_0$. All parameters used for numerical simulations are summarized in Table 4.1.

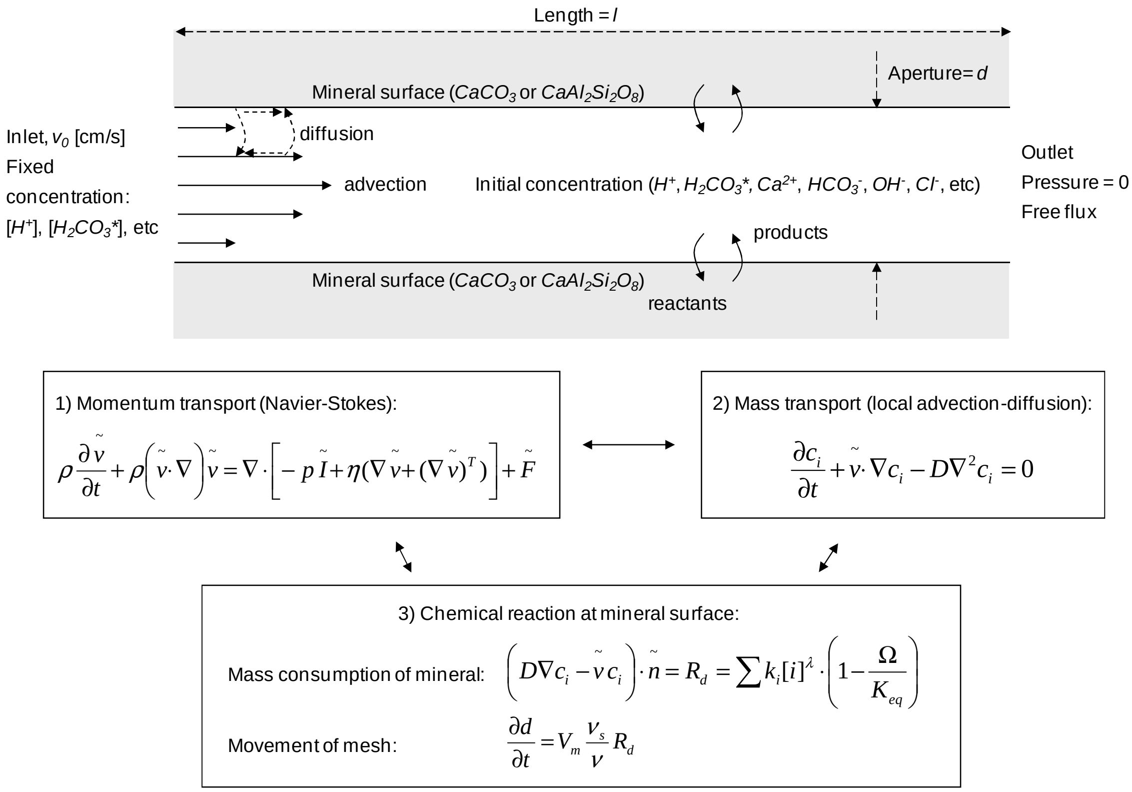

Figure 4.3 Numerical simulation scheme and governing equations for reactive fluid flow through a rock joint/pore problem. Physics models used in COMSOL: 1) Incompressible Navier-Stokes (η: dynamic viscosity of fluid, ρ: density of fluid, $\tilde{v}$: velocity field, p: pressure, $\tilde{F}$: volume force field such as gravity; gravity is disregarded in the simulation), 2) Convection and diffusion (c_i: concentration of species i, D: coefficient of molecular diffusion), and 3) Moving mesh (R_d: overall dissolution rate of mineral at the wall, k_i: reaction rate of reactant species i, [i]: concentration of reactant species i, Ω: ionic concentration product, K_{eq}: equilibrium constant, d: joint aperture, V_m: mineral molar volume, v_s/v: stoichiometric ratio between reactant species and dissolved mineral); Number of elements: 1,608 (when length l=100μm and joint aperture d=10μm). Type of mesh: triangle. Linear system solver: Direct (PARDISO).

4.4.3 Validation

We verify the numerical simulation scheme by comparing COMSOL simulation results with a closed-form solution. There is no analytical solution for reactive fluid transport in a two-dimensional pore, so we compare a 1-D analytical solution with 1-D numerical results obtained with COMSOL. The governing equation for the one-dimensional transport of reactive fluid is:

$$\frac{\partial c}{\partial t} = D\frac{\partial^2 c}{\partial x^2} - v\frac{\partial c}{\partial x} - \kappa c \tag{17}$$

For a single reactant species at an initial concentration $c(x,0)=0$ for $x>0$ and boundary conditions $c(0,t)=c_0$ and $c(\infty,t)=0$ for $t\geq 0$, the solution for the variation of the species concentration in space and time is (Boudreau, 1997):

$$\frac{c}{c_0} = \frac{1}{2}\exp(\xi_2)\left[\exp(-\xi_1)erfc\left(\frac{2\xi_1 - \tau}{2\sqrt{\tau}}\right) + \exp(\xi_1)erfc\left(\frac{2\xi_1 + \tau}{2\sqrt{\tau}}\right)\right]$$

$$\text{where } \beta^2 = \left(\frac{v^2}{4D^2} + \frac{\kappa}{D}\right)\ \xi_1 = \beta x,\ \xi_2 = \frac{vx}{2D},\ \tau = \frac{(v^2 + 4\kappa D)t}{D} \tag{18}$$

Figure 4.4 shows that 1-D numerical simulation results are in excellent agreement with results from the analytical solution. Note that two outlet boundary conditions are simulated for the finite length numerical system as compared to the infinite length analytical solution: 1) free flux, and 2) maintain the initial outlet concentration fixed $c=0$. Results bound the theoretical solution (Figure 4.4-b).

4.5 Results and Discussion

Numerical simulation results for the 2-D case relevant to CO_2 geological storage are presented herein in terms of species concentrations in space and time, the enlargement of the rock joint, and the effect of pore geometry.

4.5.1 Species Concentrations

Mineral dissolution couples with advection and diffusion to generate a concentration gradient across and along the pore/joint aperture (Li et al., 2006). Figure 4.5 shows a snap-shot of concentrations for all relevant species along a joint in calcite.

Low advection velocity allows for diffusion and homogenization across the aperture and for the consumption of most reactant species near the inlet (Figure 4.5-a). In contrast, when the advection velocity is high, diffusion fails to homogenize the concentration field across the joint, and mineral dissolution takes place uniformly along the joint length (Figure 4.5-b). The longitudinal drop in reactant species is much lower in the less reactive anorthite for the same advection velocities (Figure 4.6). For both mineralogies, a higher advection velocity yields higher concentrations of residual reactant species at the outlet due to the lower residence time.

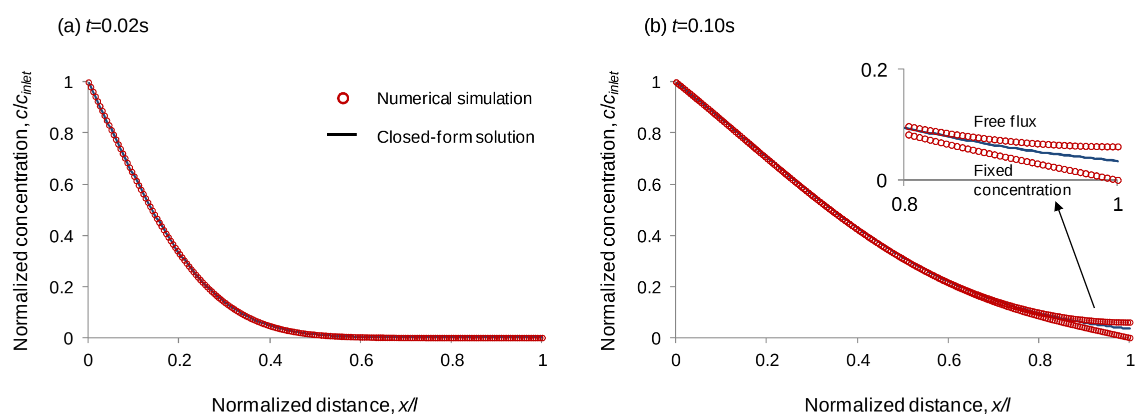

Figure 4.4 Comparison of the numerical simulation with a closed-form solution for 1-D reactive solute transport model. Assumption: homogeneous reaction of single species $CO_{2(aq)}$ for reaction $CO_{2(aq)} + H_2O \xrightarrow{k_{CO2}} H_2CO_3$ where k_{CO2}=0.135s^{-1}. Insert in (b) shows discrepancy between the closed-form solution and numerical solution for two boundary conditions: free flux or fixed initial concentration at the outlet. Fixed inlet concentration of $CO_{2(aq)}$ $[CO_{2(aq)}]_{(0,t)}$=1mol/L, initial concentration of $CO_{2(aq)}$ $[CO_{2(aq)}]_{(x>0)}$=0, fixed inlet velocity v_0=0.01cm/s, diffusion coefficient D=2*10^{-9}m^2/s, and length l=100μm.

The fluid acidity evolves as the numerical simulation proceeds. During the flow of acidified fluid along the rock joint, the pH near the inlet drops while the area near the outlet remains at the initial pH~8. The entire pore space acidifies and the area near the outlet converges to an asymptotic value pH~5 as advection continues and the system becomes saturated in terms of mineral dissolution (Figure 4.7-a). Electro-neutrality is maintained during the numerical simulation (Figure 4.7-b).

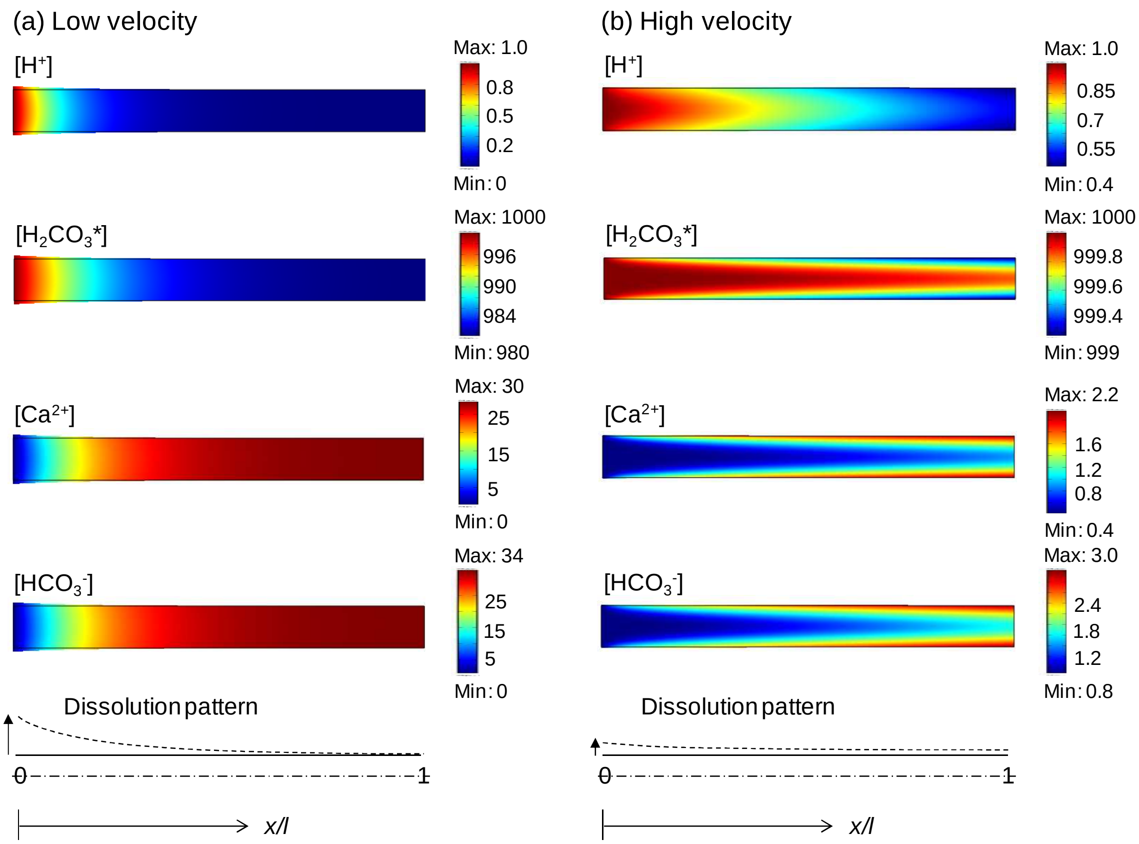

Figure 4.5 Reactive fluid transport along a joint/pore in calcite. Concentration of reactants (H^+ and H_2CO_3*) and produced species (Ca^{2+} and HCO_3^-). Joint aperture d=10μm and length l=100μm. The flow velocity is: (a) v_0=10^{-3}cm/s (Da≈9.6*10^1, and Pe≈2.7*10^{-4}) and (b) v_0=1cm/s (Da≈9.6*10^{-2}, and Pe≈2.7*10^{-1}). Concentration results are shown after: (a) 50 seconds (=l/v_0*5) and (b) 10 seconds (=l/v_0*1,000). Unit of species concentration in the graph is [mol/m^3]. All parameters are summarized in Table 4.1.

Figure 4.8 summarizes species concentrations along the centerline and at the outlet for different inlet velocities. Clearly, H^+ is readily consumed in a calcite-dominant environment, the system reaches chemical equilibrium, and H_2CO_3* passes through the rest of the joint plane unconsumed. The residual H_2CO_3* at the outlet may react with minerals and induce additional mineral dissolution in successive flow channels. In contrast to the calcite case, the low reaction rate of H^+ with anorthite ($Da<1$) allows more than two-thirds of H^+ species to reach the outlet (Figure 4.8). In general, mineral dissolution will influence a larger area in sandstones than in carbonates, under the same flow regime.

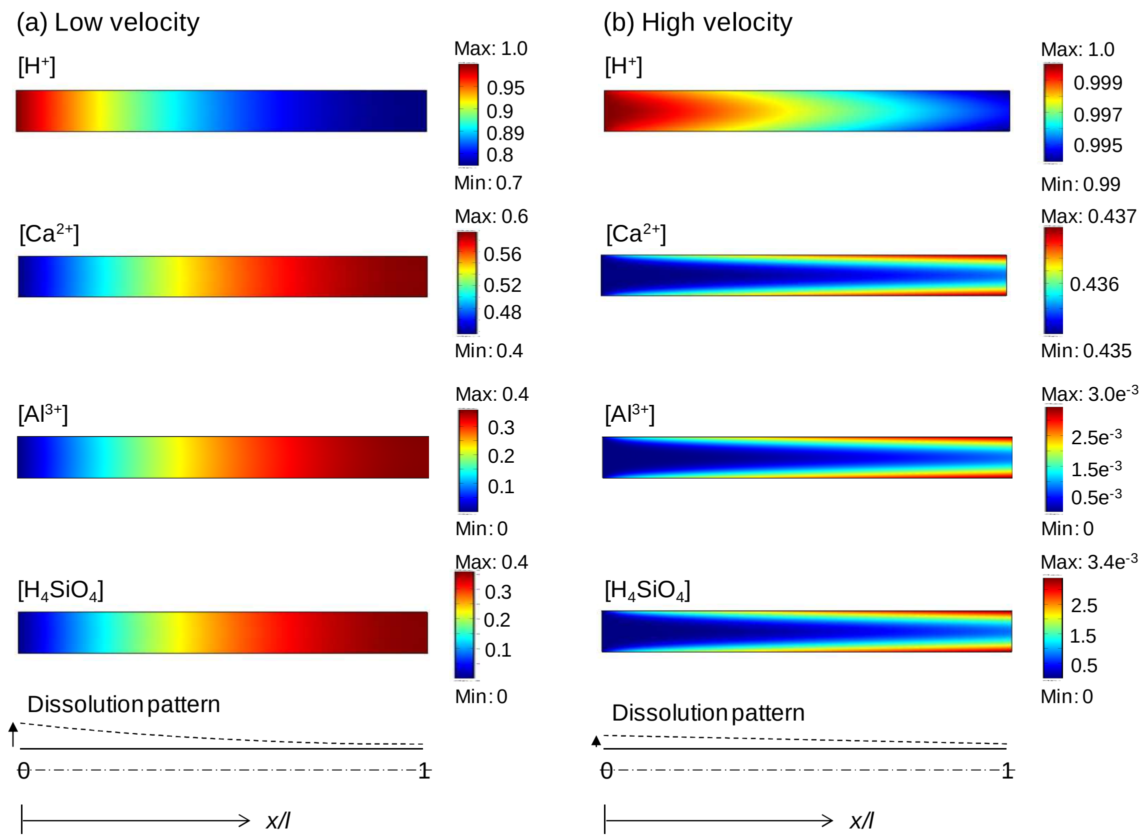

Figure 4.6 Reactive fluid transport along a joint/pore in anorthite. Concentration of reactant (H^+) and produced species (Ca^{2+}, Al^{3+}, and H_4SiO_4). Joint aperture d=10μm and length l=100μm. The flow velocity is: (a) $v_0=10^{-3}$cm/s ($Da\approx5.7*10^{-2}$, and $Pe\approx2.7*10^{-4}$) and (b) v_0=1cm/s ($Da\approx5.7*10^{-5}$, and $Pe\approx2.7*10^{-1}$). Concentrations results are shown after: (a) 5 seconds (=l/v_0*0.5) and (b) 1 seconds (=l/v_0*100). Unit of species concentration in the graph is [mol/m^3]. All parameters are summarized in Table 4.1.

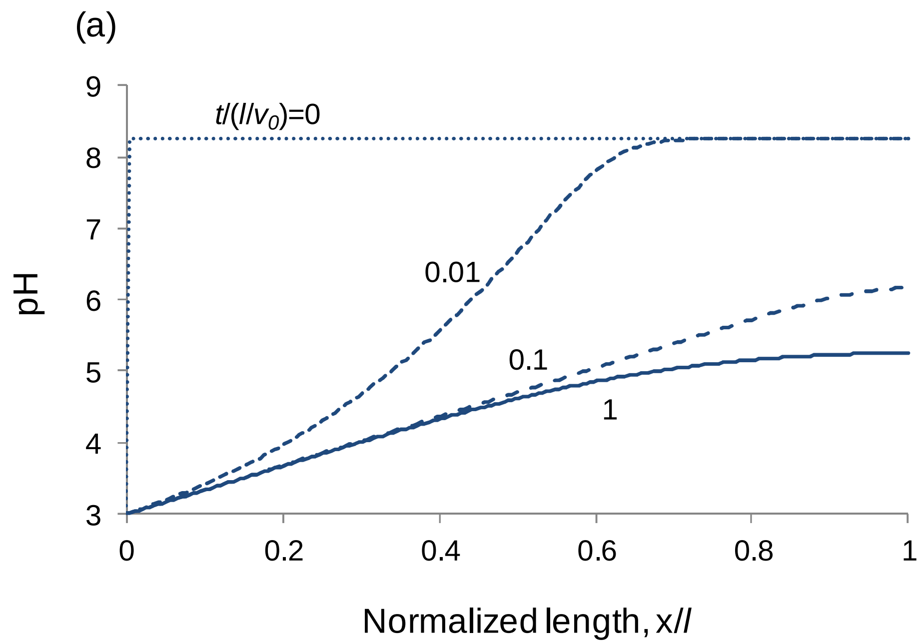

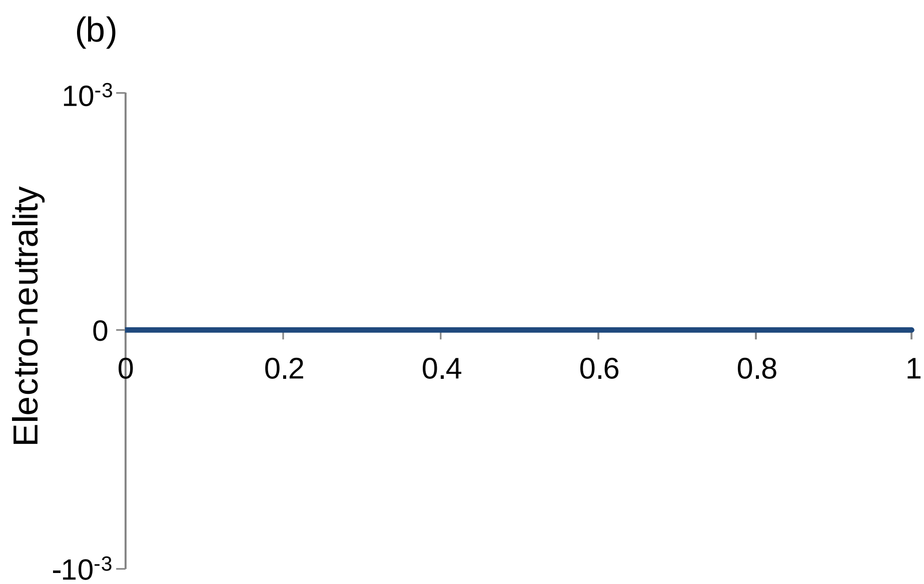

Figure 4.7 Evolution of pH in time and space. (a) pH along the joint length with respect to the normalized time $t/(l/v_0)$. (b) Verification of electro-neutrality along the joint length. Note: $v_0=10^{-2}$cm/s; $Da \approx 5.7*10^{-3}$ and $Pe \approx 2.7*10^{-3}$; beyond $t/(l/v_0) \approx 1$, pH distribution reaches quasi-steady state.

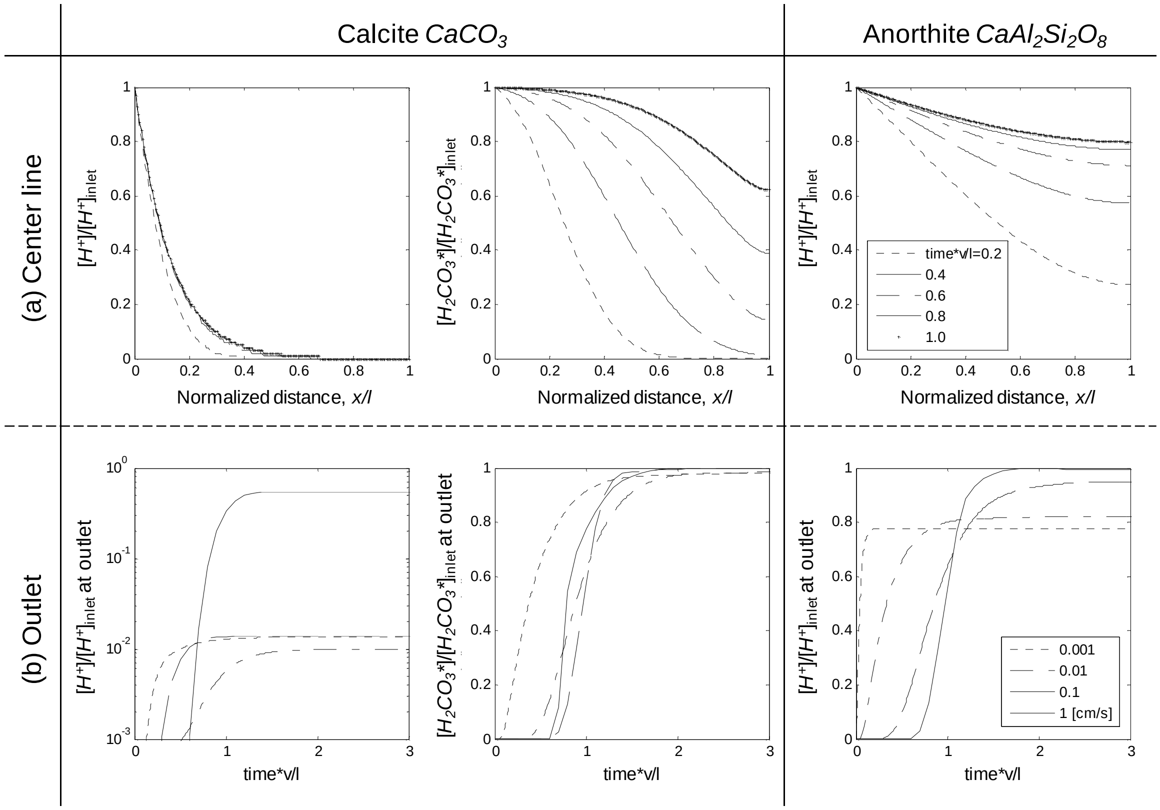

Figure 4.8 Variation of reactant species concentration: (a) along the centerline for different times (v=0.01cm/s) and (b) at the outlet for different flow velocities. All parameters are summarized in Table 4.1.

4.5.2 Enlargement

The rock joint aperture increases as the reactive fluid passes through the joint plane (Figures 4.5 & 4.6). The effect of advective velocity and reactivity are explored in Figures 4.9 and 4.10. Results show that pore enlargement may decrease either exponentially or linearly along the flow path. In all cases, the normalized enlargement $\Delta d/d$ in anorthite is three orders of magnitude lower than that of calcite (Figure 4.9). Figure 4.10 compiles all results in terms of dimensionless numbers, *Da* and *Pe*. For any *Pe* value, a lower *Da* causes the flow channel to experience a more uniform enlargement of the aperture along the joint.

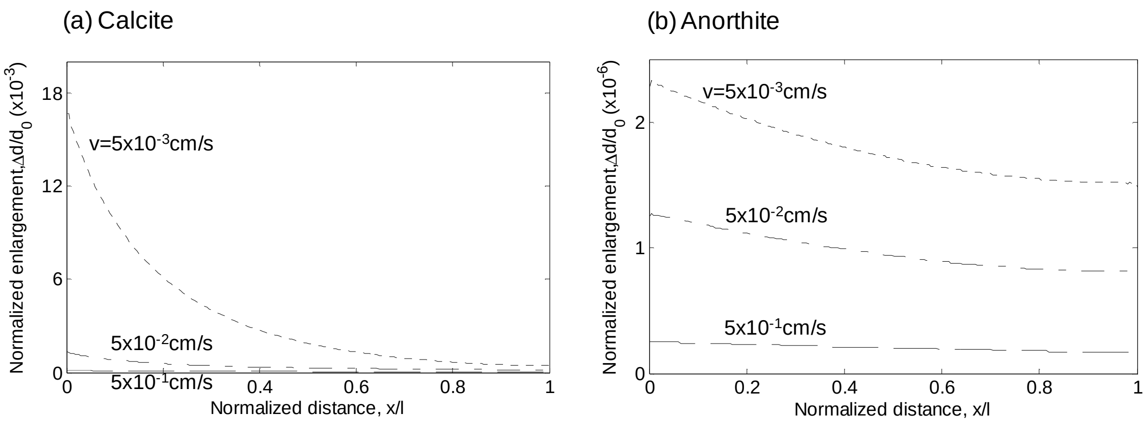

Figure 4.9 Normalized enlargement $\Delta d/d_0$ by mineral dissolution along the joint/pore wall at the moment of quasi steady-state for different velocities *v*: (a) calcite and (b) anorthite. Note: orders of enlargement are different between (a) and (b). Original joint aperture is d_0=10μm.

4.5.3 Time to Reach Quasi Steady-State Condition

The time to reach a quasi steady-state concentration at the outlet t_{qc} is determined when species concentrations at the outlet c reach 95% of the equilibrium value c_∞ at $t=\infty$ (Figure 4.11-a). Figures 4.11-(b) and (c) indicate that the time to reach quasi steady-state t_{qc} is between the advection time l/v_0 and two-folds of it ($2 \cdot l/v_0$). This implies that mineral dissolution and channel enlargement cause the system to reach quasi steady-state condition later than the advection time. Results when Pe<1 for the joint/pore in anorthite deviate from the general trend (Da<<1; Figures 4.10 & 4.11-c). When Da<1 and Pe<1, diffusion takes control over advection and dissolution, and quasi steady-state is reached faster than the advection time l/v_0.

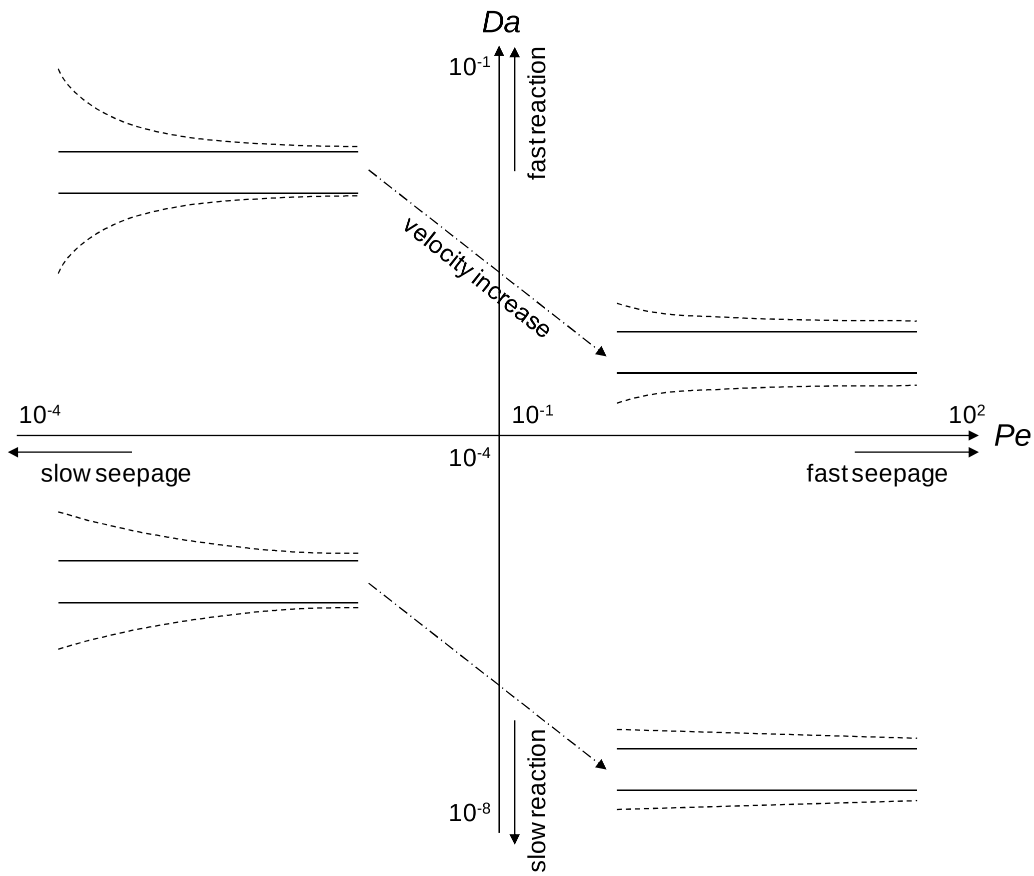

Figure 4.10 Dissolution patterns in the *Da* - *Pe* space. The sketches show dissolution patterns observed in numerical simulations of joints in either calcite or anorthite.

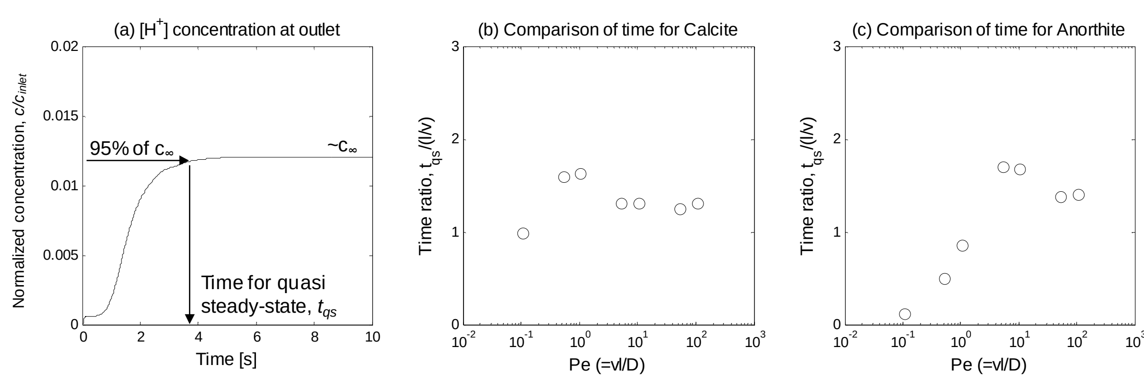

Figure 4.11 Determination of time to reach quasi steady-state of concentration t_{qs} at the outlet (95% of c_∞/c_{inlet}, where c_{inlet} is inlet concentration). The time to reach quasi steady-state of concentration at the outlet t_{qs} is normalized by the advection time l/v based on the joint length l and velocity v for (b) in calcite and (c) in anorthite.

5.4 Initial Joint Slenderness

Finally, let's examine the effect of joint slenderness by varying the aperture-to-length ratio *d/l*. When the aperture-to-length ratio *d/l* is very small $d/l \leq 0.035$, diffusive transport homogenizes species concentrations across the joint, and centerline concentrations resemble the 1-dimensional theoretical solution (Figure 4.12). An increased aperture-to-length ratio slows the diffusive transport of reactant species to the mineral surface ($t_{diff} \approx d^2/D$), and higher reactant concentrations remain along the centerline (Figure 4.12). Therefore, scaling must take into consideration both the joint length and its slenderness (see also Li et al., 2008).

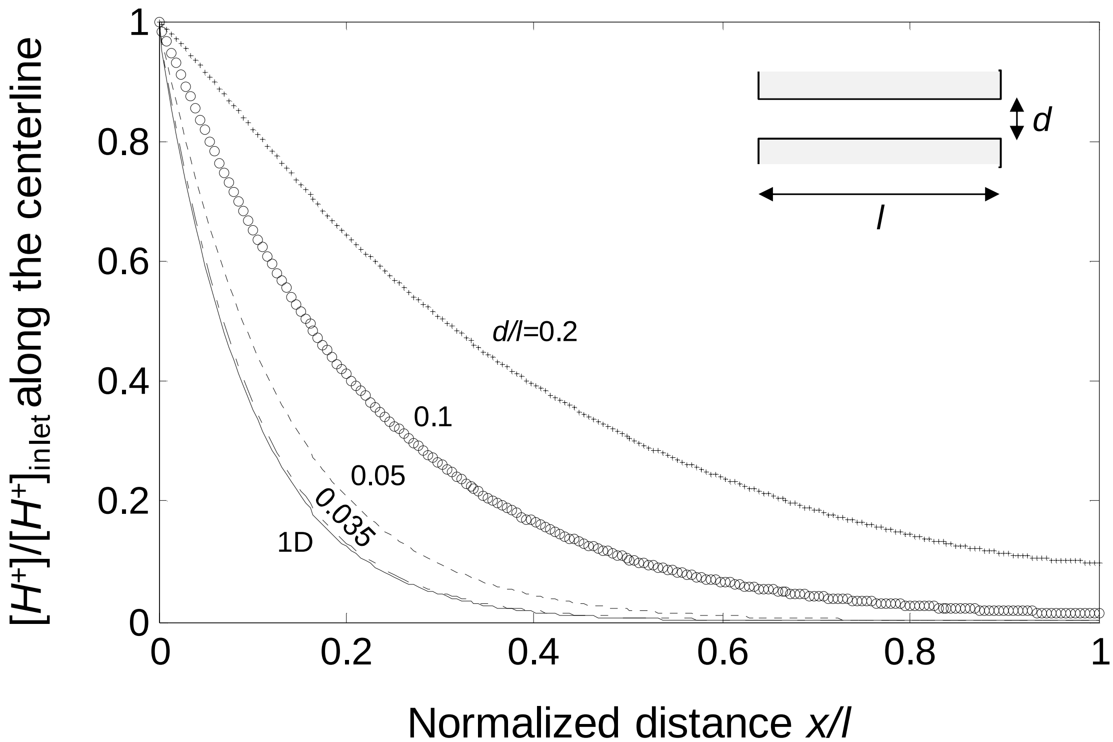

Figure 4.12 Effect of joint slenderness *d/l*. Variation of the normalized concentration of hydrogen ions $[H^+]/[H^+]_{inlet}$ at quasi steady-state for joints in calcite with different slenderness *d/l* (Note: length l=100μm, velocity v=0.01cm/s, $[H^+]_{inlet}=10^{-3}$mol/L). The theoretical 1-D solution is shown for comparison. All parameters are summarized in Table 4.1.

4.6 Conclusions

Numerical simulations for the reactive fluid transport through a rock joint/pore in calcite and anorthite were conducted taking into consideration all kinetic rate laws relevant to CO_2 geological storage including CO_2 dissolution and mineral buffering. The species concentrations at equilibrium can be tracked by numerically solving these kinetic rate laws. A novel simulation technique was used to couple laminar flow, mass transport of species, mineral dissolution, and subsequent pore enlargement. This 2-D simulation enables us to investigate interactions among governing parameter, including advection, diffusion, species concentration, and geometry during reactive fluid transport at the pore scale. Results show:

• Hydrogen ions H^+ are readily consumed in a calcite-dominant environment, the system becomes saturated, and H_2CO_3* passes through the rest of the joint plane unconsumed. In contrast, the low reaction rate of H^+ with anorthite ($Da<10^{-2}$) allows more extensive H^+ transport along the joint/pore.

• Pore enlargement may decrease either exponentially or linearly along the flow path. For any *Pe* value, a lower *Da* causes the flow channel to experience a more uniform enlargement of the aperture along the joint. Dissolution patterns define a consistent trend in the *Da* - *Pe* space.

• Mineral dissolution and pore enlargement extend the time to reach quasi steady-state, unless diffusion takes control over advection and dissolution when $Da<1$ and $Pe<1$.

• When the aperture-to-length ratio d/l is small $d/l \leq 0.035$, the system resembles the 1-D problem. An increased aperture-to-length ratio slows the diffusive transport of reactant species to the mineral surface ($t_{diff} \approx d^2/D$), and higher reactant concentrations remain along the centerline. Therefore, upscaling must take into consideration both the joint length and its slenderness.

• The simulation environment can be extended to 2-D pore networks and heterogeneous porous media. The extension, limited only by computer capacity, provides insightful results for reactive fluid flow through porous media of particular relevance to CO_2 geological storage.

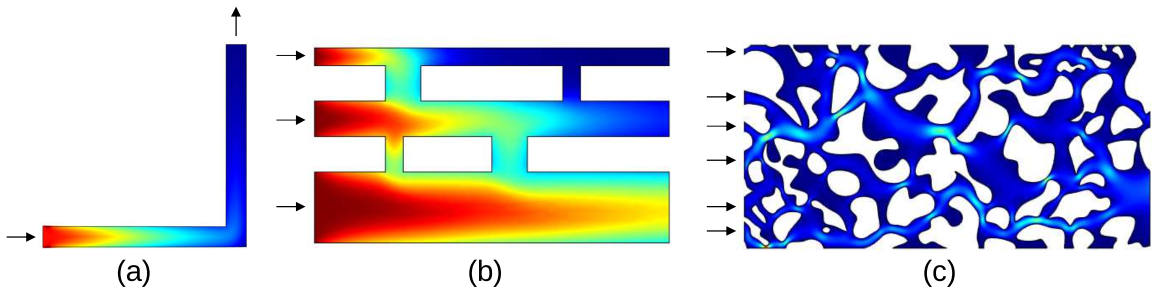

Figure 4.13 Application of the coupled reactive fluid flow simulation to (a) a two-channel model, (b) a channel network model, and (c) a scanned geometry of a porous medium (pore geometry obtained from: http://www.comsol.com).

CHAPTER 5

REACTIVE FLUID FLOW IN CO_2 STORAGE RESERVOIRS – PORE NETWORK MODEL STUDY

5.1 Introduction

Global energy consumption is projected to increase by 50% in the next 30 years (EIA, 2010; This is the status-quo scenario in Pasten and Santamarina, 2012). In the short term, this increased demand will largely rely on fossil fuels because of available reserves, low cost, the available infrastructure, and the relatively low energy production from other sources (Chapter 2). Carbon storage in geological saline aquifers is being considered to mitigate carbon emissions in the atmosphere.

CO_2 enters supercritical state when temperature and pressure condition exceed T>304.1K and P>7.38MPa (Span and Wagner, 1996), i.e., typically at reservoir depths greater than ~800m. The solubility of supercritical CO_2 in water can reach 1~2 moles/L (White et al., 2004; Gaus et al., 2005; Kharaka et al., 2006) and water acidifies to pH~3 while it retains two reactant species, hydrogen ions H^+ and aqueous carbon dioxide $CO_{2(aq)}$ (Chapter 3 - Stumm et al., 1996). The ensuing reactive fluid flow depends on mineral reactivity, advection, and diffusion.

Injected CO_2 displaces brine (two-phase flow) and CO_2-dissolved acidic water advances as a single-phase flow (Solomon et al., 2008). This study focuses on single-phase acidic water flow at the boundary between CO_2 and water in deep saline aquifers (Azaroual et al., 2007; Gaus et al., 2008) including the boundary between the aquifer and the caprock where migrating CO_2 accumulates (Figure 5.1). A pore network model is used herein to investigate reactive fluid flow within the storage reservoir. Previous studies are reviewed first.

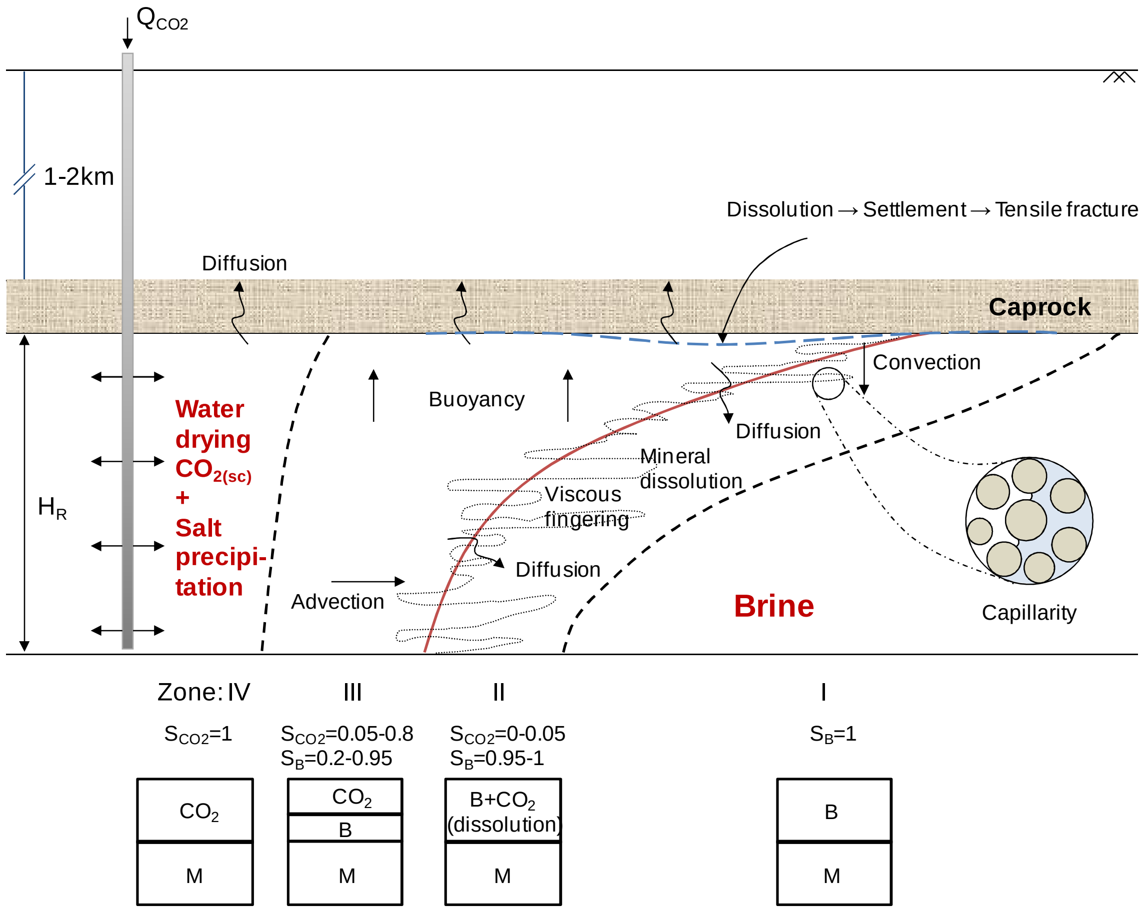

Figure 5.1 Zones around the injection well – Prevalent processes (modified from Azaroual et al., 2007). M: Mineral, B: Brine, S_{CO2}: saturation of CO_2, and S_B: saturation of brine.

5.2 Previous Studies

Reactive fluid flow through porous media has been studied using equivalent continuum models (Liu et al., 1997; Golfier et al., 2002; Panga et al., 2005; Xu et al., 2006; Kalia and Balakotaiah, 2007), single-flow channel or wormhole models (Hung et al., 1989; Buijse, 2000; Li et al., 2008), lattice Boltzman pore-scale models (Kang et al., 2010), and network models. The equivalent continuum approach requires pore-scale information such as the relationship between porosity and permeability (Liu et al., 1997;

Panga et al., 2005; Xu et al., 2006). Alternatives to the equivalent continuum model include discrete fracture network models (Pashin et al., 2008) and multiple continuum models (Steefel et al. ,2005).

Network models allow us to capture pore-scale phenomena in order to study their effect on macro-scale flow conditions (Dillard and Blunt, 2000). Network models have two main drawbacks: 1) scale limitations and 2) hydro-mechanical decoupling. Reactive fluid flow involves dissolution, which adds complexity to the network simulation code, and only a few attempts have been reported (Hoefner and Fogler, 1988; Daccord et al., 1993; Daccord et al., 1993; Fredd and Fogler, 1998; Egermann et al., 2005; Li et al., 2006; Li et al., 2007; Algive et al., 2009). Published results show that the dissolution pattern varies with the ratio between advection and reaction times (2D-Fredd and Fogler, 1998); that the exponent of the Kozeny-Carman equation changes for different dissolution scenarios, including uniform dissolution, compaction dissolution, and wormhole formation (3D-Egermann et al., 2005; Algive et al., 2009); that and reaction rates are affected by the spatial distribution of minerals (3D-Li et al., 2006; Li et al., 2007).

5.3 Development of the Network Simulation Code

The new network simulation code presented here was created to investigate fluid-mineral interaction when CO_2-dissolved water flows through a porous network, such as the CO_2 storage reservoir where advective transport prevails. Relevant chemical formulae and the algorithm are presented next.

5.3.1 Mineralogy and Mineral Dissolution

Let's consider a porous medium in a calcium carbonate formation (mineral with fastest reaction rate in saline reservoirs). Two parallel reactions prevail because of the low pH and the high concentration of aqueous CO_2 (Plummer et al., 1978):

$$CaCO_{3(s)} + H^+ \rightarrow Ca^{2+} + HCO_3^- \tag{1}$$

$$CaCO_{3(s)} + CO_{2(aq)} + H_2O \rightarrow Ca^{2+} + 2HCO_3^- \tag{2}$$

Let's assume first-order reactions with rate laws:

$$-\frac{d[H^+]}{dt} = \frac{d[Ca^{2+}]}{dt} = \frac{d[HCO_3^-]}{dt} = \kappa_1[H^+] \tag{3}$$

$$-\frac{d[H_2CO_3^*]}{dt} = \frac{d[Ca^{2+}]}{dt} = \frac{1}{2}\frac{d[HCO_3^-]}{dt} = \kappa_2[H_2CO_3^*] \tag{4}$$

where square brackets indicate species concentration, κ_i denotes the kinetic rate for each chemical reaction, and total carbonic acid H_2CO_3* denotes the summation of aqueous carbon dioxide $CO_{2(aq)}$ and true carbonic acid H_2CO_3. Reactions stop when the system reaches equilibrium and the ionic concentration product Ω [-] equals the equilibrium constant K_{eq} [-]:

$$\Omega = \frac{[Ca^{2+}]^2[HCO_3^-]^3}{[H^+][H_2CO_3^*]} = K_{eq} = 10^{-2.65} \tag{5}$$

Table 5.1 summarizes equations and parameters. Note that mineral precipitation is not considered in this study.

Table 5.1 Calcite dissolution by CO_2-dissolved water. Summary of properties used in network simulations.

(a) Equations for mineral dissolution and properties

				Chemical equation for mineral dissolution	Rate constant [mol/m^2/s]	Equilibrium constant	Ionic concentration product, Ω
Calcite	S_s=0.06m^2/g [(2)]	M_m=100g/mol	V_m=3.70*10^{-5} m^3/mol	$CaCO_{3(s)} + H^+ \overset{k_1}{\rightarrow} Ca^{2+} + HCO_3^-$	k_1=0.745 [(1)]	$K_{1eq}=10^{1.85}$ [(1)]	$\dfrac{[Ca^{2+}]^2[HCO_3^-]^3}{[H^+][H_2CO_3^*]}$
				$CaCO_{3(s)} + CO_{2(aq)} + H_2O \overset{k_2}{\rightarrow} Ca^{2+} + 2HCO_3^-$	k_2=8.6*10^{-4} [(1)]	$K_{2eq}=10^{-4.5}$ [(1)]	

(b) Boundary condition: Concentrations of species at the inlet

$[H^+]_{\text{inlet}}$	6.68*10^{-4}mol/L
$[H_2CO_3*]_{\text{inlet}}$	1mol/L
$[HCO_3^-]_{\text{inlet}}$	6.68*10^{-4}mol/L
$[Ca^{2+}]_{\text{inlet}}$	1.361*10^{-3}mol/L
$[OH^-]_{\text{inlet}}$	1.50*10^{-11}mol/L
$[Cl^-]_{\text{inlet}}$	2.72*10^{-3}mol/L

Note: S_s: mineral specific surface, M_m: mineral molar mass, V_m: mineral molar volume; kinetic rate is κ_i [1/s]=$k_i \cdot S_s \cdot M_m$ where k_i is a rate constant; Rate constants are computed for T=40°C in this study; total equilibrium constant for calcite $K_{eq}=K_{1eq}*K_{2eq}$ (Reference: [(1)] Plummer et al., 1978; Fredd and Fogler, 1998; Pokrovsky et al., 2005; Renard et al., 2005; Algive et al., 2009, and [(2)] Gaus et al., 2005).

5.3.2 Network Construction

The 2-D square network consists of tubes that intersect at nodes, where incoming species mix thoroughly. Tube diameters d [m] are log-normally distributed with mean value $\overline{d_0}$ and variance var. All tubes have identical length L_{ch} [m]. The limitation in network size NxM is partially overcome by assuming periodic longitudinal boundary conditions. Flow is driven by the pressure difference between the inlet P_{in} and the outlet P_{out} (Figure 5.2 - Network details in Table 5.2).

Table 5.2 Network model and simulation parameters.

Entity	Property
Network size (NxM)	50x50
Mineralogy	Calcite
Mean of tube diameters, $\overline{d_0}$	20μm
Distribution of tube diameters	Log-normal distribution
Coefficient of Variation, COV	0.4, 1, and 1.5
Tube length, L_{ch}	200μm
Hydraulic gradient i_h applied at the model	10, 100, and 1000
Flushed pore volume during one cycle	$10 \cdot V_p$ (V_p: one network pore volume)
Number of cycle (repetition)	100
Total flushed network pore volume	$1000 \cdot V_p$

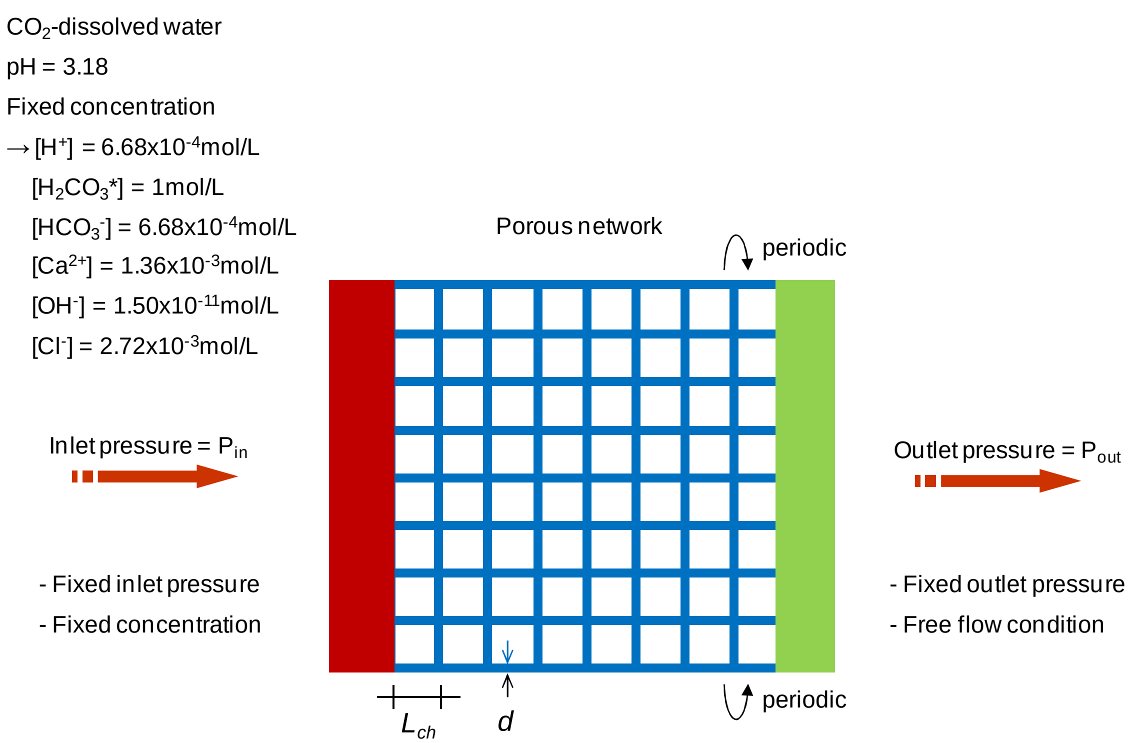

Figure 5.2 Pore network model: geometry, initial, and boundary conditions.

5.3.3 Governing Parameters

The time scales for advection t_{adv}, diffusion t_{diff}, and reaction t_{rxn} can be combined to form two dimensionless ratios, i.e., the Damköhler *Da* and Peclet *Pe* numbers:

$$Da = \frac{t_{adv}}{t_{rxn}} = \frac{\kappa L_{ch}}{v_{ave}} \tag{6}$$

$$Pe = \frac{t_{diff}}{t_{adv}} = \frac{v_{ave} L_{ch}}{D} \tag{7}$$

where the kinetic rate κ [1/s]=$k_r \cdot S_s \cdot M_m$ is a function of the rate constant k_r [mol/m^2/s], the mineral specific surface S_s [m^2/g], and the mineral molar mass M_m [g/mol]. The average pore velocity is v_{ave} [m/s], and D [m^2/s] denotes the molecular diffusion coefficient. The simulation is designed for advection-controlled situations such as those that prevail in the reservoir formation during CO_2 injection (Damköhler number $Da \leq 10^{-3}$; Peclet number $Pe > 10^2$; and hydraulic gradient $i_h \geq 10$ - Table 5.2). A small Damköhler number $Da << 1$, i.e., advection much faster than reaction, permits convenient simplifications.

5.3.4 Numerical Simulation – Algorithm

General Formulation

Velocity. Nodal fluid pressures are computed by writing the continuity equation at all nodes and solving the system of equations (details in Jang et al., 2011):

$$\sum q_i = 0 \tag{8}$$

The pressure difference ΔP [Pa] between two adjacent nodes is then used to compute the tube flow velocity v [m/s] and flow rate q [m^3/s] for each tube using Poiseuille's law as a function of the tube diameter d [m], length L_{ch} [m], and the fluid viscosity μ [Pa·s]:

$$\text{Velocity: } v = \frac{\Delta P d^2}{32 \mu L_{ch}} \tag{9}$$

$$\text{Flow rate: } q = \frac{\Delta P \pi d^4}{128 \mu L_{ch}} \tag{10}$$

Evolution of the species concentration. Mineral dissolution in a given tube lowers the concentration of reactant species and increases the concentration of produced species at the next node until saturation is reached and dissolution stops. The concentration $c_{i+1,j+1}$ for reactant species H^+ and H_2CO_3* at location $x_{i+1}=x_i+\Delta x$ and time $t_{j+1}=t_j+\Delta x$ in a tube in direction x is determined by the chemical reaction rate κ, the residence time of species inside a tube L_{ch}/v, and the concentration of reactant species $c_{i,j}$ at location x_i and time t_j. For a 1-D tube aligned in x:

$$[H^+]_{i+1,j+1} = [H^+]_{i,j} - \kappa_1 \cdot [H^+]_{i,j} \cdot \left(1 - \frac{\Omega_{i,j}}{K_{eq}}\right) \cdot \frac{L_{ch}}{v_{i,j}} \tag{11}$$

$$[H_2CO_3^*]_{i+1,j+1} = [H_2CO_3^*]_{i,j} - \kappa_2 \cdot [H_2CO_3^*]_{i,j} \cdot \left(1 - \frac{\Omega_{i,j}}{K_{eq}}\right) \cdot \frac{L_{ch}}{v_{i,j}} \tag{12}$$

where the parameter $\Omega_{i,j}$ is the ionic concentration product, and $v_{i,j}$ the velocity at location x_i and time t_j. The concentration of produced species Ca^{2+} and HCO_3^- are determined from the consumption of reactant species and the stoichiometric ratio between reactant and produced species. For a 1-D tube aligned in x:

$$[Ca^{2+}]_{i+1,j+1} = [Ca^{2+}]_{i,j} + \left(\kappa_1 [H^+]_{i,j} + \kappa_2 [H_2CO_3^*]_{i,j}\right) \cdot \left(1 - \frac{\Omega_{i,j}}{K_{eq}}\right) \cdot \frac{L_{ch}}{v_{i,j}} \tag{13}$$

$$[HCO_3^-]_{i+1,j+1} = [HCO_3^-]_{i,j} + \left(\kappa_1 [H^+]_{i,j} + 2\kappa_2 [H_2CO_3^*]_{i,j}\right) \cdot \left(1 - \frac{\Omega_{i,j}}{K_{eq}}\right) \cdot \frac{L_{ch}}{v_{i,j}} \tag{14}$$

These equations presume that advective transport prevails over diffusive transport ($Pe>1$) and is valid for advection-dominant regimes.

Initial and Boundary Conditions

The first column (i=1) is the inlet of CO_2-dissolved water; it has fixed concentration of reactant species. The concentration of total carbonic acid [H_2CO_3*] is determined using expressions proposed by Duan and Sun (2003) as shown in Chapter 3. Concentrations of hydrogen [H^+], hydroxide [OH^-], and bicarbonate [HCO_3^-] are obtained from the thermodynamic equilibrium of a carbonate system $H_2CO_3^* \leftrightarrow H^+ + HCO_3^-$ at T=40°C and P=10MPa. Concentrations of other species, such as Ca^{2+} and Cl^- at the inlet boundary are determined to satisfy electro-neutrality (Figure 5.2).

A free flux condition is used for the outlet i=M in order to simulate an infinite boundary $c_{M-2,j}-c_{M-1,j}=c_{M-1,j}-c_{M,j}$. Figure 5.2 summarizes initial and boundary conditions.

Chemical conditions must be initiated within the network to avoid numerical instabilities. We assume that the transport of species along transverse tubes is initially negligible because flow velocities are typically much lower than along longitudinal tubes. We also assume that changes in tube diameters are negligible during the initial moments. Then, the initial "pseudo-steady state" concentration field of reactant species along 1-D longitudinal tubes can be estimated by numerically solving the differential equation for reactive fluid transport (Boudreau, 1997):

$$\frac{dc}{dt} - v\frac{dc}{dx} - \kappa c = 0 \tag{15}$$

This equation is expressed in finite difference form (central approximation functions).

$$-\frac{v}{2\Delta x}\cdot c_{i+1} - \kappa \cdot c_i + \frac{v}{2\Delta x}\cdot c_{i-1} = 0 \tag{16}$$

where c_i [mol/m^3] denotes species concentration at location x_i, and the space interval is taken as the distance between adjacent nodes $\Delta x=L_{ch}$. In matrix form,

$$\underline{\underline{A}}\cdot \underline{c} = \underline{B} \tag{17}$$

where matrix $\underline{\underline{A}}$ contains coefficients in Equation 16 (that is $-v/2\Delta x$, $-\kappa$, and $v/2\Delta x$), and the vector $\underline{B}$ captures boundary conditions, i.e., fixed concentration c_{inlet} at the inlet node i=1 and free flux at the outlet node $i=M$. For example, the matrix $\underline{\underline{A}}$ and vector $\underline{B}$ for M=6 nodes are:

$$\underline{\underline{A}} = \begin{bmatrix} 1 & 0 & 0 & 0 & 0 & 0 \\ -\frac{v}{2\Delta x} & -\kappa & \frac{v}{2\Delta x} & 0 & 0 & 0 \\ 0 & -\frac{v}{2\Delta x} & -\kappa & \frac{v}{2\Delta x} & 0 & 0 \\ 0 & 0 & -\frac{v}{2\Delta x} & -\kappa & \frac{v}{2\Delta x} & 0 \\ 0 & 0 & 0 & -\frac{v}{2\Delta x} & -\kappa & \frac{v}{2\Delta x} \\ 0 & 0 & 0 & 1 & -2 & 1 \end{bmatrix}, \text{ and } \underline{B} = \begin{bmatrix} c_{inlet} \\ 0 \\ 0 \\ 0 \\ 0 \\ 0 \end{bmatrix} \tag{18}$$

The sought concentration field $\underline{c}$ of reactant species H^+ and H_2CO_3* at all nodes at the initial pseudo-steady state condition is obtained by inversing the system of equation to recover the vector $\underline{c} = \underline{\underline{A}}^{-1} \cdot \underline{B}$. Pseudo-steady state concentration for other species, such as Ca^{2+}, HCO_3^- , OH^-, and Cl^-, are determined to satisfy both equilibrium in the carbonate system and electro-neutrality with the concentrations of H^+ and H_2CO_3* at each node.

Complementary computations

Enlargement of tube diameters. The solid mineral dissolution $\Delta c_{i,j}^m$ [mol/m^3] between location x_i and x_{i+1} from time t_j to t_{j+1} is computed from the consumption of reactant species H^+ and H_2CO_3* and their stoichiometric ratios (1:1 for both reactant species). For a 1-D tube aligned in x:

$$\Delta c_{i,j}^m = \left(\kappa_1 [H^+]_{i,j} + \kappa_2 [H_2CO_3^*]_{i,j}\right) \cdot \left(1 - \frac{\Omega_{i,j}}{K_{eq}}\right) \cdot \frac{L_{ch}}{v_{i,j}} \tag{19}$$

The increase in tube diameter $\Delta d_{i,j}$ [m] between locations x_i and x_{i+1} from time t_j to t_{j+1} is proportional to flow rate $q_{i,j}$, the solid mineral dissolution $\Delta c_{i,j}^m$, the mineral molar volume V_m [m^3/mol], and the elapsed time Δt [s]. For a 1-D tube aligned in x:

$$\Delta d_{i,j} = \frac{2V_m \Delta t}{\pi L_{ch}} \cdot \frac{q_{i,j}}{d_{i,j}} \cdot \Delta c_{i,j}^m \tag{20}$$

As noted earlier, mineral dissolution is much slower than advection in most problems of reactive fluid transport related to CO_2 geological storage (Da<<1). Thus, the enlargement of tube diameters, for one replaced network pore volume V_p, is minute, and we select the time interval Δt for one iteration step to be several times β the overall advection time L_{total}/v_{ave} across the network $L_{total}=L_{ch}*(M-1)$:

$$\Delta t = \beta \frac{L_{total}}{v_{ave}} \tag{21}$$

Updated Nodal Concentrations. The new nodal concentration $c_{i+1,j+1}{}^{new}$ at location x_{i+1} at time t_{j+1} is computed assuming instantaneous mixing at the node:

$$c_{i+1,j+1}^{new} = \frac{\sum_k q_{k,j} \cdot c_{k+1,j+1}}{\sum_k q_{k,j}} \tag{22}$$

<u>Algorithm</u>

One cycle in the network simulation corresponds to the time interval Δt, and involves the following steps: (1) estimate the evolution of species concentration at the end of every tube based on species concentrations, velocity, and kinetic rates – Equations 11 to 14, (2) compute the enlargement of tube diameter Δd for every tube – Equations 19 to 21, (3) update concentration of species at all nodes – Equation 22, and (4) update nodal pressure, velocity and flow rate based on change in tube diameters – Equations 8 to 10. We repeat this cycle until the total flushed volume reaches $1000 \cdot V_p$ (Table 5.2). The algorithm is summarized in Figure 5.3.

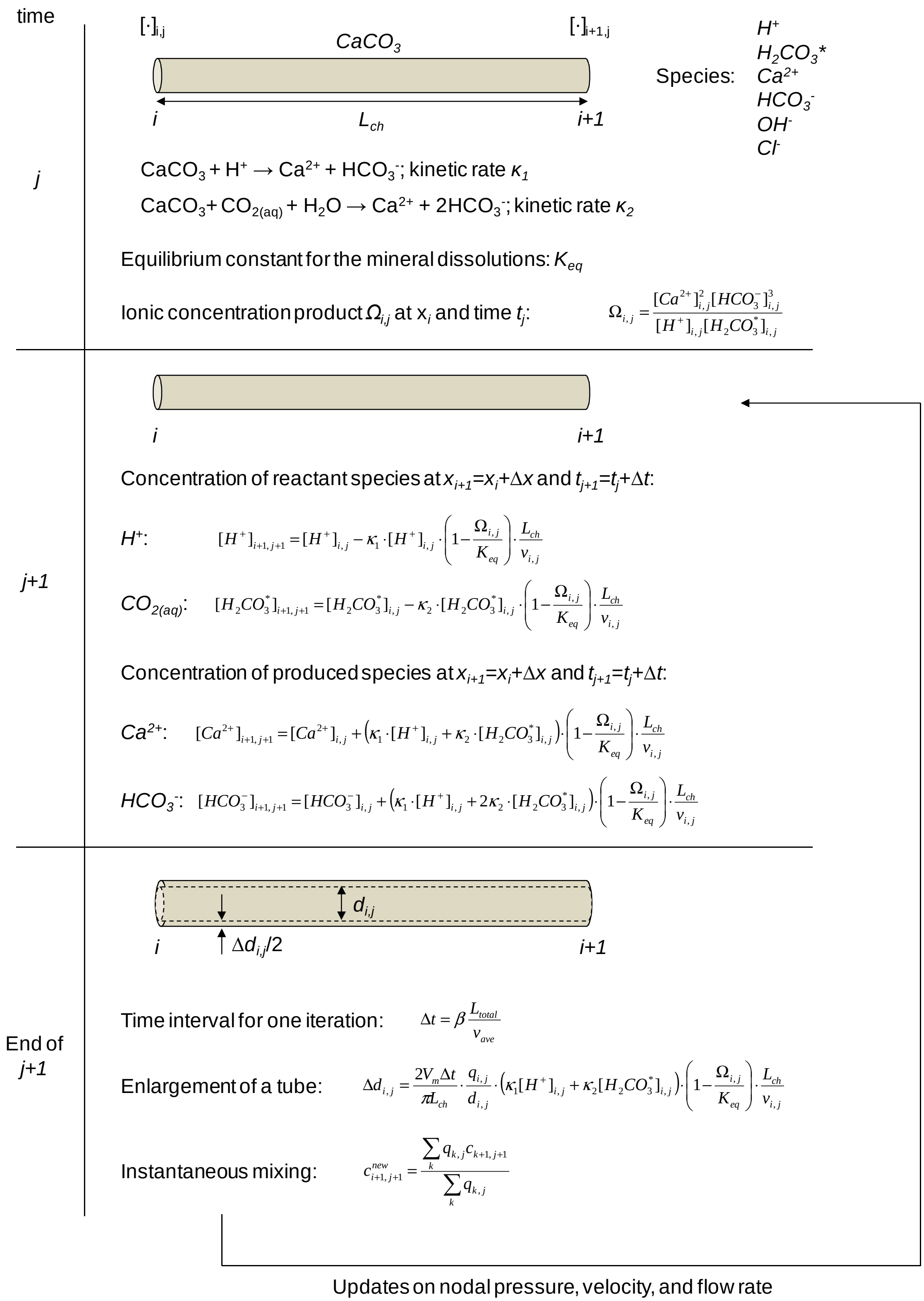

Figure 5.3 Network model simulation scheme for the advection-dominant reactive transport in the CO_2 reservoir (Notation corresponds to a tube aligned in the x-direction).

5.4 Results

Reservoir parameters and pressure conditions are selected in view of CO_2 storage reservoirs. Parameters and results are discussed next.

5.4.1 Selected Parameters

Distribution of tube diameters. The mean tube diameter $\overline{d_0}$ is selected to satisfy typical reservoir permeabilities k_{perm} [md]. Given the following empirical expression (Bachu and Bennion, 2008),

$$\frac{k_{perm}}{1md} = 0.37 \cdot \left(\frac{\overline{d_0}}{1\mu m} \right)^{2.05} \tag{23}$$

we select a value $\overline{d_0}$≈20μm for a reservoir permeability of k_{perm}≈172md which is in the range for carbonate porous rocks (Brosse et al., 2005; Egermann et al., 2005). Pore diameters are log-normally distributed with a coefficient of variation COV=0.4 for sediments (Phadnis and Santamarina, 2011); we also test COV=1.0 and 1.5 that correspond to fractured rocks (Shapiro, 2010).

In-situ hydraulic gradient. The injection pressure is limited to prevent hydraulic fracture. The hydraulic gradient i_h is highest near the injection well and diminishes inversely proportional to distance from the well. In this study, we test three different hydraulic gradients i_h=10, 100, and 1000.

5.4.2 Results

Concentration. The spatial distributions of species concentration (H^+, H_2CO_3*, Ca^{2+}, and HCO_3^-) are monitored during fluid flow (Figure 5.4). When the advection time is much longer compared to the reaction time (Da>10^{-4}), the concentration of reactant species (i.e., H^+ and H_2CO_3*) rapidly decreases near the inlet. However, reactant species migrate towards the outlet and ramify as the hydraulic gradient increases and Da<10^{-4}. The lower consumption of reactant species with higher hydraulic gradients makes the pH converge to lower values away from the inlet (Figure 5.5-a). Electro-neutrality is satisfied during the numerical simulation (Figure 5.5-b).

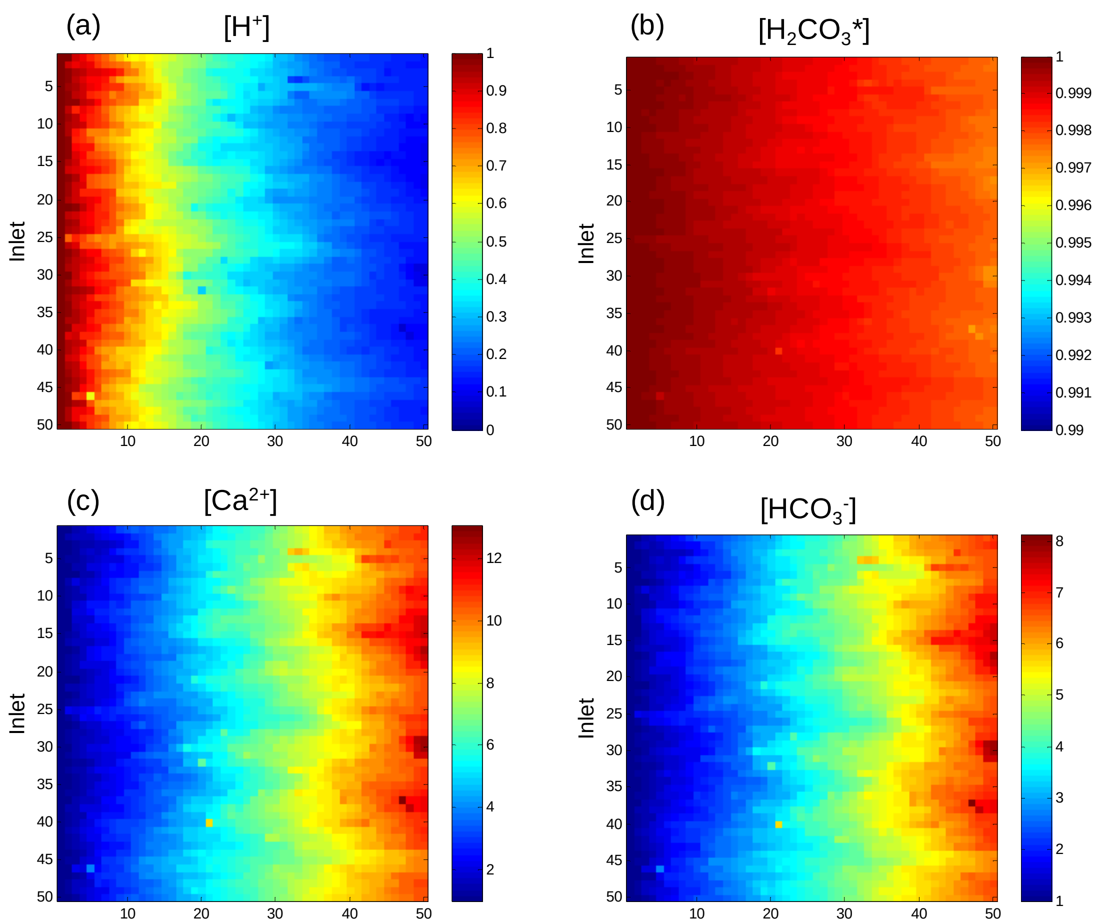

Figure 5.4 Distribution of species concentration after 1000 network pore volumes have been flushed through the system: (a) H^+, (b) H_2CO_3*, (c) Ca^{2+}, and (d) HCO_3^- (i_h=1000, Da=1.5*10^{-5}, Pe=6.8*10^3).

Pore Diameter. Tube diameter enlargement prevails near the inlet when the hydraulic gradient i_h is low (i_h<100; Da>10^{-3} Figure 5.6-a), but it extends towards the outlet as the advection velocity increases (Figure 5.6-b). Figure 5.6 shows tube diameter enlargement after 1000 network pore volumes V_p have been flushed (Note: when i_h=1000 (Da~10^{-5}), the corresponding total simulation time is two orders of magnitude longer than characteristic time for calcite dissolution by hydrogen ions H^+). For a given number of network pore volumes flushed, the higher the advection velocity the lower the eroded mass within a given model space (Figure 5.6-c).

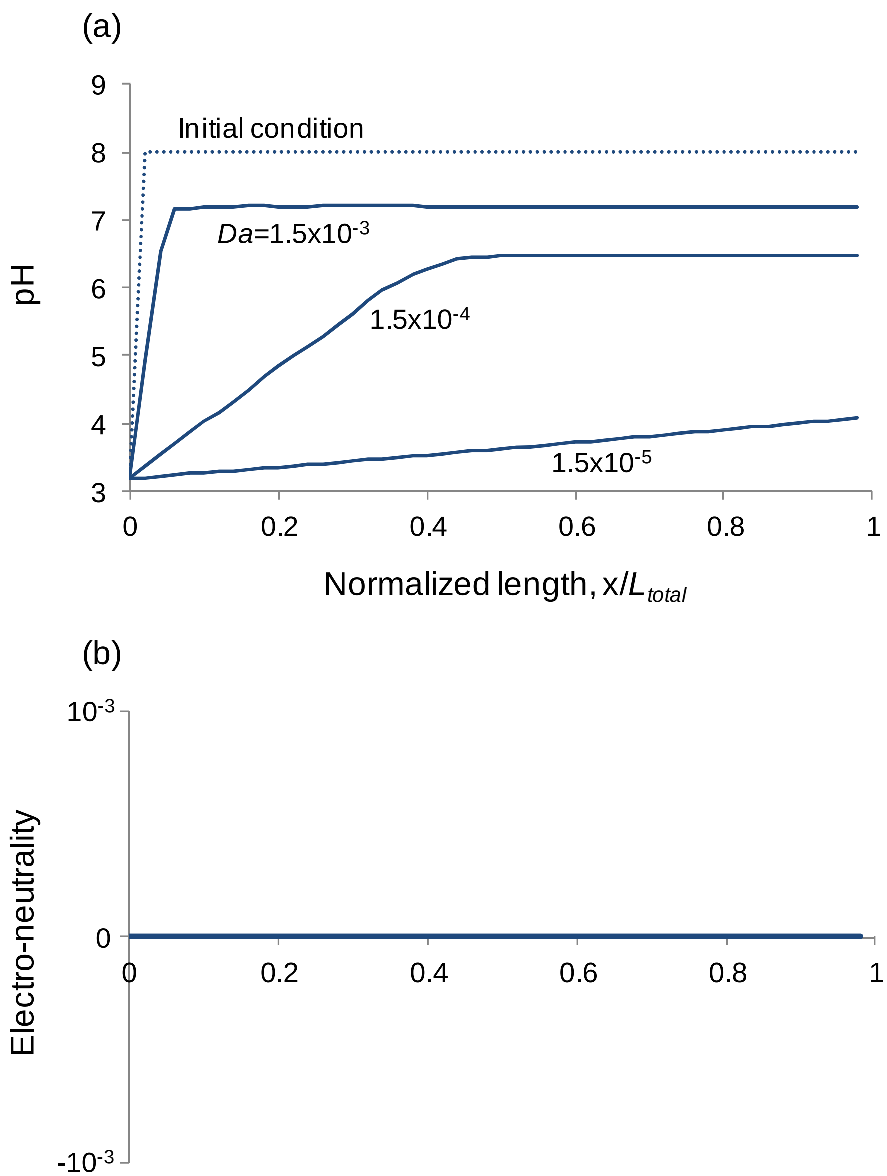

Figure 5.5 Evolution of pH in space and time. (a) The average pH along the network model after 1000 network pore volumes have been flushed through the system. (b) Verification of electro-neutrality along the network model. Note: Damköhler number decreases from Da=1.5*10^{-3} to Da=1.5*10^{-4} and Da=1.5*10^{-5} as hydraulic gradient increases from i_h=10 to i_h=100 and i_h=1000.

Flow rate. Reactive flow tends to preferentially enlarge tubes with high flow velocity. Figure 5.7 compares the normalized change in flow rate $\Delta q/q_{0,max}$ after 1000 network pore volumes under different hydraulic gradients: the initial pore size distribution (COV=0.4) evolves towards localized flow and wormhole formation. The flow pattern clearly shows that initially dominant channels experience most of the increase in the flow rate during reactive fluid flow at high gradients (Figure 5.7-b and c), however, flow remains more homogeneous after $1000 \cdot V_p$ when the hydraulic gradient is low (i_h=10; Da~10^{-3}, Figure 5.7-a).

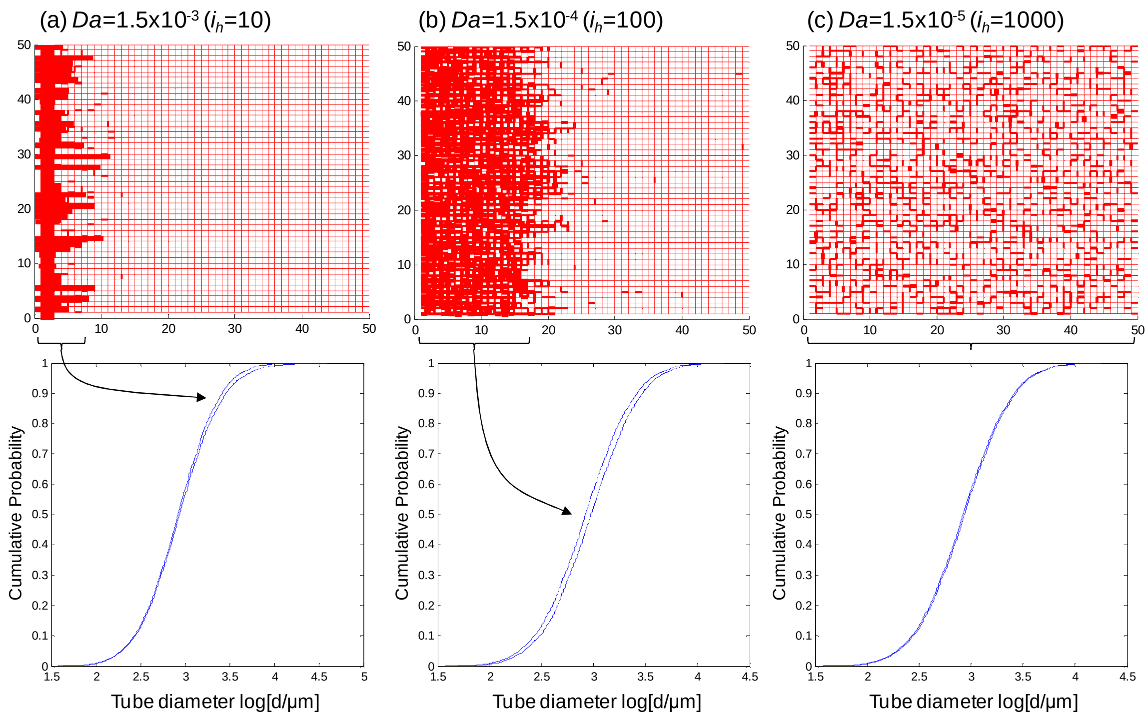

Figure 5.6 Evolution in tube diameters during reactive fluid transport. Line thickness represents normalized diameter growth $(\Delta d/d_0)*50$ (top), and cumulative distribution of initial tube diameters and tube diameters after 1000 network pore volumes have been flushed is shown in bottom (coefficient of variation COV=0.4): (a) i_h=10 (Da=1.5*10^{-3}, Pe=6.8*10), (b) i_h=100 (Da=1.5*10^{-4}, Pe=6.8*10^{2}), and (c) i_h=1000 (Da=1.5*10^{-5}, Pe=6.8*10^{3}).

Pressure. The pressure field in the porous medium changes with preferential tube enlargement. At low hydraulic gradients, high dissolution at the inlet transfers high inlet pressures further into the medium (Figure 5.8-a). As the hydraulic gradient i_h increases, dissolution extends further into the medium and pressure follows the pre-dissolution trend closer (Figures 5.8-b~d).

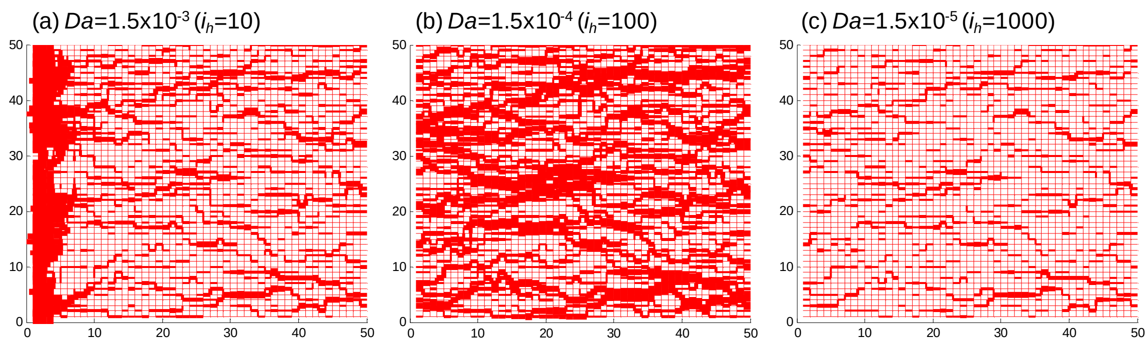

Figure 5.7 Evolution in flow rate across the network model. Line thickness represents normalized flow rate increase $(\Delta q/q_{0,max})*100$ after 1000 network pore volumes have been flushed (COV=0.4): (a) i_h=10 (Da=1.5*10^{-3}, Pe=6.8*10), (b) i_h=100 (Da=1.5*10^{-4}, Pe=6.8*10^{2}), and (c) i_h=1000 (Da=1.5*10^{-5}, Pe=6.8*10^{3}).

Porosity-permeability. Enlargement in tube diameters increases both porosity and permeability. The Kozeny-Carman equation (Carman, 1956) suggests a power relationship between relative porosity φ/φ_0 and relative permeability k/k_0:

$$\frac{k}{k_0} = \left(\frac{\phi}{\phi_0}\right)^{\alpha} \tag{24}$$

where φ_0 and k_0 are selected reference values. Consider a cylindrical tube in representative elementary volume. A change in pore diameter Δd corresponds to change in porosity $\Delta\varphi$:

$$\frac{\Delta d}{d_0} = \left(\sqrt{1 + \frac{\Delta \phi}{\phi_0}} - 1 \right) \tag{25}$$

For small changes in normalized porosity $\Delta\varphi/\varphi_0 << 1$, Equation 25 approaches:

$$\frac{\Delta d}{d_0} \approx \frac{1}{2} \frac{\Delta \phi}{\phi_0} \tag{26}$$

Thus, changes in porosity are proportional to changes in pore diameter. Equations 24 and 25 (or 26) link micro-scale change in pore size to macro-scale changes in permeability.

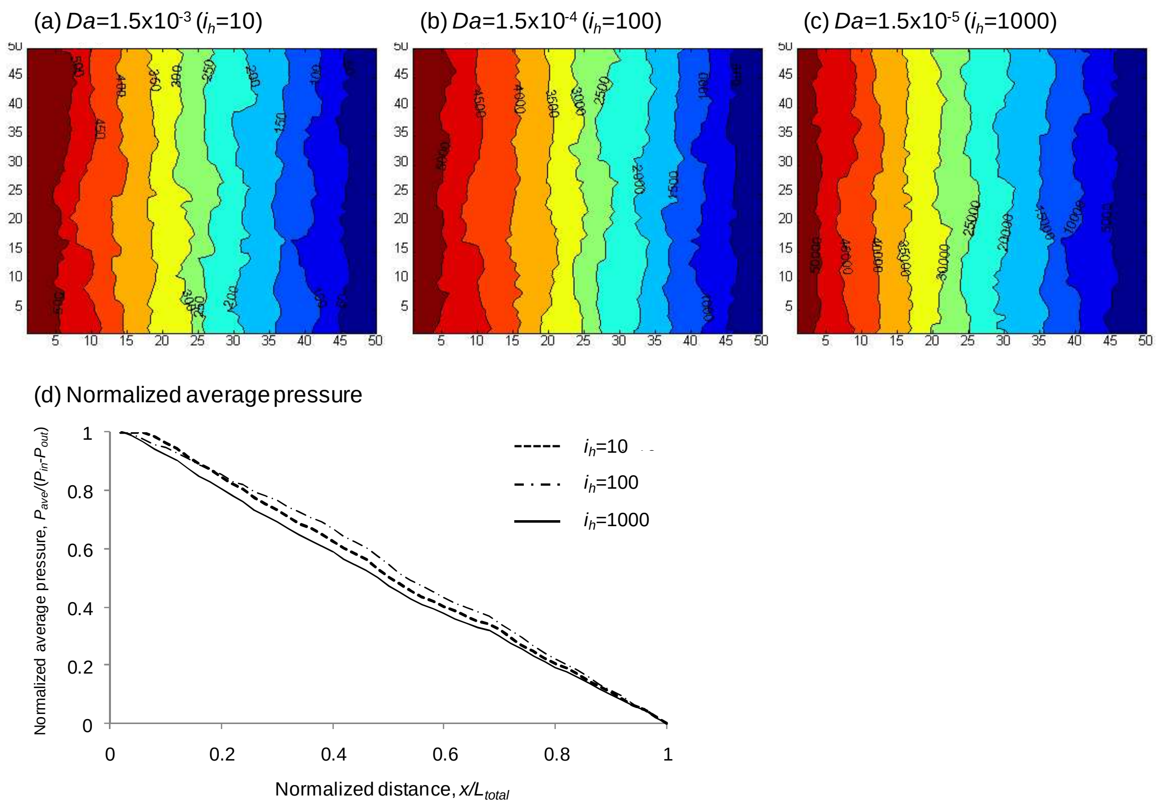

Figure 5.8 Pressure field after 1000 network pore volumes have been flushed (COV=0.4): (a) i_h=10 (Da=1.5*10^{-3}, Pe=6.8*10), (b) i_h=100 (Da=1.5*10^{-4}, Pe=6.8*10^2), (c) i_h=1000 (Da=1.5*10^{-5}, Pe=6.8*10^3), and (d) normalized average pressure with respect to the distance from inlet (initial graph is identical to the normalized average pressure when i_h=1000).

When the hydraulic gradient is high $Da<10^{-4}$ (i_h>100), the normalized mean tube diameter $\overline{d}/\overline{d_0}$ is linearly related to the normalized flow rate q/q_0 (Figure 5.9-a). However, when the hydraulic gradient is low $Da\sim10^{-3}$ (i_h=10), the trend q/q_0 vs. $\overline{d}/\overline{d_0}$ deviates from linearity and reaches a plateau, even though the normalized mean tube diameter continues increasing; this apparent paradox is explained by the localized dissolution near the inlet (Figure 5.6-a). Figure 5.10 compares the normalized flow rate and the normalized mean tube diameter for the first layer of tubes next to the inlet. When the hydraulic gradient is high $Da\sim10^{-5}$ (i_h=1,000), the relationship approaches the upper bound where every tube grows in proportion to its initial diameter. As the hydraulic gradient i_h decreases, the relationship moves downwards until it hits the plateau. Results in Figures 5.9 and 5.10 highlight the inherent bias when “average trends” are analyzed in reactive fluid flow.

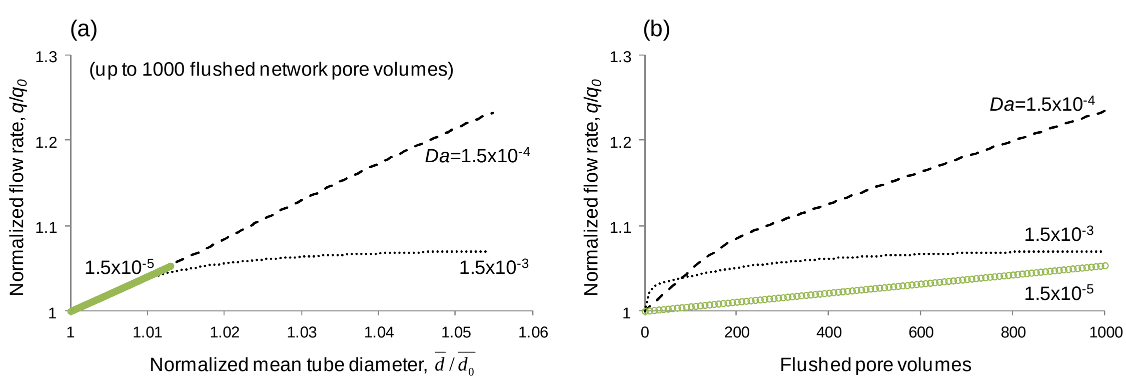

Figure 5.9 Evolution in flow rate normalized by the original total flow rate q/q_0 with respect to: (a) normalized mean tube diameter $\overline{d}/\overline{d_0}$, and (b) flushed pore volume for different Damköhler number *Da* (COV=0.4). Note: Damköhler number is $Da=1.5*10^{-3}$ for hydraulic gradient i_h=10, $Da=1.5*10^{-4}$ for i_h=100, and $Da=1.5*10^{-5}$ for i_h=1000.

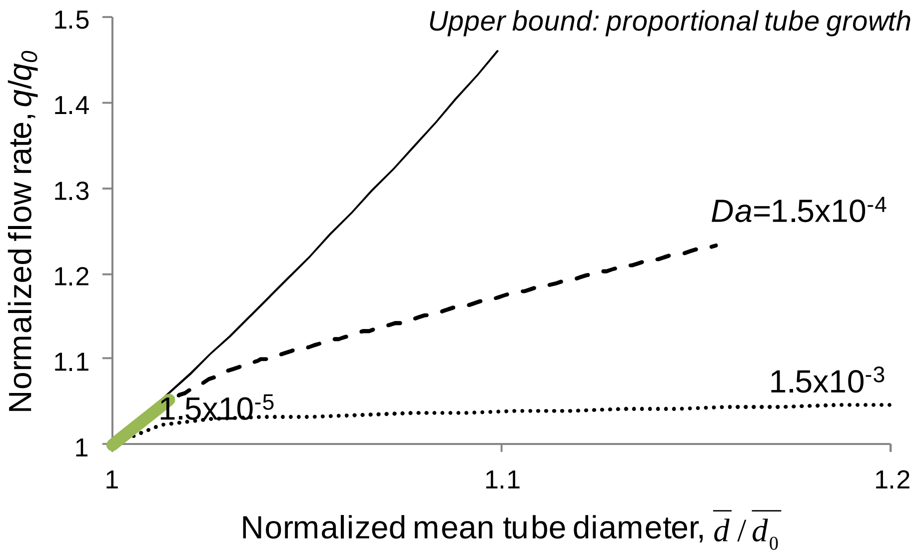

Figure 5.10 Evolution in flow rate normalized by the original total flow rate q/q_0 with respect to the normalized mean tube diameter $\overline{d}/\overline{d_0}$ for the first layer next to the inlet (COV=0.4, up to 1000 flushed network pore volumes), and the theoretical bound in which all tubes grow proportional to their original diameter values (solid line). Note: Damköhler number is Da=1.5*10^{-3} for i_h=10, Da=1.5*10^{-4} for i_h=100, and Da=1.5*10^{-5} for i_h=1000.

5.5 Discussion

5.5.1 Dissolution Pattern

We use the numerical algorithm described above to explore dissolution patterns in the context of CO_2 injection projects (for *Da*<<1). The summary plot in terms of the Damköhler number *Da* in Figure 5.11 shows that the reactive flow of water with dissolved CO_2 yields either compact dissolution near the inlet ($Da>10^{-4}$) or several branches of localized flow paths ($Da<10^{-4}$). These results agree with previous studies that show a transition from compact dissolution to uniform dissolution at around $10^{-4}<Da<10^{-3}$ (injection tests of under-saturated salt solution in a porous medium made of salt grains - Golfier et al., 2002).

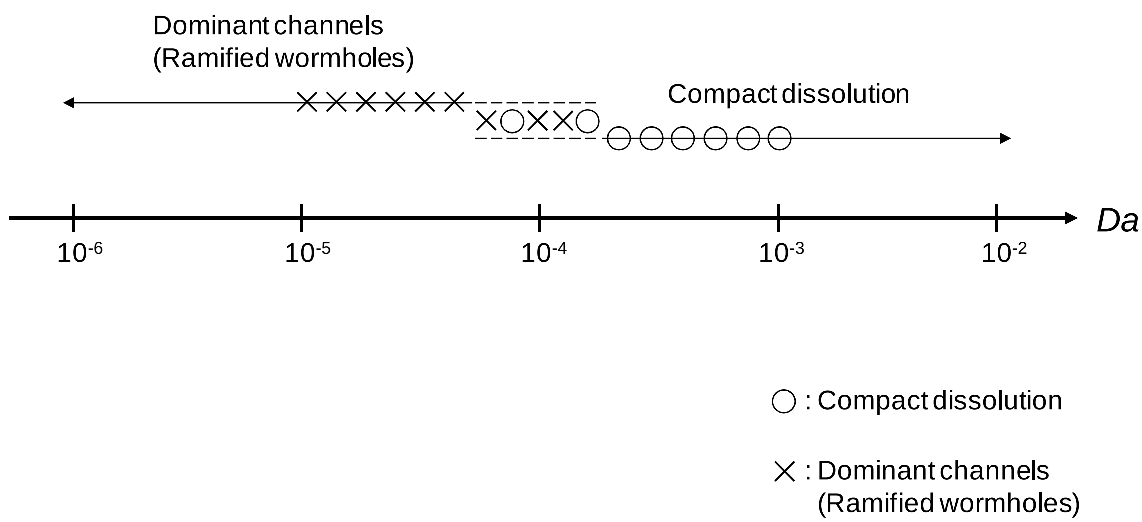

Figure 5.11 Dissolution pattern as a function of the Damköhler number *Da*, for 1000 flushed network pore volumes: CO_2-dissolved fluid flow through porous media during CO_2 geological storage. Note: network simulations were conducted for various hydraulic gradients i_h=10 ($Da=1.5*10^{-3}$), 20,…, 200 ($Da=3*10^{-4}$), and 1000 ($Da=1.5*10^{-5}$).

5.5.2 Effect of Initial Pore Size Variability

The coefficient of variation COV in pore size is larger in jointed rock masses than in sediments (compare Phadnis and Santamarina, 2011 and Shapiro, 2010). Let's examine the role of pore size variability on the evolution of mean tube diameter and flow rate by running additional simulations with COV=1.0 and 1.5. Results in Figure 5.12-a show that the normalized flow rate increases faster with higher COV values for a given increase in the normalized mean tube diameter. Hence, the exponent for the Kozeny-Carman equation α (Equation 24) increases with pore-size variability. Moreover, the range in the exponent α widens as the coefficient of variation in pore size COV increases (Figure 5.12-b): a porous medium with a higher COV is likely to have more localized fluid flow whereby few channels are responsible for most of the flow.

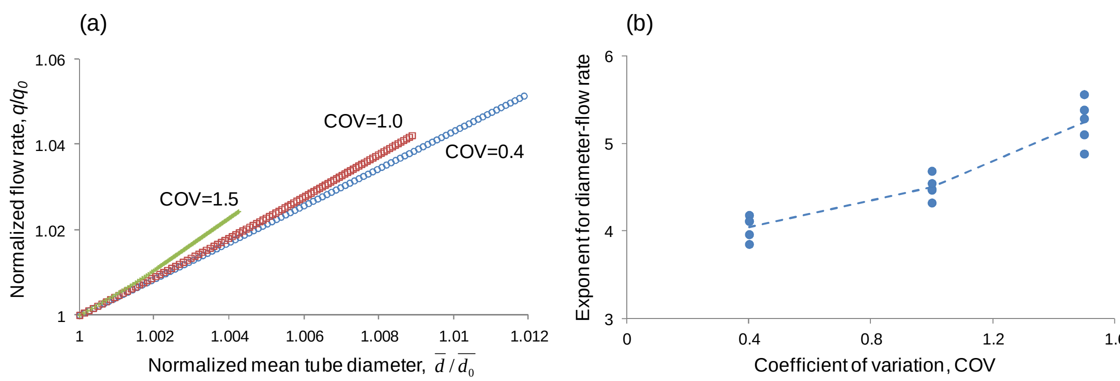

Figure 5.12 Dependency of the mean tube diameter-flow rate evolution on pore-size variability: (a) typical mean tube diameter-flow rate evolution with respect to different coefficient of variations COV, and (b) comparison of exponent α for $(q/q_0) = (\overline{d}/\overline{d_0})^{\alpha}$; all simulations were conducted up to 1000 flushed network pore volumes with hydraulic gradient i_h=1000 (Da=1.5x10^{-5}).

5.6 Conclusions

Reactive fluid flow prevails near the CO_2-water boundary, and it displaces during CO_2 injection (Figure 5.1). The dissolution rate between minerals and reactant species in the case of CO_2-dissolved water is relatively low. At the same time, the CO_2 front displaces at low velocity because injection pressure are limited to prevent hydraulic fracture.

A new network simulation code was written to investigate fluid-mineral interaction when CO_2-dissolved water flows through a calcitic porous network near the CO_2-water boundary. Simulation results include the distribution of reactive species and reaction product concentrations, the evolution of tube diameters, pressure field, and the relationship between mean tube diameter and flow rate as a result of the CO_2-dissolved reactive fluid flow. Results show:

• The concentration of reactant species rapidly decreases near the inlet when the hydraulic gradient is low and Damköhler number exceeds $Da>10^{-4}$. Reactant species migrate towards the outlet and ramify as the hydraulic gradient increases and the Damköhler number drops $Da<10^{-4}$.

• At low hydraulic gradients ($Da>10^{-4}$; $i_h<100$), tube diameter enlargement prevails near the inlet, flow remains more homogeneous, and high inlet pressure is gradually transferred further into the formation. As hydraulic gradients increase ($Da<10^{-4}$; $i_h>100$), pore enlargement extends towards the outlet and reactive flow tends to preferentially enlarges tubes with high flow rate.

• Results show that calcite storage reservoir will experience either compact dissolution near the inlet ($Da>10^{-4}$) or localized flow paths ($Da<10^{-4}$) as a result of CO_2-dissolved reactive fluid flow.

• Both the Damköhler number and pore-size variability affect the relationship between mean tube diameter and flow rate. Changes in Damköhler number result in inherent bias between average and local trends. The exponent of the Kozeny-Carman equation

$q/q_0=(\varphi/\varphi_0)^\alpha$ increases with the coefficient of variation COV in pore size. Both the Damköhler number and pore-size variability should be accounted in field-scale FEM models.

CHAPTER 6

REACTIVE FLUID FLOW THROUGH THE CAPROCK OVERLYING CO_2 STORAGE RESERVOIRS

6.1 Introduction

More than 80% of the electric power in the USA is produced by burning fossil fuels (DOE, 2010), resulting in CO_2 emissions into the atmosphere. The geological storage of CO_2 has been suggested to mitigate the potential consequences of CO_2 emissions (IPCC, 2005), whereby large quantities of CO_2 are injected typically deeper than 800m to attain supercritical CO_2 conditions in order to minimize the affected volume (Note: supercritical temperature $T \geq 304.1$K and pressure $P \geq 7.38$MPa). Supercritical CO_2 migrates upwards due to buoyancy and accumulates underneath the caprock.

Most sites considered for CO_2 storage involve low-permeability clay-rich water-saturated caprocks ($10^{-22}\text{m}^2 < k_{perm} < 10^{-19}\text{m}^2$ - Katsube and Williamson, 1994; Horseman et al., 1999; Armitage et al., 2010). The solubility of CO_2 in water can be as high as 1-to-2 moles/L under the P-T conditions in deep reservoirs (Duan and Sun, 2003). Therefore, water with high-CO_2 concentration may diffuse through the caprock even when small pores prevent CO_2 invasion and advective transport (Figure 6.1; Gaus et al., 2005). Dissolved CO_2 acidifies the formation water, changes the surface charge in clay minerals, and causes mineral dissolution (Chapter 3; Gherardi et al., 2007; Berne et al., 2010; Espinoza and Santamarina, 2012). Furthermore, discontinuities in the caprock such as cracks or faults favor localized fluid migration and erosion (Chapter 4; Bildstein et al., 2010). These observations suggest that a proper understanding of reactive fluid flow in the caprock is critical to the analysis of the long-term integrity of geologic seals in CO_2 storage projects.

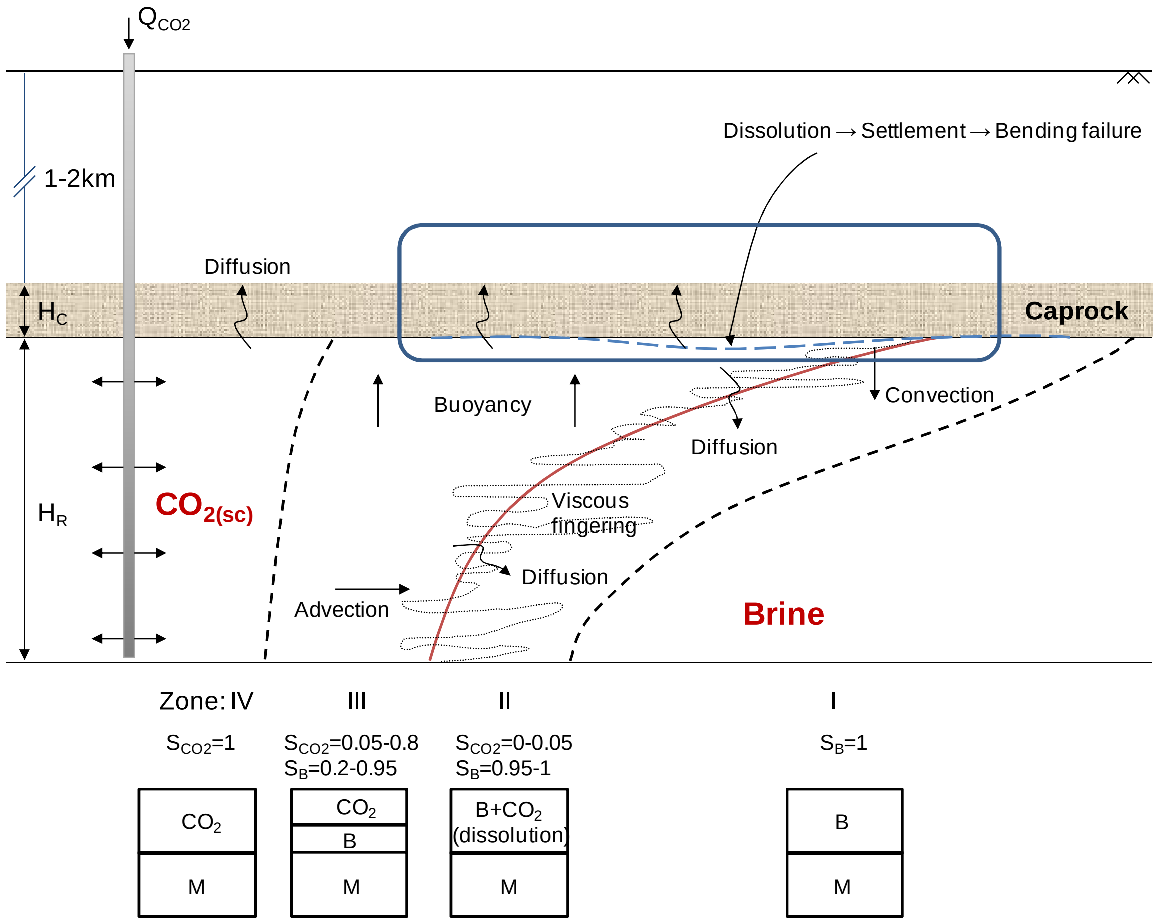

Figure 6.1 CO_2 geological storage and coupled processes: four zones around a CO_2 injection well (modified from Azaroual et al., 2007). The focal area for this study is within the rectangular frame. CO_2 plumes migrate upwards by buoyancy and accumulate underneath the caprock, and sustain the diffusion of dissolved CO_2 into the caprock (M: Mineral, B: Brine, S_{CO2}: saturation of CO_2, and S_B: saturation of brine).

Recent studies related to geochemical changes in caprocks following the accumulation of CO_2 plumes have shown that: the diffusion of dissolved CO_2 may negatively affect the porosity and sealing capacity of the caprock (Gaus et al., 2005; Johnson et al., 2004); the primary mineral composition of the caprock determines the CO_2 trapping capacity (Xu et al., 2005); buffering and mineral precipitation may preserve the sealing capacity of the caprock in a diffusion-controlled regime (Gherardi et al., 2007); and that the impact of mineral dissolution and precipitation on porosity changes may be limited to a narrow zone in the caprock next to the reservoir (Bildstein et al., 2010).

This study analyzes transport conditions in the caprock and examines the consequences of reactive CO_2-dissolved fluid flow. Simulation results are used to investigate changes in hydraulic properties in the caprock as a result of CO_2 injection. Caprock transport conditions are analyzed first, followed by a detailed description of the numerical algorithm.

6.2 Transport Conditions in the Caprock

Fluid pressure and hydraulic gradient. Injected CO_2 migrates upwards by buoyancy and accumulates underneath the caprock due to capillary trapping (Chapter 3; Kopp et al., 2009). The excess fluid pressure ΔP [Pa] at the bottom of the caprock due to presence of buoyant CO_2 is a function of the thickness of the CO_2-filled storage reservoir H_R [m], and the unit weight of CO_2 γ_{CO2} [N/m^3] and water γ_w [N/m^3] as shown in Figure 6.2:

$$\Delta P = H_R \cdot (\gamma_w - \gamma_{CO2}) \tag{1}$$

The total head difference Δh_T across the caprock thickness H_C [m] is computed from the pressure head difference $\Delta h_p = h_p^I - h_p^{II} = \Delta P/\gamma_w$ and the elevation head difference $\Delta h_e = h_e^I - h_e^{II}$:

$$\Delta h_T = \left(h_P^I - h_P^{II}\right) + \left(h_e^I - h_e^{II}\right) = \frac{\Delta P + H_C \gamma_w}{\gamma_w} - H_C = H_R \frac{\gamma_w - \gamma_{CO2}}{\gamma_w} \tag{2}$$

Therefore, the hydraulic gradient i_h across the caprock is:

$$i_h = \frac{\Delta h_T}{H_C} = \left(\frac{H_R}{H_C}\right) \cdot \left(1 - \frac{\gamma_{CO2}}{\gamma_w}\right) \tag{3}$$

The CO_2 density can vary from 200kg/m^3 to 800kg/m^3 under storage conditions that cover both cold ($i_T \leq 20$°C/km) and warm geothermal gradients ($i_T \geq 45$°C/km-IPCC, 2005).

(a) Excess fluid pressure at the bottom of caprock

$$\Delta P = (\gamma_w - \gamma_{CO2})\cdot H_R$$

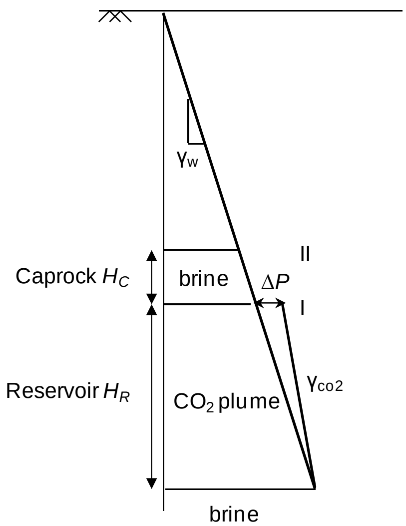

(b) Condition for capillary trapping

$$\Delta P \le P_{CEP} = \frac{4T_s(u)}{d_{pore}}$$

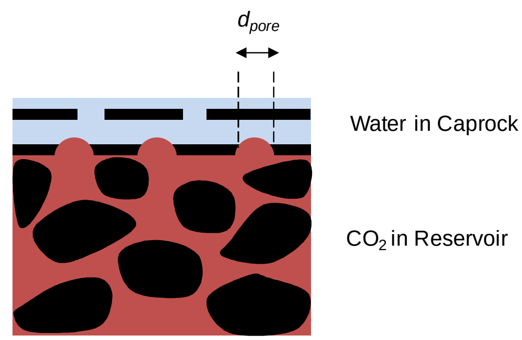

(c) If capillary trapping fails, advecting gradient is as follows:

Head difference: $\Delta h_T = h_T^I - h_T^{II}$

$$= \left(h_p^I - h_p^{II}\right) + \left(h_e^I - h_e^{II}\right)$$

$$= \frac{\Delta P + H_C\gamma_w}{\gamma_w} - H_C$$

$$= \frac{\Delta P + H_C\gamma_w}{\gamma_w} - H_C$$

$$= H_R\,\frac{\gamma_w - \gamma_{CO2}}{\gamma_w}$$

$$\Rightarrow\ i_h = \frac{\Delta h_T}{H_C} = \left(\frac{H_R}{H_C}\right)\cdot\left(1 - \frac{\gamma_{CO2}}{\gamma_w}\right)$$

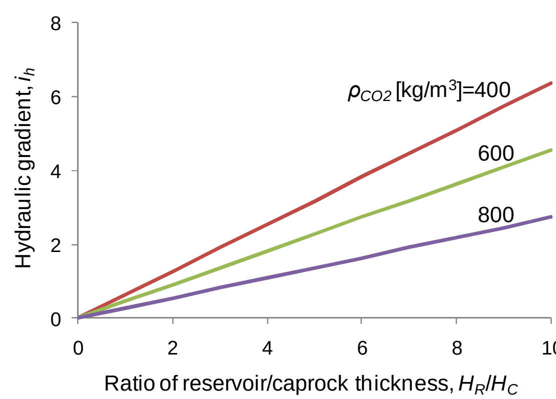

Figure 6.2 Trapping, and hydraulic gradient i_h for the upward flow through caprock with different CO_2 densities ρ_{CO2} [kg/m^3]. Parameters: storage reservoir thickness H_R [m], caprock thickness H_C [m], unit weight of brine γ_w [N/m^3], unit weight of CO_2 γ_{CO2} [N/m^3], total head h_T [m], pressure head h_p [m], elevation head h_e [m], CO_2 entry pressure P_{CEP} [Pa], interfacial tension between CO_2 and brine as a function of fluid pressure T_s(u) [N/m], characteristic pore diameter d_{pore} [m].

For these conditions, the potential hydraulic gradient is quite small (Equation 3), in fact, it is i_h<10 for most sites currently under consideration (Figure 6.2).

Reactive transport regime. The time scales for advection t_{adv}, diffusion t_{diff}, and reaction t_{rxn} can be combined to form two dimensionless ratios, i.e., the Damköhler number *Da* and Peclet's number *Pe*:

$$Da = \frac{t_{adv}}{t_{rxn}} = \frac{\kappa H_C}{v_{ave}} \tag{4}$$

$$Pe = \frac{t_{diff}}{t_{adv}} = \frac{v_{ave} H_C}{D} \tag{5}$$

where D [m^2/s] denotes the coefficient of molecular diffusion. The kinetic rate κ [1/s] = $k_r \cdot S_s \cdot M_m$ is a function of the rate constant for mineral dissolution k_r [mol/m^2/s], the mineral specific surface S_s [m^2/g], and the mineral molar mass M_m [g/mol].

If advective flow develops across the caprock, the average flow velocity v_{ave} [m/s] would be a function of the hydraulic gradient i_h across the caprock (Equation 3) according to Darcy's law:

$$v_{ave} = K_{con} \cdot i_h \tag{6}$$

The hydraulic conductivity K_{con} [cm/s] ranges between 10^{-10}cm/s and 10^{-13}cm/s for typical seal rocks in the absence of discontinuities (Note: hydraulic conductivity $K_{con}=k_{perm}\cdot\rho_w\cdot g/\mu_w$ is computed from the absolute permeability $10^{-22}\text{m}^2<k_{perm}<10^{-19}\text{m}^2$, water density ρ_w=1000kg/m^3, and water viscosity $\mu_w=10^{-3}$Pa·s). The resulting Peclet's number is much smaller than one, $10^{-6}<Pe<10^{-3}$ for the anticipated hydraulic gradients i_h<10. Therefore, diffusive transport prevails over advective transport in the caprock.

Capillary trapping. A laplacian interface between water and CO_2 develops at pore throats size d_{pore} [m] and can sustain a CO_2-water pressure difference that is proportional to the interfacial tension T_s≈35mN/m (Espinoza and Santamarina, 2010):

$$P_{CEP} = \frac{4 \cdot T_s}{d_{pore}} \tag{7}$$

The trapping number π_c is the ratio between the capillary entry pressure P_{CEP} and the pressure difference at the caprock-reservoir interface $\Delta P = H_R \cdot (\gamma_w - \gamma_{CO2})$ as shown in Equation 1,

$$\pi_c = \frac{4 \cdot T_s}{d_{pore} \cdot H_R \cdot (\gamma_w - \gamma_{CO2})} \tag{8}$$

The pore size is $d_{pore} \leq 0.1\mu m$ for most seal rocks without discontinuities, and anticipated reservoir thickness will be less than $H_R \leq 100m$ in most cases. Therefore, $\pi_c \geq 3.6$ and capillary trapping is anticipated in CO_2 storage projects.

Conclusion. Capillary trapping concurs with the prevalent diffusive transport to define a diffusion-controlled reactive transport condition in the caprock.

6.3 Numerical Simulation Model for Diffusion-Controlled Reactive Transport

The governing pore-scale equations for diffusion-dominant reactive transport are numerically solved to analyze the caprock evolution in CO_2 storage projects.

6.3.1 Mineralogy and Dissolution

The dissolution of CO_2 in water produces hydrogen ions H^+ and aqueous carbon dioxide $CO_{2(aq)}$; both species cause mineral dissolution. Calcite and kaolinite are selected to analyze a worst-case scenario and a more common mineralogy frequently encountered in potential reservoir caprock.

Calcite. Carbonate content in shales varies from 1% to 65% (Guéguen and Palciauskas, 1994; Wollenweber et al., 2010). The two dominant calcium carbonate dissolution reactions at high H^+ and $CO_{2(aq)}$ concentrations are (Plummer et al., 1978):

$$CaCO_{3(s)} + H^+ \rightarrow Ca^{2+} + HCO_3^- \tag{9}$$

$$CaCO_{3(s)} + CO_{2(aq)} + H_2O \rightarrow Ca^{2+} + 2HCO_3^- \tag{10}$$

Kaolinite. Kaolinite is selected to examine clayey caprocks. We adopt the model by Li et al. (2006) to represent the dissolution of kaolinite. The reaction consumes six moles of H^+ to produce two moles of Al^{3+} and two moles of H_4SiO_4:

$$Al_2Si_2O_5(OH)_{4(s)} + 6H^+ \rightarrow 2Al^{3+} + 2H_4SiO_4 + H_2O \tag{11}$$

First-order kinetics. The formulation assumes first-order kinetics:

$$-\frac{d[react]}{dt} = \frac{\nu_{produced}}{\nu_{react}} \frac{d[produced]}{dt} = \kappa[react] \tag{12}$$

where square brackets indicate species concentration, $\nu_{produced}/\nu_{react}$ defines stoichiometric ratio between produced and reactant species, and κ [1/s] denotes the kinetic rate for each chemical equation. The system reaches equilibrium and mineral dissolution stops when the ionic concentration product Ω [-] equals the equilibrium constant K_{eq} [-]:

$$\Omega = \frac{\Pi[produced]^\nu}{\Pi[react]^\nu} = K_{eq} \tag{13}$$

where Π indicates product of components in series. Mineral precipitation is not considered in this study. All parameters and rate constants are summarized in Table 6.2.

Table 6.1 Parameters used for numerical simulations and analyses

Parameter	Property
Number of nodes, N	100
Length between nodes, Δx	0.1mm (calcite) 0.1m (kaolinite)
Mineralogy	Calcite & Kaolinite
Courant number, $D \cdot \Delta t/(\Delta x)^2$ (D [m^2/s]: coefficient of diffusion)	0.1
Characteristic time for diffusion, t_{ch}	$L_{total}^2/D=(N \cdot \Delta x)^2/D$
Initial porosity, φ_0	0.04
Mean pore diameters, d_0	10nm
Interfacial tension between CO_2 and water, T_s	35mN/m
Thickness of reservoir, H_R	100m
Density difference between CO_2 and water, $\Delta\rho$	400kg/m^3

Table 6.2 Chemical properties for calcite and kaolinite used in the numerical simulation

(a) Equations for mineral dissolution and properties

				Chemical equation for mineral dissolution	Rate constant [mol/m^2/s]	Equilibrium constant	Ionic concentration product, Ω
Calcite	S_s=0.06m^2/g [3]	M_m=100g/mol	V_m=3.70*10^{-5} m^3/mol	$CaCO_{3(s)} + H^+ \xrightarrow{k_1} Ca^{2+} + HCO_3^-$	k_1=0.745 [1]	K_{1eq}=10$^{1.85}$ [1]	$\frac{[Ca^{2+}]^2[HCO_3^-]^3}{[H^+][H_2CO_3^*]}$
				$CaCO_{3(s)} + CO_{2(aq)} + H_2O \xrightarrow{k_2} Ca^{2+} + 2HCO_3^-$	k_2=8.6*10^{-4} [1]	K_{2eq}=10$^{-4.5}$ [1]	
Kaolinite	S_s=1.16m^2/g [3]	M_m=222g/mol	V_m=9.95*10^{-5} m^3/mol	$Al_2Si_2O_5(OH)_{4(s)} + 6H^+ \xrightarrow{k_H} 2Al^{3+} + 2H_4SiO_4 + H_2O$	k_H=2.79*10^{-11} [2]	K_{eq}=10$^{3.80}$ [2]	$\frac{[Al^{3+}]^2[H_4SiO_4]^2}{[H^+]^6}$

(b) Boundary condition: Concentrations of species in calcite-dominant environment

Inlet concentration	Initial concentration
$[H^+]_{inlet}$=6.68*10^{-4}mol/L	$[H^+]_{initial}$=1.0*10^{-8}mol/L
$[H_2CO_3^*]_{inlet}$=1mol/L	$[H_2CO_3^*]_{initial}$=1.0*10^{-5}mol/L
$[HCO_3^-]_{inlet}$=6.68*10^{-4}mol/L	$[HCO_3^-]_{initial}$=4.47*10^{-4}mol/L
$[Ca^{2+}]_{inlet}$=1.36*10^{-3}mol/L	$[Ca^{2+}]_{initial}$=1.59*10^{-3}mol/L
$[OH^-]_{inlet}$=1.50*10^{-11}mol/L	$[OH^-]_{initial}$=1.0*10^{-6}mol/L
$[Cl^-]_{inlet}$=2.72*10^{-3}mol/L	$[Cl^-]_{initial}$=2.72*10^{-3}mol/L

(c) Boundary condition: Concentrations of species in kaolinite-dominant environment

$[H^+]_{inlet}$=6.68*10^{-4}mol/L	$[H^+]_{initial}$=1.0*10^{-8}mol/L
$[H_2CO_3^*]_{inlet}$=1mol/L	$[H_2CO_3^*]_{initial}$=1.0*10^{-5}mol/L
$[HCO_3^-]_{inlet}$=6.68*10^{-4}mol/L	$[HCO_3^-]_{initial}$=4.47*10^{-4}mol/L
$[OH^-]_{inlet}$=1.50*10^{-11}mol/L	$[OH^-]_{initial}$=1.0*10^{-6}mol/L
$[Al^{3+}]_{inlet}$=8.91*10^{-12}mol/L	$[Al^{3+}]_{initial}$=8.91*10^{-12}mol/L
$[H_4SiO_4]_{inlet}$=8.91*10^{-12}mol/L	$[H_4SiO_4]_{initial}$=8.91*10^{-12}mol/L
$[Na^+]_{inlet}$=1.0*10^{-12}mol/L	$[Na^+]_{initial}$=4.48*10^{-4}mol/L

(d) Coefficient of molecular diffusion: D=2.0*10^{-9}m^2/s [4]

Note: S_s: mineral specific surface, M_m: mineral molar mass, V_m: mineral molar volume; kinetic rate is κ_i [1/s]=$k_i \cdot S_s \cdot M_m$ where k_i is a rate constant; Rate constants are computed for T=40°C in this study; total equilibrium constant for calcite $K_{eq}=K_{1eq}*K_{2eq}$. References/comments: [1] Plummer et al., 1978; Fredd and Fogler, 1998; Pokrovsky et al., 2005; Renard et al., 2005; Algive et al., 2009, [2] Li et al., 2006, [3] Xu et al., 2006, [4] The average molecular diffusion coefficient is selected to satisfy electro-neutrality).

6.3.2 Numerical Simulation – Algorithm

Reactants. The equation for diffusion-dominant reactive transport predicts, the concentration c [mol/m^3] of reactant species (i.e., H^+ and H_2CO_3*; total carbonic acid H_2CO_3* denotes the summation of aqueous carbon dioxide $CO_{2(aq)}$ and true carbonic acid H_2CO_3) in the caprock in the absence of advection (Peclet's number Pe<<1 and trapping number π_c>1); for one-dimensional transport:

$$\frac{dc}{dt} + \kappa c = D\frac{d^2c}{dx^2} \tag{14}$$

Let's add a saturation criterion ($1-\Omega/K_{eq}$) into Equation 14 in terms of the ratio between the ionic concentration product Ω and the equilibrium constant K_{eq}:

$$\frac{dc}{dt} + \kappa c\left(1 - \frac{\Omega}{K_{eq}}\right) = D\frac{d^2c}{dx^2} \tag{15}$$

Equation 15 is expressed in finite difference form to estimate the species concentration $c_{i,j+1}$ at location x_i and time $t_{j+1}=t_j+\Delta t$ with information of species concentrations at location x_i, $x_{i-1}=x_i-\Delta x$, and $x_{i+1}=x_i+\Delta x$ at time t_j (Note: $\Omega_{i,j}$ is the ionic concentration product at location x_i and time t_j):

$$c_{i,j+1} = c_{i,j}\cdot\left(1-\kappa\cdot\Delta t\cdot\left(1-\frac{\Omega_{i,j}}{K_{eq}}\right)\right) + D\frac{\Delta t}{\Delta x^2}\left(c_{i-1,j} - 2\cdot c_{i,j} + c_{i+1,j}\right) \tag{16}$$

Thus, the concentrations of H^+ and H_2CO_3* are computed as follows:

for calcite dissolution

$$[H^+]_{i,j+1} = [H^+]_{i,j}\cdot\left(1-\kappa_1\cdot\Delta t\cdot\left(1-\frac{\Omega_{i,j}}{K_{eq}}\right)\right) + D\frac{\Delta t}{\Delta x^2}\left([H^+]_{i-1,j} - 2[H^+]_{i,j} + [H^+]_{i+1,j}\right) \tag{17}$$

$$[H_2CO_3^*]_{i,j+1} = [H_2CO_3^*]_{i,j}\cdot\left(1-\kappa_2\cdot\Delta t\cdot\left(1-\frac{\Omega_{i,j}}{K_{eq}}\right)\right) + D\frac{\Delta t}{\Delta x^2}\left([H_2CO_3^*]_{i-1,j} - 2[H_2CO_3^*]_{i,j} + [H_2CO_3^*]_{i+1,j}\right) \tag{18}$$

for kaolinite dissolution

$$[H^+]_{i,j+1} = [H^+]_{i,j} \cdot \left(1 - \kappa_H \cdot \Delta t \cdot \left(1 - \frac{\Omega_{i,j}}{K_{eq}}\right)\right) + D\frac{\Delta t}{\Delta x^2}\left([H^+]_{i-1,j} - 2[H^+]_{i,j} + [H^+]_{i+1,j}\right) \tag{19}$$

Products. The concentrations of produced species (i.e., Ca^{2+} and HCO_3^- in calcite and Al^{3+} and H_4SiO_4 in kaolinite) are determined from the consumption of reactant species in terms of stoichiometric ratios between reactant and produced species. Furthermore, they are subjected to diffusion as well, hence:

for Ca^{2+}: $$[Ca^{2+}]_{i,j+1} = [Ca^{2+}]_{i,j} + \left(\kappa_1[H^+]_{i,j} + \kappa_2[H_2CO_3^*]_{i,j}\right)\cdot\left(1 - \frac{\Omega_{i,j}}{K_{eq}}\right)\cdot\Delta t + D\frac{\Delta t}{\Delta x^2}\left([Ca^{2+}]_{i-1,j} - 2[Ca^{2+}]_{i,j} + [Ca^{2+}]_{i+1,j}\right) \tag{20}$$

for HCO_3^-: $$[HCO_3^-]_{i,j+1} = [HCO_3^-]_{i,j} + \left(\kappa_1[H^+]_{i,j} + 2\kappa_2[H_2CO_3^*]_{i,j}\right)\cdot\left(1 - \frac{\Omega_{i,j}}{K_{eq}}\right)\cdot\Delta t + D\frac{\Delta t}{\Delta x^2}\left([HCO_3^-]_{i-1,j} - 2[HCO_3^-]_{i,j} + [HCO_3^-]_{i+1,j}\right) \tag{21}$$

for Al^{3+}: $$[Al^{3+}]_{i,j+1} = [Al^{3+}]_{i,j} + \left(\frac{\kappa_H[H^+]_{i,j}}{3}\right)\cdot\left(1 - \frac{\Omega_{i,j}}{K_{eq}}\right)\cdot\Delta t + D\frac{\Delta t}{\Delta x^2}\left([Al^{3+}]_{i-1,j} - 2[Al^{3+}]_{i,j} + [Al^{3+}]_{i+1,j}\right) \tag{22}$$

for H_4SiO_4: $$[H_4SiO_4]_{i,j+1} = [H_4SiO_4]_{i,j} + \left(\frac{\kappa_H[H^+]_{i,j}}{3}\right)\cdot\left(1 - \frac{\Omega_{i,j}}{K_{eq}}\right)\cdot\Delta t + D\frac{\Delta t}{\Delta x^2}\left([H_4SiO_4]_{i-1,j} - 2[H_4SiO_4]_{i,j} + [H_4SiO_4]_{i+1,j}\right) \tag{23}$$

Boundary conditions. The first node i=1 represents the interface between the caprock and the reservoir, and it has a fixed concentration of reactant species. The concentration of total carbonic acid [H_2CO_3*] is determined using expressions proposed by Duan and Sun (2003). Concentrations of hydrogen [H^+], hydroxide [OH^-], and bicarbonate [HCO_3^-] are obtained from the thermodynamic equilibrium of carbonate system $H_2CO_3^*\leftrightarrow H^+ + HCO_3^-$

at reservoir conditions T=40°C and P=10MPa. The initial concentration of other species (Ca^{2+}, Al^{3+}, H_4SiO_4, and Cl^-) at the inlet boundary i=1 at time j=1 are determined to satisfy electro-neutrality; thereafter values $c_{i=1,j}$ are allowed to change to prevent the backward diffusion of dissolved species (i.e., $c_{1,j}=c_{2,j}$ for time step j>1).

Three different boundary conditions are considered at the outlet i=N: a) fixed initial concentration $c_{N,j}=c_{N,1}$ for all j>1, b) free flux to simulate an infinite boundary $c_{N-2,j}-c_{N-1,j}=c_{N-1,j}-c_{N,j}$, and c) closed boundary by forcing $c_{N,j}=c_{N-1,j}$ to impose a null exit gradient.

Initial concentrations of species in the 1-D space are determined to be in thermodynamic-equilibrium and to satisfy electro-neutrality at pH=8, except the inlet (2≤j≤N). Species concentrations evolve as the numerical simulation proceeds (Equations 17 to 23). Tables 6.1 and 6.2 summarize parameters and geochemical values used in numerical simulations and analyses hereafter.

Mineral dissolution. The mineral mass consumption during the time interval t_j to t_{j+1} between location x_i and x_{i+1} is computed from the consumption of reactant species and the corresponding stoichiometric ratios:

$$\Delta c_{i,j}^{m} = \left(\kappa_1[H^+]_{i,j} + \kappa_2[H_2CO_3^*]_{i,j}\right)\cdot\left(1-\frac{\Omega_{i,j}}{K_{eq}}\right)\cdot\Delta t \text{ ; calcite dissolution} \quad (24)$$

$$\Delta c_{i,j}^{m} = \left(\frac{\kappa_H[H^+]_{i,j}}{6}\right)\cdot\left(1-\frac{\Omega_{i,j}}{K_{eq}}\right)\cdot\Delta t \text{ ; kaolinite dissolution} \quad (25)$$

Algorithm stability. The algorithm is summarized in Figure 6.3 for calcite and in Figure 6.4 for kaolinite. This formulation is stable when the diffusion coefficient D, kinetic rate κ, and the time and space intervals satisfy $D\cdot\Delta t/\Delta x^2$<<1 and $\kappa\cdot\Delta t$<<1; thus, we set the time interval $\Delta t=0.01\cdot\Delta x^2/D\leq 0.1/\kappa$. One cycle in the numerical simulation implies a finite time interval Δt and results in updated species concentrations and mass consumption at all nodes. We repeat this cycle until the total simulation time reaches $t=10\cdot L_{total}^2/D$.

time

$CaCO_3$

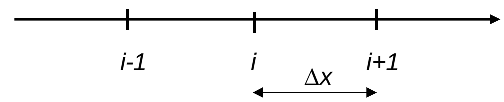

Species: H^+, $H_2CO_3^*$, HCO_3^-, Ca^{2+}, OH^-, Cl^-

j

$CaCO_3 + H^+ \rightarrow Ca^{2+} + HCO_3^-$; kinetic rate κ_1

$CaCO_3 + CO_{2(aq)} + H_2O \rightarrow Ca^{2+} + 2HCO_3^-$; kinetic rate κ_2

Equilibrium constant for the mineral dissolutions: K_{eq}

Ionic concentration product $\Omega_{i,j}$ at location x_i and time t_j: $\Omega_{i,j} = \frac{[Ca^{2+}]_{i,j}^2 [HCO_3^-]_{i,j}^3}{[H^+]_{i,j}[H_2CO_3^*]_{i,j}}$

$j+1$

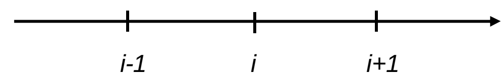

Governing equation: $\frac{dc}{dt} + \kappa c\left(1 - \frac{\Omega}{K_{eq}}\right) = D\frac{d^2c}{dx^2}$

Concentration of reactant species at location x_i and time $t_{j+1}=t_j+\Delta t$:

$$[H^+]_{i,j+1} = [H^+]_{i,j}\left(1 - \kappa_1 \cdot \Delta t \cdot \left(1 - \frac{\Omega_{i,j}}{K_{eq}}\right)\right) + D\frac{\Delta t}{\Delta x^2}\left([H^+]_{i-1,j} - 2[H^+]_{i,j} + [H^+]_{i+1,j}\right)$$

$$[H_2CO_3^*]_{i,j+1} = [H_2CO_3^*]_{i,j}\left(1 - \kappa_2 \cdot \Delta t \cdot \left(1 - \frac{\Omega_{i,j}}{K_{eq}}\right)\right) + D\frac{\Delta t}{\Delta x^2}\left([H_2CO_3^*]_{i-1,j} - 2[H_2CO_3^*]_{i,j} + [H_2CO_3^*]_{i+1,j}\right)$$

Concentration of produced species at location x_i and time $t_{j+1}=t_j+\Delta t$:

$$[Ca^{2+}]_{i,j+1} = [Ca^{2+}]_{i,j} + \left(\kappa_1[H^+]_{i,j} + \kappa_2[H_2CO_3^*]_{i,j}\right)\cdot\left(1 - \frac{\Omega_{i,j}}{K_{eq}}\right)\cdot \Delta t + D\frac{\Delta t}{\Delta x^2}\left([Ca^{2+}]_{i-1,j} - 2[Ca^{2+}]_{i,j} + [Ca^{2+}]_{i+1,j}\right)$$

$$[HCO_3^-]_{i,j+1} = [HCO_3^-]_{i,j} + \left(\kappa_1[H^+]_{i,j} + 2\kappa_2[H_2CO_3^*]_{i,j}\right)\cdot\left(1 - \frac{\Omega_{i,j}}{K_{eq}}\right)\cdot \Delta t + D\frac{\Delta t}{\Delta x^2}\left([HCO_3^-]_{i-1,j} - 2[HCO_3^-]_{i,j} + [HCO_3^-]_{i+1,j}\right)$$

Mass consumption of mineral:

$$\Delta c_{i,j}^m = \left(\kappa_1[H^+]_{i,j} + \kappa_2[H_2CO_3^*]_{i,j}\right)\cdot\left(1 - \frac{\Omega_{i,j}}{K_{eq}}\right)\cdot \Delta t$$

Figure 6.3 One-dimensional numerical simulation scheme for diffusive reactive transport in calcium carbonate caprocks.

time

$Al_2Si_2O_5(OH)_4$

i-1 i i+1

Δx

Species: H^+, $H_2CO_3^*$, HCO_3^-, OH^-, Al^{3+}, H_4SiO_4, Na^+

j

$Al_2Si_2O_5(OH)_4 + 6H^+ \rightarrow 2Al^{3+} + 2H_4SiO_4 + H_2O$; kinetic rate κ_H

- Equilibrium constant for the mineral dissolutions: K_{eq}

- Ionic concentration product $\Omega_{i,j}$ at location x_i and time t_j: $\Omega_{i,j} = \dfrac{[Al^{3+}]_{i,j}^2 [H_4SiO_4]_{i,j}^2}{[H^+]_{i,j}^6}$

j+1

i-1 i i+1

Governing equation: $\dfrac{dc}{dt} + \kappa c\left(1 - \dfrac{\Omega}{K_{eq}}\right) = D\dfrac{d^2c}{dx^2}$

Concentration of reactant species at location x_i and time $t_{j+1}=t_j+\Delta t$:

$$[H^+]_{i,j+1} = [H^+]_{i,j} - \kappa_H \cdot [H^+]_{i,j} \cdot \left(1 - \frac{\Omega_{i,j}}{K_{eq}}\right) \cdot \Delta t + D\frac{\Delta t}{\Delta x^2}\left([H^+]_{i-1,j} - 2[H^+]_{i,j} + [H^+]_{i+1,j}\right)$$

Concentration of produced species at location x_i and time $t_{j+1}=t_j+\Delta t$:

$$[Al^{3+}]_{i,j+1} = [Al^{3+}]_{i,j} + \left(\frac{\kappa_H [H^+]_{i,j}}{3}\right) \cdot \left(1 - \frac{\Omega_{i,j}}{K_{eq}}\right) \cdot \Delta t + D\frac{\Delta t}{\Delta x^2}\left([Al^{3+}]_{i-1,j} - 2[Al^{3+}]_{i,j} + [Al^{3+}]_{i+1,j}\right)$$

$$[H_4SiO_4]_{i,j+1} = [H_4SiO_4]_{i,j} + \left(\frac{\kappa_H [H^+]_{i,j}}{3}\right) \cdot \left(1 - \frac{\Omega_{i,j}}{K_{eq}}\right) \cdot \Delta t + D\frac{\Delta t}{\Delta x^2}\left([H_4SiO_4]_{i-1,j} - 2[H_4SiO_4]_{i,j} + [H_4SiO_4]_{i+1,j}\right)$$

Mass consumption of mineral:

$$\Delta c_{i,j}^m = \left(\frac{\kappa_H [H^+]_{i,j}}{6}\right) \cdot \left(1 - \frac{\Omega_{i,j}}{K_{eq}}\right) \cdot \Delta t$$

Figure 6.4 One-dimensional numerical simulation scheme for diffusive reactive transport in kaolinitic caprocks.

6.3.3 Verification

The numerical simulation code was verified with a closed-form solution for 1-dimensional reactive fluid transport (initial concentration condition $c(x,0)=0$ for $x>0$, and boundary conditions $c(0,t)=c_{inlet}$ and $c(\infty,t)=0$ for $t \geq 0$; Boudreau, 1997):

$$\frac{c}{c_{inlet}} = \frac{1}{2}\exp(\xi_2)\left[\exp(-\xi_1)erfc\left(\frac{2\xi_1-\tau}{2\sqrt{\tau}}\right)+\exp(\xi_1)erfc\left(\frac{2\xi_1+\tau}{2\sqrt{\tau}}\right)\right]$$

$$\text{where } \beta^2 = \left(\frac{v^2}{4D^2}+\frac{\kappa}{D}\right) \; \xi_1 = \beta x, \; \xi_2 = \frac{vx}{2D}, \; \tau = \frac{(v^2+4\kappa D)t}{D} \qquad (26)$$

Results in Figure 6.5 corroborate the numerical simulation code. Differences at the tail of the simulation reflects the simulated boundary conditions for a finite length system $L_{total}=N \cdot \Delta x$ as compared to the infinite length analytical solution. The following section presents numerical results for multiple species, stoichiometry, and boundary conditions that are relevant to CO_2 geological storage.

6.4 Results

The numerical code was used to study the distribution of all reactant and produced species during diffusion-controlled transport when either calcite or kaolinite dominates the caprock.

Species concentration. Due to the high calcite reactivity, the simulation must be restricted to very short total length L_{total}=10mm to satisfy numerical stability and to observe the interplay between reaction and diffusion. Hence, a free-flux outlet boundary condition is selected for this very-short length calcite simulations. This close look highlights that reactant species are readily consumed near the caprock-reservoir interface. On the other hand, all three boundary conditions are explored for kaolinite mineralogy since the length represents a typical full caprock thickness L_{total}=10m.

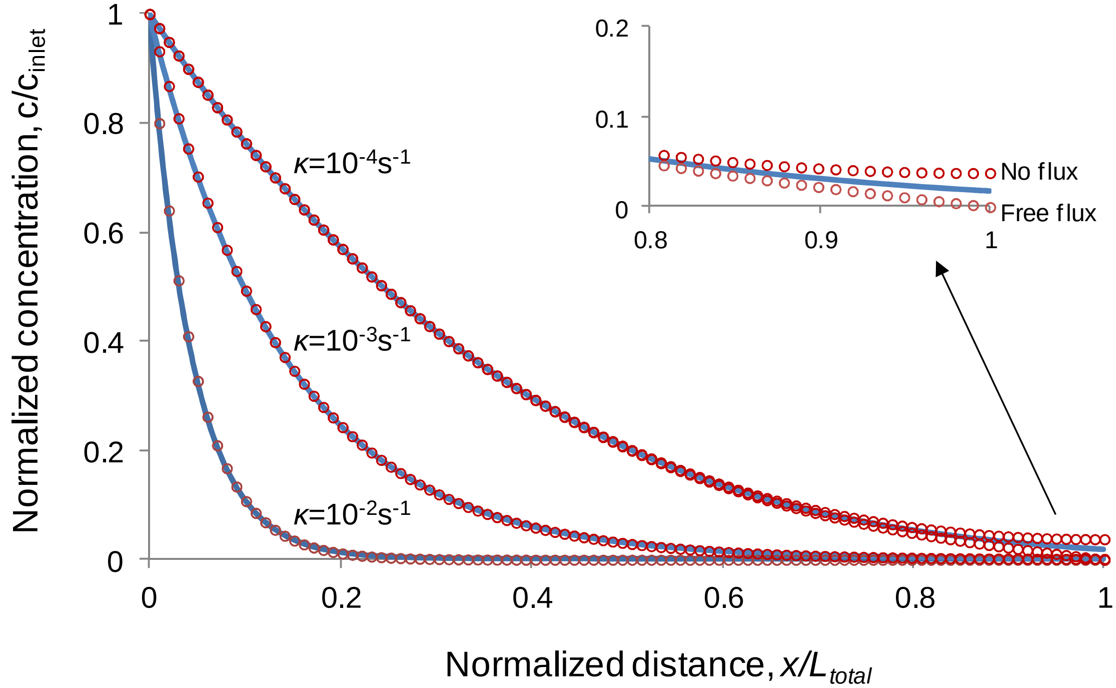

Figure 6.5 Verification of the numerical simulation code. Comparison of results from the numerical simulations and the closed-form solution for 1-dimensional diffusive transport after t/t_{ch}=0.1. Solid line: closed-form solution, Open circle: numerical simulation. Inserted graph zooms in discrepancies with the closed-form solution for two boundary conditions: free flux and no flux at the outlet (Note: saturation criterion ($1-\Omega/K_{eq}$) is disregarded during simulations, and reaction rate varies from $\kappa=10^{-2}s^{-1}$ to $10^{-3}s^{-1}$ and $10^{-4}s^{-1}$; characteristic time ratio of diffusion to mineral dissolution $Da\cdot Pe=\kappa\cdot L_{total}^{2}/D$=5 ($\kappa=10^{-2}s^{-1}$), 0.5 ($\kappa=10^{-3}s^{-1}$), 0.05 ($\kappa=10^{-4}s^{-1}$); fixed inlet concentration $[c]_{inlet}$=0.001mol/L; initial concentration $[c]_{(x>0)}$=0; diffusion coefficient $D=2*10^{-9}m^2/s$; and total length L_{total}=10mm).

Figures 6.6 and 6.7 show the concentration of reactant species (H^+ and H_2CO_3*) and produced species (Ca^{2+}, HCO_3^-, Al^{3+}, and H_4SiO_4) in calcite and kaolinite-rich caprocks. The characteristic diffusion time is t_{ch}≈3hr for calcite (L_{total}=10mm) and t_{ch}≈340yr for kaolinite (L_{total}=10m). The concentration of reactant species H^+ in the calcite caprock rapidly decreases near the inlet due to the high reactivity and slow diffusive transport (Figure 6.6-a). The other reactant species H_2CO_3* in calcite and H^+ in kaolinite caprock evolve towards a linear gradient as the simulation time prolongs beyond the diffusive characteristic time $t_{ch}=L_{total}^2/D$ when the free flux outlet condition is imposed (Figures 6.6-b and Figure 6.7-a). The concentrations of produced species also evolve towards a constant gradient when the free flux condition is set at the outlet (Figures 6.6-c, d and Figure 6.7-b). Forcing the initial concentration to remain constant at the outlet is similar to the free flux boundary condition and leads to similar results. However, when the boundary is closed (i.e., null gradient at the outlet), both reactant and produced species eventually distribute homogeneously along the entire length as the system reaches saturation (Figures 6.7-c and d). Note that the closed boundary yields acidification throughout the entire caprock.

Calcite

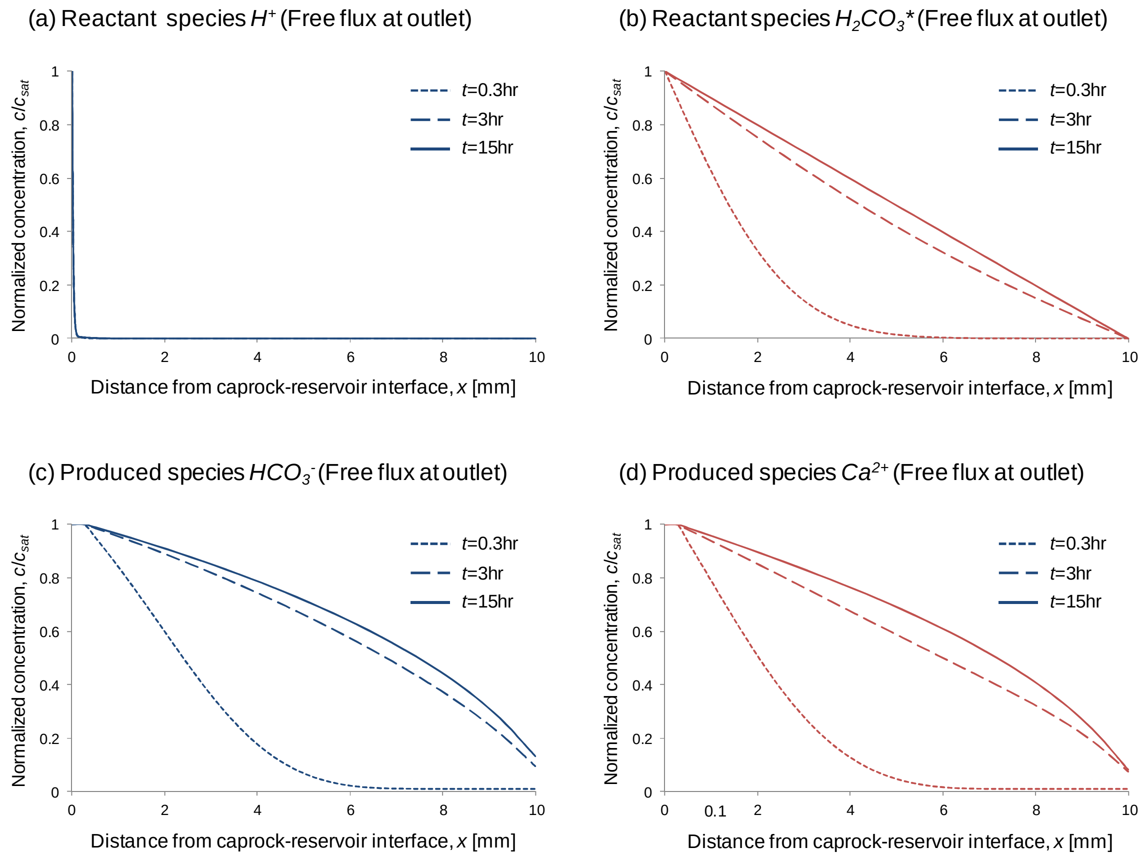

Figure 6.6 Distribution of species concentrations normalized by their saturation concentrations in calcite. (a) Reactant species H^+, (b) reactant species H_2CO_3*, (c) produced species HCO_3^-, and (d) produced species Ca^{2+} (Note: free flux condition at the outlet; total length is L_{total}=10mm; characteristic diffusion time is $t_{ch}=L_{total}^2/D\approx$3hr).

Kaolinite

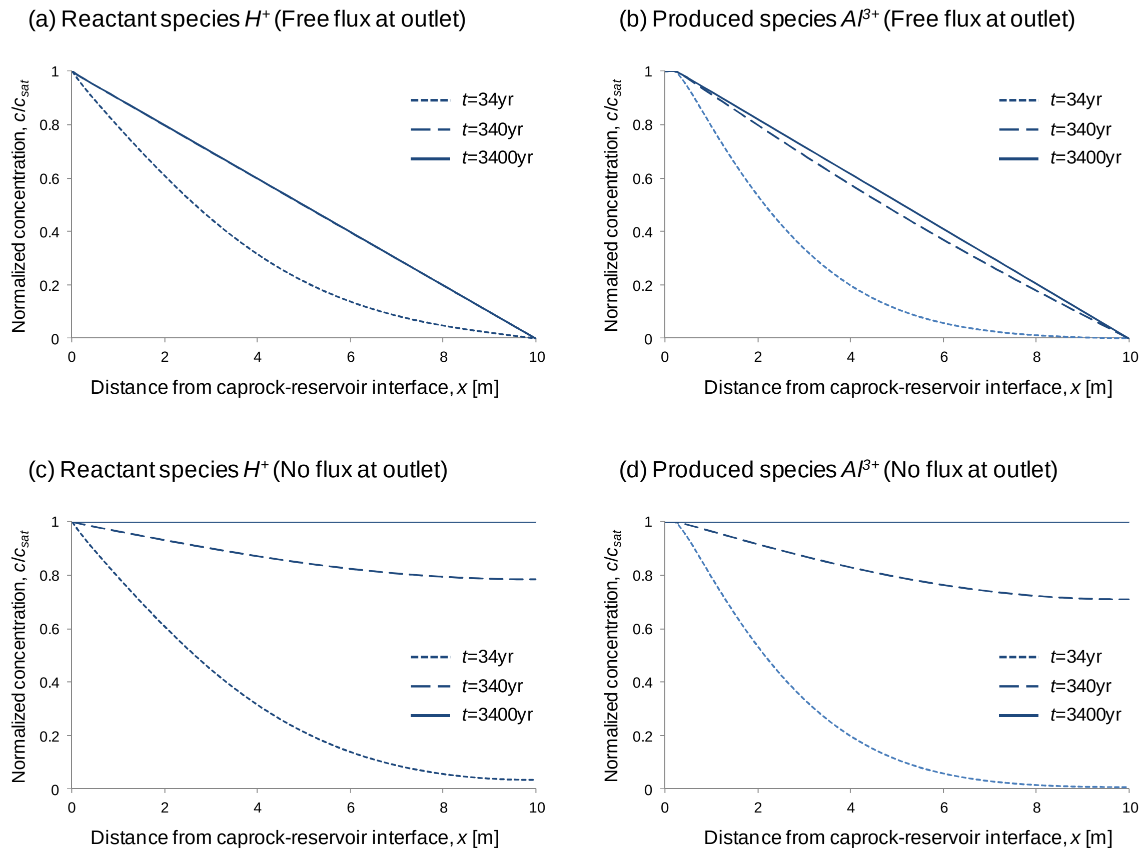

Figure 6.7 Distribution of species concentrations normalized by their saturation concentrations in kaolinite. (a) Reactant species H^+, (b) produced species Al^{3+} (free flux condition at the outlet), (c) reactant species H^+, and (d) produced species Al^{3+} (no flux condition at the outlet). Note: total length L_{total}=10m; characteristic diffusion time $t_{ch}=L_{total}^2/D\approx$340yr.

The mineral dissolution rate and boundary conditions affect the evolution of pH in the caprock. In the calcite caprock, the acidity near the inlet increases rapidly to pH~5 and converges to pH=8 near the outlet where free flow condition is imposed. Mineral dissolution buffers the solution within a narrow thickness next to the caprock-reservoir interface (Figures 6.8-a and b). In contrast, acidity drops to values lower than pH~5 along the entire kaolinitic caprock as the simulation time extends beyond the diffusive characteristic time (Figure 6.9-a). Acidification is more pronounced when the outlet boundary is closed (Figure 6.9-b). Electro-neutrality is maintained during the numerical simulation (Figures 6.8-c, 6.9-c, and d).

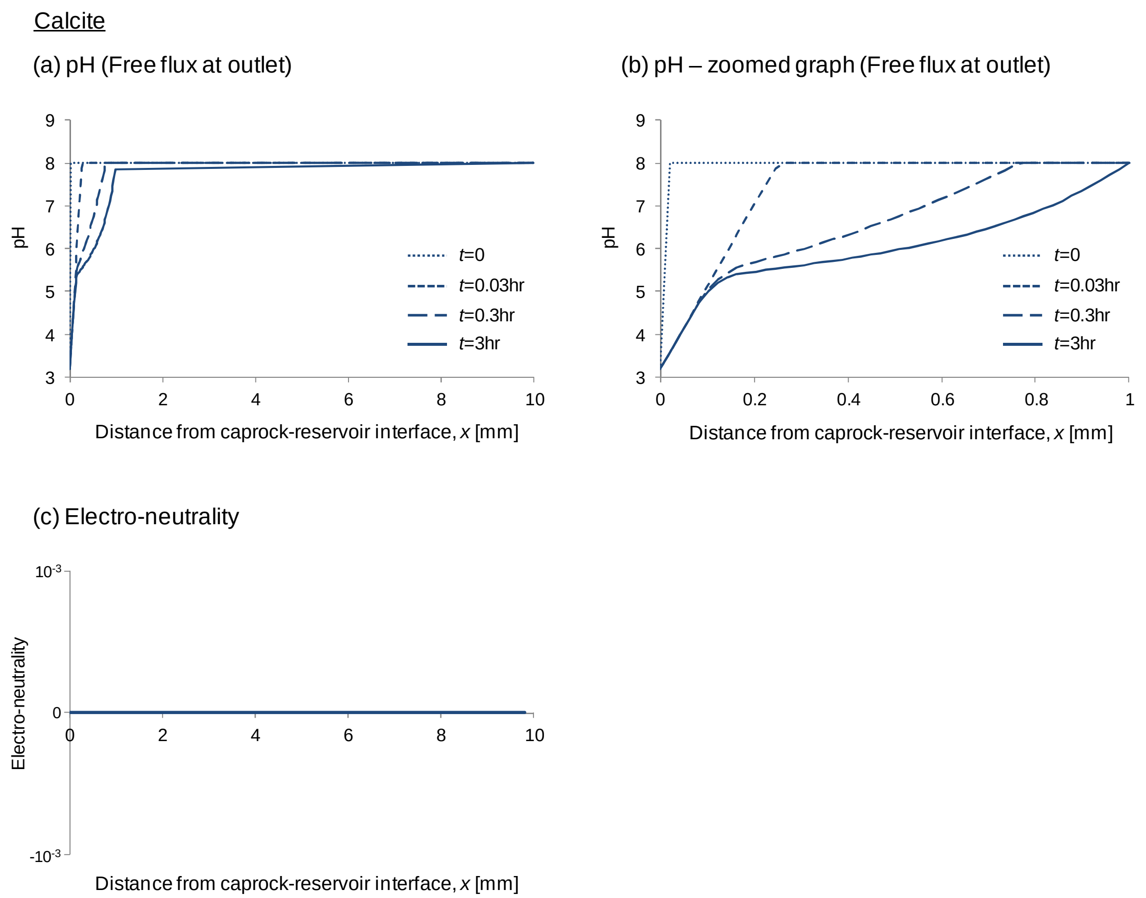

Figure 6.8 Evolution of pH in calcitic caprocks. (a) pH along the entire model length, (b) pH – zoomed in to x=1mm from the caprock-reservoir interface, and (c) electro-neutrality along the model (Note: free flux condition at the outlet; total length is L_{total}=10mm; characteristic diffusion time is $t_{ch}=L_{total}^2/D\approx$3hr).

Kaolinite

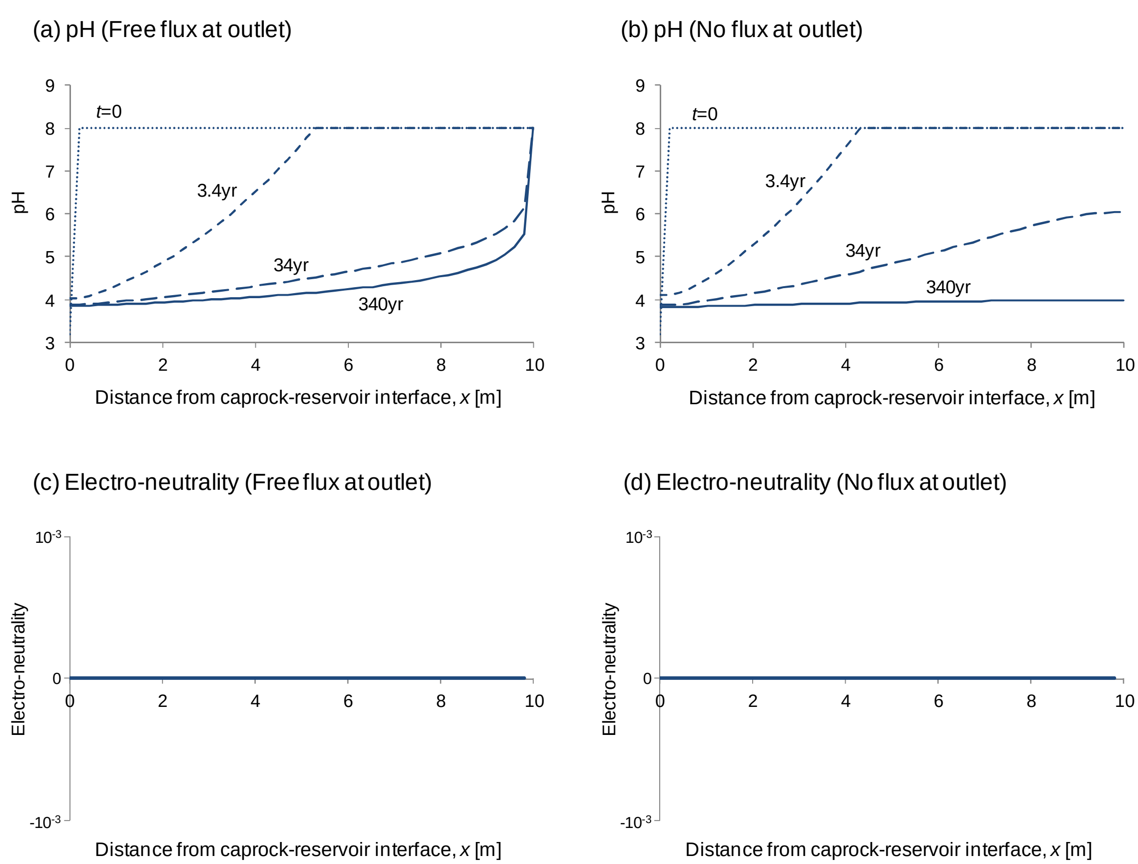

Figure 6.9 Evolution of pH in kaolinitic caprocks. (a) pH along the entire model length (free flux condition at the outlet), (b) pH along the entire model length (no flux condition at the outlet), and (c) & (d) electro-neutrality along the model (Note: total length is L_{total}=10m; characteristic diffusion time is $t_{ch}=L_{total}^2/D \approx 340$yr)

6.5 Analyses and Discussion

Porosity. The change in pore volume ΔV_p [m^3] as a consequence of mineral dissolution can be computed from the mass consumption of mineral per pore volume Δc^m [mol/m^3] and the initial pore volume V_p^0 [m^3]:

$$\Delta V_p = \Delta c^m \cdot V_m \cdot V_p^0 \tag{27}$$

where V_m [m^3/mol] is the mineral molar volume. The change in porosity $\Delta\varphi$ [-] due to the increase in pore volume ΔV_p is a function of the initial total volume V_T^0 [m^3] and the initial porosity φ_0 [-]=V_p^0/V_T^0:

$$\Delta\phi = \frac{\Delta V_p}{V_T^0} = \frac{\Delta c^m \cdot V_m \cdot V_p^0}{V_T^0} = \Delta c^m \cdot V_m \cdot \phi_0 \tag{28}$$

Pore diameter. The change in pore diameter Δd [m] can be estimated assuming that only one cylindrical flow channel exists in the representative elementary volume REV. The initial porosity φ_0 [-] with initial pore diameter d_0 [m], and the new porosity φ_1 [-] after the pore diameter increases by Δd in a REV of length l [m] are:

$$\phi_0 = \frac{\pi d_0^2}{4l^2} \tag{29}$$

$$\phi_1 = \frac{\pi(d_0 + \Delta d)^2}{4l^2} \tag{30}$$

Combining Equations 29 and 30, the change in pore diameter Δd as a function of the change in porosity $\Delta\varphi$ is:

$$\Delta d = \left(\sqrt{1 + \frac{\Delta\phi}{\phi_0}} - 1\right) \cdot d_0 \tag{31}$$

Permeability. Convective flow of denser CO_2-dissolved water can eventually expose the caprock to water once again (Zone III - Figure 6.1) after it experienced mineral dissolution while in contact with CO_2. The initial permeability k_0 [m^2] for cylindrical flow channels is a function of the pore diameter d_0 [m] as predicted by the Hagen-Poiseuille's equation:

$$k_0 = \frac{d_0^2}{32} \tag{32}$$

Increase in pore diameter Δd causes the permeability to increase to:

$$k_1 = \frac{(d_0 + \Delta d)^2}{32} = \frac{d_0^2}{32} \cdot \left(1 + \frac{\Delta d}{d_0}\right)^2 = \frac{d_0^2}{32} \cdot \left(1 + \frac{\Delta\phi}{\phi_0}\right) \tag{33}$$

And the permeability ratio k_1/k_0 is a function of the change in porosity:

$$\frac{k_1 - k_0}{k_0} = \frac{\Delta\phi}{\phi_0} \tag{34}$$

Change in caprock properties. These analyses can be combined with the results of diffusion-controlled reactive transport to anticipate changes in caprock properties. Consider calcite: porosity, pore diameter, and permeabilitiy change within x=0.2mm (x/L_{total}<0.02) from the caprock-reservoir interface. Beyond x=0.2mm, the system reaches saturation and mineral dissolution no longer takes place. Near the caprock-reservoir interface, the increase in porosity is $\Delta\varphi$~0.06, the normalized increase in pore diameter is $\Delta d/d_0$~0.6, and the normalized increase in permeability is $(k_1-k_0)/k_0$~1.5 within the first 15 hrs (Figure 6.10). In other words, there is a very rapid erosion of a skin-layer at the interface. Further erosion can take place if dissolution products are removed by diffusion, advection, or convection in the reservoir. If skin removal is localized, the caprock may experience an unsupported free span and break in tension if the length of the free span is about 20% of the caprock thickness (Chapter 3).

In the case of kaolinite, mineral dissolution extends to about x=1m (x/L_{total}<0.1) 3400 years after CO_2 injection in the reservoir. Changes in porosity, pore diameter, and permeability are shown in Figure 6.11. Estimated changes in porosity $\Delta\varphi$~$5*10^{-5}$, normalized increase in pore diameter $\Delta d/d_0$~$6*10^{-4}$, and normalized increase in permeability $(k_1-k_0)/k_0$~0.001 are quite small even 3400 years after CO_2 injection when the upper caprock boundary is open and allows for free flux (Figures 6.11-a, b, and c). These changes are even smaller when the upper caprock boundary is closed (no flux at the outlet; Figures 6.11-d, e, and f). Based on these results, we can anticipate that capillary trapping will be stable in long-term CO_2 storage projects when clayey caprocks are involved.

In both cases, mineral dissolution is restricted to a region near the bottom of the caprock as the system reaches saturation in diffusion-controlled reactive transport.

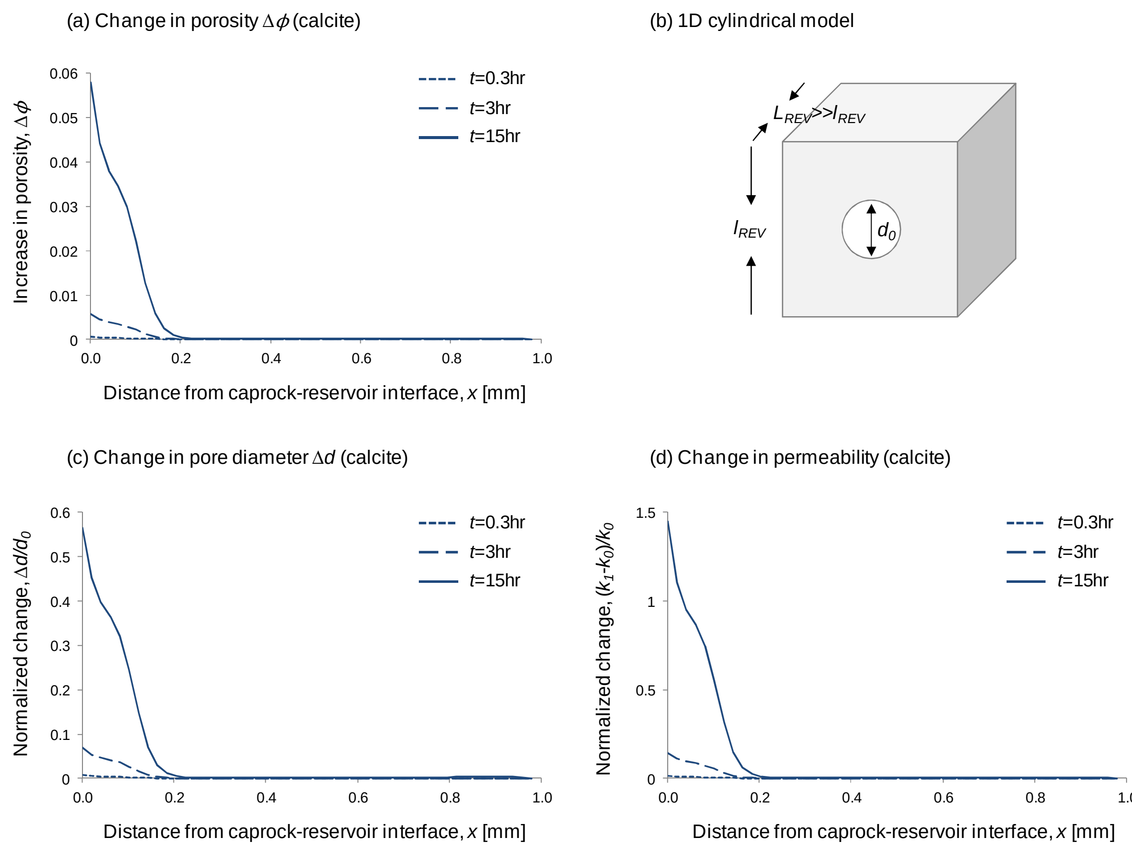

Figure 6.10 Evolution of calcite caprock properties with respect to the distance from the caprock-reservoir interface (zoomed in to x=1mm): (a) change in porosity $\Delta\varphi=\Delta c^m \cdot V_m \cdot \varphi_0$ (initial porosity is assumed φ_0=0.04), (b) 1D cylindrical model to estimate change in pore diameter $\Delta d/d_0=(1+\Delta\varphi/\varphi_0)^{0.5}-1$, (c) normalized change in pore diameter $\Delta d/d_0$, and (d) normalized change in permeability $(k_1-k_0)/k_0=\Delta\varphi/\varphi_0$ (Note: all changes are computed based on the mass consumption of mineral Δc^m [mol/m^3]; total length is L_{total}=10mm, simulation proceeds until time reaches $t\approx$15hr).

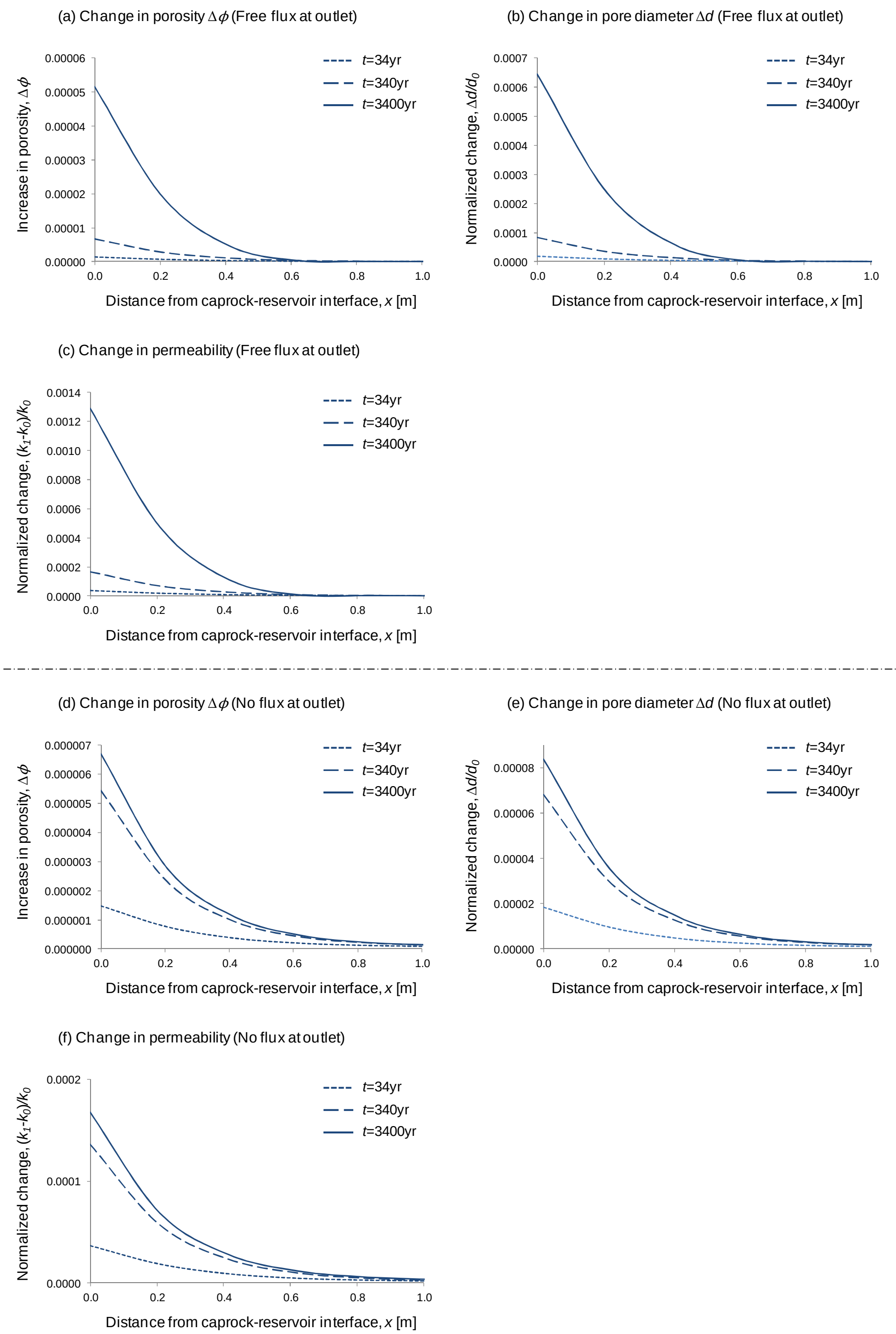

Figure 6.11 Evolution of kaolinite-rich caprock properties with respect to the distance from the caprock-reservoir interface (zoomed in to x=1m): (a) change in porosity $\Delta\varphi$ (initial porosity is φ_0=0.04), (b) normalized change in pore diameter $\Delta d/d_0$, and (c) normalized change in permeability $(k_1\text{-}k_0)/k_0$ (Note: free flux condition at the outlet), (d) change in porosity $\Delta\varphi$, (e) normalized change in pore diameter $\Delta d/d_0$, and (f) normalized change in permeability k_1/k_0 (Note: no flux condition at the outlet; all changes are computed based on the mass consumption of mineral Δc^m [mol/m^3]; total length is L_{total}=10m; simulation proceeds until time reaches t≈3400yr).

Governing parameters. The multiplication of the Damköhler and Peclet's numbers $Da \cdot Pe = \kappa \cdot H_C^2 / D$ defines the ratio between the characteristic times for diffusion and mineral dissolution. In calcite, $Da \cdot Pe > 10^8$ for a caprock thickness H_C=10m, hence, mineral dissolution prevails over diffusion. In contrast, the much lower kinetic rate for kaolinite results in $10^{-1} < Da \cdot Pe < 1$ for a clayey caprock of thickness H_C=10m; this confirms that there is full coupling between diffusion and dissolution in a kaolinite-rich caprock.

6.6 Conclusions

Capillary trapping prevents the invasion of liquid or supercritical CO_2 into the caprock, and diffusion governs the transport of dissolved species in the caprock. The evolution of caprock properties as a result of the diffusion-dominant reactive transport is critical to determine the caprock long-term integrity. We wrote a 1-D numerical simulation code to investigate the transport of dissolved species through the caprock, taking into account the saturation state. Results show the evolution of species concentrations, mass consumption, and hydro-mechanical implications. Salient observations follow:

• The concentration of species evolves towards a constant gradient as the simulation time extends beyond the characteristic diffusion time for both calcite and kaolinite when free flux is allowed at the outlet. In contrast, species eventually distribute homogeneously along the entire length as the system reaches saturation when the boundary is closed.

• Acidity near the inlet increases rapidly to pH~5 and mineral dissolution buffers the solution within a narrow thickness next to the calcite-rich caprock. In contrast, acidity drops to values lower than pH~5 along the entire kaolinitic caprock as the simulation time extends beyond the diffusive characteristic time; acidification is more pronounced when the outlet boundary is closed.

• Changes in porosity, pore diameter, and permeability as a consequent of diffusive reactive transport can be estimated from the mineral mass consumption. Results for calcite anticipate a change in porosity $\Delta\varphi$~0.06, normalized increase in pore diameter $\Delta d/d_0$~0.6, and normalized increase in permeability $(k_1-k_0)/k_0$~1.5 within x=0.2mm from the caprock-reservoir interface and the first 15hrs after injection. The dissolved skin may leave the caprock locally unsupported and bending-tensile cracks may form. Further erosion can take place if dissolution products are removed by diffusion, advection, or convection in the reservoir.

• Diffusion and dissolution are fully coupled in the kaolinite-rich caprock. Mineral dissolution extends to about x=1m from the caprock-reservoir interface after more than 3000 years. Capillary trapping will continue performing in long-term CO_2 storage projects judging by the small changes in porosity and absolute permeability computed in this study.

CHAPTER 7

CO_2 BREAKTHROUGH AND LEAK - SEALING EXPERIMENTS ON SHALE AND CEMENT

7.1 Introduction

Geologic carbon sequestration can be used to avoid CO_2 emissions that result from burning fossil fuels. Injected CO_2 migrates upward and accumulates underneath the caprock (Bielinski et al., 2008; Okwen et al., 2010). Caprocks and cement plugs should prevent CO_2 leakage for thousands of years (Chapter 2; Gaus et al., 2008).

The breakthrough pressure seals can sustain P_{bt} must exceed the pressure difference between the CO_2 phase P_{CO2} and the water phase P_w, $P_{bt}>P_{CO2}-P_w$ (Chapter 6; Fig 7.1-a; Kopp et al., 2009; Saadatpoor et al., 2009; Ehlig-Economides and Economides, 2010; Bergmo et al., 2011). The breakthrough pressure P_{bt} depends on the formation pore radius r_p and the interfacial tension T_s between water and CO_2, $P_{bt}\approx 2\cdot T_s/r_p$. The characteristic pore radius in shale caprocks is $5\text{nm}<r_p<100\text{nm}$ (Katsube and Williamson, 1994; Bachu and Bennion, 2008; Armitage et al., 2010), therefore, the estimated CO_2 breakthrough pressure is between 0.1MPa and 5MPa in a fracture-free formation (Hildenbrand et al., 2002; Hildenbrand et al., 2004; Li et al., 2005; Wollenweber et al., 2010). Most candidate sites for CO_2 geological storage satisfy this condition in the absence of discontinuities (White et al., 2004; Gaus et al., 2005; Bachu and Bennion, 2008; Doughty et al., 2008; Sharma et al., 2009).

Discontinuities are inherent to caprocks and reflect the formation history such as bedding planes, faults, fractures, and joints (Hoek and Brown, 1990). Discontinuities lower the CO_2 breakthrough pressure because of their larger pore size (Downey, 1984) and become preferential conduits for CO_2 leakage (Bildstein et al., 2010; Dooley et al., 2010; Figure 7.1-b).

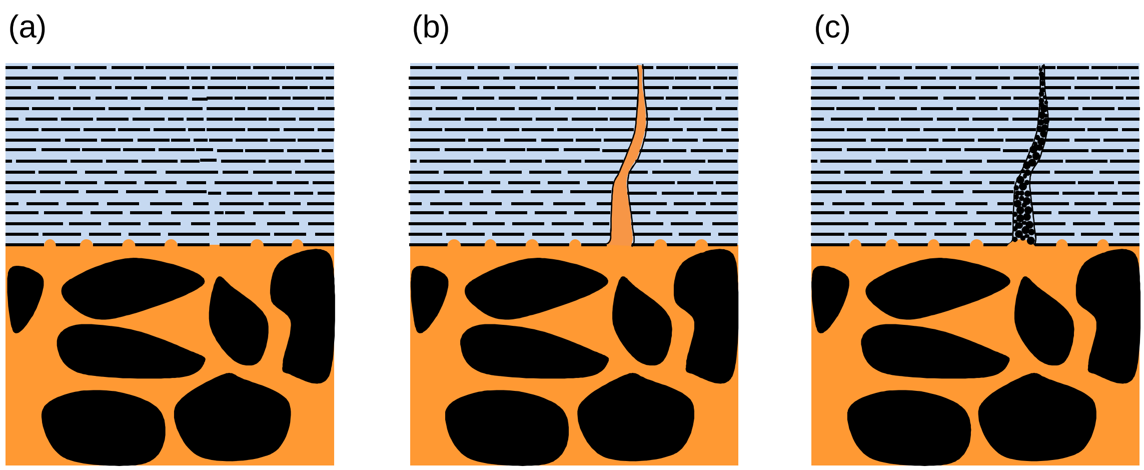

Figure 7.1 Capillary trapping at the interface between caprock and CO_2 storage reservoirs. (a) Ideal condition in which intact caprock overlies CO_2 storage reservoirs (characteristic pore radius of caprock is orders of magnitude smaller than that of storage reservoir), (b) undesirable condition in which caprock retains a crack that can provide leakage path for CO_2 injected in the storage reservoir, and (c) proposed solution that plugs the crack with sub-micron particles and recovers the initial pore radius.

Similarly, the well cement that fills the annulus between borehole and casing must have a high CO_2 breakthrough pressure to prevent CO_2 leakage (Benson and Hepple, 2005; IPCC, 2005), and there must be discontinuities within the cement plugs or at the cement-caprock interface (Kutchko et al., 2007; Viswanathan et al., 2008; Wigand et al., 2009). Clearly, the role of the cement fill is most critical during injection when the CO_2 pressure is highest.

Several strategies have been proposed to address the risk of CO_2 leakage (Réveillère et al., 2012): 1) control overpressure of CO_2, 2) enhance CO_2 immobilization in the form of dissolution or capillary trapping, 3) form a hydraulic barrier in the overlaying layer, and 4) modify the fracture hydraulic properties. Several attempts have been made to control hydraulic properties, such as microbial clogging (Bryant and Britton, 2008; Cunningham et al., 2009) and the injection of polymer gels (Sydansk et al., 2005).

In this research, we investigate the CO_2-breakthrough pressure for caprock shales and cement specimens, and seek to find feasible strategies to effectively plug discontinuities (Fig 7.1-c).

7.2 Experimental Study

Breakthrough and sealing tests are conducted on core plugs using a uniquely designed device to apply high fluid pressure under constant effective stress.

7.2.1 Experimental Device

The high-pressure cell ($P \leq 20$MPa) has an enclosed steel spring to apply a vertical effective stress $\sigma_v' \leq 3$MPa (Figure 7.2-a; Espinoza, 2011). The test is designed for radial flow to minimize the preferential leaks between the specimen and the chamber in conventional 1-D plug tests (Figure 7.2-b). The outlet pipe connects to a pipet to measure flowthrough water and to observe CO_2 leaks. The high-pressure cell is modified to run sealing tests and houses two inlet ports, one for CO_2 and the other to inject the sealing solution as needed (Figure 7.2-a).

7.2.2 Materials – Specimens

Cores of the shale caprock at a Kansas CO_2 pilot test site (Southern Kansas, Watney and Bhattacharya, 2011) were drilled, cut, and surface polished to prepare the annular specimens (outside diameter d_c~40mm, inside diameter d_p~3.17mm, and height 25mm<h<35mm). The specimens exhibited horizontal hairline cracks in the form of layer separation, probably due to stress relaxation during coring and recovery (Figures 7.3-a and b).

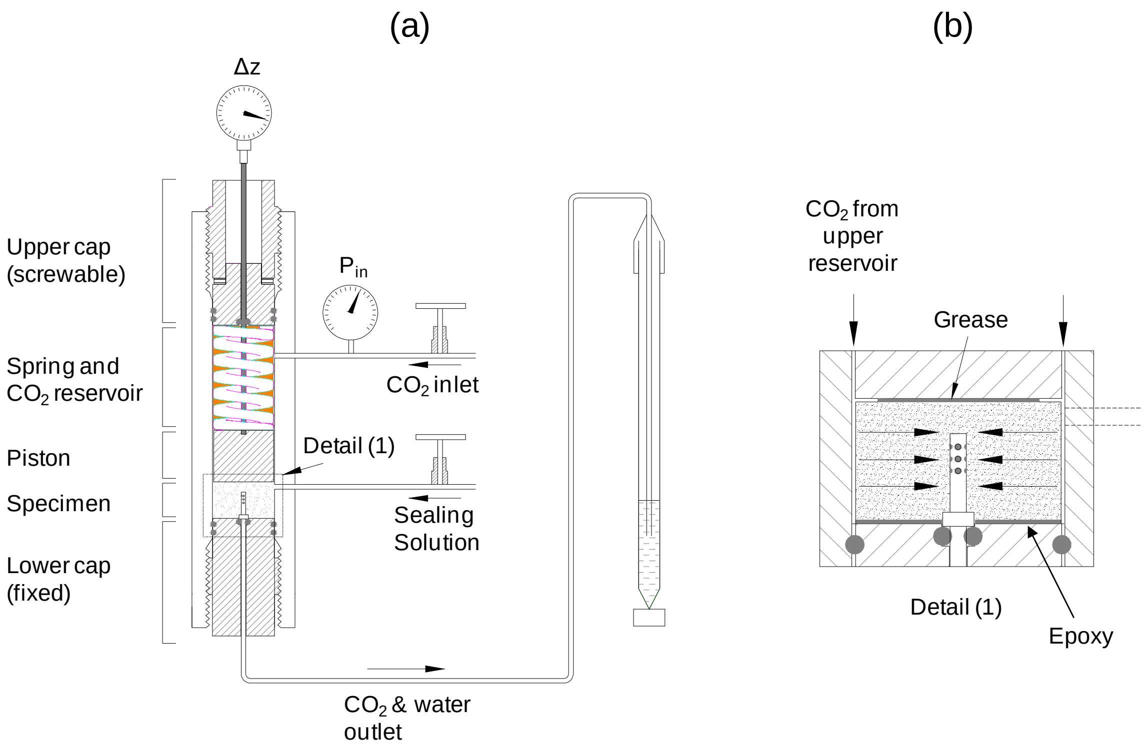

Figure 7.2 Experimental device. (a) Entire setup of CO_2-breakthrough test and sealing treatment where the internal spring applies effective stress on a specimen, CO_2 enters the inside of the cell through a upper tube, sealing solution (suspension) enters the inside of the cell through a lower one, and CO_2 and water come out and stay in a collection pipet and (b) detail (1) in (a) where CO_2 infiltrates the specimen from its outside and reaches the tube in the center, which is connected to the collection pipet.

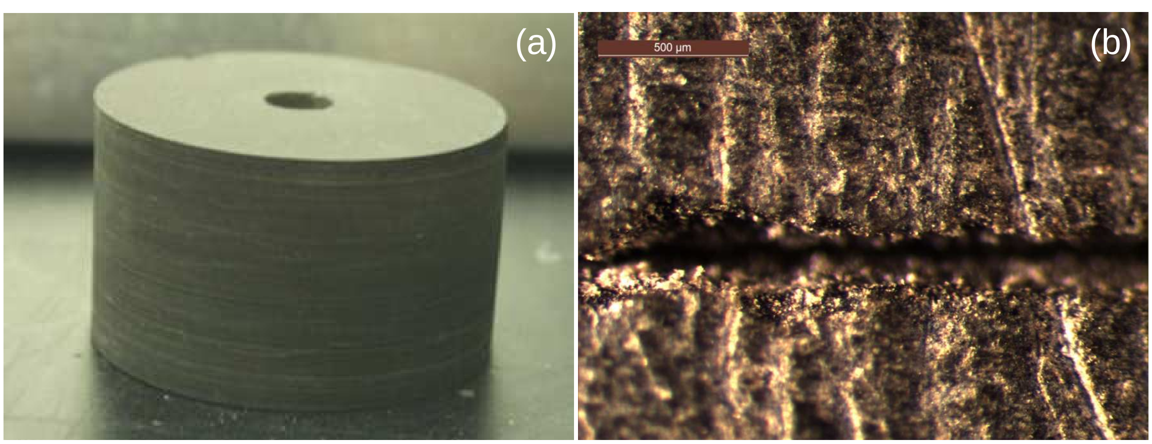

Figure 7.3 Shale rock specimen. (a) Core prepared for the CO_2-breakthrough test and (b) microscopic image of interlayer crack that might develop during coring and core recovery.

Cement specimens were prepared using class-A well-cement at a water-cement ratio w/c=0.4 and cured under 100% humidity for 28 days. The estimated porosity is around φ=0.4 (computed from saturated and dry weights).

7.2.3 Sealing Strategy

Fine migration and accumulation at pore throats can clog and seal porous media (oil recovery: Sharma and Yortsos, 1987; Khilar and Fogler, 1998. Bio-processes: Lee et al., 2004; Trask et al., 2007). We attempt to seal cracks using sub micron-size particles in order to decrease the characteristic pore radius r_p within cracks. The test procedure includes suspension injection under reservoir *P-T* conditions followed by the re-injection of CO_2 (Figure 7.4-a). The selected water-based suspensions are prepared with bentonite (1gram of GEL-PureGold bentonite, and 20ml of water) and kaolin (1gram SA1-Wilkinson kaolin, 1gram dispersant, and 20ml of water).

7.2.4 Test Procedure – Data Interpretation

Saturated shale specimens were stored in a 100% humidity box for one month to reach equilibrium. The specimen was mounted into the high-pressure cell with epoxy at bottom boundary and grease on the top to prevent boundary leaks between the specimen and stainless steel caps (Figure 7.2-b). A vertical stress σ_v'~1MPa was applied in all tests using the internal steel spring. Initially, water fills the annulus around the specimen.

Two inlet pressure histories are imposed in this study (Note: the outlet pressure is atmospheric in all cases). One involves the gradual step-wise increase in CO_2 pressure until the breakthrough is reached and CO_2 continuously comes out (b-1 in Figure 7.4-b). The other pressure history starts by imposing a CO_2 pressure 3~4 times higher than the anticipated breakthrough value; and closing the inlet valve. Then, CO_2 escapes through the outlet port until the pressure drops to the specimen's shut-off pressure P_d as water re-imbibition closes pores starting with the smallest pores first (Hildenbrand et al., 2002; b-2 in Figure 7.4-b; Note: water-saturated CO_2 must be used in this case to prevent drying the formation). Breakthrough and shut-off pressures reflect the smallest pore along the percolating path. Figure 7.5 illustrates water drainage and re-imbibition. The shut-off pressure P_d will be lower than the breakthrough pressure P_{bt} if water re-imbibition does not take place (Hildenbrand et al., 2002), therefore the shut-off pressure is a conservative estimate for the sealing capacity of the caprock.

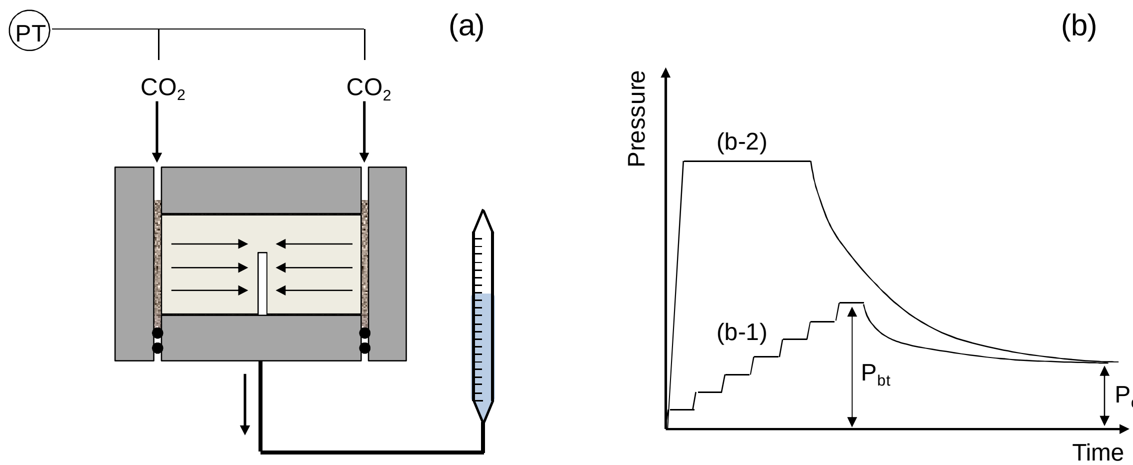

Figure 7.4 CO_2-breakthrough test and sealing treatment. (a) Schematic of sealing treatments where suspension is injected prior to the CO_2 injection. Following the suspension, CO_2 is re-injected, and pressurized CO_2 displaces the suspension on the inside of the specimen and causes sub-micron particles in the suspension to fill in cracks and (b) typical graph of pressure history - (b-1): Initial CO_2-breakthrough test. When CO_2 percolates, its pressure starts to decline. The highest value of CO_2 pressure defines a breakthrough pressure P_{bt}. (b-2): Sealing treatment. With excess pressure, CO_2 starts to percolate the specimen, and the excess pressure of CO_2 gradually decreases. When the last inter-connected path of CO_2 is shut off, no more CO_2 comes out of the system. At the moment, the shut-off pressure P_d denotes the largest effective pore radius, and this value compares to the breakthrough pressure.

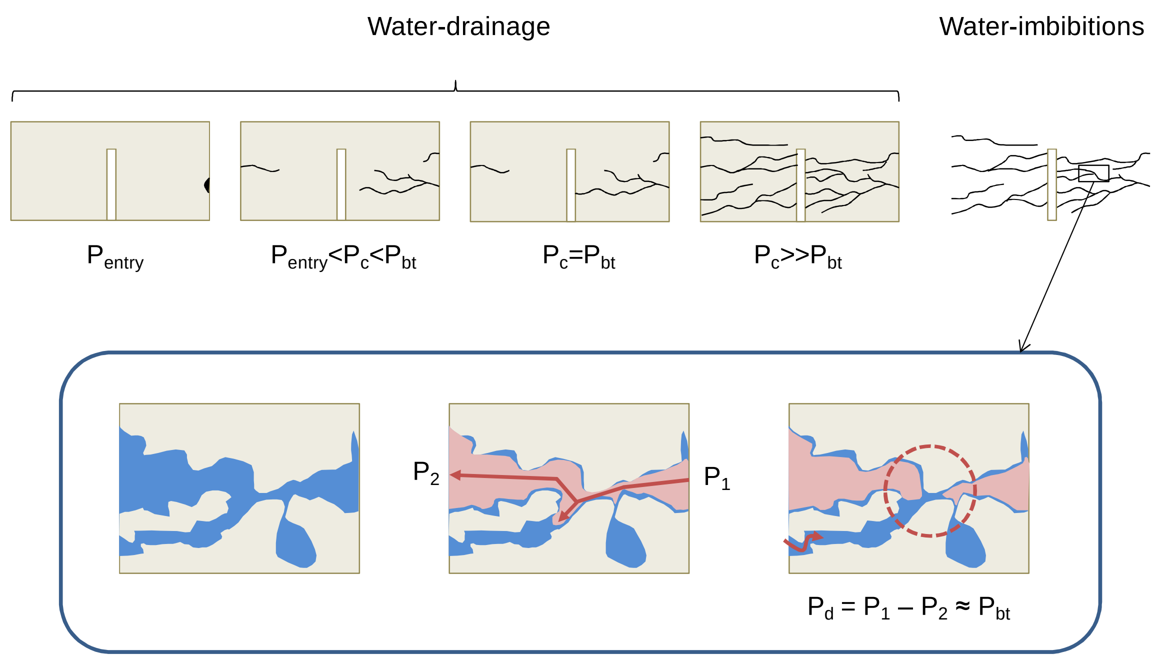

Figure 7.5 Data interpretation – CO_2 breakthrough, water re-imbibitions, and the largest effective pore radius. 1) CO_2 pressure exceeds the percolation threshold and continuous CO_2 flow paths develop across a specimen, 2) after the breakthrough of CO_2, excess pressure in the CO_2 phase decreases, which leads to the water re-imbibitions starting with the smallest pores first and progressing to larger pores, 3) the successive loss of inter-connected CO_2 paths results in a gradual decrease in the flow rate of CO_2, and no more CO_2 comes out when the last inter-connected CO_2 path is shut off. At the moment, the pressure difference in the CO_2 and water phase denotes the largest effective pore radius of the specimen and is defined as shut-off pressure P_d (Hildenbrand et al., 2002).

7.3 Experimental Results and Discussion

We measure the initial CO_2-breakthrough pressure P_{bt} in the annular plugs, followed by sealing treatments and shut-off pressure measurement. Post-test forensic analyses provide insight into crack sealing and transport mechanisms.

7.3.1 Shale Plugs

Initial CO_2 injection. The three shale specimens exhibited very low CO_2-breakthrough pressure P_{bt}≈20kPa-to-30kPa (Figures 7.6-a and c, Table 7.1). This pressure range corresponds to 4μm~6μm pore radius (from $r_p=2T_s/P_{bt}$ where the interfacial tension is assumed as T_s=60mN/m under pressure P<1MPa), which is much larger than the nano-meter pore radius expected for intact shales.

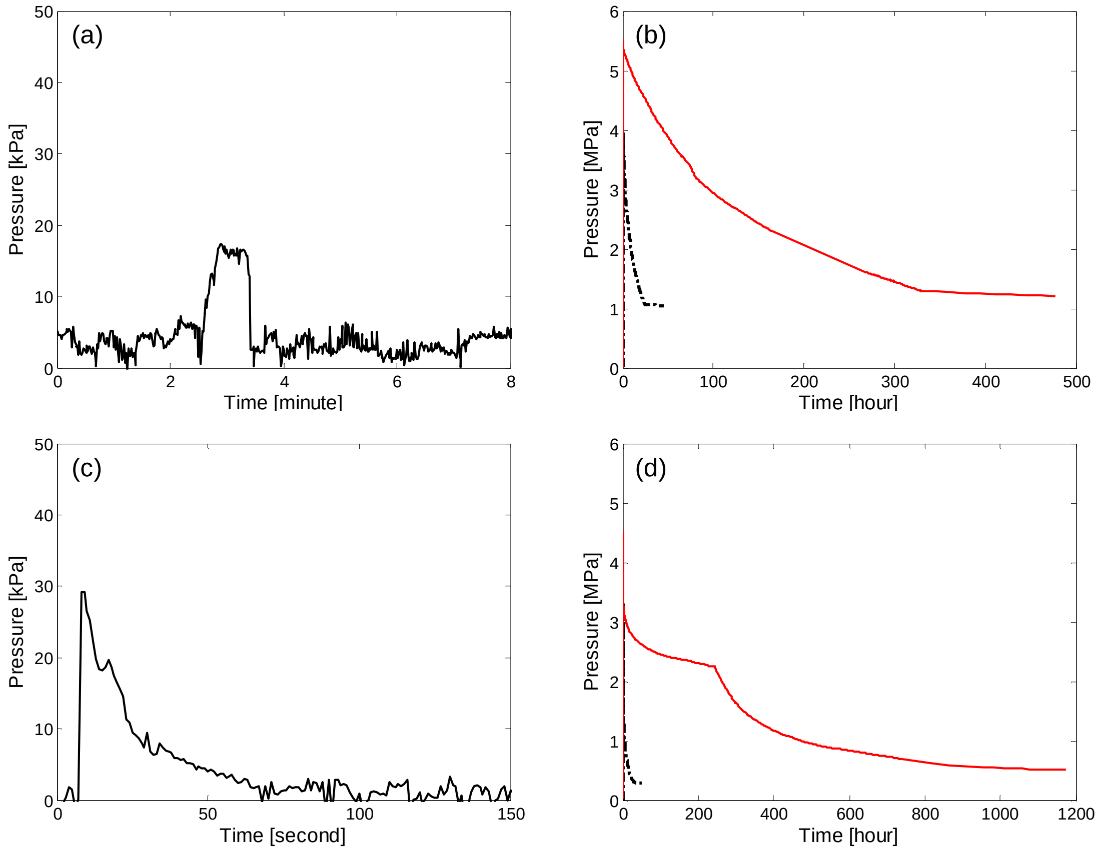

Figure 7.6 Test results for shale specimens. (a) Initial CO_2-breakthrough test for specimen #1 results in the breakthrough pressure P_{bt}~20kPa, (b) sealing treatments for specimen #1 in which the residual pressure difference P_d (shut-off pressure) is measured. The dotted line is from the first treatment and the solid line from the second treatment; both treatments involve the injection of bentonite slurry before the re-injection of CO_2. The first and second treatments yield P_d~1.05MPa and P_d~1.25MPa, respectively, (c) initial CO_2-breakthrough test for specimen #2 results in P_{bt}~30kPa, and (d) sealing treatments for specimen #2. The dotted line is from the first treatment: injecting bentonite slurry. The solid line is from the second treatment: injecting kaolin slurry before the re-injection of CO_2. The first and second treatments yield P_d~0.31MPa and P_d~0.55MPa, respectively.

Cracks. While visual inspection does not reveal cracks (Figure 7.3-a), careful examination under the microscope shows the presence of hairline cracks parallel to the bedding planes in all plugs (Figure 7.3-b). These cracks are parallel to the imposed flow direction in these tests and may have developed during coring and stress relaxation.

Sealing treatment. Clay slurries were injected (~8ml) under constant vertical effective stress (σ_v'~1MPa) to fill the annular gap (4ml) between the test specimen and the high-pressure cell (Figure 7.4-a). Then, CO_2 was re-pressurized above the anticipated breakthrough pressure to determine the new shut-off pressure. Specimens underwent a series of bentonite or kaolin slurry treatments and CO_2 re-injections:

• Shale specimen #1 (Figures 7.6-a and b): before treatment P_{bt}=0.02MPa; after first bentonite treatment P_d~1.05MPa; after second bentonite treatment P_d~1.25MPa. A lower pressure decline rate was observed: 0.12MPa/hr for the first treatment vs. 0.01MPa/hr for the second treatment.

• Shale Specimen #2 (Figures 7.6-c and d): before treatment P_{bt}=0.02MPa; after first bentonite treatment P_d~0.31MPa; after second kaolin treatment P_d~0.55MPa. The leak-off rate and excess pressure drop decreased after the following treatment as well: 0.11MPa/hr for the first treatment vs. 0.004MPa/hr for the second treatment.

• Shale Specimen #3: before treatment P_{bt}=0.01MPa; after first bentonite treatment P_d~0.50MPa; after second bentonite treatment P_d~0.58MPa.

The water displaced during plug tests is shown in Figure 7.7 (Specimen #2, during ~45hours for the first treatment and ~1200hours for the second treatment). The flow rate is highest during the initial period of CO_2 leakage. Displaced water is transparent, without clays in suspension.

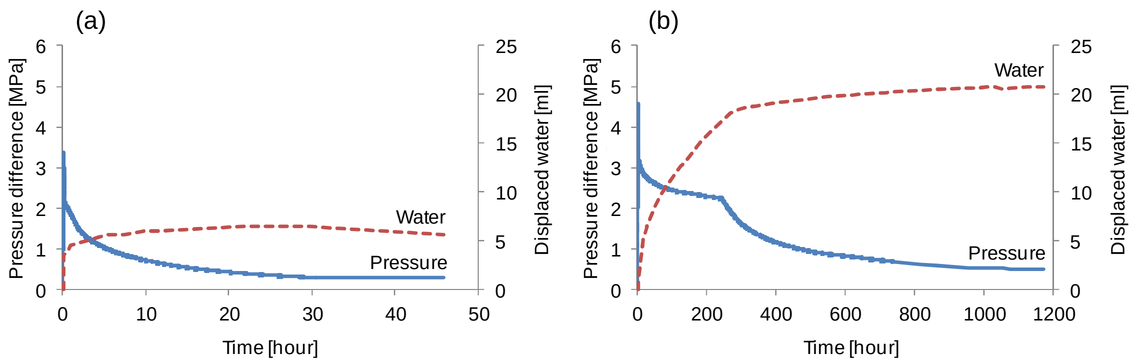

Figure 7.7 Displaced water during plug tests after sealing treatments – Water comes out of the shale specimen as pressurized CO_2 displaces both the suspension outside of the specimen and the water inside of it. Displaced water is transparent: no sub-micron particle in suspension. After the pressure difference between CO_2 and the outlet P_d stabilizes, a small amount of water enters back into the specimen. This observation supports the occurrence of water re-imbibitions as the excess pressure of CO_2 gradually diminishes. (a) first sealing treatment (bentonite slurry) and (b) second sealing treatment (kaolin slurry) for specimen #2..

Forensic analyses. Forensic studies after disassembly were conducted using microscopy and XRD analysis. The microphotograph in Figure 8 shows that hairline cracks filled with sub-micron particles (compare Figures 7.8-a with 7.3-b). Exposed fracture surfaces (forced to open in tension) show clay deposition and the formation of clogging rings (Figure 7.8-b). XRD analysis confirms the presence of bentonite along cracks in bentonite treated specimen #2 (Figure 7.8-c). There is no evidence of new minerals that may have formed during these short-time plug tests (Figure 7.8-c).

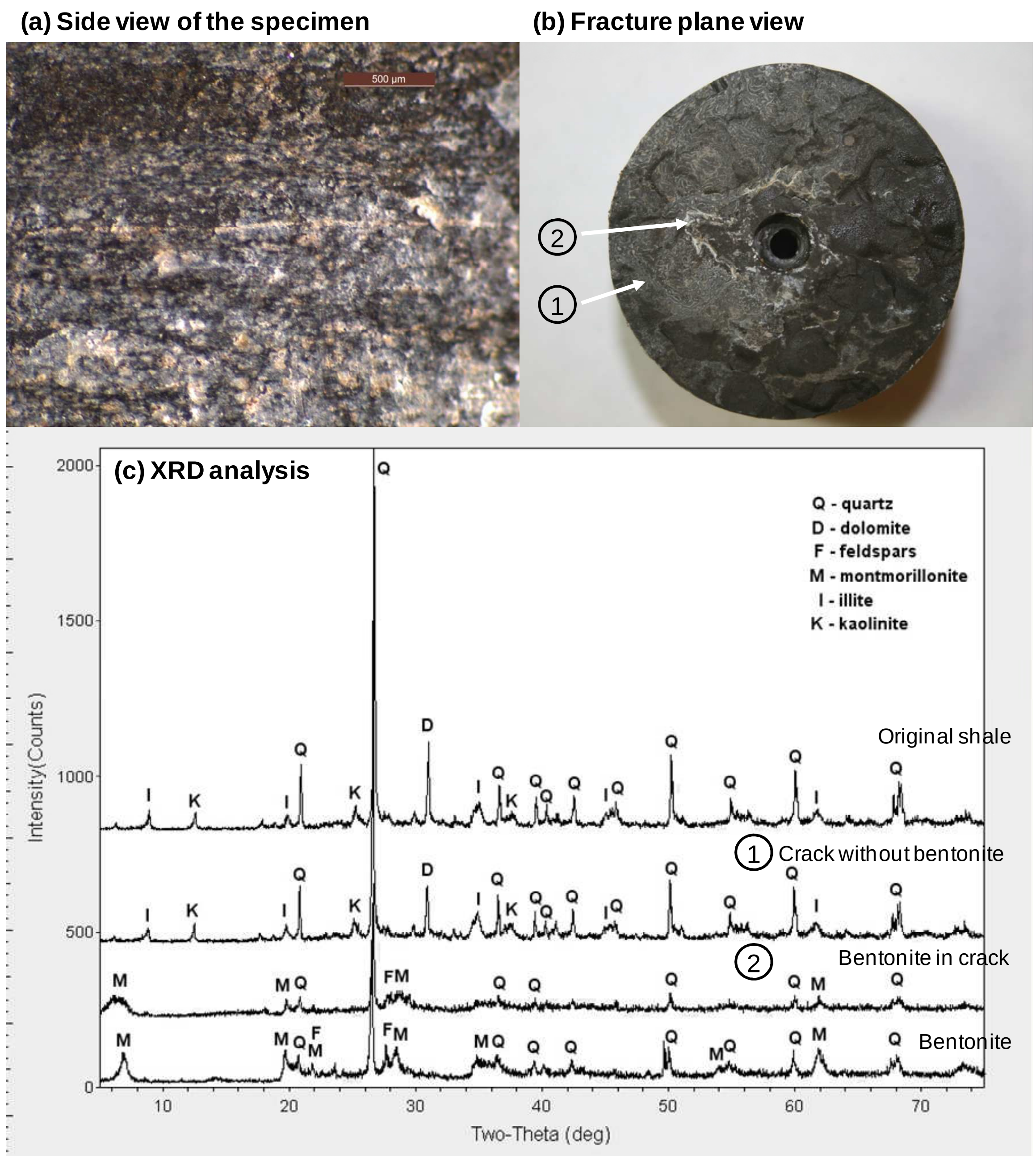

Figure 7.8 Post-test forensic analyses for shale specimens. (a) A microphotograph shows that a crack in the shale specimen is filled with sub-micron clay particles (bentonite) after sealing treatments, (b) sub-micron particles deposited in the gap between cracks after sealing treatments, (c) XRD analysis for original shale specimen and bentonite, and shale and bentonite after the sealing treatments.

Table 7.1 Summary of the CO_2 breakthrough tests and sealing treatments on the shale and cement specimens

Sample No.	P_{bt} [MPa] or P_d [MPa]*	Remarks
Shale #1	0.019	
	1.05*	1st sealing attempt (with bentonite slurry)
	1.25*	2nd sealing attempt (with bentonite slurry)
Shale #2	0.020	
	0.31*	1st sealing attempt (with bentonite slurry)
	0.55*	2nd sealing attempt (with kaolin slurry)
Shale #3	0.010	
	0.50*	1st sealing attempt (with bentonite slurry)
	0.58*	2nd sealing attempt (with bentonite slurry)
Cement #1	6.15*	Shut-off pressure
Cement #2	0.93*	Shut-off pressure
Cement #3	1.85*	Shut-off pressure

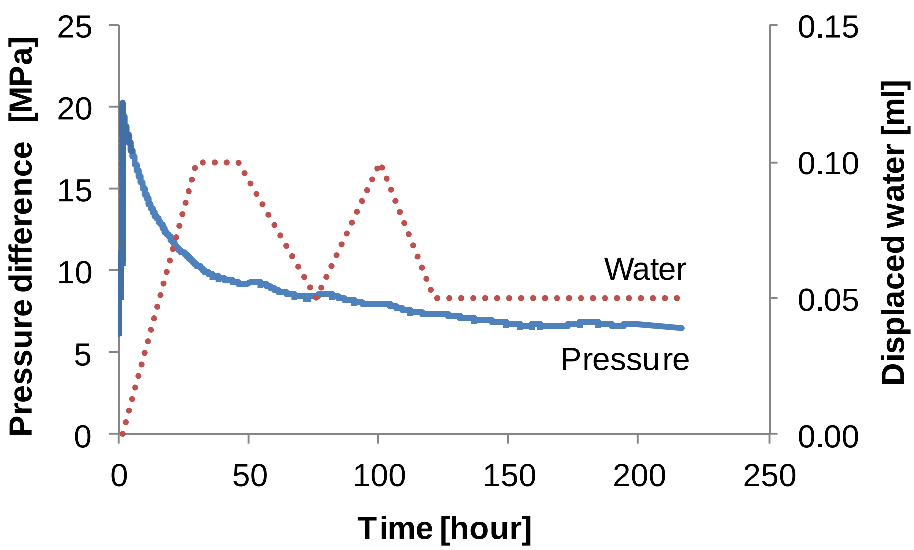

Figure 7.9 Test results for cement specimen #1. CO_2 is pressurized up to 20MPa. The excess pressure of CO_2 gradually decreases, eventually stabilizing around P_d~6.15MPa. During the pressure decline, the amount of displaced water is less than 0.2ml. Therefore, a very small fraction of pore space (~10^{-3}) was used for the CO_2 flow.

7.3.2 Cement Plugs

Three cement specimens were tested to assess their sealing capacity (Table 7.1). The specimens shows no cracks after curing.

Breakthrough pressure. The "cement #1" plug showed no CO_2 leakage at P~5MPa for two months. Then, we increased the pressure to 20MPa and closed the CO_2-inlet valve. The CO_2 pressure gradually dropped and stabilized around P_d~6.15MPa after two weeks. The CO_2 pressure no longer decreased for the next three weeks. This shut-off pressure P_d~6.15MPa yields a characteristic pore radius r_p~11nm (assuming T_s≈35mN/m at P_d~6.15MPa). CO_2 percolated the other two specimens under P~4MPa, and the shut-off pressures were P_d~0.93MPa and P_d~1.85MPa (Table 1); these values correspond to characteristic pore radius r_p~75nm and r_p~38nm, respectively, in agreement with reported mean pore radius for cement pastes r_{mean}=40nm~50nm (Reinhardt and Gaber, 1990; Rimmelé et al., 2008).

Forensic analyses. Microscopy and XRD analyses reveal extensive coloration along the specimen periphery as a result of cement carbonation (orange color in Figure 7.10-a & XRD analysis in Figure 7.10-c). Diffusive transport limits the carbonation front to a certain skin thickness (Kutchko et al., 2007; Rimmelé et al., 2008; Brandvoll et al., 2009). Diffusion of CO_2 to mineral boundaries also resulted in reaction rims around grains (Figure 7.10-b). The reaction rims consist of silica gel $SiO_2{,}nH_2O$ and/or calcium carbonate $CaCO_3$ as a result of reactions from calcium silicate hydrate *C-S-H* and calcium hydroxide $Ca(OH)_2$ with hydrogen ions H^+ and bicarbonate HCO_3^- (Wigand et al., 2009; Duguid et al., 2011; Liteanu and Spiers, 2011).

Discussion. Volumetric shrinkage 3~5% may take place in well cements during curing (Sabins and Rozieres, 1995). If we assume a radial shrinkage strain ε_r=0.01 for an annulus thickness t_a=10mm, the resulting gap is $t_{gap}=t_a \cdot \varepsilon_r$=100μm. This value is much larger than the characteristic pore radius of cements in this study, and the gap becomes the preferential leakage path with a breakthrough pressure $P_{gap}=T_s/t_{gap}$≈1kPa. Indeed, 4~19% of the production wells were reported to experience gas leakage in Canada and North Sea (Nygaard, 2010). Therefore, emphasis should be placed on breakthrough pressure and sealing strategies for probable gaps between the cement and the caprock.

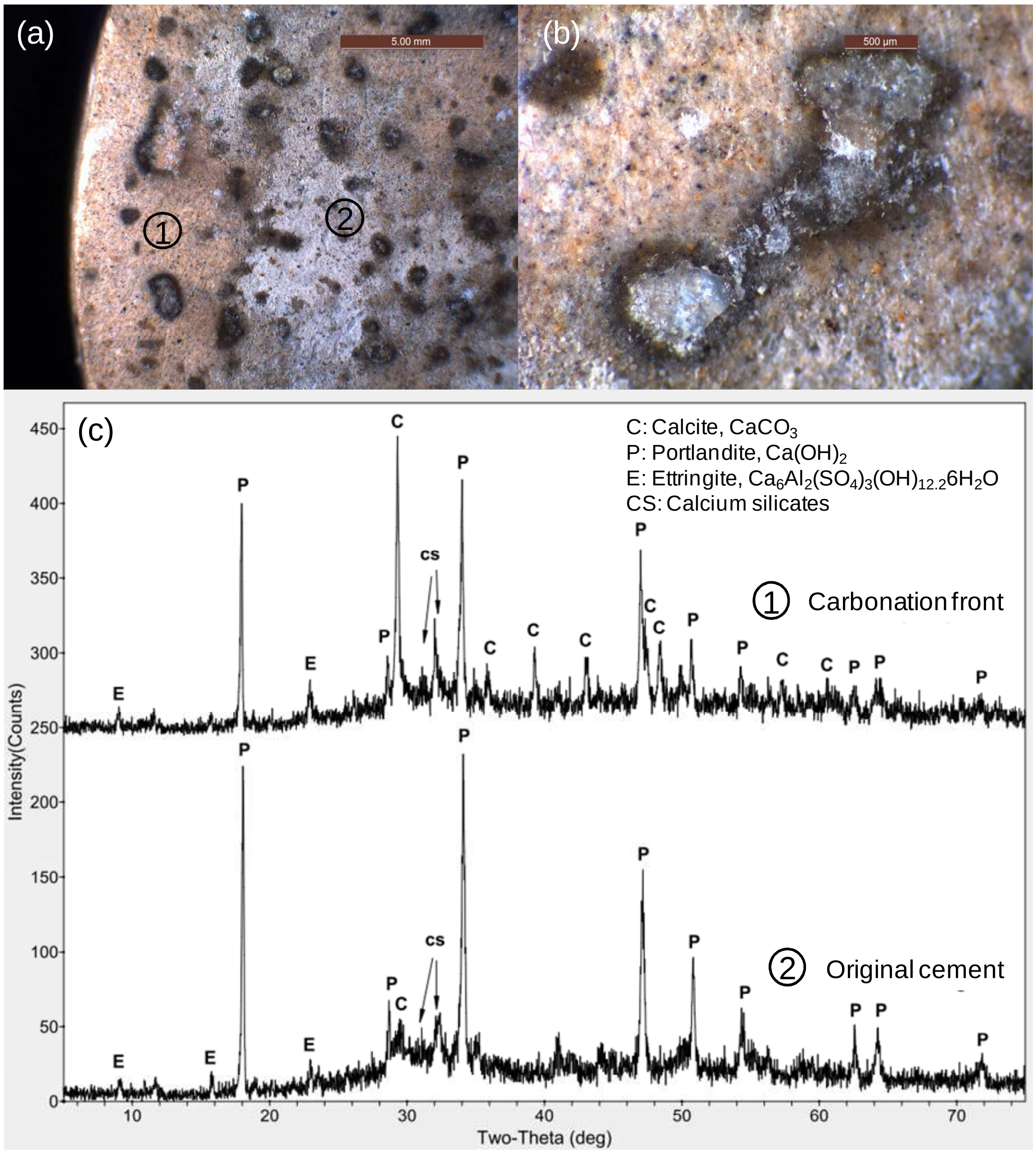

Figure 7.10 Post-test forensic analyses for cement specimens. (a) Carbonation front on the specimen periphery (orange color), (b) reaction rim around a grain, and (c) XRD analysis for the original cement and the reaction front.

7.4 Conclusions

Caprock and well-cement must confine the CO_2 injected in storage reservoir. We investigated the CO_2-breakthrough pressure for shale caprocks and cement specimens, and explored a viable sealing strategy to correct CO_2 leakage. Salient observations follow:

• While pores in shale are in the nm-scale and can sustain MPa-scale capillary pressures, orders of magnitude lower breakthrough pressures are measured when discontinuities are aligned with the pressure gradient. We anticipate that this conclusion applies to fractures parallel to the bedding planes, transverse tensile fractures due to unsupported span (Chapter 3), or shear fractures in compression (Chapter 3).

• Sub-micron clay particles can be injected to fill cracks. Sealing treatments cause a marked increase in shut-off pressure. The permeability to CO_2 decreased as the specimen experienced successive sealing treatments.

• Intact cement plugs can generate a shut-off pressure as high as P_d~6MPa. Extensive carbonation with orange color and reaction rims around grains were observed on the plug surface.

• The cement-rock gap that results from cement contraction is the preferential flow path.

CHAPTER 8

ENGINEERED CO_2 INJECTION FOR GEOLOGICAL STORAGE

8.1 Introduction

Fossil fuels account for ~85% of all energy consumption and result in 30Gton of CO_2 emissions per year worldwide (Tsouris et al., 2010). Our dependency on fossil fuels will continue for the coming decades, until alternative energy sources can satisfy both current and anticipated demands (EIA, 2010; Pasten and Santamarina, 2012). In the meantime, carbon capture and storage allows for a more sustainable use of fossil fuels (Baines and Worden, 2004; Dooley et al., 2006).

Geological formations that are candidates for CO_2 geological storage include depleted hydrocarbon reservoirs, oil reservoirs (as part of enhanced oil recovery), unminable coal seams, salt caverns, and deep saline aquifers (IPCC, 2005). The use of depleted hydrocarbon reservoirs and salt caverns for CO_2 storage competes with natural gas storage, and does not necessarily match the geographic distribution of CO_2 sources (EIA, 2004; Pusch et al., 2010). Deep saline aquifers are most promising because of their large storage capacities (~10^3 and 10^4 $GtCO_2$), their ubiquitous presence in the USA, and their advantageous proximity to stationary CO_2 emission sources (such as coal power plants-IPCC, 2005).

The CO_2 storage capacity G_{CO2} [Gton] is a function of the storage reservoir's areal extent A_t [km^2], the mean storage thickness h_g [m]$<H_R$ (where H_R [m] is the thickness of the reservoir layer; Chapter 3), porosity φ [-], CO_2 density ρ_{CO2} [kg/m^3], and a storage efficiency factor E [-] (NETL, 2010): $G_{CO2}=A_t \cdot h_g \cdot \varphi \cdot \rho_{CO2} \cdot E$. Typically, the storage efficiency factor is low and ranges between E=0.005 and 0.055 (NETL, 2010; Okwen et al., 2010), and formation porosities range between φ=0.1 and 0.3 (IPCC, 2005; Bachu

and Bennion, 2008). Let's consider that the worldwide mass of CO_2 emissions over the next 50 years G_{CO2}=730 $GtCO_2$ (Chapter 2) will be injected under supercritical conditions (density ρ_{CO2}=600kg/m^3) with a storage thickness h_g=10m with porosity φ=0.2. Assuming the maximum storage efficiency factor E=0.055 results in a ~1,000,000 km^2 storage area, similar to the area of Texas, USA or France. Large areal extent increases the probability of unexpected phenomena such as leaks along intersecting faults, hydro-chemo-mechanical effects, fault erosion and reactivation, and induced seismicity, among others. Therefore, the goal of this study is to identify viable CO_2-injection strategies to optimize the efficiency of CO_2 storage in the pore space of deep saline reservoirs. This will minimize residual brine saturation, salt precipitation and injection difficulties, water acidification and mineral dissolution, as well as the possibility of piping, internal shear, and differential settlement. Engineered injection will also hinder long-term convective flow, and further enhance the long-term geological storativity of CO_2.

8.2 Underlying Concepts

Let's start with the identification of processes that may affect CO_2 storage projects (refer to Chapter 2 and subsequent Chapters).

8.2.1 Coupled Processes

Viscous fingering. The viscosity of supercritical CO_2 at reservoir conditions is more than ten times lower than that of water or brine (Fenghour et al., 1998), and results in unstable injection fronts and the formation of viscous fingers (Chapter 2). Viscous fingering yields high residual water saturation, a large water-CO_2 interface, poor sweep efficiency ($E\leq$0.055), and large reservoir volumes. Consequently, monitoring strategies must cover large areas, compensation must include additional property owners (Gresham et al., 2010), and the probability of encountering potential leakage paths increases.

Acidification and mineral dissolution. Injected CO_2 dissolves into brine and decreases pH. In turn, acidified water prompts mineral dissolution (Kharaka et al., 2006). Extensive experimental evidence, discrete element simulations, and network model simulations show that mineral dissolution can cause: 1) a pronounced decrease in lateral stresses, so that the sediment reaches failure under zero lateral strain and extensive shear planes develop (Shin and Santamarina, 2009), 2) localized reactive fluid transport and internal piping (Fredd and Fogler, 1998), 3) skin erosion below the caprock (Chapter 6), and 4) differential settlement of the cap rock that may lead to bending failures and open mode discontinuities (Chapter 3). Shear, tensile, and piping discontinuities will facilitate CO_2 leakage.

Fluid convection. The dissolution of CO_2 and minerals in water increases the water density, and induces convective fluid circulation that sustains persistent coupled hydro-chemo-mechanical phenomena (Chapter 3; Pruess and Zhang, 2008).

Injectivity. As water in the residual brine diffuses into supercritical CO_2, excess salts precipitate (e.g., calcite, halite, and anhydrate), the formation conductivity decreases, and injectivity is compromised (Zone IV – Chapter 3; André et al., 2007).

8.2.2 Governing Ratios

The mobility number M is the ratio of the viscosity of CO_2 μ_{CO2} to that of water μ_w:

$$M = \frac{\mu_{CO2}}{\mu_w} \tag{1}$$

Supercritical CO_2 storage yields a mobility number $10^{-1}<M<10^{-2}$ (Adams and Bachu, 2002), where viscous fingering may prevail (Lenormand et al., 1988). The capillary number C defines the ratio between viscous and capillary forces:

$$C = \frac{q\mu_{CO2}}{T_s \cos\theta} \tag{2}$$

where q is flow rate [m^3/s/m^2], T_s [N/m] interfacial tension, and θ [deg] contact angle (Lenormand et al., 1988). The bond number B is the ratio of gravity-driven CO_2 migration $(\rho_w-\rho_{CO2})gkk_{rCO2}$ to capillary force $T_s cos\theta$, where ρ_i [kg/m^3] is the density of each phase, k [m^2] is permeability, and k_{rCO2} [-] is relative permeability of CO_2 (Pennell et al., 1996):

$$B = \frac{(\rho_w - \rho_{CO2})gkk_{rCO2}}{T_s \cos\theta} \tag{3}$$

Low bond number B and high capillary number C leads to high CO_2 storage capacity (Kopp et al., 2009).

8.2.3 Concepts relevant to Engineered CO_2 Injection

Following the previous analysis, we seek to engineer the injection of CO_2 to prevent viscous fingering and to improve sweep efficiency. Engineered CO_2 injection can be based on the following strategies, used individually or in combination.

Increased CO_2 viscosity. Higher CO_2 viscosity is needed to promote a more homogeneous displacement pattern. Previous CO_2 viscosity control studies have been targeted at CO_2-enhanced oil recovery, and considered (1) emulsification/foams using surfactants (Kam and Rossen, 2003; Kovscek and Bertin, 2003; Levitt et al., 2009) and (2) thickening agents such as polymers (Huh and Rossen, 2008; Alvarado and Manrique, 2010; Enick et al., 2010). These efforts were reported to increase the ratio of oil recovery up to 80% (Lake and Venuto, 1990; Levitt et al., 2009).

Sequential fluid injection. Viscous fingering can be minimized and CO_2 displacement enhanced by the intermediate injection of fluid with density, viscosity, and wetting properties that are between the properties of brine and CO_2 (Alvarado and Manrique, 2010). Furthermore, the intermediate fluid could be miscible in both brine and CO_2. For example, acetone could act as intermediate fluid (viscosity≈0.3mPa·s at T=30°C and P=0.1MPa, density≈780kg/m^3 (at T=35°C and P=0.1MPa - Kinart et al., 2002), and it is miscible with water and CO_2 (Tanaka et al., 1987; Pečar and Doleček, 2005; Liu and Kiran, 2007)). A properly selected/engineered intermediate fluid injected prior to or simultaneously with CO_2 will alter the fluid displacement topology and improve storage efficiency. For example, the intermediate injection of water enhances oil recovery by 50% (Lake and Venuto, 1990).

Bio-clogging. Microbial activity can be stimulated in water-filled flow paths (Bryant and Britton, 2008) as long as pore exceeds a d_{pore}~1μm size (Rebata-Landa and Santamarina, 2006). Bio-clogging will cause flow to divert to low-permeability channels. Compiled results suggest that bio-clogging will be most effective in sediments with permeability 10md≤k≤10Darcy (Rebata-Landa and Santamarina, 2012).

Decreased interfacial tension. The CO_2-H_2O interfacial tension T_s impedes CO_2 invasion into small pores, and contributes to residual water saturation (Suekane et al., 2005; Chalbaud et al., 2009). The CO_2-H_2O interfacial tension can be modified with surfactants such as pluronic block copolymers, PDMS-g-PEO-PPO copolymers, PEPE, PFPE, Ethoxylated acetylenic surfactants, and methylated branched hydrocarbon surfactants (da Rocha et al., 1999; Ryoo et al., 2003; Stone et al., 2004; Dickson et al., 2005). The interface can be altered by actively imposing electromagnetic fields as well (Francisca et al., 2008). The use of surfactants is explored next.

8.3 This Study: Interfacial Tension Control

Let's explore the conditions for interfacial tension control and implications. First, we measure water-CO_2 interfacial tension with and without surfactants. Then we conduct fluid displacement experiments within a porous micro-model. Finally, we complement and extend experimental results using numerical network model simulations.

8.3.1 Surface Tension Control

Surfactant. The surfactant selected for this study is SURFONIC POA-25R2 (HUNTSMAN), which is a reversed block copolymer composed of hydrophilic polyoxyethylene and CO_2-philic polyoxypropylene (Figure 8.2). The selected surfactant was reported to lower CO_2-water interfacial tension at a ~0.1% volumetric concentration of surfactant, temperature T=45°C, and pressure P=27MPa (da Rocha et al., 1999). This surfactant is a water soluble, nonionic surface active agent, and has hydrophilic/lipophilic balance HLB=6.3. The nonionic surfactant molecules diffuse in water, adsorb at interface, and change the local electric field as they partition between two phases (De Gennes et al., 2004). The anticipated variation of surface tension σ as a function of surfactant concentration C_s [mol/m^3] and surface excess concentration Γ [mol/m^2] is captured in Gibbs adsorption equation (Dickson et al., 2005):

$$\frac{d\sigma}{d\log C_s} = -\Gamma RT \tag{4}$$

Test procedure – Interfacial tension measurement. We use the device described in Espinoza and Santamarina (2011) to investigate the change in CO_2-water interfacial tension as a function of pressure, with and without the surfactant. The high-pressure chamber is first subjected to three cycles of vacuum and CO_2 flushing (99.99% purity) to remove air. Then water or water mixed with surfactant is injected using a high-pressure syringe to form a droplet that hangs at the tip of a stainless steel needle at a CO_2 pressure P≈0.1MPa. The system is pressurized with CO_2 in steps, from the initial 0.1MPa pressure to 10MPa. We use a high-resolution camera to capture the shape of the pendent drop through a sapphire window (Figure 8.1-a). Recorded images are analyzed using Laplace's equation in parametric form to determine interfacial tension T_s (Rotenberg et al., 1983):

$$T_s\left(\frac{d\phi}{ds} + \frac{\sin\phi}{x}\right) = \frac{2T_s}{R_0} + \Delta\rho g z \tag{5}$$

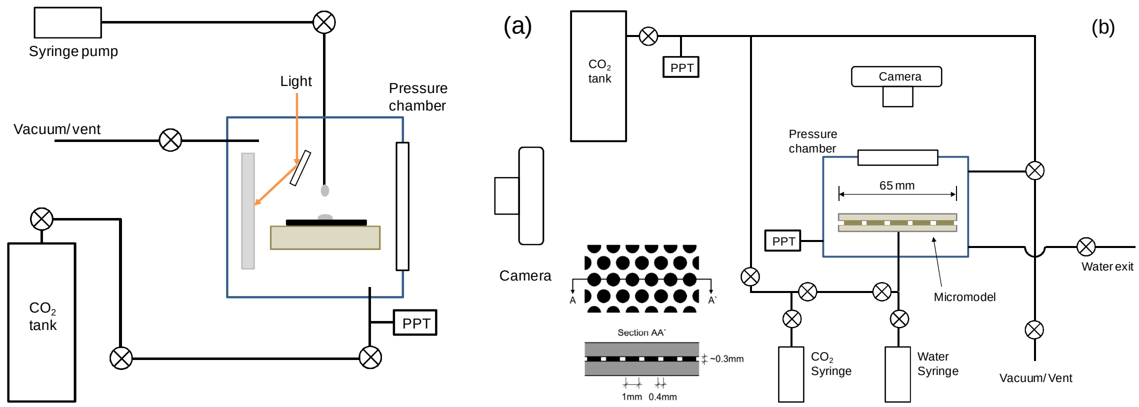

Figure 8.1 Experimental devices. (a) Measurement of interfacial tension T_s and (b) CO_2 injection test using a micro-model.

where R_0 denotes the curvature at the droplet apex, and $\Delta\rho$ density difference between droplet and surrounding fluid (Figure 8.3-a). The density difference $\Delta\rho$ between CO_2 and water is computed using expressions in Duan and Sun (2003). The inverted interfacial tension T_s is the value that minimizes the square error between the theoretical droplet shape and the experimentally captured image. The error surface is a function of the two unknowns, interfacial tension T_s and maximum curvature R_0; it is convex as shown in Figure 8.4. Figure 8.4 also shows the sensitivity in the determination of the interfacial tension T_s ±0.2mN/m.

Results. The effect of surfactant is readily seen in the shape of the pendent drop (Figure 8.5-a). The interfacial tension of CO_2-water-surfactant decreases from ~50mN/m (at 0.1MPa) to ~4mN/m along the liquid-gas boundary (Figure 8.5-b). The trend parallels the interfacial tension for CO_2-water but is lower by an almost constant shift of 25~35mN/m.

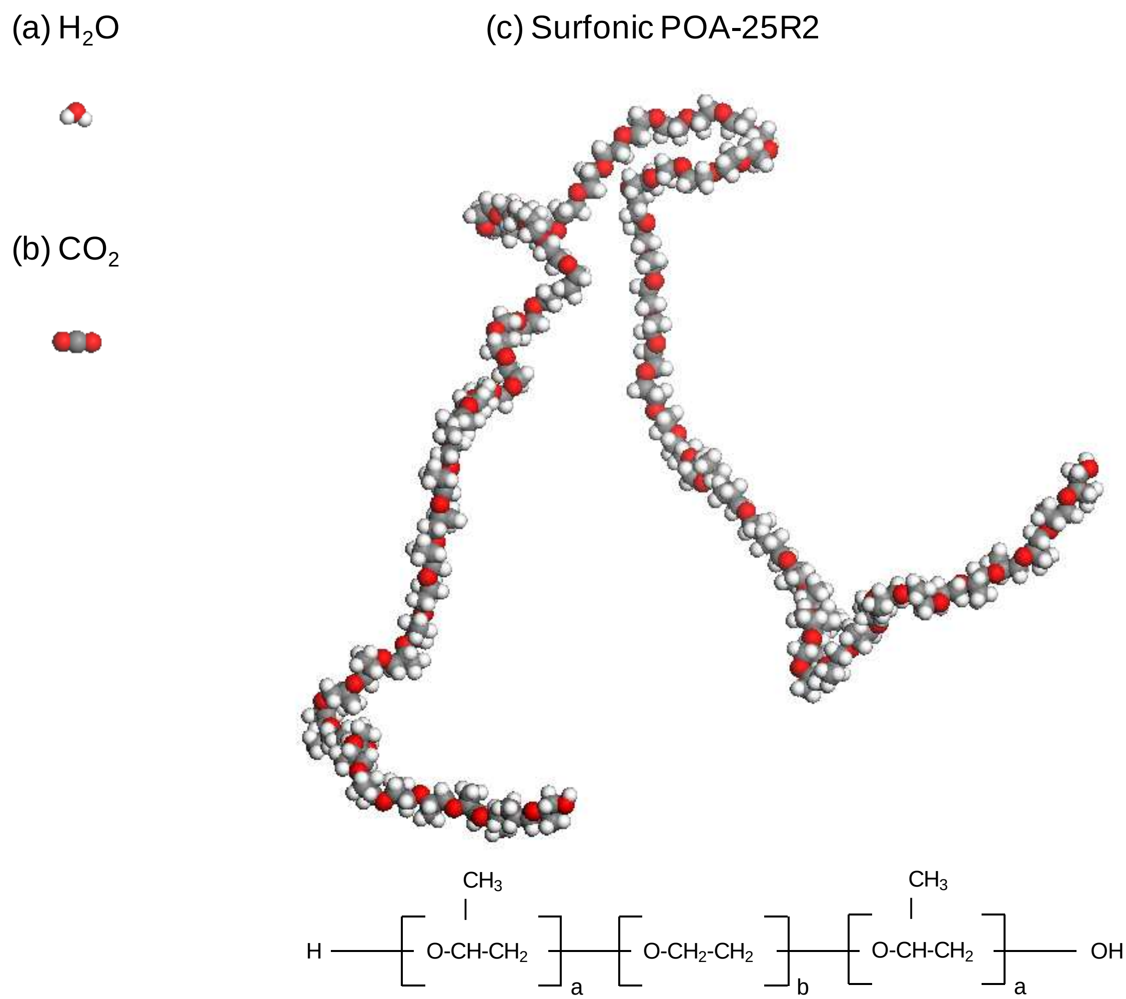

Figure 8.2 Molecular structure of: (a) H_2O, (b) CO_2, and (c) selected surfactant that consists of central hydrophilic chain of polyoxyethylene and two flanked hydrophobic chains of polyoxypropylene (Surfonic POA-25R2, a=22, b=38; molecular structure is inspired from: Prasad et al., 1979, Kozlov et al., 2000; visualization of molecular structure is in courtesy of Zhao, Q.).

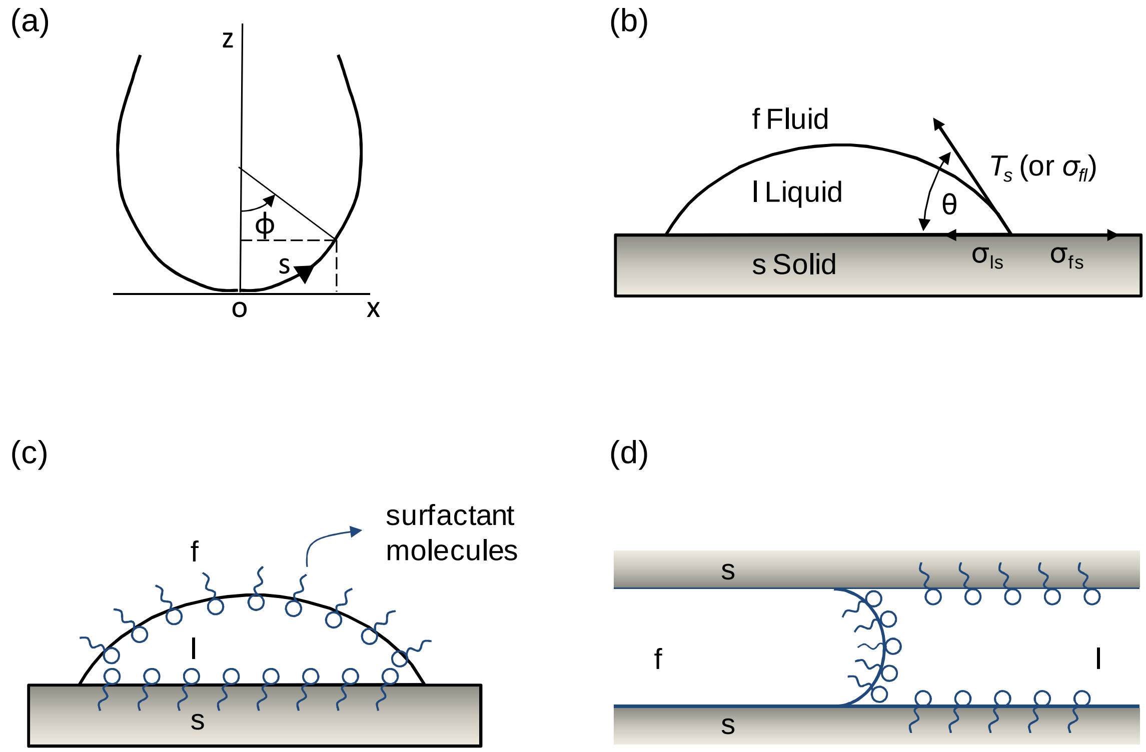

Figure 8.3 Surface tension, contact angle, and surfactant. (a) Definition of the coordinate system for a pendant drop (from Rotenberg et al., 1983), (b) equilibrium state. Components: surrounding fluid *f*, liquid droplet *l*, and solid substrate *s*, (c) distribution of surfactant molecules in the system of partially wetting droplet, and (d) distribution of surfactant molecules in the tube that is partially filled with liquid (water) and fluid (CO_2).

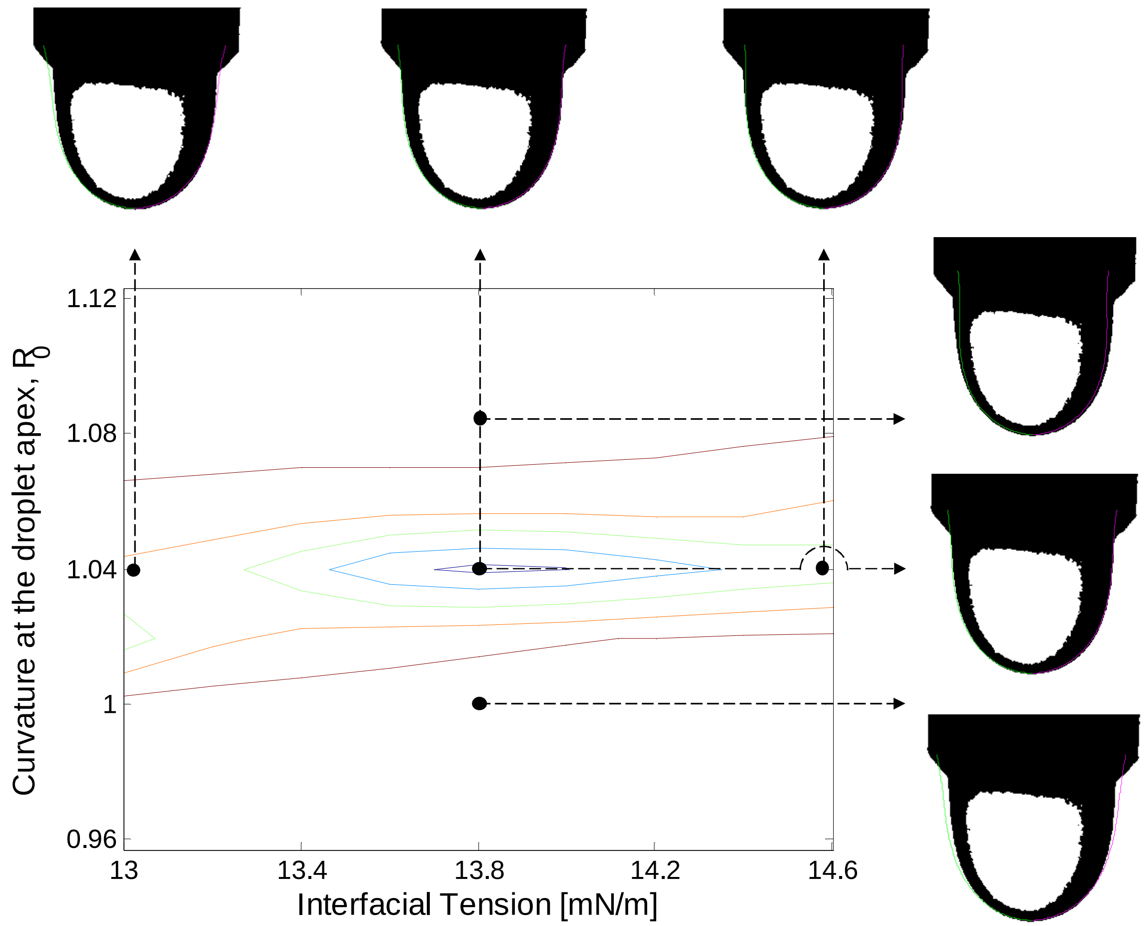

Figure 8.4 Sensitivity analysis. Error surfaces as a function of interfacial tension T_s and the curvature radius at the apex of a pendent drop R_0. Images show both the theoretical shape of a pendent drop that corresponds to conditions in the graph and the shape of an actual pendent drop that was obtained from a test (Pressure P=5.4MPa, temperature T=25°C, density of water ρ_{water}≈998.4kg/m^3, and density of CO_2 ρ_{CO2}≈154.6kg/m^3; the density of CO_2 is calculated based on formulae that is proposed by Duan and Sun, 2003).

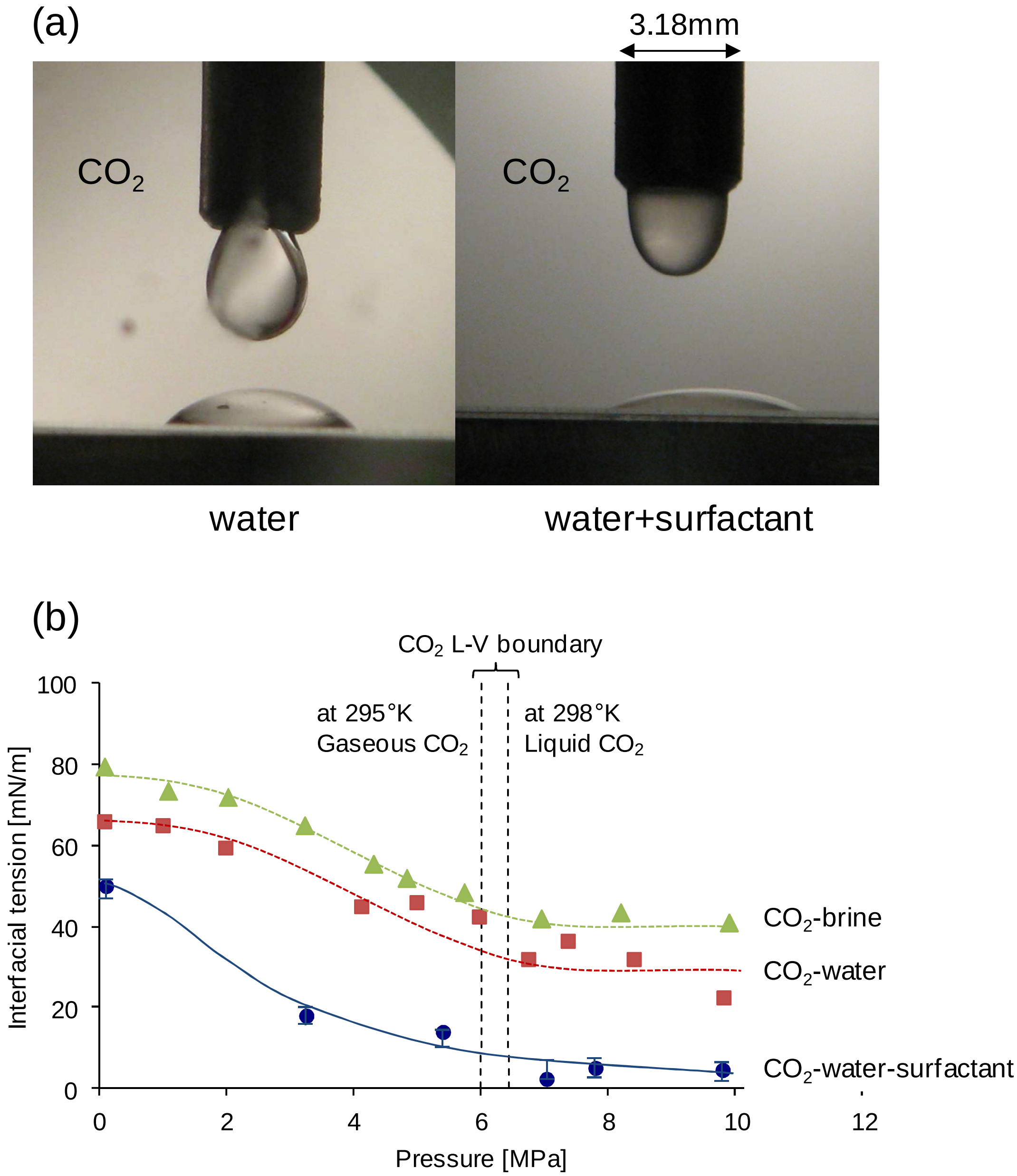

Figure 8.5 The effect of surfactant and pressure on interfacial tension T_s. (a) Images: sessile and pendent droplets of water (Left, P=5.79MPa, and T=24.5°C) and water+surfactant (POA-25R2; wt=0.4%; Right, P=5.4MPa, and T=25°C). Note: The substrate is quartz (SiO_2). (b) Fluid pressure effect on interfacial tension: triangle=brine, square=water (from Espinoza and Santamarina, 2010), and circle=water+surfactant; POA-25R2, wt=0.4%).

8.3.2 Water Displacement by CO_2 Injection in a Pore Micro-model

Test procedure. We conducted water displacement studies by injecting CO_2 into a pore micro-model saturated with water with and without surfactant. The original device described in Jang (2011) was modified for this study to allow for separate water and CO_2 injections (Figure 8.1-b). The micro-model was prepared through photo-fabrication and glass etching processes to create a regular pattern of 0.3mm high cylindrical glass pillars and a porous network with 0.4mm pore size; a flat glass plate is glued above. The micro-model rests inside the high-pressure chamber. First, all air is evacuated by three cycles of vacuum followed by CO_2 flushing (99.99% purity). Then, we fill the micro-model with water (or water with surfactant) while the chamber is under vacuum. While we pressurize the chamber with CO_2, CO_2 bubbles trapped inside the micro-model dissolve in the water. At the target fluid pressure, we inject water (or water with surfactant) again into the micro-model using a high-pressure syringe to attain almost full water saturation in the micro-model. Finally, we inject CO_2 through the center of the micro-model. A high resolution camera is used to capture invasion patterns.

Results. Figure 8.6-a shows images captured at four different conditions: 1) Gaseous CO_2 displaced water at ~0.1MPa, 2) gaseous CO_2 displaced water in the presence of surfactant at ~0.1MPa, 3) liquid CO_2 displaced water at ~7MPa, and 4) liquid CO_2 displaced water in the presence of surfactant at ~7MPa. Menisci at CO_2-water interfaces within the micro-model confirm that interfacial tension T_s decreases as fluid pressure increases and in the presence of the surfactant: the interface curvature between CO_2 and water becomes flatter as the test condition varies from 1 to 4 (Figure 8.6-a), in agreement with the decrease in interfacial tension reported in Figure 8.5.

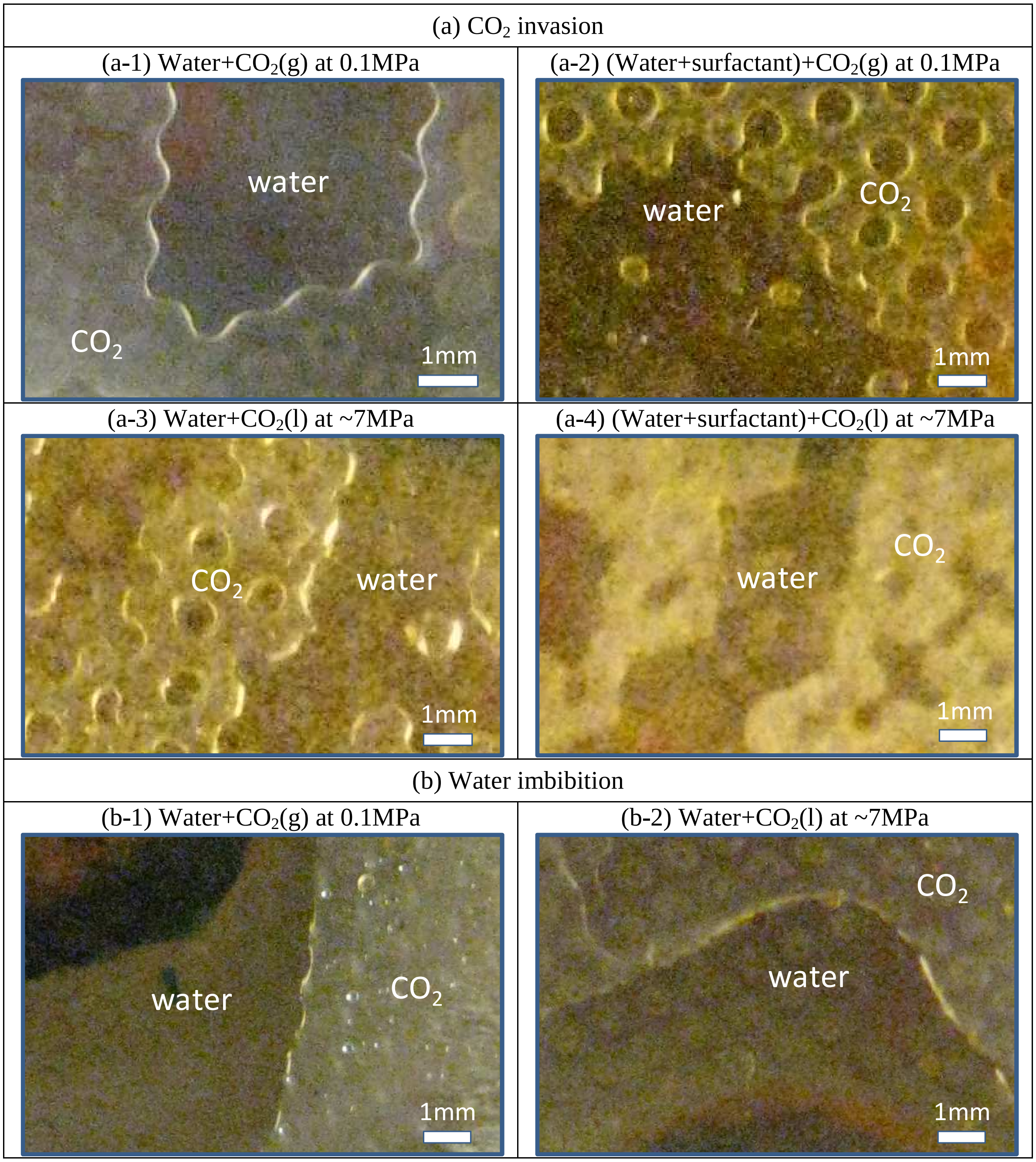

Figure 8.6 The interface of a CO_2-water system in the micro-model. (a) CO_2 injection: (a-1) log$M$≈-2.0, log$C$≈-6.2, (a-2) log$M$≈-1.3, log$C$≈-5.3, (a-3) log$M$≈-1.1, log$C$≈-4.9, and (a-4) log$M$≈-0.4, log$C$≈-3.4 (T=~25°C for all conditions, $M=\mu_{CO2}/\mu_w$, and $C=q\mu_{CO2}/(T_s cos\theta)$; variation of contact angle was disregarded in estimating the capillary number C, $cos\theta$=1) and (b) water imbibition.

The sweep efficiency E in this 2-D model can be estimated as the ratio of area occupied by CO_2 to the area of the entire micro-model. At a low pressure (~0.1MPa), gaseous CO_2 (T_s~70mN/m) fingers through the micro-model displacing water in a very small area with a measured E<0.1. The other extreme corresponds to water with surfactant and at high pressure (T_s~5mN/m), and shows that liquid CO_2 displaces water evenly until it eventually breaks through the model perimeter resulting in a sweep efficiency that surpasses E>40%. Figure 8.7 summarizes sweep efficiencies as a function of interfacial tension T_s.

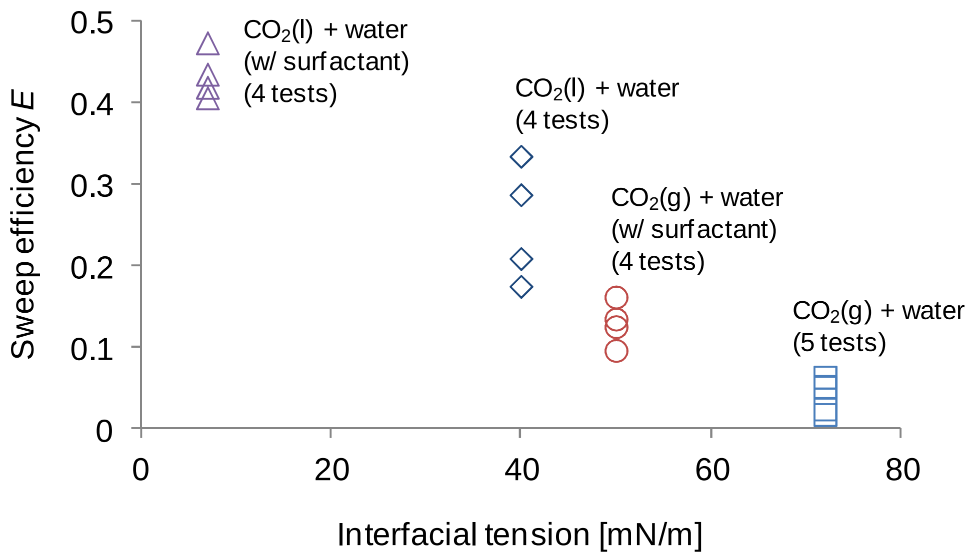

Figure 8.7 Comparison of the sweep efficiency E with respect to interfacial tension T_s. Note: as interfacial tension T_s decreases, capillary number $C=q\mu_{CO2}/(T_s cos\theta)$ increases from log$C$≈-6.2 to -5.3, -4.9, and -3.4 (variation of contact angle was disregarded in this analysis, $cos\theta$=1).

8.3.3 Numerical Study – Network Model

We run network model simulations to further investigate the effect of interfacial tension on CO_2 displacement patterns and sweep efficiency trends. The network simulation algorithm was developed for the case of immiscible drainage where a non-wetting fluid is injected into a medium saturated with a wetting fluid (Lenormand et al., 1988; Aker et al., 1998; Ferer et al., 2003).

Network construction. The 2-D square network model consists of tubes that intersect at nodes. Tube diameters d are log-normally distributed with mean value $\overline{d_0}$=20μm and coefficient of variation COV=0.4. All tubes have identical length L_{ch}=200μm. The limitation in network size 10x10 is partially overcome by assuming periodic conditions for the longitudinal boundaries. The network is filled with water at the beginning of the simulation.

Initial condition. A pressure difference between the inlet and the outlet ΔP_{tot} [Pa] is imposed to compute initial nodal pressures in the network and the water saturated total flow rate q_{tot}. Nodal fluid pressures are computed by writing the continuity equation at all nodes and solving the system of equations (details in Jang et al., 2011):

$$q_a + q_b + q_l + q_r = 0 \tag{6}$$

where q_a denotes flow rate to center from above, q_b flow rate to center from below, q_l flow rate from left to center, and q_r flow rate from right to center. The pressure difference ΔP between two adjacent nodes is then used to compute the initial flow velocity v_0 [m/s] and flow rate q_0 [m^3/s] for each tube using Poiseuille's law as a function of the tube diameter d [m], length L_{ch} [m], and the fluid viscosity μ [Pa·s]:

$$\text{Initial velocity: } v_0 = \frac{\Delta P d^2}{32\mu L_{ch}} \tag{7}$$

$$\text{Initial flow rate: } q_0 = \alpha_w \cdot \Delta P \text{ ; initial conductance } \alpha_w = \frac{\pi d^4}{128\mu L_{ch}} \tag{8}$$

where α_w denotes the initial conductance of a tube that is filled with water. The water saturated flow rate q_{tot} is obtained by summing all flow rates for tubes in the first layer.

CO_2 invasion. The non-wetting CO_2 is injected at the inlet with the same constant flow rate q_{tot} computed for the water saturated network (under the imposed ΔP_{tot}). We assume that both water and CO_2 are incompressible.

The non-wetting CO_2 invades a tube only if the pressure difference between the two fluids P_{CO2}-P_w exceeds the tube's capillary pressure $P_c=4\cdot T_s\cdot cos\theta/d$. As the non-wetting CO_2 displaces the wetting water, the pressure drops along the tube due to both viscous loss (Lenormand et al., 1988) and capillary pressure (Aker et al., 1998). The flow rate q through the tube is computed based on Poiseuille's law and the total pressure drop across the tube, from node *i-1* to node *i*:

$$q = \alpha_{eff}\left(P_{CO2}^{i-1} - P_w^i - P_c\right)\Big|_+ \text{; effective conductance } \alpha_{eff} = \frac{\pi d^4}{128\mu_{eff} L_{ch}} \tag{9}$$

where μ_{eff} denotes the effective viscosity, which is the average of the two viscosities weighted with the length fraction of each fluid in the tube (Lenormand et al., 1988). The positive sign in Equation 9 denotes a positive value, in other words, the flow rate is q=0 if the pressure difference between the two fluids P_{CO2}^{i-1}-P_w^{i} is smaller than the tube's capillary pressure $P_{CO2}^{i-1}-P_w^{i}<P_c$.

Nodal pressure. The pressure field in the network model is updated based on mass conservation, i.e., continuity: the pressure P_{center} at a central node *center* in the 2-D porous network is obtained by complying the mass conservation from all adjacent tubes (Ferer et al., 2003):

$$\begin{aligned}\left(\alpha_{eff}^a + \alpha_{eff}^b + \alpha_{eff}^l + \alpha_{eff}^r\right)P_{center} &= \left(\alpha_{eff}^a P_a + \alpha_{eff}^b P_b + \alpha_{eff}^l P_l + \alpha_{eff}^r P_r\right) \\ &\quad + \left(f^a \alpha_{eff}^a P_c^a + f^b \alpha_{eff}^b P_c^b + f^l \alpha_{eff}^l P_c^l + f^r \alpha_{eff}^r P_c^r\right)\end{aligned} \tag{10}$$

where P_a denotes pressure at a node above, P_b pressure at a node below, P_l pressure at a left node, and P_r pressure at a right node. Superscripts for the effective viscosity α_{eff} and factor f represent tubes connected to the central node: a for a tube above, b for a tube below, l for a left tube, and r for a right tube. The factor f is zero f=0 if no meniscus exists in a tube and one f=1 if meniscus exists in the tube. The system of equation is iteratively resolved simultaneously updating the position of menisci within tubes until equilibrium is reached.

Invasion. The evolution of invasion uses a hybrid algorithm to avoid numerical instability. First, a flow-controlled condition is computed where fluids advance in each tube for a pre-selected time interval Δt and at a velocity that is computed with the known nodal pressures. The time interval Δt is determined so that maximum advance of any meniscus is less than 10% of the tube length $\Delta t \leq 0.1 L_{ch}/v_{max}$. Second, equilibrium is re-established by re-computing nodal pressures while enforcing equal nodal pressures at the inlet and at outlet nodes. We repeat each Δt-cycle until CO_2 reaches outlet nodes (details in Ferer et al., 2003).

Results. We varied the capillary factor $T_s cos\theta$=35mN/m (liquid CO_2-water condition) to $T_s cos\theta$=5mN/m and 1mN/m (liquid CO_2 and water with surfactant) to compare the effect of capillarity $T_s cos\theta$ on sweep efficiency E. As capillarity decreases, viscous drag prevails over capillarity, CO_2 invades more evenly and the sweep efficiency E increases (Figure 8.8). The pattern of CO_2 invasion exhibits a transition from localized displacement or fingering along large tubes to a more homogeneous pattern of stable displacement when the capillarity approaches $T_s cos\theta$~5mN/m.

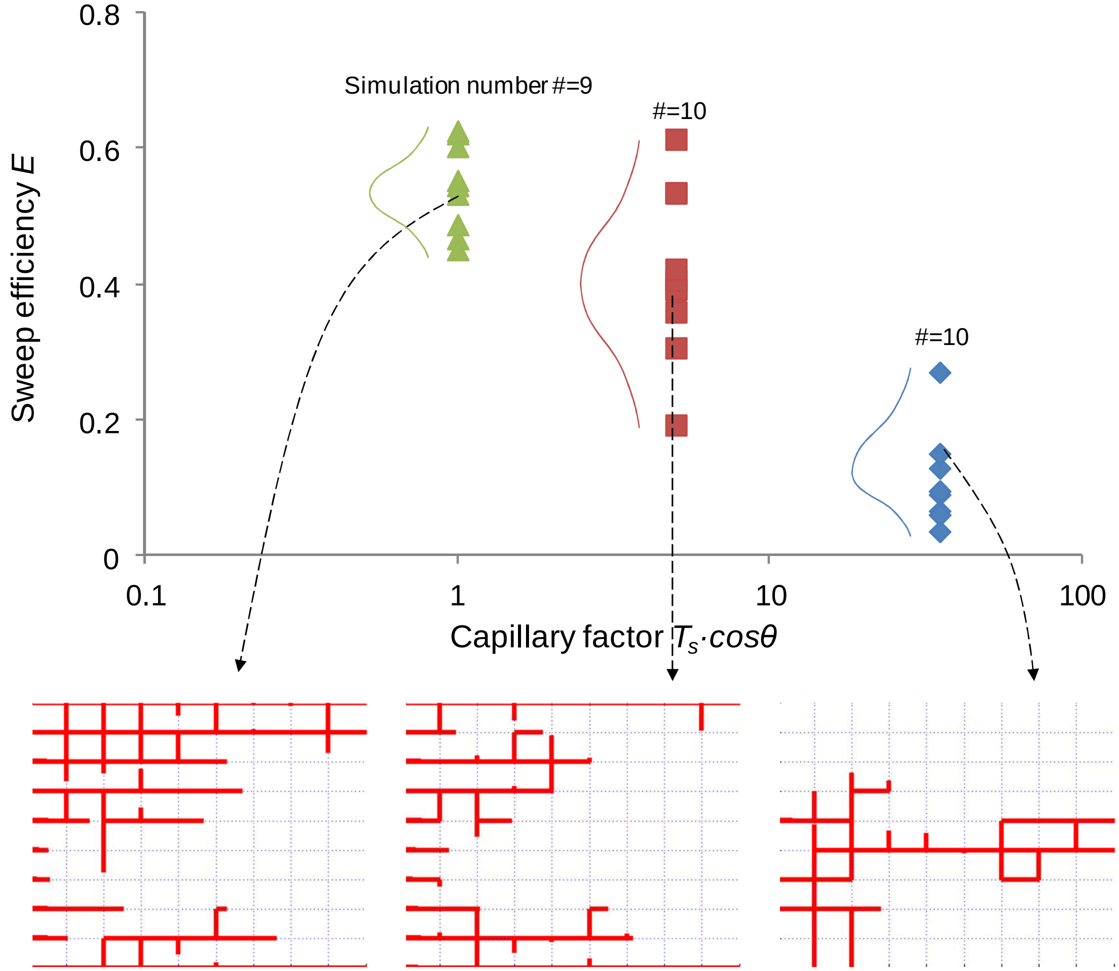

Figure 8.8 Network simulations. CO_2 invasion pattern and its sweep efficiency with different capillary factor $T_s \cdot cos\theta$ (Note: 10x10 pore network model, the average diameter of tubes d_0=20µm, the length of each tube L_{ch}=200µm, the coefficient of variation of tube diameters COV=0.4, the viscosity of water $\mu_w=10^{-3}$Pa·s, the viscosity of CO_2 $\mu_{CO2}=5*10^{-4}$Pa·s, the density of water ρ_w=1000kg/m^3, initial pressure difference between the inlet and the outlet ΔP_{tot}=70kPa, and constant flow rate q_0=0.5m^3/s/m^2).

8.4 Discussion

Surfactant, pressure, and interfacial tension. The interfacial tension between CO_2 and water decreases from ~70mN/m to 25mN/m as the fluid pressure increases, and reaches a constant value ~30mN/m beyond the CO_2 gas-liquid boundary (studies at 278K-to-373K and up to ~70MPa can be found in: Massoudi and King, 1975; Chun and Wilkinson, 1995; Dickson et al., 2006; Kvamme et al., 2007; Sutjiadi-Sia et al., 2007; Espinoza and Santamarina, 2010). As pressure increases, the CO_2 densifies as well as the concentration of dissolved CO_2 near the CO_2-water interface increases, and the interfacial tension decreases (Massoudi and King, 1975; Chun and Wilkinson, 1995; Espinoza and Santamarina, 2010).

Surfactant molecules align at the polar/non-polar interface between CO_2 and water and fold (Figures 8.3-c and d - Prasad et al., 1979), modify local electric field, and weaken the surface tension by adding repulsion forces at the surface. The interfacial CO_2-water tension in the presence of surfactant decreases from ~50mN/m to ~4mN/m as pressure increases from 0.1MPa to ~7MPa, and reaches a constant value ~4mN/m across the CO_2 gas-liquid boundary (Figure 8.5). The trend parallels the results for CO_2-water without surfactant but with an almost constant shift between ~30mN/m. Apparently, the surfactant concentration at the interface remains constant with pressure.

Contact angle and interfacial tension. The Young-Dupre equation relates the contact angle to interfacial tensions (Figure 8.3-b):

$$\cos\theta = \frac{\sigma_{fs} - \sigma_{ls}}{T_s} \tag{11}$$

Therefore, the factor $T_s \cdot \cos\theta = \sigma_{fs} - \sigma_{ls}$ is not a function of the CO_2-water interfacial tension. Yet, experimental results show consistent difference in invasion topology when the interfacial tension T_s is modified (Figure 8.7). This observation implies either σ_{fs} and/or σ_{ls} must change with pressure and surfactant as well.

Indeed, the interfacial tension σ_{fs} between CO_2 and solid mineral decreases as CO_2 pressure increases from 0.1MPa to ~7MPa (Dickson et al., 2006; Sutjiadi-Sia et al., 2008). On the other hand, while the interfacial tension σ_{ls} between water and mineral remains relatively constant as the fluid pressure increases (Dickson et al., 2006; Espinoza and

Santamarina, 2010), it increases as the concentration of surfactant increases probably due to hydrogen bonding between the CO_2-philic (or hydro-phobic) tail of nonionic surfactant molecules and adsorbent glass SiO_2 (Szymczyk and Jańczuk, 2008). Thus, the factor $T_s \cdot cos\theta$ effectively decreases as the interfacial tension T_s decreases.

Size of surfactant. The selected surfactant, pluronic block copolymer has a molecular weight mw=4224g/mol and an estimated molecular size of ~20nm (Figure 8.2). The two hydro-phobic tails repel each other as the surfactant concentration at the interface increases. This long molecule could resist invading pores of 2nm~3nm diameter, perhaps as large as 10nm. The fraction of pores d_{pore}<1nm is very small in most shale (<1% - Bachu and Bennion, 2008).

Sweep efficiency in 3-D. Investigation of the sweep efficiency in this chapter has been based on 2-D micro-model experiments and 2-D network model simulations. As the pore coordination number increases in 3-D, so do the degrees of freedom during invasion, and lower 3-D sweep efficiencies are anticipated.

8.5 Conclusions

Efficient injection and the long-term stability of saline aquifers could be negatively affected by emergent hydro-chemo-mechanically coupled phenomena, such as viscous fingering, acidification and mineral dissolution, mineral precipitation, and fluid convection. We can engineer CO_2 injection to prevent these negative effects. Possible alternatives include: increased CO_2 viscosity, sequential fluid injection, bio-clogging, and decreased interfacial tension. In this study, we attempted to lower the interfacial tension. Salient observation follows:

• Surfactants that have hydrophilic heads and CO_2-philic tails can lower the interfacial tension between CO_2 and water. In this study, a long-chain nonionic surfactant (weight percent wt≈0.4%) lowered the CO_2-water interfacial tension from T_s~50mN/m to

T_s~4mN/m at a pressure of $P \geq 7$MPa. The parallelism in T_s-P trends with and without surfactants suggests a pressure-independent concentration of surfactants at the interface.

• Capillarity, governed by the product of CO_2-water interfacial tension T_s and contact angle θ is independent of T_s as per Young's equation $T_s \cdot cos\theta = \sigma_{fs} - \sigma_{ls}$. However, pressure and surfactants also affect the force between σ_{fs} mineral-CO_2 and σ_{ls} water-mineral interfacial tension.

• Experimental CO_2 injection tests in pore micro-models and parallel network model simulations demonstrate that the sweep efficiency of CO_2 invasion can be effectively enhanced by lowering the interfacial tension. In fact, the sweep efficiency can surpasses 40% in 2-D systems (lower values are expected in 3-D systems).

• Engineered CO_2 injection methods such as the use of surfactants can minimize emergent hydro-chemo-mechanically coupled phenomena and improve the long-term integrity of storage sites, enhance the injectivity of CO_2, and optimize pore space occupancy underground.

CHAPTER 9

CONCLUSIONS

This research addresses emergent hydro-chemo-mechanically coupled phenomena, their implications on CO_2 geological storage, and engineered CO_2 injection method. The scope of the work included data compilation from published studies, geochemical analysis based on mass balance calculations and geomechanical analysis for different zones, pore-scale reactive fluid transport, upscale of the reactive fluid flow in both CO_2 reservoirs (2-D network model) and overlying caprock (1-D simulation), sealing capacity of shale-caprock and well-cement and sealing strategy, and engineered injection strategy to improve sweep efficiency. Complementary analyses, numerical simulations, and experimental works support the applicability of the results in each section. The main observations are presented separately for each study.

CO_2 Geological Storage – Geotechnical Implications

- The physical properties of CO_2 such as density, viscosity, interfacial tension, and bulk compressibility depend on the pressure and temperature conditions.
- Geometric boundaries, spatial heterogeneity, flow conditions, and the emergence of viscous fingering affect the volume of the geological formation injected with CO_2.
- Water acidification in the presence of CO_2 enhances mineral dissolution, and denser CO_2-dissolved water triggers self-mixing.
- Complex hydro-chemo-mechanical interactions, which lead to emergent phenomena, may hinder the storativity of injected carbon dioxide.
- The contrasting physical properties of CO_2 and water support the application of geophysical monitoring methods based on elastic and electromagnetic waves.

CO_2 Geological Storage: A Mass Balance Analysis and Implications

- Four different zones in the reservoir around injection wells are identified, staring from far-field zone I, to intermediate zone II and III, and to near-well zone IV.
- In leveled sediments, the CO_2 pool thickness may be limited by lateral capillary trapping rather than by the sediment layer thickness. Typical pools will be only a few meters thick in the absence of geometric traps.
- The time for convection may be as low as few years in pervious reservoirs. Short convection times will aggravate dissolution consequence, and either compaction-driven shear failure or caprock bending failure may occur. In particular, the unsupported free span of the caprock cannot exceed 20% of the caprock thickness.
- The continuous influx of dry CO_2 dries the residual brine near the wellbore. The precipitation of secondary minerals increases the mineral volume by a maximum of 5%. A minor decrease in CO_2 permeability is anticipated.

CO_2 Geological Storage: Pore-Scale Reactive Fluid Transport (Rock Joint and Pores)

- Newly devised simulation technique enables us to investigate interactions among governing parameters, including advection, diffusion, species concentration, and geometry.
- Reactant species are readily consumed in a calcite-dominant environment, while low reaction rate allows more extensive transport of them in sandstones.
- Pore enlargement may decrease either exponentially or linearly along the flow path. Dissolution patterns define a consistent trend in the *Da* - *Pe* space.
- An increased aperture-to-length ratio slows the diffusive transport to the mineral surface. Upscaling must take into consideration both the joint length and its slenderness.

Reactive Fluid Flow in CO_2 Storage Reservoirs – Pore Network Model Study

- We develop a new network simulation code to investigate fluid-mineral interaction when CO_2-dissolved water flows through a porous network near the CO_2-water boundary. The new code provides results including the distribution of species concentration, tube diameters, flow rate, and pressure field.
- Porous media in a calcite formation will experience either compact dissolution near the inlet ($Da>10^{-4}$) or localized flow paths ($Da<10^{-4}$) as a result of CO_2-dissolved reactive fluid flow.
- Both the Damköhler number and pore-size variability affect the relationship between mean tube diameter and flow rate. Changes in Damköhler number result in inherent bias between average and local trends. Both the Damköhler number and pore-size variability should be accounted in field-scale FEM models.

Reactive Fluid Flow Through the Caprock Overlying CO_2 Storage Reservoirs

- Capillary trapping prevents the invasion of liquid or supercritical CO_2 into the caprock, and diffusion governs the transport of dissolved species in the caprock.
- Most reactant species are consumed within ~0.2mm from the caprock-reservoir interface in the calcite environment. Estimated increases in porosity $\Delta\varphi$~0.06 and permeability $(k_1-k_0)/k_0$~1.5 for the first 15hrs are significant. The dissolved skin may leave the caprock locally unsupported and bending-tensile cracks may form.
- Diffusion and dissolution are fully coupled in the kaolinite-rich caprock. Mineral dissolution extends to about ~1m from the caprock-reservoir interface. Capillary trapping will continue performing in long-term CO_2 storage projects judging by the small changes in porosity and permeability.

CO_2 Breakthrough and Leak - Sealing Experiments on Shale and Cement

- Very low CO_2-breakthrough pressure P_{bt}~20kPa are measured when discontinuities are aligned with the pressure gradient. This observation applies to fractures parallel to bedding planes, transverse tensile fractures due to unsupported span, or shear fractures in compression.
- Sub-micron clay particles can be injected to fill cracks. Sealing treatments cause a marked increase in shut-off pressure P_d~1MPa. The CO_2 permeability decreases as the shale specimen experiences successive sealing treatments.
- Intact cement plugs can generate a shut-off pressure as high as P_d~6MPa. Extensive carbonation with orange color and reaction rims around grains were observed on the plug surface.
- Emphasis should be placed on breakthrough pressure and sealing strategies for probable gaps between the cement and the caprock that result from cement contraction.

Engineered CO_2 Injection for Geological Storage

- The selected long-chain nonionic surfactant lowers the CO_2-water interfacial tension to T_s~4mN/m at pressure $P \geq 7$MPa. The parallelism in T_s-P trends with and without surfactants suggests a pressure-independent surfactant concentration at the interface.
- Pressure and surfactants also affect the force between mineral and CO_2 and interfacial tension between water and mineral.
- Experimental CO_2 injection tests in pore micro-models and parallel network model simulations demonstrate that the sweep efficiency of CO_2 invasion E can be effectively enhanced to E~40% in 2-D systems by lowering the interfacial tension.
- Engineered CO_2 injection methods such as the use of surfactants can minimize emergent hydro-chemo-mechanically coupled phenomena, enhance the injectivity of CO_2, and optimize pore space occupancy underground.

REFERENCES

Adams, J., and Bachu, S. (2002). "Equations of state for basin geofluids: algorithm review and intercomparison for brines." *Geofluids*, 2(4), 257-271.

Aker, E., JØrgen MÅlØy, K., Hansen, A., and Batrouni, G. (1998). "A two-dimensional network simulator for two-phase flow in porous media." *Transport in Porous Media*, 32(2), 163-186.

Algive, L., Bekri, S., and Vizika-kavvadias, O. "Reactive pore network modeling dedicated to the determination of the petrophysical property changes while injecting CO_2." *Proc., SPE Annual Technical Conference and Exhibition*, 2009. Society of Petroleum Engineers, 124305-MS.

Alnes, H., Eiken, O., and Stenvold, T. (2008). "Monitoring gas production and CO_2 injection at the Sleipner field using time-lapse gravimetry." *Geophysics*, 73(6), WA155-WA161.

Alvarado, V., and Manrique, E. (2010). "Enhanced Oil Recovery: An Update Review." *Energies*, 3(9), 1529-1575.

André, L., Audigane, P., Azaroual, M., and Menjoz, A. (2007). "Numerical modeling of fluid-rock chemical interactions at the supercritical CO_2-liquid interface during CO_2 injection into a carbonate reservoir, the Dogger aquifer (Paris Basin, France)." *Energy Conversion and Management*, 48(6), 1782-1797.

Armitage, P. J., Worden, R. H., Faulkner, D. R., Aplin, A. C., Butcher, A. R., and Iliffe, J. (2010). "Diagenetic and sedimentary controls on porosity in Lower Carboniferous fine-grained lithologies, Krechba field, Algeria: A petrological study of a caprock to a carbon capture site." *Marine and Petroleum Geology*, 27(7), 1395-1410.

Arts, R., Eiken, O., Chadwick, A., Zweigel, P., van der Meer, L., and Zinszner, B. (2004). "Monitoring of CO_2 injected at Sleipner using time-lapse seismic data." *Energy*, 29(9-10), 1383-1392.

Augustin, L., Barbante, C., Barnes, P. R. F., Barnola, J. M., Bigler, M., Castellano, E., Cattani, O., Chappellaz, J., Dahl-Jensen, D., and Delmonte, B. (2004). "Eight glacial cycles from an Antarctic ice core." *Nature*, 429(6992), 623-628.

Azaroual, M., Pruess, K., and Fouillac, C. "Feasibility of using supercritical CO_2 as heat transmission fluid in the EGS (Enhanced Geothermal Systems) integrating the carbon storage constraints." *Proc., ENGINE - Enhanced Geothermal Innovative Network for Europe. Workshop 2: Exploring high temperature reservoirs: new challenges for geothermal energy*.

Bachu, S., and Adams, J. (2003). "Sequestration of CO_2 in geological media in response to climate change: capacity of deep saline aquifers to sequester CO_2 in solution." *Energy Conversion and Management*, 44(20), 3151-3175.

Bachu, S., and Bennion, B. (2008). "Effects of in-situ conditions on relative permeability characteristics of CO_2-brine systems." *Environmental Geology*, 54(8), 1707-1722.

Baines, S. J., and Worden, R. H. (2004). "The long-term fate of CO_2 in the subsurface: natural analogues for CO_2 storage." *Geological Society, London, Special Publications*, 233(1), 59-85.

Benson, S. M., and Hepple, R. P. "Detection and options for remediation of leakage from underground CO_2 storage projects." *Proc., Proceeding of the 7th International Conference on Greenhouse Gas Technologies (GHGT7)*, Elsevier, Volume II: 1329-1335.

Bergmo, P. E. S., Grimstad, A.-A., and Lindeberg, E. (2011). "Simultaneous CO_2 injection and water production to optimise aquifer storage capacity." *International Journal of Greenhouse Gas Control*, 5(3), 555-564.

Berne, P., Bachaud, P., and Fleury, M. (2010). "Diffusion Properties of Carbonated Caprocks from the Paris Basin." *Oil & Gas Science and Technology-Revue De L Institut Francais Du Petrole*, 65(3), 473-484.

Biagi, S., Gherardi, F., and Gianelli, G. (2006). "A simulation study of CO_2 sequestration in the Arno River plain (Tuscany, Italy)." *Energy sources*, 28(9-12), 923-932.

Bielinski, A., Kopp, A., Schutt, H., and Class, H. (2008). "Monitoring of CO_2 plumes during storage in geological formations using temperature signals: Numerical investigation." *International Journal of Greenhouse Gas Control*, 2(3), 319-328.

Bildstein, O., Kervévan, C., Lagneau, V., Delaplace, P., Crédoz, A., Audigane, P., Perfetti, E., Jacquemet, N., and Jullien, M. (2010). "Integrative modeling of caprock integrity in the context of CO_2 storage: evolution of transport and geochemical properties and impact on performance and safety assessment." *Oil & Gas Science and Technology–Revue de l'Institut Français du Pétrole*, 65(3), 485-502.

Bjerrum, L., Kennard, R. M., Gibson, R. E., and Nash, J. (1972). "Hydraulic fracturing in field permeability testing." *Geotechnique*, 22(2), 319-332.

Blunt, M., Fayers, F. J., and Orr, F. M. (1993). "Carbon-dioxide in enhanced oil-recovery." *Energy Conversion and Management*, 34(9-11), 1197-1204.

Bohnhoff, M., Zoback, M. D., Chiaramonte, L., Gerst, J. L., and Gupta, N. (2010). "Seismic detection of CO_2 leakage along monitoring wellbores." *International Journal of Greenhouse Gas Control*, 4(4), 687-697.

Boudreau, B. P. (1997). *Diagenetic models and their implementation: Modelling transport and reactions in aquatic sediments*, Springer, Berlin.

Brandvoll, Ø., Regnault, O., Munz, I. A., Iden, I. K., and Johansen, H. (2009). "Fluid–solid interactions related to subsurface storage of CO_2 Experimental tests of well cement." *Energy Procedia*, 1(1), 3367-3374.

Brosse, E., Magnier, C., and Vincent, B. (2005). "Modelling fluid-rock interaction induced by the percolation of CO_2-enriched solutions in core samples: the role of reactive surface area." *Oil & Gas Science and Technology*, 60(2), 287-305.

Brown, M. A., and Southworth, F. (2006). "Mitigating climate change through green buildings and smart growth." Georgia Institute of Technology.

Bryant, S., and Britton, L. (2008). "Mechanistic understanding of microbial plugging for improved sweep efficiency." *US DOE NETL report DE-FC26-04NT15524*.

Buijse, M. (2000). "Understanding wormholing mechanisms can improve acid treatments in carbonate formations." *Old Production & Facilities*, 15(3), 168-175.

Calabrese, M., Masserano, F., and Blunt, M. J. (2006). "Simulation of physical-chemical processes during carbon dioxide sequestration in geological structures." *8th International Conference on Greenhouse Gas Control Technologies, GHGT-8*Norway.

Carman, P. C. (1956). *Flow of gases through porous media*, Butterworths Scientific Publications London, San Diego, CA.

CDIAC (2009). "Global, regional, and national fossil-fuel CO_2 emissions." ORNL, http://cdiac.ornl.gov/trends/emis/overview_2008.html.

Ceglarska-Stefanska, G., and Zarebska, K. (2002). "Expansion and Contraction of Variable Rank Coals During the Exchange Sorption of CO_2 and CH_4." *Adsorption Science and Technology*, 20(1), 49-62.

Ceglarska-Stefańska, G., and Zarębska, K. (2002). "The competitive sorption of CO_2 and CH_4 with regard to the release of methane from coal." *Fuel Processing Technology*, 77, 423-429.

Cha, M. S. (2012). "Consequences of mineral dissolution in sediments." Ph.D, Georgia Institute of Technology, Atlanta.

Chalbaud, C., Robin, M., Lombard, J. M., Martin, F., Egermann, P., and Bertin, H. (2009). "Interfacial tension measurements and wettability evaluation for geological CO_2 storage." *Advances in Water Resources*, 32(1), 98-109.

Charpentier, F., Bureau, B., Troles, J., Boussard-Plédel, C., Michel-Le Pierrès, K., Smektala, F., and Adam, J. L. (2009). "Infrared monitoring of underground CO_2 storage using chalcogenide glass fibers." *Optical Materials*, 31(3), 496-500.

Chi, S. M., Morsi, B. I., Klinzing, G. E., and Chiang, S. H. (1988). "Study of interfacial properties in the liquid carbon dioxide-water-coal system." *Energy & Fuels*, 2(2), 141-145.

Chiquet, P., Daridon, J. L., Broseta, D., and Thibeau, S. (2007). "CO_2/water interfacial tensions under pressure and temperature conditions of CO_2 geological storage." *Energy Conversion and Management*, 48(3), 736-744.

Chou, L., Garrels, R. M., and Wollast, R. (1989). "Comparative study of the kinetics and mechanisms of dissolution of carbonate minerals." *Chemical Geology*, 78(3-4), 269-282.

Chun, B.-S., and Wilkinson, G. T. (1995). "Interfacial tension in high-pressure carbon dioxide mixtures." *Ind. Eng. Chem. Res.*, 34(12), 4371-4377.

Cinar, Y., Riaz, A., and Tchelepi, H. "Experimental study of CO_2 injection into saline formations."

COMSOL (2008). "COMSOL: Multiphysics Modeling and Engineering Simulation Software."Stockholm, Sweden.

Connolly, C. A., Walter, L. M., Baadsgaard, H., and Longstaffe, F. J. (1990). "Origin and evolution of formation waters, Alberta basin, western Canada sedimentary basin. I. chemistry." *Applied Geochemistry*, 5(4), 375-395.

Cunningham, A. B., Gerlach, R., Spangler, L., and Mitchell, A. C. (2009). "Microbially enhanced geologic containment of sequestered supercritical CO_2." *Energy Procedia*, 1(1), 3245-3252.

da Rocha, S. R. P., Harrison, K. L., and Johnston, K. P. (1999). "Effect of surfactants on the interfacial tension and emulsion formation between water and carbon dioxide." *Langmuir*, 15(2), 419-428.

Daccord, G., Lenormand, R., and Lietard, O. (1993). "Chemical dissolution of a porous-medium by a reactive fluid. 1. Model for the wormholing phenomenon." *Chemical Engineering Science*, 48(1), 169-178.

Daccord, G., Lietard, O., and Lenormand, R. (1993). "Chemical dissolution of a porous-medium by a reactive fluid. 2. Convection vs. reaction, behavior diagram." *Chemical Engineering Science*, 48(1), 179-186.

Daley, T., Myer, L., Peterson, J., Majer, E., and Hoversten, G. (2008). "Time-lapse crosswell seismic and VSP monitoring of injected CO_2 in a brine aquifer." *Environmental Geology*, 54(8), 1657-1665.

Daley, T. M., Solbau, R. D., Ajo-Franklin, J. B., and Benson, S. M. (2007). "Continuous active-source seismic monitoring of CO_2 injection in a brine aquifer." *Geophysics*, 72, A57.

De Gennes, P. G., Brochard-Wyart, F., and Quéré, D. (2004). *Capillarity and wetting phenomena: drops, bubbles, pearls, waves*, Springer Verlag.

Delage, P., Schroeder, C., and Cui, Y. J. (2008). "Subsidence and capillary effects in chalks." *Arxiv preprint arXiv:0803.1308*.

Dickson, J. L., Gupta, G., Horozov, T. S., Binks, B. P., and Johnston, K. P. (2006). "Wetting phenomena at the CO_2/water/glass interface." *Langmuir*, 22(5), 2161-2170.

Dickson, J. L., Smith Jr, P. G., Dhanuka, V. V., Srinivasan, V., Stone, M. T., Rossky, P. J., Behles, J. A., Keiper, J. S., Xu, B., and Johnson, C. (2005). "Interfacial properties of fluorocarbon and hydrocarbon phosphate surfactants at the water-CO_2 interface." *Industrial & engineering chemistry research*, 44(5), 1370-1380.

Dillard, L. A., and Blunt, M. J. (2000). "Development of a pore network simulation model to study nonaqueous phase liquid dissolution." *Water Resources Research*, 36(2), 439-454.

DOE (2010). "Fossil Fuels, http://www.energy.gov/energysources/fossilfuels.htm, accessed on 11/14/2010."

Dong, H., and Blunt, M. J. (2009). "Pore-network extraction from micro-computerized-tomography images." *Phys. Rev. E*, 80, 036307.

Dooley, J. J., Dahowski, R. T., Davidson, C. L., Wise, M. A., Gupta, N., Kim, S. H., and Malone, E. L. (2006). "Carbon Dioxide Capture and Geologic Storage: A core element of a Global Energy Technology Strategy to address climate change." *A Technology Report from the Second Phase of the Global Energy Technology Strategy Program*.

Dooley, J. J., Trabucchi, C., and Patton, L. (2010). "Design considerations for financing a national trust to advance the deployment of geologic CO_2 storage and motivate best practices." *International Journal of Greenhouse Gas Control*, 4(2), 381-387.

Doughty, C., Freifeld, B. M., and Trautz, R. C. (2008). "Site characterization for CO_2 geologic storage and vice versa: the Frio brine pilot, Texas, USA as a case study." *Environmental Geology*, 54(8), 1635-1656.

Downey, M. W. (1984). "Evaluating seals for hydrocarbon accumulations." *AAPG Bulletin*, 68(11), 1752-1763.

Drever, J. I. (1997). *The geochemistry of natural waters: surface and groundwater environments*, Prentice Hall.

Duan, Z., and Sun, R. (2003). "An improved model calculating CO_2 solubility in pure water and aqueous NaCl solutions from 273 to 533 K and from 0 to 2000 bar." *Chemical Geology*, 193(3-4), 257-271.

Duguid, A., Radonjic, M., and Scherer, G. W. (2011). "Degradation of cement at the reservoir/cement interface from exposure to carbonated brine." *International Journal of Greenhouse Gas Control*, 5, 1413-1428.

Egermann, P., Bekri, S., and Vizika, O. "An integrated approach to assess the petrophysical properties of rocks altered by rock/fluid interactions (CO_2 injection)." *Proc., International Symposium of the Society of Core Analysis*, 1-14.

Ehlig-Economides, C., and Economides, M. J. (2010). "Sequestering carbon dioxide in a closed underground volume." *Journal of Petroleum Science and Engineering*, 70(1-2), 123-130.

EIA, U. (2004). "The basics of underground natural gas storage." <http://www.eia.gov/>.

EIA, U. (2010). "Annual energy outlook 2011: Reference case." R. Newell, ed.Washington, DC.

Emberley, S., Hutcheon, I., Shevalier, M., Durocher, K., Gunter, W. D., and Perkins, E. H. (2004). "Geochemical monitoring of fluid-rock interaction and CO_2 storage at the Weyburn CO_2-injection enhanced oil recovery site, Saskatchewan, Canada." *Energy*, 29(9-10), 1393-1401.

Enick, R. M., Beckman, E. J., Johnson, J. K., and Hamilton, A. (2010). "Synthesis and evaluation of CO_2 thickeners designed with molecular modeling, DE-FG26-04NT-15533." University of Pittsburgh.

Ennis-King, J., and Paterson, L. (2007). "Coupling of geochemical reactions and convective mixing in the long-term geological storage of carbon dioxide." *International Journal of Greenhouse Gas Control*, 1(1), 86-93.

Espinoza, D. N. (2011). "Carbon geological storage - Underlying phenomena and implications." Ph.D., Georgia Institute of Technology, Atlanta.

Espinoza, D. N., Kim, S. H., and Santamarina, J. C. (2011). "CO_2 geological storage—Geotechnical implications." *KSCE Journal of Civil Engineering*, 15(4), 707-719.

Espinoza, D. N., and Santamarina, J. C. (2010). "Water-CO_2-mineral systems: Interfacial tension, contact angle, and diffusion—Implications to CO_2 geological storage." *Water Resources Research*, 46(7), W07537.

Espinoza, D. N., and Santamarina, J. C. (2012). "Clay interaction with liquid and supercritical CO_2: The relevance of electrical and capillary forces." *In Print*.

Fenghour, A., Wakeham, W. A., and Vesovic, V. (1998). "The viscosity of carbon dioxide." *Journal of Physical and Chemical Reference Data*, 27(1), 31-44.

Ferer, M., Bromhal, G. S., and Smith, D. H. (2003). "Pore-level modeling of immiscible drainage: validation in the invasion percolation and DLA limits." *Physica A: Statistical Mechanics and its Applications*, 319, 11-35.

Ferronato, M., Gambolati, G., Janna, C., and Teatini, P. (2010). "Geomechanical issues of anthropogenic CO_2 sequestration in exploited gas fields." *Energy Conversion and Management*, 51(10), 1918-1928.

Fleury, M., Pironon, J., Nindre, L., Bildstein, O., Berne, P., Lagneau, V., Broseta, D., Pichery, T., Fillacier, S., Lescanne, M., and Vidal, O. (2010). "Evaluating sealing efficiency of caprocks for CO_2 storage: an overview of the Geocarbone Integrity program and results." *Oil & Gas Science and Technology*, 65(3), 435-444.

Francisca, F., Fratta, D., and Wang, H. (2008). "Electrowetting on mineral and rock surfaces." *Geophysical Research Letters*, 35(6), L06402.

Fredd, C. N., and Fogler, H. S. (1998). "Influence of transport and reaction on wormhole formation in porous media." *AIChE Journal*, 44(9), 1933-1949.

Fredd, C. N., and Fogler, H. S. (1998). "The kinetics of calcite dissolution in acetic acid solutions." *Chemical Engineering Science*, 53(22), 3863-3874.

Gale, J. (2004). "Geological storage of CO_2: What do we know, where are the gaps and what more needs to be done?" *Energy*, 29(9-10), 1329-1338.

Garcia, J. E. (2001). "Density of aqueous solutions of CO_2." *Lawrence Berkeley National Laboratory*.

Gasperikova, E., and Hoversten, G. M. (2006). "A feasibility study of nonseismic geophysical methods for monitoring geologic CO_2 sequestration." *The Leading Edge*, 25(10), 1282-1288.

Gaus, I., Audigane, P., Andre, L., Lions, J., Jacquemet, N., Durst, P., Czernichowski-Lauriol, I., and Azaroual, M. (2008). "Geochemical and solute transport modelling for CO_2 storage, what to expect from it?" *International Journal of Greenhouse Gas Control*, 2(4), 605-625.

Gaus, I., Azaroual, M., and Czernichowski-Lauriol, I. (2005). "Reactive transport modelling of the impact of CO_2 injection on the clayey cap rock at Sleipner (North Sea)." *Chemical Geology*, 217(3-4), 319-337.

Gherardi, F., Xu, T., and Pruess, K. (2007). "Numerical modeling of self-limiting and self-enhancing caprock alteration induced by CO_2 storage in a depleted gas reservoir." *Chemical Geology*, 244(1-2), 103-129.

Global-Carbon-Project (2010). "The Carbon Budget 2009."

Golfier, F., Zarcone, C., Bazin, B., Lenormand, R., Lasseux, D., and Quintard, M. (2002). "On the ability of a Darcy-scale model to capture wormhole formation during the dissolution of a porous medium." *Journal of Fluid Mechanics*, 457(213), 213-254.

Golomb, D. (1993). "Ocean disposal of CO_2 - feasibility, economics and effects." *Energy Conversion and Management*, 34(9-11), 967-976.

Gresham, R. L., McCoy, S. T., Apt, J., and Morgan, M. G. (2010). "Implications of compensating property owners for geologic sequestration of CO_2." *Environmental science & technology*, 44(8), 2897-2903.

Guéguen, Y., and Palciauskas, V. (1994). *Introduction to the Physics of Rocks*, Princeton Univ Press.

Gunter, W. D., Perkins, E. H., and Hutcheon, I. (2000). "Aquifer disposal of acid gases: modelling of water-rock reactions for trapping of acid wastes." *Applied Geochemistry*, 15(8), 1085-1095.

Hanor, J. S. (1994). "Physical and chemical controls on the composition of waters in sedimentary basins." *Marine and petroleum geology*, 11(1), 31-45.

Hassanzadeh, H., Pooladi-Darvish, M., Elsharkawy, A. M., Keith, D. W., and Leonenko, Y. (2008). "Predicting PVT data for CO_2-brine mixtures for black-oil simulation of CO_2 geological storage." *International Journal of Greenhouse Gas Control*, 2(1), 65-77.

Hassanzadeh, H., Pooladi-Darvish, M., and Keith, D. W. (2007). "Scaling behavior of convective mixing, with application to geological storage of CO_2." *AIChE journal*, 53(5), 1121-1131.

Heddle, G., Herzog, H., and Klett, M. (2003). "The economics of CO_2 storage." *Massachusetts Institute of Technology, Laboratory for Energy and the Environment*(MIT LFEE 2003-003RP).

Hellevang, H. (2006). "Interactions between CO_2, saline water and minerals during geological storage of CO_2."

Hetényi, M., and Michigan, U. o. (1946). *Beams on elastic foundation*, G. Cumberlege, Oxford university press.

Hildenbrand, A., Schlömer, S., Krooss, B., and Littke, R. (2004). "Gas breakthrough experiments on pelitic rocks: comparative study with N_2, CO_2 and CH_4." *Geofluids*, 4(1), 61-80.

Hildenbrand, A., Schlömer, S., and Krooss, B. M. (2002). "Gas breakthrough experiments on fine-grained sedimentary rocks." *Geofluids*, 2(1), 3-23.

Hoefner, M. L., and Fogler, H. S. (1988). "Pore evolution and channel formation during flow and reaction in porous media." *AIChE Journal*, 34(1), 45-54.

Hoek, E., and Brown, E. T. (1990). *Underground excavations in rock*, Spon Press.

Homsy, G. (1987). "Viscous fingering in porous media." *Annual Review of Fluid Mechanics*, 19(1), 271-311.

Horseman, S. T., Harrington, J. F., and Sellin, P. (1999). "Gas migration in clay barriers." *Engineering Geology*, 54(1), 139-149.

House, K. Z., Schrag, D. P., Harvey, C. F., and Lackner, K. S. (2006). "Permanent carbon dioxide storage in deep-sea sediments." *Proceedings of the National Academy of Sciences of the United States of America*, 103(33), 12291-12295.

Huh, C., and Rossen, W. (2008). "Approximate pore-level modeling for apparent viscosity of polymer-enhanced foam in porous media." *SPE Journal*, 13(1), 17-25.

Hung, K. M., Hill, A. D., and Sepehrnoori, K. (1989). "A mechanistic model of wormhole growth in carbonate matrix acidizing and acid fracturing." *Journal of Petroleum Technology*, 41(1), 59-66.

IEA (2009). "CO_2 emissions from fuel combustion highlights." 115p.

IPCC (2001). "Climage Change 2001: The scientific basis. Contribution of working group I to the third assessment of report of the intergovernmental panel on climate change." J. T. Houghton, Y. Ding, D.J. Griggs, M. Noguer, P.J. van der Linden, X. Dai, K. Maskell, and C.A. Johnson, ed.Cambridge, United Kingdom and New York, USA, 881.

IPCC (2005). "IPCC special report on carbon dioxide capture and storage." *Prepared by working group III of the intergovernmental panal on climate change*, B. Metz, O. Davidson, H. C. de Coninck, M. Loos, and L. A. Meyer, ed., Cambridge University Press, Cambridge, United Kingdom and New York, USA, 442.

Israelachvili, J. N. (2011). *Intermolecular and surface forces, 3rd Ed.*, Academic press, London.

Jaccard, M. K. (2005). *Sustainable fossil fuels: The unusual suspect in the quest for clean and enduring energy*, Cambridge Univ Pr.

Jaky, J. (1944). "The coefficient of earth pressure at rest." *Journal of the Society of Hungarian Architects and Engineers*, 7, 355-358.

Jang, J., Narsilio, G. A., and Santamarina, J. C. (2011). "Hydraulic conductivity in spatially varying media - a pore scale investigation." *Geophysical Journal International*, 184(3), 1167-1179.

Jaworski, G. W., Duncan, J. M., and Seed, H. B. (1981). "Laboratory study of hydraulic fracturing." *J. Geotech. Eng. Div., Am. Soc. Civ. Eng.;(United States)*, 107(6), 713-732.

Johnson, J. W., Nitao, J. J., and Morris, J. P. (2004). "Reactive transport modeling of cap rock integrity during natural and engineered CO_2 storage." *Carbon Dioxide Capture for Storage in Deep Geologic Formations*, 2(UCRL-JRNL-204386).

Juanes, R., Spiteri, E., Orr Jr, F., and Blunt, M. (2006). "Impact of relative permeability hysteresis on geological CO_2 storage." *Water Resour. Res*, 42(12), W12418.

Kaldi, J. G., and Gibson-Poole, C. M. (2008). "Storage capacity estimation, site selection and characterization for CO_2 storage projects." *Report No: RPT08-1001, CO_2CRC, Canberra, ACT, AU.*

Kalia, N., and Balakotaiah, V. (2007). "Modeling and analysis of wormhole formation in reactive dissolution of carbonate rocks." *Chemical Engineering Science*, 62(4), 919-928.

Kam, S. I., and Rossen, W. R. (2003). "A model for foam generation in homogeneous media." *SPE Journal*, 8(4), 417-425.

Kang, Q., Lichtner, P. C., Viswanathan, H. S., and Abdel-Fattah, A. I. (2010). "Pore scale modeling of reactive transport involved in geologic CO_2 sequestration." *Transport in Porous Media*, 82(1), 197-213.

Kaszuba, J. P., Janecky, D. R., and Snow, M. G. (2005). "Experimental evaluation of mixed fluid reactions between supercritical carbon dioxide and NaCl brine: Relevance to the integrity of a geologic carbon repository." *Chemical Geology*, 217(3-4), 277-293.

Katsube, T. J., and Williamson, M. A. (1994). "Effects of diagenesis on shale nano-pore structure and implications for sealing capacity." *Clay Minerals*, 29(4), 451-461.

Kempka, T., Waschbusch, M., Azzam, R., and Fernandez-Steeger, T. M. (2008). "Reducing ground subsidence involving geological CO_2 storage during longwall mining operations." *Quarterly Journal of Engineering Geology and Hydrogeology*, 41, 439-448.

Kharaka, Y. K., Cole, D. R., Hovorka, S. D., Gunter, W. D., Knauss, K. G., and Freifeld, B. M. (2006). "Gas-water-rock interactions in Frio formation following CO_2 injection: Implications for the storage of greenhouse gases in sedimentary basins." *Geology*, 34(7), 577-580.

Khilar, K. C., and Fogler, H. S. (1998). *Migrations of fines in porous media*, Springer.

Kiessling, D., Schmidt-Hattenberger, C., Schuett, H., Schilling, F., Krueger, K., Schoebel, B., Danckwardt, E., and Kummerow, J. (2010). "Geoelectrical methods for monitoring geological CO_2 storage: First results from cross-hole and surface-downhole measurements from the CO2SINK test site at Ketzin (Germany)." *International Journal of Greenhouse Gas Control*, 4(5), 816-826.

Kinart, C. M., Kinart, W. J., and Cwiklinska, A. (2002). "Density and viscosity at various temperatures for 2-methoxyethanol + acetone mixtures." *Journal of Chemical & Engineering Data*, 47(1), 76-78.

Kneafsey, T. J., and Pruess, K. (2010). "Laboratory flow experiments for visualizing carbon dioxide-induced, density-driven brine convection." *Transport in Porous Media*, 82(1), 123-139.

Kopp, A., Class, H., and Helmig, R. (2009). "Investigations on CO_2 storage capacity in saline aquifers: Part 1. Dimensional analysis of flow processes and reservoir characteristics." *International Journal of Greenhouse Gas Control*, 3(3), 263-276.

Kovscek, A. R., and Bertin, H. J. (2003). "Foam mobility in heterogeneous porous media." *Transport in porous media*, 52(1), 17-35.

Kutchko, B. G., Strazisar, B. R., Dzombak, D. A., Lowry, G. V., and Thaulow, N. (2007). "Degradation of well cement by CO_2 under geologic sequestration conditions." *Environmental science & technology*, 41(13), 4787-4792.

Kvamme, B., Kuznetsova, T., Hebach, A., Oberhof, A., and Lunde, E. (2007). "Measurements and modelling of interfacial tension for water plus carbon dioxide systems at elevated pressures." *Computational Materials Science*, 38(3), 506-513.

Lagneau, V., Pipart, A., and Catalette, H. (2005). "Reactive transport modelling of CO_2 sequestration in deep saline aquifers." *Oil and Gas Science and Technology-Revue de l'IFP-Institut Francais du Petrole*, 60(2), 231-248.

Lake, L. W., and Venuto, P. B. (1990). "A niche for enhanced oil recovery in the 1990s." *Oil & Gas Journal*, 88(17), 62-67.

Land, L. S., and Prezbindowski, D. R. (1981). "The origin and evolution of saline formation water, Lower Cretaceous carbonates, south-central Texas, USA." *Journal of Hydrology*, 54(1-3), 51-74.

Larsen, J. W. (2004). "The effects of dissolved CO_2 on coal structure and properties." *International Journal of Coal Geology*, 57(1), 63-70.

Lasaga, A. C. (1984). "Chemical kinetics of water-rock interactions." *Journal of Geophysical Research*, 89(B6), 4009-4025.

Lee, J. Y., Buxton, G. A., and Balazs, A. C. (2004). "Using nanoparticles to create self-healing composites." *The Journal of chemical physics*, 121, 5531.

Lei, X., and Xue, Z. (2009). "Ultrasonic velocity and attenuation during CO_2 injection into water-saturated porous sandstone: Measurements using difference seismic tomography." *Physics of the Earth and Planetary Interiors*, 176(3-4), 224-234.

Lenormand, R., Touboul, E., and Zarcone, C. (1988). "Numerical models and experiments on immiscible displacements in porous media." *Journal of Fluid Mechanics*, 189(1), 165-187.

Leuning, R., Etheridge, D., Luhar, A., and Dunse, B. (2008). "Atmospheric monitoring and verification technologies for CO_2 geosequestration." *International Journal of Greenhouse Gas Control*, 2(3), 401-414.

Levitt, D., Jackson, A., Heinson, C., Britton, L., Malik, T., Dwarakanath, V., and Pope, G. (2009). "Identification and evaluation of high-performance EOR surfactants." *SPE Reservoir Evaluation & Engineering*, 12(2), 243-253.

Li, H., Wilhelmsen, Ř., Lv, Y., Wang, W., and Yan, J. (2011). "Viscosities, thermal conductivities and diffusion coefficients of CO_2 mixtures: Review of experimental data and theoretical models." *International Journal of Greenhouse Gas Control*.

Li, L., Peters, C. A., and Celia, M. A. (2006). "Upscaling geochemical reaction rates using pore-scale network modeling." *Advances in Water Resources*, 29(9), 1351-1370.

Li, L., Peters, C. A., and Celia, M. A. (2007). "Effects of mineral spatial distribution on reaction rates in porous media." *Water Resources Research*, 43(1), W01419.

Li, L., Steefel, C. I., and Yang, L. (2008). "Scale dependence of mineral dissolution rates within single pores and fractures." *Geochimica et Cosmochimica Acta*, 72(2), 360-377.

Li, S., Dong, M., Li, Z., Huang, S., Qing, H., and Nickel, E. (2005). "Gas breakthrough pressure for hydrocarbon reservoir seal rocks: implications for the security of long-term CO_2 storage in the Weyburn field." *Geofluids*, 5(4), 326-334.

Lindquist, W. B., Venkatarangan, A., Dunsmuir, J., and Wong, T. F. (2000). "Pore and throat size distributions measured from synchrotron X-ray tomographic images of Fontainebleau sandstones." *Journal of Geophysical Research*, 105(B9), 21509-21521,21527.

Liteanu, E., and Spiers, C. J. (2011). "Fracture healing and transport properties of wellbore cement in the presence of supercritical CO_2." *Chemical Geology*, 281(3), 195-210.

Liu, K., and Kiran, E. (2007). "Viscosity, density and excess volume of acetone + carbon dioxide mixtures at high pressures." *Industrial & Engineering Chemistry Research*, 46(16), 5453-5462.

Liu, X., Ormond, A., Bartko, K., Ying, L., and Ortoleva, P. (1997). "A geochemical reaction-transport simulator for matrix acidizing analysis and design." *Journal of Petroleum Science and Engineering*, 17(1-2), 181-196.

Massoudi, R., and King, A. D. (1975). "Effect of pressure on surface-tension of aqueous-solutions - adsorption of hydrocarbon gases, carbon-dioxide, and nitrous-oxide on aqueous-solutions of sodium-chloride and tetra-normal-butylammonium bromide at 25 degrees." *Journal of Physical Chemistry*, 79(16), 1670-1675.

Mavko, G., Mukerji, T., and Dvorkin, J. (2009). *The rock physics handbook, second edition. Tools for seismic analysis of porous media.*, Cambridge University Press, New York.

Mayne, P. W., and Kulhawy, F. H. (1982). "K_0-OCR Relationships in Soil." *Journal of the Geotechnical Engineering Division-ASCE*, 108(6), 851-872.

Mazumder, S., Karnik, A., and Wolf, K. H. (2006). "Swelling of Coal in Response to CO_2 Sequestration for ECBM and its Effect on Fracture Permeability." *SPE Journal*, 11(3), 390-398.

Meyer, R., May, F., Müller, C., Geel, K., and Bernstone, C. (2008). "Regional search, selection and geological characterization of a large anticlinal structure, as a candidate site for CO_2-storage in northern Germany." *Environmental Geology*, 54(8), 1607-1618.

Mohamed, I., and Nasr-El-Din, H. "Formation damage due to CO_2 sequestration in deep saline carbonate aquifers." *Proc., SPE International Symposium and Exhibition on Formation Damage Control*, SPE-151142-MS.

Nakatsuka, Y., Xue, Z. Q., Garcia, H., and Matsuoka, T. (2010). "Experimental study on CO_2 monitoring and quantification of stored CO_2 in saline formations using resistivity measurements." *International Journal of Greenhouse Gas Control*, 4(2), 209-216.

NETL, M. (2010). "Carbon capture and storage database version 2 <http://www.netl.doe.gov/technologies/carbon_seq/database>."

NETL, M. (2010). "Carbon sequestration Atlas of the United States and Canada." *US Department of Energy, Office of Fossil Energy, National Energy Technology Laboratory*.

Newell, D. L., Kaszuba, J. P., Viswanathan, H. S., Pawar, R. J., and Carpenter, T. (2008). "Significance of carbonate buffers in natural waters reacting with supercritical CO_2: Implications for monitoring, measuring and verification (MMV) of geologic carbon sequestration." *Geophysical Research Letters*, 35(23), L23403.

Nordbotten, J. M., Celia, M. A., and Bachu, S. (2005). "Injection and storage of CO_2 in deep saline aquifers: Analytical solution for CO_2 plume evolution during injection." *Transport in Porous Media*, 58(3), 339-360.

Nygaard, R. (2010). "Well design and well integrity." <http://www.ucalgary.ca/wasp/Well%20Integrity%20Analysis.pdf>. (06/07, 2012).

Obriot, J., Ge, J., Bose, T. K., and St-Arnaud, J. M. (1993). "Determination of the density from simultaneous measurements of the refractive index and the dielectric constant of gaseous CH_4, SF_6, and CO_2." *Fluid Phase Equilibria*, 86, 314-350.

Okwen, R. T., Stewart, M. T., and Cunningham, J. A. (2010). "Analytical solution for estimating storage efficiency of geologic sequestration of CO_2." *International Journal of Greenhouse Gas Control*, 4(1), 102-107.

Oldenburg, C. M., Lewicki, J. L., and Hepple, R. P. (2003). "Near-surface monitoring strategies for geologic carbon dioxide storage verification." Lawrence Berkeley National Laboratory.

Onishi, K., Ueyama, T., Matsuoka, T., Nobuoka, D., Saito, H., Azuma, H., and Xue, Z. (2009). "Application of crosswell seismic tomography using difference analysis with data normalization to monitor CO_2 flooding in an aquifer." *International Journal of Greenhouse Gas Control*, 3(3), 311-321.

Pacala, S., and Socolow, R. (2004). "Stabilization wedges: solving the climate problem for the next 50 years with current technologies." *Science*, 305(5686), 968-972.

Palomino, A. M., and Santamarina, J. C. (2005). "Fabric map for kaolinite: Effects of pH and ionic concentration on behavior." *Clays and Clay Minerals*, 53(3), 211-223.

Panga, M. K. R., Ziauddin, M., and Balakotaiah, V. (2005). "Two scale continuum model for simulation of wormholes in carbonate acidization." *AIChE Journal*, 51(12), 3231-3248.

Parkhurst, D. L., Appelo, C., and Survey, G. (1999). *User's guide to PHREEQC (Version 2): A computer program for speciation, batch-reaction, one-dimensional transport, and inverse geochemical calculations*, US Geological Survey Reston, VA.

Pashin, J., Jin, G., Zheng, C., Chen, S., and McIntyre, M. (2008). "Discrete Fracture Network Models for Risk Assessment of Carbon Sequestration in Coal." Geological Survey of Alabama.

Pasten, C., and Santamarina, J. C. (2012). "Energy and quality of life." *In submission*.

Pauwels, H., Fouillac, C., and Fouillac, A. M. (1993). "Chemistry and isotopes of deep geothermal saline fluids in the Upper Rhine Graben: Origin of compounds and water-rock interactions." *Geochimica et Cosmochimica Acta*, 57(12), 2737-2749.

Pečar, D., and Doleček, V. (2005). "Volumetric properties of ethanol–water mixtures under high temperatures and pressures." *Fluid Phase Equilibria*, 230(1), 36-44.

Pekot, J. L., and Reeves, S. R. (2002). "Modeling coal matrix shrinkage and differential swelling with CO_2 injection for enhanced coalbed methane recovery and carbon sequestration applications." Advanced Resources International - U.S. Department of Energy, Houston, Texas.

Peng, D. Y., and Robinson, D. B. (1976). "A new two-constant equation of state." *Industrial & Engineering Chemistry Fundamentals*, 15(1), 59-64.

Pennell, K. D., Pope, G. A., and Abriola, L. M. (1996). "Influence of viscous and buoyancy forces on the mobilization of residual tetrachloroethylene during surfactant flushing." *Environmental Science & Technology*, 30(4), 1328-1335.

Phadnis, H. S., and Santamarina, J. C. (2011). "Bacteria in sediments: pore size effects." *Geotechnique Letters*, 1, 91-93.

Plummer, L. N., Wigley, T. M. L., and Parkhurst, D. L. (1978). "The kinetics of calcite dissolution in CO_2-water systems at 5 to 60 degC and 0.0 to 1.0 atm CO_2." *American Journal of Science*, 278, 179-216.

Pokrovsky, O. S., Golubev, S. V., and Schott, J. (2005). "Dissolution kinetics of calcite, dolomite and magnesite at 25 C and 0 to 50 atm pCO_2." *Chemical Geology*, 217(3-4), 239-255.

Prasad, K. N., Luong, T. T., FlorenceJoelle Paris, A. T., Vaution, C., Seiller, M., and Puisieux, F. (1979). "Surface activity and association of ABA polyoxyethylene--polyoxypropylene block copolymers in aqueous solution." *Journal of Colloid and Interface Science*, 69(2), 225-232.

Pruess, K., and Zhang, K. (2008). "Numerical modeling studies of the dissolution-diffusion-convection process during CO_2 storage in saline aquifers." *Lawrence Berkeley National Laboratory*.

Pusch, G., Ionescu, G. F., May, F., Voigtländer, G., Stecken, L., and Vosteen, H. D. (2010). "Common Features of Carbon Dioxide and Underground Gas Storage (1)." *Oil Gas: European Magazine*, 36(3), 131-137.

Rebata-Landa, V., and Santamarina, J. C. (2006). "Mechanical limits to microbial activity in deep sediments." *Geochemistry Geophysics Geosystems*, 7(11), Q11006.

Rebata-Landa, V., and Santamarina, J. C. (2012). "Biological clogging of soils under radial flow." under review.

Reinhardt, H. W., and Gaber, K. (1990). "From pore size distribution to an equivalent pore size of cement mortar." *Materials and Structures*, 23(1), 3-15.

Renard, F., Gundersen, E., Hellmann, R., Collombet, M., and Le Guen, Y. (2005). "Numerical modeling of the effect of carbon dioxide sequestration on the rate of pressure solution creep in limestone: Preliminary results." *Oil & Gas Science and Technology*, 60(2), 381-399.

Réveillère, A., Rohmer, J., and Manceau, J. C. (2012). "Hydraulic barrier design and applicability for managing the risk of CO_2 leakage from deep saline aquifers." *International Journal of Greenhouse Gas Control*, 9, 62-71.

Riaz, A., Hesse, M., Tchelepi, H. A., and Orr, F. M. (2006). "Onset of convection in a gravitationally unstable diffusive boundary layer in porous media." *Journal of Fluid Mechanics*, 548(1), 87-111.

Rimmelé, G., Barlet-Gouédard, V., Porcherie, O., Goffé, B., and Brunet, F. (2008). "Heterogeneous porosity distribution in Portland cement exposed to CO_2-rich fluids." *Cement and Concrete Research*, 38(8), 1038-1048.

Rosenbauer, R. J., Koksalan, T., and Palandri, J. L. (2005). "Experimental investigation of CO_2-brine-rock interactions at elevated temperature and pressure: Implications for CO_2 sequestration in deep-saline aquifers." *Fuel processing technology*, 86(14-15), 1581-1597.

Rotenberg, Y., Boruvka, L., and Neumann, A. (1983). "Determination of surface tension and contact angle from the shapes of axisymmetric fluid interfaces." *Journal of colloid and interface science*, 93(1), 169-183.

Rutqvist, J., Birkholzer, J., Cappa, F., and Tsang, C. F. (2007). "Estimating maximum sustainable injection pressure during geological sequestration of CO_2 using coupled fluid flow and geomechanical fault-slip analysis." *Energy Conversion and Management*, 48(6), 1798-1807.

Rutqvist, J., Birkholzer, J., and Tsang, C. F. (2008). "Coupled reservoir–geomechanical analysis of the potential for tensile and shear failure associated with CO_2 injection in multilayered reservoir–caprock systems." *International Journal of Rock Mechanics and Mining Sciences*, 45(2), 132-143.

Rutqvist, J., and Tsang, C. F. (2002). "A study of caprock hydromechanical changes associated with CO_2-injection into a brine formation." *Environmental Geology*, 42(2), 296-305.

Ryoo, W., Webber, S. E., and Johnston, K. P. (2003). "Water-in-carbon dioxide microemulsions with methylated branched hydrocarbon surfactants." *Industrial & engineering chemistry research*, 42(25), 6348-6358.

Saadatpoor, E., Bryant, S. L., and Sepehrnoori, K. (2009). "Effect of capillary heterogeneity on buoyant plumes: A new local trapping mechanism." *Energy Procedia*, 1(1), 3299-3306.

Sabins, F., and Rozieres, D. (1995). "Shrinkage and Expansion in Oil Well Cements." *API Work Group on Shrinkage*.

Santamarina, J. C. (2001). "Soil behavior at the microscale: particle forces." *Symp. Soil Behavior and Soft Ground Construction, in honor of Charles C. Ladd*MIT.

Saripalli, P., and McGrail, P. (2002). "Semi-analytical approaches to modeling deep well injection of CO_2 for geological sequestration." *Energy Conversion and Management*, 43(2), 185-198.

Sawamura, S., Egoshi, N., Setoguchi, Y., and Matsuo, H. (2007). "Solubility of sodium chloride in water under high pressure." *Fluid phase equilibria*, 254(1-2), 158-162.

Shapiro, A. M. (2010). "Addressing the complexities of contamination and remediation in fractured rock aquifers." *Federal Remediation Technologies Roundtable*.

Sharma, M., and Yortsos, Y. (1987). "Fines migration in porous media." *AIChE journal*, 33(10), 1654-1662.

Sharma, S., Cook, P., Berly, T., and Lees, M. (2009). "The CO_2CRC Otway Project: Overcoming challenges from planning to execution of Australia’s first CCS project." *Energy procedia*, 1(1), 1965-1972.

Shi, J. Q., and Durucan, S. (2009). "A coupled reservoir-geomechanical simulation study of CO_2 storage in a nearly depleted natural gas reservoir." *Energy Procedia*, 1(1), 3039-3046.

Shi, J. Q., Xue, Z., and Durucan, S. (2007). "Seismic monitoring and modelling of supercritical CO_2 injection into a water-saturated sandstone: Interpretation of P-wave velocity data." *International Journal of Greenhouse Gas Control*, 1(4), 473-480.

Shin, H., and Santamarina, J. C. (2009). "Mineral Dissolution and the Evolution of k_0." *Journal of Geotechnical and Geoenvironmental Engineering*, 135(8), 1141-1147.

Shin, H., and Santamarina, J. C. (2010). "Fluid-driven fractures in uncemented sediments: Underlying particle-level processes." *Earth and Planetary Science Letters*, 299(1), 180-189.

Shin, H., Santamarina, J. C., and Cartwright, J. A. (2008). "Contraction-driven shear failure in compacting uncemented sediments." *Geology*, 36(12), 931-934.

Shin, H., Santamarina, J. C., and Cartwright, J. A. (2010). "Displacement field in contraction-driven faults." *Journal of Geophysical Research*, 115(B7), B07408.

Sloan, E. D., and Koh, C. A. (2008). *Clathrate hydrates of natural gases, 3rd Ed.*, CRC Press, Boca Raton, FL.

Solomon, S. (2007). *Climate Change 2007: the physical science basis: contribution of Working Group I to the Fourth Assessment Report of the Intergovernmental Panel on Climate Change*, Cambridge Univ Pr.

Solomon, S., Carpenter, M., and Flach, T. A. (2008). "Intermediate storage of carbon dioxide in geological formations: A technical perspective." *International Journal of Greenhouse Gas Control*, 2(4), 502-510.

Soltanzadeh, H., and Hawkes, C. D. (2009). "Assessing fault reactivation tendency within and surrounding porous reservoirs during fluid production or injection." *International Journal of Rock Mechanics and Mining Sciences*, 46(1), 1-7.

Somerton, W. H., Soylemezolu, I. M., and Dudley, R. C. (1975). "Effect of stress on permeability of coal." *International Journal of Rock Mechanics and Mining Science & Geomechanics Abstracts*, 12(5-6), 129-145.

Span, R., and Wagner, W. (1996). "A new equation of state for carbon dioxide covering the fluid region from the triple point temperature to 1,100 K at pressures up to 800 MPa." *Journal of Physical and Chemical Reference Data*, 25(6), 1509-1596.

Sposito, G. (1994). *Chemical equilibria and kinetics in soils*, Oxford University Press, USA.

Spycher, N., Pruess, K., and Ennis-King, J. (2003). "CO_2-H_2O mixtures in the geological sequestration of CO_2. I. Assessment and calculation of mutual solubilities from 12 to 100 C and up to 600 bar." *Geochimica et Cosmochimica Acta*, 67(16), 3015-3031.

Stone, M. T., Smith Jr, P. G., da Rocha, S. R. P., Rossky, P. J., and Johnston, K. P. (2004). "Low interfacial free volume of stubby surfactants stabilizes water-in-carbon dioxide microemulsions." *The Journal of Physical Chemistry B*, 108(6), 1962-1966.

Strazisar, B. R., Wells, A. W., Diehl, J. R., Hammack, R. W., and Veloski, G. A. (2009). "Near-surface monitoring for the ZERT shallow CO_2 injection project." *International Journal of Greenhouse Gas Control*, 3(6), 736-744.

Streit, J. E., and Hillis, R. R. (2004). "Estimating fault stability and sustainable fluid pressures for underground storage of CO_2 in porous rock." *Energy*, 29(9-10), 1445-1456.

Stumm, W., Morgan, J. J., and Drever, J. I. (1996). *Aquatic Chemistry*, John Wiley and Sons, New York.

Suekane, T., Soukawa, S., Iwatani, S., Tsushima, S., and Hirai, S. (2005). "Behavior of supercritical CO_2 injected into porous media containing water." *Energy*, 30(11-12), 2370-2382.

Sutjiadi-Sia, Y., Jaeger, P., and Eggers, R. (2008). "Interfacial tension of solid materials against dense carbon dioxide." *Journal of Colloid and Interface Science*, 320(1), 268-274.

Sutjiadi-Sia, Y., Marckmann, H., Eggers, R., Holzknecht, C., and Kabelac, S. (2007). "The effect of in liquids dissolved dense gases on interfacial and wetting characteristics." *Forschung Im Ingenieurwesen-Engineering Research*, 71(1), 29-45.

Sydansk, R. D., Xiong, Y., Al-Dhafeeri, A. M., Schrader, R. J., and Seright, R. S. (2005). "Characterization of partially formed polymer gels for application to fractured production wells for water-shutoff purposes." *SPE Production & Facilities*, 20(3), 240-249, SPE 89401.

Szymczak, P., and Ladd, A. J. C. (2009). "Wormhole formation in dissolving fractures." *Journal of Geophysical Research*, 114, B06203.

Szymczyk, K., and Jańczuk, B. (2008). "Wettability of a glass surface in the presence of two nonionic surfactant mixtures." *Langmuir*, 24(15), 7755-7760.

Takenouchi, S., and Kennedy, G. (1965). "Dissociation pressures of the phase $CO_2 \cdot 5.75H_2O$." *Journal of Geology*, 73, 383–390.

Tanaka, Y., Matsuda, Y., Fujiwara, H., Kubota, H., and Makita, T. (1987). "Viscosity of (water+ alcohol) mixtures under high pressure." *International journal of thermophysics*, 8(2), 147-163.

Trask, R., Williams, H., and Bond, I. (2007). "Self-healing polymer composites: mimicking nature to enhance performance." *Bioinspiration & biomimetics*, 2, P1.

Tsouris, C., Aaron, D. S., and Williams, K. A. (2010). "Is Carbon Capture and Storage Really Needed? 1." *Environmental Science & Technology*, 44(11), 4042-4045.

van Genuchten, M. T. (1980). "A closed-form equation for predicting the hydraulic conductivity of unsaturated soils." *Soil Sci. Soc. Am. J*, 44(5), 892-898.

Verdon, J., and Woods, A. W. (2007). "Gravity-driven reacting flows in a confined porous aquifer." *Journal of Fluid Mechanics*, 588, 29-41.

Vidal-Gilbert, S., Tenthorey, E., Dewhurst, D., Ennis-King, J., Van Ruth, P., and Hillis, R. (2010). "Geomechanical analysis of the Naylor Field, Otway Basin, Australia: Implications for CO_2 injection and storage." *International Journal of Greenhouse Gas Control*, 4(5), 827-839.

Viswanathan, H. S., Pawar, R. J., Stauffer, P. H., Kaszuba, J. P., Carey, J. W., Olsen, S. C., Keating, G. N., Kavetski, D., and Guthrie, G. D. (2008). "Development of a hybrid process and system model for the assessment of wellbore leakage at a geologic CO_2 sequestration site." *Environmental science & technology*, 42(19), 7280-7286.

Watney, W. L., and Bhattacharya, S. (2011). "Modeling CO_2 sequestration in saling aquifer and depleted oil reservoir to evaluate regional CO_2 sequestration potential of Ozark Plateau Aquifer System, South-Central Kansas." *6th Quarter Progress Report (DE-FE0002056)*.

Watson, M. N., Zwingmann, N., and Lemon, N. M. (2004). "The Ladbroke Grove-Katnook carbon dioxide natural laboratory: A recent CO_2 accumulation in a lithic sandstone reservoir." *Energy*, 29(9-10), 1457-1466.

Weir, G. J., White, S. P., and Kissling, W. M. (1996). "Reservoir storage and containment of greenhouse gases." *Transport in porous media*, 23(1), 37-60.

Wellman, T., Grigg, R., McPherson, B., Svec, R., and Peter, C. "Evaluation of CO_2-brine-reservoir rock interaction with laboratory flow tests and reactive transport modeling." *Proc., SPE International Syposium on Oilfield Chemistry*, SPE-80228.

White, D. J., Burrowes, G., Davis, T., Hajnal, Z., Hirsche, K., Hutcheon, I., Majer, E., Rostron, B., and Whittaker, S. (2004). "Greenhouse gas sequestration in abandoned oil reservoirs: The International Energy Agency Weyburn pilot project." *GSA today*, 14(7), 4-10.

White, S. P., Allis, R. G., Moore, J., Chidsey, T., Morgan, C., Gwynn, W., and Adams, M. (2005). "Simulation of reactive transport of injected CO_2 on the Colorado Plateau, Utah, USA." *Chemical Geology*, 217(3-4), 387-405.

Wielopolski, L., and Mitra, S. (2010). "Near-surface soil carbon detection for monitoring CO_2 seepage from a geological reservoir." *Environmental Earth Sciences*, 60(2), 307-312.

Wigand, M., Carey, J. W., Schütt, H., Spangenberg, E., and Erzinger, J. (2008). "Geochemical effects of CO_2 sequestration in sandstones under simulated in situ conditions of deep saline aquifers." *Applied Geochemistry*, 23(9), 2735-2745.

Wigand, M., Kaszuba, J. P., Carey, J. W., and Hollis, W. K. (2009). "Geochemical effects of CO_2 sequestration on fractured wellbore cement at the cement/caprock interface." *Chemical Geology*, 265(1), 122-133.

Wollenweber, J., Alles, S., Busch, A., Krooss, B. M., Stanjek, H., and Littke, R. (2010). "Experimental investigation of the CO_2 sealing efficiency of caprocks." *International Journal of Greenhouse Gas Control*, 4(2), 231-241.

World-Resources-Institute (2010). "Climate Analysis Indicator Tool (CAIT) version 7.0." <http://cait.wri.org/>.

World-Resources-Institute (2010). "Earth Trends (Energy and resources-country profiles) http://earthtrends.wri.org." (2010-12-01).

Xu, T., Apps, J. A., and Pruess, K. (2005). "Mineral sequestration of carbon dioxide in a sandstone-shale system." *Chemical Geology*, 217(3-4), 295-318.

Xu, T., Sonnenthal, E., Spycher, N., and Pruess, K. (2006). "TOUGHREACT--A simulation program for non-isothermal multiphase reactive geochemical transport in variably saturated geologic media: applications to geothermal injectivity and CO_2 geological sequestration." *Computers & Geosciences*, 32(2), 145-165.

Xue, Z., Ohsumi, T., and Koide, H. (2005). "An experimental study on seismic monitoring of a CO_2 flooding in two sandstones." *Energy*, 30(11-12), 2352-2359.

Zerai, B., Saylor, B. Z., and Matisoff, G. (2006). "Computer simulation of CO_2 trapped through mineral precipitation in the Rose Run Sandstone, Ohio." *Applied Geochemistry*, 21(2), 223-240.

Zhai, Z., and Sharma, M. M. "A new approach to modeling hydraulic fractures in unconsolidated sands." *Proc., SPE Annual Technical Conference and Exhibition*.

Zhang, Y. (2008). *Geochemical kinetics*, Princeton Univ Pr.

VITA

SEUNGHEE KIM

Seunghee was born in Seoul, Korea. He attended Gyeonggi Science High School in Suwon, Gyeonggi, Korea where he developed a kin interest for mathematics and physics. He received a B.S. at 2003 and a M.S. at 2005 in the Civil and Environmental Engineering from Korea Advanced Institute of Science and Technology (KAIST), Daejeon, Korea. He completed the military service while working at Dongho Co. Ltd. and the Korea Institute of Construction Technology (KICT). He was accepted at the Georgia Institute of Technology in 2008 and received a Ph.D. in the Civil and Environmental Engineering at 2012. Seunghee will pursue an academic career.